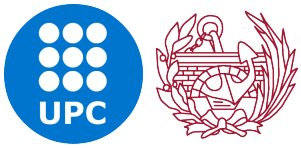

School of Civil Engineering of Barcelona
UPC BARCELONATECH

Visco-plasticity of zero-thickness interfaces with softening, and application to the study of fault reactivation

Doctoral Thesis submitted by:
Irene Jaqués Adell

Supervised by:
Ignacio Carol

Doctoral Program in Geotechnical Engineering
Area of Civil and Environmental Engineering
School of Civil Engineering (ETSECCPB)

Barcelona, November 2022

Agraïments

Prendre la decisió de fer el doctorat no va ser fàcil però ara puc dir que va ser l'opció encertada. Aquests anys dedicats a la recerca m'han permès créixer i millorar els coneixements en l'àmbit de la Geomecànica i, alhora, també m'ha permès desenvolupar una gran capacitat de treball tant individual com en equip.

En primer lloc m'agradaria agrair l'ajuda i suport del meu director de tesi, el professor Ignasi Carol. Podria anomenar moltes virtuts però especialment voldria remarcar la seva immensa paciència, la voluntat i capacitat de transmetre coneixements, la seva incansable dedicació independentment del dia i l'hora, i també les idees originals que han permès obrir nous camins de recerca i avançar. Per tot això i molt més, puc dir que sense ell aquesta tesi no hagués sigut possible. Gràcies.

Agrair també al Daniel, sempre disposat a ajudar en qualsevol moment. Li estic mol agraïda per la seva generositat, pel seu recolzament tant en temes tècnics com d'implementació en el codi i pels seus consells respecte a la gestió del doctorat que han segut fonamentals.

Vull fer una especial menció a la Laura, companya i amiga que sempre ha estat quan l'he necessitat. Una persona essencial que m'ha ajudat a créixer en tots els sentits. Poder comptar amb la seva sempre equilibrada opinió i amb els seus consells sobre qualsevol tema, tant personal com tècnic, ha estat un privilegi i una gran sort.

Fent referència als orígens, estic molt agraïda al Carles i a l'Ignasi A. amb qui vaig començar a treballar en el tema de tensions inicials. Ells em van ajudar sempre en els moments de confusió i van tenir la generositat de dedicar-me temps per resoldre qualsevol tipus de dubte. Posteriorment, l'Ignasi A. va continuar compartint amb mi els seus desenvolupaments en visco-plasticitat els quals van ser el punt de partida d'aquesta tesi.

Durant aquests cinc anys i mig he tingut la sort de poder formar part d'un grup de recerca extraordinari com és MECMAT. He tingut l'oportunitat de conèixer gent magnífica que d'una manera o altra han contribuït en el desenvolupament d'aquest treball com son els professors Pere Prat i Carlos María López, i la resta de companys: l'Ariadna, la Lola, l'Adrià, l'Andreu, la Caterina i el Joaquin.

Voldria agrair al Lluís la seva amabilitat donant ànims amb l'alegria que el caracteritza i oferint ajuda tècnica en els moments d'averies elèctriques al D2, gràcies a ell he pogut restablir les connexions remotes amb l'ordinador del despatx i seguir treballant amb normalitat. També agrair al Rodrigo qui sempre ha estat pendent de la meva feina, del meu estat d'ànim i, sempre que ho he necessitat, m'ha donat força per avançar.

És ben cert que qui té un amic té un tresor i jo tinc la sort de comptar amb la Mariona, l'Andrea i la Cristina R. Mai podré agrair prou el seu recolzament incondicional, la seva paciència i la seva comprensió davant les meves excentricitats, a vegades difícils de gestionar. En aquest sentit, vull donar-li les gràcies a la Camila, la meva companya de pis, per acompanyar-me durant l'últim any i mig que ha segut el més difícil. La seva capacitat per intuir els bons i mals moments oferint aquella abraçada tan necessària, els seus consells: "Hay que disfrutar del proceso", les conversacions que em permetien exterioritzar i alliberar preocupacions, tot plegat m'ha ajudat a continuar treballant amb ganes i voluntat de millorar.

També agrair la generositat i amabilitat de la Lisa i el Joao oferint sempre el seu suport de forma desinteressada. En tot moment han mostrat interès per la feina desenvolupada durant aquests anys de doctorat i m'han ajudat quan ha segut necessari.

Finalment, agrair a la meva família. La meva mare Anita, el meu pare Vicente, el meu germà Juan i el meu tiet José Antonio. No hi ha paraules per agrair tot el que han fet per mi. Per la confiança, pel continu recolzament, per donar-me el seu punt de vista davant una decisió important, per l'ajuda, pels consells, per la infinita paciència, per tot això i molt més. Moltes gràcies.

Per últim, mencionar també l'aportació econòmica en forma de beca FI-AGAUR rebuda durant els tres primers anys de doctorat a càrrec de la Generalitat de Catalunya.

Irene Jaqués Adell, Barcelona Novembre 2022

Abstract

In the current context of both energy and environmental needs, there has been an increase in activities related to extraction and injection of fluids in the underground. It is known that a possible consequence of these activities is the reactivation of faults and, therefore, there has recently been of growing interest to understand under what conditions these events may occur and to try to avoid them or minimize their effects. In this sense, the main aim of this thesis is to develop tools that can contribute to a better understanding of the geomechanical processes that take place during fault reactivation events, either when they occur naturally or are induced by any human activity.

In the present thesis a methodology is proposed to identify when an instability may be triggered and, also, quantify the amount of energy released during the unstable process. Moreover, the methodology proposed can be applied in both mechanical and hydro-mechanical cases, which implies that instability may be generated by either mechanical actions or fluid injections/extractions. The numerical model is based on the Finite Element Method in which fractures are represented by zero-thickness interface elements equipped with constitutive laws based on Fracture Mechanics principles. In particular, the constitutive model used consists of the reformulation of an existing fracture-based interface constitutive law (*Normal/Shear Cracking Model*) in terms of visco-plasticity with Hardening/Softening.

Two instability control strategies have also been implemented: (1) a new Indirect Displacement Control method based on the visco-plastic dissipation (IDC-Wvp) and (2) an adaptation of the Visco-plastic Relaxation method (VPR). Regarding the first one, it has been found that the method can only be easily applied in purely mechanical cases, and for this reason VPR has finally been the method used to model unstable cases including mechanical and hydro-mechanical.

A procedure has been developed for identifying the occurrence of mechanical instabilities such as snap-back or similar sudden events. This procedure is based on the continuous tracking of the various types of energy dissipation occurring along the discontinuity at the level of the constitutive visco-plastic model. It has been found that when a mechanical instability takes place, a jump is observed in the dissipation diagrams, and a difference emerges between two types of visco-plastic dissipation: total VP dissipation and VP dissipation based on projected stresses. This difference turns out to correspond to the Viscous energy dissipated by the interface during the transit through the instability, and therefore it can be associated to the energy released by the unstable event.

Finally, the methodology proposed in this thesis was verified through academic examples which represent different fracture mechanisms that can be produced in a geomechanical scenario. Moreover, some more realistic examples are also presented where instability is induced by the effects of

fluid pressure or fluid flow.

Overall this thesis tries to contribute to develop numerical tools for the assessment of fault reactivation problems, not only to identify the existence of an instability, but also to quantify the energy released in these processes, energy that then may be eventually linked with the earthquake magnitude.

Resum

En el context actual de necessitats tant energètiques com ambientals, s'ha produït un increment de les activitats relacionades amb l'extracció i injecció de fluids al subsòl. Com és ben sabut, una de les possibles conseqüències d'aquestes activitats és la reactivació de falles i, per aquesta raó, l'interès per entendre millor sota quines condicions es produeixen aquests esdeveniments s'ha incrementat amb la intenció d'intentar evitar-los o minimitzar els seus efectes. En aquest context, l'objectiu principal d'aquesta tesi és proporcionar les eines necessàries que permetin entendre millor els processos geomecànics que es produeixen en els esdeveniments de reactivació de falles, tant si es produeixen de forma natural com si son induïts per qualsevol activitat humana.

En aquesta tesi es proposa una metodologia per identificar quan es pot desencadenar una inestabilitat i, també, avaluar la quantitat d'energia alliberada durant el procés inestable. A més, la metodologia proposada es pot aplicar tant en casos mecànics com hidro-mecànics, la qual cosa implica que la inestabilitat es pot generar tant per accions mecàniques com per injeccions/extraccions de fluids. El model numèric es basa en el mètode d'Elements Finits on les fractures estan representades per elements junta de gruix zero equipades amb lleis constitutives basades en els principis de la Mecànica de Fractura. El procediment desenvolupat consisteix en la reformulació de la ja existent llei constitutiva no lineal per fractures anomenada *Normal/Shear Cracking Model* en termes de visco-plasticitat amb "Hardening/Softening".

També s'han implementat dues estratègies de control de la inestabilitat: (1) un nou mètode de control de desplaçament indirecte basat en la dissipació visco-plàstica (IDC-Wvp) i (2) una adaptació del mètode de Relaxació Visco-plàstica (VPR). Pel que fa al primer, s'ha comprovat que el mètode només es pot aplicar fàcilment en casos purament mecànics, i per aquest motiu l'estratègia VPR ha estat finalment el mètode utilitzat per modelar casos inestables incloent mecànics i hidro-mecànics.

Una de les contribucions més importants d'aquesta tesi és el desenvolupament d'un procediment capaç d'identificar l'aparició d'inestabilitats mecàniques com ara "snap-back" o altres esdeveniments semblants que es produeixen de forma sobtada. Aquest procediment es basa en l'anàlisi de l'evolució dels diferents tipus de dissipació d'energia que es produeixen al llarg de la discontinuïtat a nivell del model constitutiu visco-plàstic. S'ha vist que quan es produeix una inestabilitat mecànica, s'observa un salt en els diagrames de dissipació, i sorgeix una diferència entre dos tipus de dissipació visco-plàstica: la dissipació VP total i la dissipació VP basada en les tensions projectades. Aquesta diferència correspon a l'energia Viscosa dissipada per la junta durant el trànsit per la inestabilitat, i, per tant, es podria associar a l'energia alliberada per l'esdeveniment inestable.

Finalment, s'ha verificat la metodologia proposada en aquesta tesi a través de diversos exemples acadèmics els quals representen diferents mecanismes de fractura que es poden produir en l'àmbit de la Geomecànica. A més, també es presenten alguns exemples més realistes on la inestabilitat és induïda pels efectes de pressió o cabal imposats de fluid.

Globalment, aquesta tesi intenta contribuir al desenvolupament de mètodes numèrics per l'avaluació dels problemes de reactivació de falles, no només identificant l'existència d'una inestabilitat, sinó també quantificant l'energia alliberada en aquests processos, energia que després es podria relacionar directament amb la magnitud del terratrèmol.

Contents

Chapter 1

Introduction

Contents

1.1 Background and Motivation

Seismicity due to fault reactivations caused by human activities was firstly recorded and recognized in Johannesburg in 1894 (McDonald, 1982) attributed to the Witwatersrand gold production, which had started in 1886 (Cook et al., 1966). Since then, many other cases of induced seismicity have been identified and studied all over the world.

Induced earthquakes can occur as a result of many types of activities and be generated by different failure mechanisms. As a starting point, mining-induced earthquakes are those in which seismicity is stimulated by quarry or deep mining. In this kind of events the cause-effect relationship is well established. Quarries and deep-level mining cause the water table to be depressed because pumping operations to prevent flooding. This change in the water table generates alterations in pore pressure of the surrounding area consequently leading to stress changes in depth. Under certain conditions, these underground alterations can trigger a reactivation of existing disturbances or cause new fractures in the rock. Continuing with surface activities, reservoir impoundment can also stimulate seismicity due to the subsequent increase in pore pressure. Moreover, filling and

emptying cycles generate changes in the pore pressure that, if they are quick enough, may also trigger fault instability.

Seismicity may be induced also by fluid injection at depth, which can increase the pore pressure in the zone surrounding the injection point, therefore affecting existing faults or fractures in the area. The processes involved in the generation of this anthropogenic (or man-caused) seismicity include pore pressure increase which decrease the effective normal stress and therefore also the frictional shear strength in rock fractures, sometimes leading to abrupt shifts along existing rupture surfaces, volume changes which affect rock stresses and may lead to new fractures or to the reactivation of existing ones and, finally, chemical changes. Chemical agents, such as acids, are often used in fracking operations to increase the water permeability of the rock. Due to the dissolution and deposition caused by the introduction of the chemicals, the rock normal volume and stress is altered, thus leading to a change in shear strength due to rock friction. If shear strength is reduced, naturally built-up stresses need to be released. In addition, another type of seismicity stimulated by underground activities consists of earthquakes caused by the exploitation of major oil and gas fields. Oil or gas production reduces pore pressure within the reservoir, causing contraction and inducing total and effective stress changes in nearby areas. Moreover, underground injection or extraction of fluids or gases causes changes of the volume in the interstitial spaces of the rock generating disturbances in the near fractures and potentially making them unstable.

Finally, geothermal energy exploitation may also stimulate seismicity. To the mechanisms mentioned above that induce seismicity such as pore pressure increase, volume changes, etc. in the case of geothermal energy we can also add the mechanism of thermo-elastic deformation. In geothermal energy production, cold water is injected into the rock, where it heats up, and is then transported back to the surface. A side effect of this is that the rock surrounding the injection well cools down and contracts, while the rock surrounding the extraction well heats up and dilates. The resulting stresses may lead to shifts in the existing fractures.

As it was mentioned at the beginning of this section and trying to make a general historical review, stimulated seismicity was firstly studied in Johannesburg in 1894 (McDonald, 1982) when seismic events were felt (by the population) and later, these earthquakes were attributed to the Witwatersrand gold production, which had started in 1886 (Cook et al., 1966). In Europe the scientific community began to focus on mining seismicity in 1908 when the first seismological observatory was established in Bochum in the Ruhr coal Basin (Germany) to monitor these phenomena. After that, in the late 1920s, the first seismic network was installed in the Upper Silesia coal basin, Poland (Gibowicz and Kijko, 1994). Moreover, seismicity associated with petroleum production

became apparent in 1920s, with reservoir impoundment in the late 1930s, with high-pressure liquid injection at depth in the mid-1960s, and with natural gas production in the late 1960s (McGarr et al., 2002).

Nowadays, it is known that stimulated seismicity can have multiple origins associated with underground and surface activities. The most relevant seismic events that have been attributed to human activity have been recorded in the Human-induced Earthquake Database (HiQuake) (Foulger et al., 2018). This database contains over 700 cases covering the period from 1868 to 2016 which have been classified into four categories such as caused by surface operations, by extraction of mass from the surface, by introduction of mass into the subsurface and by explosions. Some of the most relevant cases in the data base are:

Surface operations

- Water impoundment behind dams (Zipingpu dam, Wenchuan, China, 2008 (Klose, 2012) and Koyna Dam, India, 1967 (Gupta, 2002)).

Extraction from the subsurface

- Groundwater extraction (Lorca, Spain, 2011) (González et al., 2012).
- Mining (Völkershausen Ernst Thaelmann/Merkers potash mine, Germany, 1989 (Bennett et al., 1994; Knoll, 1990) and Klerksdrop district, South Africa, 2005 (Durrheim et al., 2006)).
- Solution mining (Zigong salt mine, Sichuan Province, China, 1985) (Li et al., 2007).
- Tunnel excavation (Gotthard Base Tunnel, Switzerland, 2002-2006) (Husen et al., 2012).
- Hydrocarbons:
  - Gas production (Gazli reservoir, Uzbekistan, 1976 and 1984 (Simpson and Leith, 1985) and Groningen Field, Netherlands (Van Eck et al., 2006; Van Wees et al., 2014)).
  - Oil production (Coalinga and Whittier Narrows events, California, USA, 1985) (McGarr, 1991).
- Geothermal energy extraction (Cerro Prieto Field, Imperial Valley, Mexico, 1987) (Glowacka and Nava, 1996).

Injection into the subsurface

- Liquid:

  - Wastewater disposal (Pawnee and Prague earthquakes, Oklahoma, USA, 2016 and 2011 respectively) (Yeck et al., 2017; Keranen et al., 2013).
  - Water injected for enhanced oil recovery (Wilmington Oilfield, Los Angeles Basin, California, 1971) (Nicholson and Wesson, 1992).
  - Enhanced Geothermal Systems – EGS (Basel, Switzerland, 2006) (Zang et al., 2014).
  - Geothermal reinjection (The Geysers field, California, USA, 2004) (Majer and Peterson, 2007; Stark, 1990).
  - Shale-gas hydrofracturing (Crooked Lake, Alberta, Canada, 2013) (Schultz et al., 2015).
  - Allowing mines to flood (Cacoosing Valley, Pennsylvania, USA, 1994) (Seeber et al., 1998).

- Gas:
  - Natural gas storage (the Castor project in the old Amposta Field, Spain,2013) (Cesca et al., 2014; Gaite et al., 2016).
  - Carbon Capture and Storage – CCS (In Salah, Algeria, 2010) (Verdon et al., 2013).

Explosions

- Underground nuclear tests in Amchitka, Alaska, notably both the Milrow (1969) and Cannikin (1971) tests. (McKeown and Dickey, 1969; Engdahl, 1972).

Induced seismicity is an important problem that scientific society and companies must face in recent and future times. For that reason, it is necessary to obtain the maximum information from the field installing an extensive seismic network before and after starting the activity, with the maximum information about underground conditions. And all this should be accompanied by the appropriate development of a geomechanical model. Modeling each case of study contributes to a better understanding of the ground response to an external fluid injection, the effects on faults or discontinuities found in the surrounding area and the rupture mechanisms that can stimulate seismicity. In addition, numerical modeling is a very efficient tool for drawing results and conclusions about the phenomenon and evaluating the possibility of developing practical recommendations to avoid fault reactivations induced by fluid injection, which is the main motivation of this thesis.

1.2 Thesis objectives

The main objective of this thesis is to develop a methodology capable of describing the hydro-mechanical phenomena related to fault reactivation using numerical models, and more specifically the Finite Element Method. These reactivations may lead to seismic activity generating earthquakes the magnitude of which depends on the area of the fault plane affected, the fault offset, the speed of the movement and the depth of the faults involved in the process. All these factors may influence the amount of energy released. Seismic events stimulated by the human activities mentioned in the previous section occur relatively often and depending on their magnitude may cause major problems by either damaging structures and generating delays in the development of projects, or causing environmental damage or effects on the daily activity of the population living near the affected area.

The fact that this kind of seismicity may be the result of certain industrial or construction operations (e.g. fluid injections), has motivated more studies or research on the subject to increase knowledge about the reactivation mechanisms and under what conditions seismic reactivations may occur. Increasing knowledge about this type of phenomena leads to perform better analysis of the problem and to propose control methods to avoid seismic events of such magnitudes that can generate both material and personal damage. The content of this thesis is focused on this line of research and the aim is to develop a procedure based on numerical modelling that allows the Engineer a better understanding of the conditions under which discontinuities become unstable and consequently, a seismic event may be generated. The analysis is intended to be carried out from the point of view (framework) of a quasi-static approach and Fracture Mechanics.

As it can be seen in some laboratory tests such as Wedge Splitting Test (WST) or Three- Point Bending Test of concrete or rock, there is a range of specimen dimensions and parameter values for which, even under displacement control conditions, after a certain critical load level has been reached, specimen failure develops in an uncontrollable manner. In other words, once the unstable failure has started, even if the prescribed displacements are stopped the fracture continues to spread through the specimen.

When this type of failure mechanism occurs and it takes place in the context of a coupled H-M problem, the standard iterative calculation tools available such as Newton-Raphson or Arc-Length may be not applicable. Therefore, in order to overcome this problem, the general objective of this thesis is to develop a new methodology that may be used to solve the H-M problem including the case of mechanical instabilities, and that indicates when these instabilities take place and, if possible, also quantify the energy released during those events. Considering also the numerical and

theoretical tools available in the research group, from this general objective, the following specific objectives may be enumerated:

1. Understanding failure mechanisms involved in fault reactivation processes in order to propose a methodology capable to numerically simulate these phenomena in the most accurate way possible.

2. Formulating a new visco-plastic approach for zero-thickness interface elements as a basis of the new methodology to tackle the fault reactivation problem.

3. Identifying the fault reactivation problem as an unstable process, some control methodologies need to be proposed to evaluate the crack propagation and understand the fracture behavior in each case.

4. Evaluating fault reactivation phenomenon as a hydro-mechanical (H-M) problem, the methodology proposed needs to be adapted and implemented in the Finite Element code of the research group in order to be able to model the H-M coupled phenomena.

5. Verification of all methodologies proposed with academic examples representing practical geomechanical cases in order to identify when the instability occurs.

6. Application of the methodology proposed to cases with more complexity in order to do a step forward to more realistic cases of fault reactivation by fluid injection.

7. Evaluation of the energy balance in order to quantify the energy released in unstable cases.

1.3 Methodology

This thesis is developed in the context of Geomechanics, and involves concepts of Fracture Mechanics, Visco-plasticity, zero-thickness interface elements, energy and work, numerical methods as Finite Element Method and hydro-mechanical coupling. The methodologies proposed in this thesis are envisaged to face problems in different areas of study such as geotechnical and petroleum engineering, as well as mining, geothermal energy extraction and some sectors of civil engineering such as water impoundment behind dams, groundwater extraction and tunnelling.

The present thesis has been developed in the context of the MECMAT research group (Group of Mechanics of Engineering Materials). The group is constantly working to developing new theories and numerical tools that contribute to a better understanding of fracture mechanics in quasi-brittle

materials such as rocks or concrete, and to solving engineering problems in the area. With this purpose, innovative approaches in the rock mechanics field have been proposed and implemented in the group's main FE code DRAC. Many researchers have been involved in the development of this code over the years (López, 1999; Caballero, 2005; Segura, 2007; Idiart, 2009; Garolera, 2017; Liaudat, 2018; Crusat, 2018; Pérez, 2018; Martínez, 2020; Rodríguez, 2020; De Francisco, 2021) since it was first proposed by I. Carol and P. Prat in early 90s (Prat et al., 1993).

The main lines of work which have been concentrated most of the effort are detailed below:

Literature review. First of all, an exhaustive literature review was carried out to identify the different scientific approaches proposed in order to study quantitatively the fault reactivation problems. As the result, it was concluded that an analysis carried out from the viewpoint of quasi-statics and fracture mechanics seems not to exist in the literature. In addition, no references have been found concerning the identification of an instability and quantification of the energy released in these unstable processes. After this initial (and to a certain extent, also unexpected and surprising) finding, the bibliographic research has been focused on three key aspects such as Visco-plasticity theory, iterative methods that could be useful to propose a new numerical tool capable of controlling sudden fracture propagation processes, and energy balance assessment.

Visco-plastic constitutive law. Formulation and implementation of energy-based softening visco-plastic constitutive law for interface elements as an extension of an elastic-perfectly visco-plastic interface model previously proposed in the research group by Aliguer et al. (2017).

IDC-Wvp method. Development of a new Indirect Displacement Control method based on the visco-plastic dissipation (IDC-Wvp) using time as a controlling magnitude.

VPR method. Implementation of Visco-plastic Relaxation (VPR) as an instability control method that makes it possible to use two types of time simultaneously, both physical and fictitious time.

Energy balance. Evaluation of the energy balance in order to recognize all existing energy dissipation mechanisms and quantify the energy released that could determine the size of the seismic event.

Fault reactivation simulations. Adjusting all methodologies to hydro-mechanical coupling and trying to reproduce a stimulated fault reactivation problem in a way as real as possible.

1.4 Thesis organization

The thesis document is organized in five chapters: the Introduction is the first chapter, the second chapter is devoted to describe the new energy-based visco-plastic constitutive law considering hardening/softening for zero-thickness interfaces, this is followed by the third chapter dedicated to introduce the instability control methods in visco-plasticity, then the energy balance assessment is contained in the fourth chapter and, finally, the fifth chapter summarizes the most important contributions of this thesis and the future lines of research.

The present Introduction starts explaining the background and motivation that has led to this research work, then the objectives and the methodology followed in the thesis development are detailed and, to conclude, a brief description of the chapters involved in this thesis is provided.

The second chapter contains a comprehensive description of the visco-plastic approach proposed for the existing elasto-plastic constitutive law for zero-thickness interfaces. First, some preliminary considerations regarding visco-plasticity, zero-thickness interface elements and stress-driven integration algorithms are presented and the already existing perfect visco-plastic constitutive law, previously developed in the research group, is also introduced. Then, the extension to hardening/softening visco-plasticity is presented and, to conclude, the highlights of the hydro-mechanical coupled formulation are also mentioned in this chapter.

The third chapter focuses on the instability control methods in visco-plasticity. The new Indirect Displacement Control method based on visco-plastic dissipation (IDC-Wvp) and the Visco-plastic Relaxation method (VPR) are described. Moreover, some academic examples which represent different fracture mechanisms that usually occur in geomechanical problems are presented in order to verify the control strategies presented in this chapter.

The fourth chapter is dedicated to energy balance assessment. The energy approach starts introducing all energy dissipation terms that may be involved in both mechanical and hydro-mechanical problems. Then the energy balance is described and, finally, the calculation of different examples (mechanical, hydraulic and hydro-mechanical) validates the developments previously presented. An important achievement is included in this chapter which is the fact of determining the amount of energy released in an unstable process.

Finally, last chapter summarizes the conclusions of the work presented in this thesis, together with some ideas for future research. In addition, in order to give more details about some developments, the following appendices are included:

- Chapter 2: The developments of the limit cases required to avoid numerical problems of the

m-AGC tangent operator are described in Appendix A.

- Chapter 3: The limit cases of the derivative terms involved in IDC-Wvp method are provided in Appendix B and C distinguishing between (1) the case in which the target is specified in terms of total dissipation (tension case) and (2) the case in which the target is specified in terms of fracture dissipation in compression case. Additionally, Appendix D shows the VPR algorithm.

- Chapter 4: Some developments required to obtain the closed-form expression of the work generated due to the fluid flow through rod elements are contained in Appendix E.

Chapter 2

Visco-plasticity and zero-thickness interface elements

Contents

2.1 Introduction

Fault reactivation processes can be addressed from different viewpoints and there is considerable literature concerning this topic. In the following, a brief summary is presented of the main methodologies that have been proposed:

- Walters et al. (2015) presents a comprehensive framework considering the scientific factors necessary for a hazard and risk-assessment workflow in a format that is site adaptable and can be updated as hazard and risk evolve with time. They offer suggestions for how to incorporate anthropogenic factors that may influence the occurrence of stimulated seismicity in a site-specific manner, as well as the exposed populations, properties, structures and infrastructure. Summarizing, they propose a risk assessment for human-caused earthquakes based on factors such as:

  - Natural hazard which includes geological setting, earthquake history, hydrological properties and geomechanical state.
  - Operational factors involving formation characteristics, injection operations, operating experience and level of monitoring.
  - Exposure level of population, critical facilities, structures and infrastructure and environment.

  This kind of studies provides a probabilistic assessment of the possibility that an earthquake can be triggered in a certain area, which might be useful as a preliminary study before any new human activity is initiated in a certain geographical area subject to seismic risk.

In addition, three more different approaches can be found in literature: analytical, semi-analytical and numerical.

- Analytical and Semi-analytical models can be mentioned together. These methods make some assumptions concerning the shape and extension of the reservoir (area of study) and the pore pressure values, as a way to simplify the problem and be able to use closed-form solutions that range from poro-elastic theory and Mohr-Coulomb failure criterion (Streit and Hillis, 2002; Hawkes et al., 2005; Segall et al., 1994; Zoback, 2007) to the theory of inclusions

combined with Coulomb failure stress change methodology (ΔCFS) (Segall and Fitzgerald, 1998; Soltanzadeh and Hawkes, 2008, 2009). Some applications can be found in Moeck et al. (2009) and Neves et al. (2009).

- Numerical models are a very powerful tool that allows the Engineer to analyze and make decisions in geomechanical problems in a more accurate way. In this sense, almost all characteristics of a certain problem (geometry, material properties, failure properties, *in situ* stresses, boundary conditions, hydraulic conditions, stages of fluid injection or extraction, etc.) have to be well defined in order to make the model simulation as realistic as possible. Numerical modelling of fault reactivation problems can be addressed by using different numerical techniques such as the Finite Element Method (FEM) (Vidal-Gilbert et al., 2009; Vilarrasa et al., 2016; Zeppilli et al., 2021), the Finite Difference Method (FDM) (Rutqvist et al., 2016; Rinaldi et al., 2015; Zhang et al., 2009) and the Discrete Element Method (DEM) (Alassi, 2008; Yoon et al., 2015).

Other authors combine both analytical and numerical approaches in their research about the problem of fluid-driven fractures (Detournay and Garagash, 2003; Detournay, 2016). Focusing on the behavior of the region near the fracture tip, they combine elasticity, linear elastic fracture mechanics (LEFM) and lubrication flow inside the fracture obtaining a stiff non-linear system of equations which makes it possible to approach the time evolution of fracture extent, width and fluid pressure distribution in the fracture. Moreover, Lecampion et al. (2017) compare hydraulic fracturing laboratory experiments with theoretical predictions from a numerical solution of the governing equations of hydraulic fracture mechanics mentioned above.

In order to provide an innovative approach to deal with fault reactivation problem induced by fluid injection, this thesis proposes a new methodology based on the combination of fracture mechanics, zero-thickness interface elements and visco-plasticity.

In the same way, in the context of CO2 sequestration the resulting overpressure may promote reactivation of sealed fractures or the creation of new ones in the caprock seal, Vilarrasa et al. (2010) used a visco-plastic continuum model to study the failure mechanism.

In the present thesis visco-plasticity theory is also used. However, the way in which this approach is used differs essentially from the references mentioned above. Here, induced fault reactivation is associated to a mechanical instability occurring in a fracture and the concept of instability is understood as a crack propagation event that starts and continues to develop even if the load, displacement or fluid injection/extraction operation that has triggered it, is stopped altogether.

In the context described, the main goal of this thesis is to propose a methodology capable of

detecting the initiation of such instability, following the crack propagation during the unstable propagation process until it stops, and estimating the overall energy liberated during the event. For that purpose, it is necessary to choose an always-growing parameter that can be used as a time variable to control method. Fictitious time may be the parameter which better fits this requirement as time is an always growing variable. For this reason, a visco-plastic approach has been used as the first attempt in this thesis.

In addition, as already mentioned, fault reactivation may be induced by fluid injection and this means that the problem also needs to be approached as a fully coupled Hydro-Mechanical problem. For this reason, the most relevant aspects of the hydro-mechanical formulation developed and implemented in the FE code of the research group, are also briefly described in this chapter (Sec. 2.7).

2.2 Preliminary considerations

In this section, the main aspects of visco-plasticity are reviewed and discussed as well as their use in the context of the FEM analysis including fracture-based zero-thickness interface elements.

2.2.1 Visco-plastic models

The three most commonly used formulations of visco-plasticity are those by Perzyna (1966), Duvaut and Lions (1972) and the *consistency visco-plastic model* by Wang et al. (1997). Perzyna and Duvaut-Lions visco-plasticity models are extensions of classical plasticity, with the novety that stresses are allowed to be temporarily outside of the yield surface, the so-called "overstress" state. After stresses have reached a point outside the yield surface, and for a constant external prescribed deformation, the overstress state generates visco-plastic deformations which in turn cause the stresses to progressively return to the yield surface in the course of time. Among these two visco-plastic models, the Perzyna model has become more popular althouhg a disadvantage has been pointed out related to the lack of enforcement of the consistency condition (Schwer, 1994). Also, the visco-plastic loading surface may not be well defined in the corner regions when a multi-surface formulation is used (Simo et al., 1988; Ju, 1990; Schwer, 1994). To overcome some of these disadvantages the Duvaut-Lions approach was proposed (Duvaut and Lions, 1972). In this approach, the visco-plastic strain rate is based on the difference between the visco-plastic stresses and some projected elasto-plastic stresses. More details of the various approaches to visco-plasticity are explained below.

2.2.1.1 Perzyna visco-plasticity

The cracking surface $F = 0$ determines the limit between elastic state ($F \leq 0$) and the visco-plastic state ($F > 0$), in which a visco-plastic strain rate is assumed with expression:

$$\dot{\boldsymbol{\varepsilon}}^{vp} = \frac{1}{\eta} \langle \psi (F) \rangle \boldsymbol{m} \tag{2.1}$$

$$\psi (F) = \left[\frac{F}{\overline{F}} \right]^N \tag{2.2}$$

where η is the viscosity of the material, $\overline{F}$ represents a normalizing factor, usually chosen as a reference value of the yield surface, N is a parameter that should satisfy $N \geq 1$ and defines the order of the Perzyna's visco-plasticity, the flow rule is $\boldsymbol{m} = \frac{\partial Q}{\partial \boldsymbol{\sigma}}$ and $Q(\boldsymbol{\sigma})$ is the visco-plastic potential typical of non-associated formulations. The Mc Cauley brackets in equation (2.1) indicate that:

$$\langle \psi (F) \rangle = \begin{cases} \psi (F), & F > 0 \\ 0, & F \leq 0 \end{cases} \tag{2.3}$$

2.2.1.2 Duvaut-Lions visco-plasticity

In this alternative approach, the visco-plastic strain rate and (if hardedning/softening is considered) the model hardening/softening law are formulated as:

$$\dot{\boldsymbol{\varepsilon}}^{vp} = \frac{1}{\tau} (\boldsymbol{D}^e)^{-1} : (\boldsymbol{\sigma} - \overline{\boldsymbol{\sigma}}) \tag{2.4}$$

$$\dot{\kappa} = -\frac{1}{\tau} (\kappa - \overline{\kappa}) \tag{2.5}$$

where τ designates the relaxation time, $\boldsymbol{D}^e$ denotes the linear elasticity tensor and $(\overline{\boldsymbol{\sigma}}, \overline{\kappa})$ mean the "backbone" stress and the set of internal state variables of the corresponding rate-independent elasto-plastic problem, respectively (in the case of perfect visco-plasticity, the H/S variable κ and equation (2.5) may be disregarded). As it can be seen in equation (2.4), in the case of Duvaut-Lions the visco-plastic strain rate is determined by the difference between the total stress and the stress in the inviscid backbone model. This is in contrast with the Perzyna model in which the value of the yield surface determines the visco-plastic strain rate.

2.2.1.3 Consistency model

Additionally, visco-plasticity can be modelled by incorporation of the time-dependency in a yield function, in the context of a fictitious elasto-plastic formulation. This approach denoted here as "consistency model" was proposed by Ponthot (1995) and followed up by Wang et al. (1997) and others (Carosio et al., 2000; Heeres et al., 2002; Lorefice et al., 2008), considers a yield surface which depends not only on stress and H/S parameter, but also on a time rate with expressions such as the fictitious loading function:

$$F\left(\boldsymbol{\sigma}, \kappa, \dot{\kappa}\right) = 0 \tag{2.6}$$

and

$$F\left(\boldsymbol{\sigma}, \kappa, \dot{\kappa}\right) = \boldsymbol{n}\colon\dot{\boldsymbol{\sigma}} - h\dot{\kappa} - \xi\ddot{\kappa} = 0 \tag{2.7}$$

where $\boldsymbol{n}$ is the stress gradient of the yield surface, h the hardening modulus and ξ the viscosity, all them defined as follows:

$$\boldsymbol{n} = \frac{\partial F}{\partial \boldsymbol{\sigma}},\ h = \frac{\partial F}{\partial \kappa},\ \xi = \frac{\partial F}{\partial \dot{\kappa}} \tag{2.8}$$

Additionally, κ is the equivalent plastic strain ($\boldsymbol{\varepsilon}^p$) which represents the plastic deformation history and is defined as:

$$\dot{\kappa} = \sqrt{2/3\,\dot{\boldsymbol{\varepsilon}}^p\colon\dot{\boldsymbol{\varepsilon}}^p} \tag{2.9}$$

In the consistency approach the yield surface can expand and shrink not only by hardening or softening effects, but also by rate effects.

Among the three visco-plastic formulations reviewed above, Perzyna visco-plasticity has been used in this thesis, to be implemented in the context of the the FEM with zero-thickness interface elements.

2.2.2 Zero-thickness interface elements

Zero-thickness interface elements, sometimes also called "cohesive elements", were introduced by Goodman (Goodman et al., 1968) for geotechnical analysis using the FEM, and in more recent times are becoming popular for their many possible applications. In the simplest scenario of linear elastic behaviour, interface elements inserted in between standard continuum elements may be used to represent the presence of a thin, deformable layer without the need to use extremely fine meshes. If considered linear elastic but assuming sufficiently high stiffness values, interface elements may lead to stresses and deformations of the continuum elements practically identical

to those that would be obtained in the same domain without any interface elements inserted. And that may be used as a means to obtain, besides the regular stresses and deformations of the continuum, also the normal and shear stress tractions transmitted across the planes in which interface elements have been inserted. Stress tractions may be of high interest for instance along interfaces in between different material layers or in between different materials. If equipped with non-linear constitutive laws exhibiting a maximum strength condition, interface elements may also be used to represent frictional sliding planes, cracks or fractures. For this purpose, the precise type and characteristics of the constitutive law are essential. A frictional contact surface may be represented with perfect plasticity, while a developing crack will require a constitutive model with softening which incorporates fracture energy parameters. In the late 90s, a model of this type was proposed by the research group (Carol et al., 1997), and the same model was later developed further and improved (Caballero et al., 2008).

A useful extension of the zero-thickness interface elements and constitutive laws is in the field of visco-plasticity (Caballero et al., 2009). Potential applications range from representation of physical time-dependent behaviour (such as for instance failure under sustained load), to purely numerical strategies such as Visco-plastic Relaxation (VPR) with which the stationary solution of an inviscid problem is obtained via a fictitious (non-physical) time (Underwood, 1983; Zhang and Yu, 1989; Haseganu and Steigmann, 1994). In recent years, an elastic-perfectly visco-plastic interface model was proposed (Aliguer et al., 2017), together with a discussion on the schemes necessary for the various possible applications. In the inviscid limit (time tending to infinity) the model response approaches an elastic-perfectly plastic version of the group's fracture model.

The energy-based softening visco-plastic model developed in this work is a step forward from the elastic-perfectly visco-plastic interface model mentioned before.

2.2.3 Stress-driven integration algorithm

The rate-dependent (visco-plastic) formulation requires a time integration strategy to discretize time in increments and evaluate linearized relation between stress and strain increments for each time step. Usually, the algorithms proposed in the literature are strain-driven, i.e. they are based on the initial stress scheme used in Finite Elements, in which the strain increments are prescribed to the constitutive equations, which then return the resulting stress (Hughes and Taylor, 1978; Perić, 1993; Ponthot, 2002).

In contrast, stress-driven schemes are less common, in spite that, for some models such as visco-plastic models, the implementation of stress-prescribed schemes is conceptually much simpler and

numerically advantageous (explicit integration of the constitutive equations and simple coding). After the original constant-stress implementation of Zienkiewicz and Cormeau (Zienkiewicz and Cormeau, 1974) that may be considered the most elementary form of stress-driven visco-plastic schemes, to the knowledge of the authors, the only previous proposals of this type are (Caballero et al., 2009) and (Aliguer et al., 2017), and were developed for perfect visco-plasticity. In the present thesis, the scheme proposed in Aliguer et al. (2017) has been extended to the case of Hardening/Softening, and an updated consistent tangent stiffness operator has been developed to improve the convergence at finite element level. Finally, it is also shown that in the inviscid limit the predictions of the energy-based softening visco-plastic model developed in this thesis approach those of the full version of the fracture-based elasto-plastic model previously proposed by the group (Carol et al., 1997).

A final remark, concerns the comparison with previous work of Lorefice et al. (2008). The visco-plastic approach proposed by Lorefice et al. (2008), applied the *consistency visco-plastic model* of Ponthot (1995) and Wang et al. (1997) to extend to visco-plasticity the H/S interface model previously proposed by Carol et al. (1997). This constitutes a clearly different approach to the one followed in the present thesis, but it is interesting to note that the final expressions of the algorithmic tangent operator (denoted in this thesis as "*m-AGC* tangent operator" after Aliguer et al. (2017)), turn out somewhat similar to those of by Lorefice et al. (2008). Further investigation of these similarities, however, lies beyond the scope of the present thesis.

2.3 Perfect Perzyna visco-plasticity and *m-AGC* tangent operator

2.3.1 Perfect Perzyna visco-plasticity

Perzyna visco-plasticity (Perzyna, 1966) is based on the assumption that the total strain is composed by two parts: the elastic part $\boldsymbol{\varepsilon}^{el}$ and the visco-plastic part $\boldsymbol{\varepsilon}^{vp}$.

$$\boldsymbol{\varepsilon} = \boldsymbol{\varepsilon}^{el} + \boldsymbol{\varepsilon}^{vp} \tag{2.10}$$

The elastic part is assumed to be related to stresses via isotropic linear elasticity:

$$\boldsymbol{\varepsilon}^{el} = \boldsymbol{D}_0^{-1} : \boldsymbol{\sigma} \tag{2.11}$$

where $\boldsymbol{D}_0$ is the elastic stiffness matrix, symmetric and positive definite, and $\boldsymbol{D}_0^{-1}$ indicates its inverse, which is the elastic compliance matrix and may be also denoted as $\boldsymbol{C}_0$.

The main feature of perfect visco-plasticity is the fact that the cracking surface only depends on the stress state. Therefore, following the guidelines explained previously in the Perzyna visco-plasticity section, the visco-plastic strain rate can be written as:

$$\dot{\boldsymbol{\varepsilon}}^{vp} = \frac{1}{\eta} \left\langle \left[\frac{F(\boldsymbol{\sigma})}{\overline{F}} \right]^N \right\rangle \boldsymbol{m} \tag{2.12}$$

As already mentioned, η is the viscosity of the material, $\overline{F}$ represents a normalizing factor, N defines the order of the Perzyna's visco-plasticity which is going to be considered as $N = 1$ from now on, $\boldsymbol{m}$ denotes the flow rule and the Mc Cauley brackets are represented by the angled brackets.

2.3.2 Discrete time increments and *m-AGC* tangent operator

The existing elastic perfect visco-plastic model developed by Aliguer et al. (2017) constitutes the starting point for the extended version proposed in this thesis, which consisits mainly of adding Hardening/Softening, to the original formulation. In this section, the main relevant aspects of the original perfect visco-plastic model, are summarized.

A time integration strategy is essential for the rate-dependent (visco-plastic) formulation. It consists of (1) discretizing time in increments and (2) evaluating linearized relations between stress and strain increments for each time step. Strain-driven algorithms are the more popular in the literature; they are based on the initial stress scheme used in Finite Elements, in which the strain increments are prescribed to the constitutive equations, which then return the resulting stress (Hughes and Taylor, 1978; Perić, 1993; Ponthot, 2002).

On the other hand, stress-driven schemes are less common. The original constant-stress implementation was proposed by Zienkiewicz and Cormeau (Zienkiewicz and Cormeau, 1974) and may be considered the most elementary form of stress-driven visco-plastic schemes. In addition, Caballero et al. (2009) developed their visco-plastic multilaminate model for jointed rocks using this type of stress-prescribed schemes. Its implementation in FEM code is conceptually much simpler and numerically advantageous (explicit integration of the constitutive equations and simple coding).

In the stress-driven scheme, it is assumed that the stress increment $\Delta\boldsymbol{\sigma}$ (that takes place during a time increment Δt) is prescribed, and the corresponding strain is calculated. By integrating in time, the visco-plastic strain rate (Eq. 2.12) may be expressed as:

$$\Delta\boldsymbol{\varepsilon}^{vp} = \int_{t_0}^{t_1} \dot{\boldsymbol{\varepsilon}}^{vp} dt = \int_{t_0}^{t_1} \frac{1}{\eta} \left\langle \left(\frac{F(\boldsymbol{\sigma})}{\overline{F}} \right) \right\rangle \boldsymbol{m}\, dt \tag{2.13}$$

The integral of the equation (2.13) is approximated by first order expansion as:

$$\Delta\boldsymbol{\varepsilon}^{vp} = \frac{\Delta t}{\eta\overline{F}}\left[(1-\theta)\,F\left(\boldsymbol{\sigma}_{ini}\right)\boldsymbol{m}\left(\boldsymbol{\sigma}_{ini}\right) + \theta F\left(\boldsymbol{\sigma}_{fin}\right)\boldsymbol{m}\left(\boldsymbol{\sigma}_{fin}\right)\right] \tag{2.14}$$

Subscripts *ini* and *fin* denote the stresses at the beginning and end of the time increment respectively. Moreover, θ is a constant scalar factor that may take a fixed value between 0 and 1. If $\theta = 0$, the formula above is equivalent to the forward Euler scheme. The other limit case is when $\theta = 1$ and the formula is equivalent to the traditional backward Euler scheme. Note also that, except for the case $\theta = 0$ in which all variables are known at the beginning of the increment, for any other value of $\theta > 0$ the calculation will require iterations at structural level, because the expression involves the stresses at the end of the increment, which are not known *a priori*.

Expression (Eq. 2.14), properly developed, leads to the relation between $\Delta\boldsymbol{\sigma}$ and $\Delta\boldsymbol{\varepsilon}$, which provides the constitutive tangential compliance and initial strain vector necessary for the iterative calculations.

The total strain increment expression is then obtained as:

$$\Delta\boldsymbol{\varepsilon} = \boldsymbol{C}'' \colon \Delta\boldsymbol{\sigma} + \Delta\boldsymbol{\varepsilon}^{0} \tag{2.15}$$

where

$$\boldsymbol{C}'' = \boldsymbol{C}_0 + \frac{1}{\frac{\eta\overline{F}}{\Delta t\theta}}\,\boldsymbol{m}_{ini} \otimes \boldsymbol{n}_{ini} \tag{2.16}$$

and

$$\Delta\boldsymbol{\varepsilon}^{0} = \frac{\Delta t}{\eta\overline{F}}\,F_0\,\boldsymbol{m}_{ini} \tag{2.17}$$

In the previous equations $\boldsymbol{C}''$ may be identified as discrete compliance operator and $\Delta\boldsymbol{\varepsilon}^0$ as the initial strain term. $\boldsymbol{C}''$ may be rewritten in the alternative form:

$$\boldsymbol{C}'' = \boldsymbol{C}_0 + \frac{1}{H''}\,\boldsymbol{m}_{ini} \otimes \boldsymbol{n}_{ini} \tag{2.18}$$

with $H'' = \frac{\eta\overline{F}}{\Delta t\theta}$ and $\boldsymbol{n}_{ini} = \frac{\partial F}{\partial \boldsymbol{\sigma}}$. Due to the structure of the visco-plastic compliance tensor, it can be explicitly inverted via Shermann-Morrison formula (Sherman and Morrison, 1950) to obtain:

$$\Delta\boldsymbol{\sigma} = \boldsymbol{D}'' \colon \left(\Delta\boldsymbol{\varepsilon} - \Delta\boldsymbol{\varepsilon}^{0}\right) \tag{2.19}$$

$$\boldsymbol{D}'' = \boldsymbol{D}_0 - \frac{\boldsymbol{D}_0 \colon \boldsymbol{m}_{ini} \otimes \boldsymbol{n}_{ini} \colon \boldsymbol{D}_0}{H'' + \boldsymbol{n}_{ini} \colon \boldsymbol{D}_0 \colon \boldsymbol{m}_{ini}} \tag{2.20}$$

where $\boldsymbol{D}''$ is denoted the *m-AGC* tangent operator which may be expressed explicitly thanks to the convenient structure of the compliance (Eq. 2.18), similar to classical elasto-plasticity. The explicit expression for $\boldsymbol{D}''$ (Eq. 2.20) is a great advantage of this approach because it eliminates the need of inverting the compliance tensor numerically at each Gauss point for each iteration, as is common for most existing integration schemes for visco-plastic models.

2.4 Extension to Hardening/Softening Perzyna visco-plasticity

2.4.1 Perzyna visco-plasticity with Hardening/Softening

In contrast to the previous perfect visco-plastic approach, the formulation of the new *m-AGC* tangent operator with Hardening/Softening requires to establish a closed-form expression of F as a function of time, as follows. In that case, Perzyna visco-plastic strain rate may be written as:

$$d\boldsymbol{\varepsilon}^{vp} = \frac{1}{\eta \overline{F}} \left\langle F\left(\boldsymbol{\sigma}, \boldsymbol{p}\right) \right\rangle \boldsymbol{m}\, dt \tag{2.21}$$

where the yield function $F\left(\boldsymbol{\sigma}, \boldsymbol{p}\right)$ depends now not only on stress components $(\boldsymbol{\sigma})$, but also on geometric parameters $(\boldsymbol{p})$ which in turn are controlled by one or more history variables $\left(\boldsymbol{\Xi}^{hist}\right)$. For that reason, its derivative can be expressed as:

$$dF = \left.\frac{\partial F}{\partial \boldsymbol{\sigma}}\right|_{\boldsymbol{p}} d\boldsymbol{\sigma} + \left.\frac{\partial F}{\partial \boldsymbol{p}}\right|_{\boldsymbol{\sigma}} \frac{\partial \boldsymbol{p}}{\partial\, \boldsymbol{\Xi}^{hist}} \frac{\partial\, \boldsymbol{\Xi}^{hist}}{\partial \boldsymbol{\varepsilon}^{vp}} d\boldsymbol{\varepsilon}^{vp} \tag{2.22}$$

Replacing the visco-plastic strain rate expression (Eq. 2.21) into the equation (2.22), one obtains:

$$dF = \left.\frac{\partial F}{\partial \boldsymbol{\sigma}}\right|_{\boldsymbol{p}} d\boldsymbol{\sigma} + \left.\frac{\partial F}{\partial \boldsymbol{p}}\right|_{\boldsymbol{\sigma}} \frac{\partial \boldsymbol{p}}{\partial\, \boldsymbol{\Xi}^{hist}} \frac{\partial\, \boldsymbol{\Xi}^{hist}}{\partial \boldsymbol{\varepsilon}^{vp}} : \boldsymbol{m} \frac{\left\langle F\left(\boldsymbol{\sigma}, \boldsymbol{p}\right) \right\rangle}{\eta \overline{F}}\, dt \tag{2.23}$$

This equation (Eq. 2.23) may be rewritten as:

$$dF = \boldsymbol{n} d\boldsymbol{\sigma} - H \frac{\left\langle F\left(\boldsymbol{\sigma}, \boldsymbol{p}\right) \right\rangle}{\eta \overline{F}}\, dt \tag{2.24}$$

where $-H = \left.\frac{\partial F}{\partial \boldsymbol{p}}\right|_{\boldsymbol{\sigma}} \frac{\partial \boldsymbol{p}}{\partial\, \boldsymbol{\Xi}^{hist}} \frac{\partial\, \boldsymbol{\Xi}^{hist}}{\partial \boldsymbol{\varepsilon}^{vp}} : \boldsymbol{m}$ and $\boldsymbol{n} = \left.\frac{\partial F}{\partial \boldsymbol{\sigma}}\right|_{\boldsymbol{p}}$. The derivatives involved in H are detailed in Section 2.5.2.

Dividing by dt, expression (Eq. 2.24) becomes the rate of F:

$$\dot{F} = \boldsymbol{n}\colon\dot{\boldsymbol{\sigma}} - H\frac{\langle F\left(\boldsymbol{\sigma},\boldsymbol{p}\right)\rangle}{\eta\overline{F}} \tag{2.25}$$

which, after rearranging may be expressed as:

$$\dot{F} + H\frac{\langle F\left(\boldsymbol{\sigma},\boldsymbol{p}\right)\rangle}{\eta\overline{F}} = \boldsymbol{n}\colon\dot{\boldsymbol{\sigma}} \tag{2.26}$$

Note that the structure of the previous differential equation (Eq. 2.26) is similar to the one that can be obtained with the development of a Maxwell element. As it can be seen in the following figure (Fig. 2.1), the Maxwell element consists of a spring (elastic element) with a spring constant E, which is connected in series to a viscous dashpot (viscous element) with a damping coefficient η. The elongation of the Maxwell element ε (Eq. 2.27) can be split into an elastic portion ε_e and a viscous portion ε_v and its incremental expression follows the same structure.

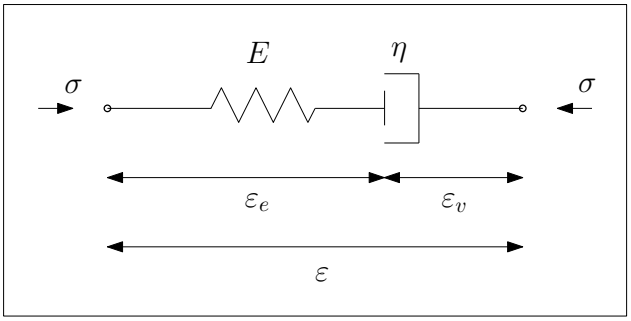

Figure 2.1: Maxwell element.

$$\varepsilon = \varepsilon_e + \varepsilon_v \rightarrow d\varepsilon = d\varepsilon_e + d\varepsilon_v \tag{2.27}$$

Moreover, the stress tensor concerning the elastic portion can be written as $\sigma = E\,\varepsilon_e$ and stress increments can be expressed from strain increments as $d\sigma = E\,d\varepsilon_e$, in other terms $d\varepsilon_e = \frac{d\sigma}{E}$. Regarding the viscous portion, $\sigma = \eta\,\dot{\varepsilon}_v = \eta\,\frac{d\varepsilon_v}{dt}$ and, therefore, $d\varepsilon_v = \frac{\sigma}{\eta}\,dt$.

Replacing $d\varepsilon_e$ and $d\varepsilon_v$ in equation (2.27) leads to:

$$d\varepsilon = \frac{d\sigma}{E} + \frac{\sigma}{\eta}dt \rightarrow \frac{d\varepsilon}{dt} = \frac{d\sigma}{dt}\frac{1}{E} + \frac{\sigma}{\eta} \tag{2.28}$$

which, after substitution of $\eta = \tau\, E$ and convenient rearrangement, becomes:

$$\dot{\sigma} + \frac{1}{\tau}\,\sigma = E\,\dot{\varepsilon} \tag{2.29}$$

Now, comparing Maxwell element equation (2.29) with equation (2.26), one can rewrite the F rate expression as:

$$\dot{F} + \frac{1}{\tau}\,F = b \tag{2.30}$$

where parameters and variables have been renamed such that $\frac{1}{\tau} = \frac{H}{\eta \overline{F}}$, $b = \boldsymbol{n} : \dot{\boldsymbol{\sigma}}$ and $\langle F\,(\boldsymbol{\sigma}, \boldsymbol{p})\rangle$ is simply equal to F. Now, a certain time interval is considered, that is small enough so that τ and b may be considered constant, and the differential equation may be solved in closed form.

Differential equation (2.30), is of the type $\dot{y}\,(t) + \frac{1}{\tau}\,y\,(t) = b$, and its general solution requires to obtain both the homogeneous and inhomogeneous (particular) solutions. Regarding the homogeneous solution it can be obtained as:

$$\dot{y}\,(t) + \frac{1}{\tau}\,y\,(t) = 0 \rightarrow \dot{y}\,(t) = -\frac{1}{\tau}\,y\,(t) \rightarrow \frac{\dot{y}\,(t)}{y\,(t)} = -\frac{1}{\tau} \tag{2.31}$$

Integrating in time the last expression (Eq. 2.31), the general solution $y\,(t)$ is obtained.

$$\int \frac{\dot{y}\,(t)}{y\,(t)}\,dt = -\frac{1}{\tau}\int dt \rightarrow \ln y\,(t) = -\frac{1}{\tau}t \rightarrow y\,(t) = A\,e^{-\frac{1}{\tau}t} \tag{2.32}$$

In sum, the homogeneous solution is:

$$y_h\,(t) = A\,e^{-\frac{1}{\tau}t} \tag{2.33}$$

$$\dot{y}_h\,(t) = -A\,\frac{1}{\tau}\,e^{-\frac{1}{\tau}t} \tag{2.34}$$

To obtain a particular solution, the method of variation of constants is used. In this method constant A is replaced by a function of time, and the resulting expression is introduced in the original differential equation. To do this, first the derivative of the particular solution is obtained:

$$\dot{y}_p\,(t) = \dot{A}\,(t)\,e^{-\frac{1}{\tau}t} - A\,(t)\,\frac{1}{\tau}\,e^{-\frac{1}{\tau}t} \tag{2.35}$$

Replacing now in the original differential equation, one obtains:

$$\left(\dot{A}\,(t)\,e^{-\frac{1}{\tau}t} - A\,(t)\,\frac{1}{\tau}\,e^{-\frac{1}{\tau}t}\right) + \frac{1}{\tau}\left(A\,(t)\,e^{-\frac{1}{\tau}t}\right) = b \rightarrow \dot{A}\,(t) = b\,e^{\frac{1}{\tau}t} \tag{2.36}$$

and from this, $A\,(t)$ can be obtained by integration.

$$\int \dot{A}\,(t)\,dt = \int b\,e^{\frac{1}{\tau}t}dt \rightarrow A\,(t) = b\,\tau\,e^{\frac{1}{\tau}t} \tag{2.37}$$

Replacing, finally $A\,(t)$ for A in the homogeneous solution (Eq. 2.33), one gets the particular solution:

$$y_p\,(t) = b\,\tau\,\underbrace{e^{\frac{1}{\tau}t}e^{-\frac{1}{\tau}t}}_{=1} \rightarrow y_p\,(t) = b\,\tau \tag{2.38}$$

The general solution of the differential equation is then obtained by adding together the homogeneous and particular solutions.

$$y\,(t) = \underbrace{A\,e^{-\frac{1}{\tau}t}}_{\text{hom.sol.}} + \underbrace{b\,\tau}_{\text{part.sol.}} \tag{2.39}$$

Finally, it only remains to determine the expression of the integration constant A by enforcing the boundary conditions:

$$y\,(t = t_0) = F\,(\boldsymbol{\sigma}_0, \boldsymbol{p}_0) = F_0 \tag{2.40}$$

$$F_0 = A\,e^{-\frac{1}{\tau}t_0} + b\,\tau \rightarrow A = (F_0 - b\,\tau)\,e^{\frac{1}{\tau}t_0} \tag{2.41}$$

Replacing now A into equation (2.39), one obtains:

$$y\,(t) = F\,(\boldsymbol{\sigma}, \boldsymbol{p}) = F\,(t) \tag{2.42}$$

$$F\,(t) = (F_0 - b\,\tau)\,e^{\frac{1}{\tau}t_0}\,e^{-\frac{1}{\tau}t} + b\,\tau = F_0\,e^{\frac{t_0 - t}{\tau}} + b\,\tau\left(1 - e^{\frac{t_0 - t}{\tau}}\right) \tag{2.43}$$

Recovernig now that $\frac{1}{\tau} = \frac{H}{\eta\overline{F}} \rightarrow \tau = \frac{\eta\overline{F}}{H}$ and $b = \boldsymbol{n} : \dot{\boldsymbol{\sigma}}$, the final expression of $F(t)$ for the interval is obtained:

$$F\,(t) = F_0\,e^{\frac{-H}{\eta\overline{F}}(t - t_0)} + \frac{\eta\overline{F}}{H}\,(\boldsymbol{n} : \dot{\boldsymbol{\sigma}})\left(1 - e^{\frac{-H}{\eta\overline{F}}(t - t_0)}\right) \tag{2.44}$$

2.4.2 Formulation of the new *m-AGC* tangent operator with Hardening/Softening

Once the closed-form solution of the yield function ($F\,(t)$) is obtained and considering the visco-plastic strain rate $\dot{\boldsymbol{\varepsilon}}^{vp} = \frac{1}{\eta}\frac{F(t)}{\overline{F}}\boldsymbol{m}$, the visco-plastic strain increment may be calculated as:

$$\Delta\boldsymbol{\varepsilon}^{vp} = \int_{t_0}^{t_1} \dot{\boldsymbol{\varepsilon}}^{vp}dt = \int_{t_0}^{t_1} \frac{1}{\eta}\frac{F\,(t)}{\overline{F}}\boldsymbol{m}\,dt = \frac{\boldsymbol{m}}{\eta\overline{F}}\int_{t_0}^{t_1} F\,(t)\,dt \tag{2.45}$$

Developing the integral part of the previous visco-plastic strain rate equation (Eq. 2.45), note that only F depends on time while H and $\boldsymbol{m}$ are considered constants within a time increment.

$$\begin{aligned}\int_{t_0}^{t_1} F(t)\,dt &= \int_{t_0}^{t_1}\left[F_0\, e^{\frac{-H}{\eta\overline{F}}(t-t_0)} + \frac{\eta\overline{F}}{H}(\boldsymbol{n}:\dot{\boldsymbol{\sigma}})\left(1-e^{\frac{-H}{\eta\overline{F}}(t-t_0)}\right)\right]dt = \\ &= F_0\left[\frac{\eta\overline{F}}{H}\left(1-e^{\frac{-H}{\eta\overline{F}}(t_1-t_0)}\right)\right] + \frac{\eta\overline{F}}{H}(\boldsymbol{n}:\dot{\boldsymbol{\sigma}})\left[(t_1-t_0)+\frac{\eta\overline{F}}{H}\left(e^{\frac{-H}{\eta\overline{F}}(t_1-t_0)}-1\right)\right]\end{aligned} \tag{2.46}$$

Substituting this expression into equation (2.45) and considering $\Delta t = t_1 - t_0$ and $\dot{\boldsymbol{\sigma}} = \frac{\Delta\boldsymbol{\sigma}}{\Delta t}$, the visco-plastic strain increment can be rewritten as:

$$\Delta\boldsymbol{\varepsilon}^{vp} = \frac{1}{H}\left[1+\frac{\eta\overline{F}}{H\Delta t}\left(e^{\frac{-H\Delta t}{\eta\overline{F}}}-1\right)\right]\boldsymbol{m}\otimes\boldsymbol{n}\colon\Delta\boldsymbol{\sigma} + \frac{F_0}{H}\left(1-e^{\frac{-H\Delta t}{\eta\overline{F}}}\right)\boldsymbol{m} \tag{2.47}$$

Finally, the total strain increment is calculated considering both elastic and visco-plastic strain increments ($\Delta\boldsymbol{\varepsilon} = \Delta\boldsymbol{\varepsilon}^{el} + \Delta\boldsymbol{\varepsilon}^{vp}$). As a result, the following expression is obtained:

$$\begin{aligned}\Delta\boldsymbol{\varepsilon} &= \boldsymbol{C}_0\colon\Delta\boldsymbol{\sigma} + \frac{1}{H}\left[1+\frac{\eta\overline{F}}{H\Delta t}\left(e^{\frac{-H\Delta t}{\eta\overline{F}}}-1\right)\right]\boldsymbol{m}\otimes\boldsymbol{n}\colon\Delta\boldsymbol{\sigma} + \frac{F_0}{H}\left(1-e^{\frac{-H\Delta t}{\eta\overline{F}}}\right)\boldsymbol{m} = \\ &= \left(\boldsymbol{C}_0 + \frac{1}{H}\left[1+\frac{\eta\overline{F}}{H\Delta t}\left(e^{\frac{-H\Delta t}{\eta\overline{F}}}-1\right)\right]\boldsymbol{m}\otimes\boldsymbol{n}\right)\colon\Delta\boldsymbol{\sigma} + \frac{F_0}{H}\left(1-e^{\frac{-H\Delta t}{\eta\overline{F}}}\right)\boldsymbol{m}\end{aligned} \tag{2.48}$$

From previous equation (2.48), the initial strain term $\left(\Delta\boldsymbol{\varepsilon}^0\right)$ and the visco-plastic compliance tensor ($\boldsymbol{C}''$) can be defined as:

$$\Delta\boldsymbol{\varepsilon}^0 = \frac{F_0}{H}\left(1-e^{\frac{-H\Delta t}{\eta\overline{F}}}\right)\boldsymbol{m} \tag{2.49}$$

$$\boldsymbol{C}'' = \boldsymbol{C}_0 + \frac{1}{H}\left[1+\frac{\eta\overline{F}}{H\Delta t}\left(e^{\frac{-H\Delta t}{\eta\overline{F}}}-1\right)\right]\boldsymbol{m}\otimes\boldsymbol{n} \tag{2.50}$$

Due to its structure, the visco-plastic compliance tensor (Eq. 2.50) can be explicitly inverted via Shermann-Morrison formula (Sherman and Morrison, 1950) and the equation (2.48) can be rewritten using stiffness terms (Eq. 2.51).

$$\Delta\boldsymbol{\sigma} = \boldsymbol{D}''\colon\Delta\boldsymbol{\varepsilon} + \Delta\boldsymbol{\sigma}^0 \tag{2.51}$$

where

$$\boldsymbol{D}'' = \boldsymbol{D}_0 - \frac{\boldsymbol{D}_0\colon\boldsymbol{m}\otimes\boldsymbol{n}\colon\boldsymbol{D}_0}{H'' + \boldsymbol{n}\colon\boldsymbol{D}_0\colon\boldsymbol{m}} \tag{2.52}$$

$$\Delta\boldsymbol{\sigma}^0 = -\boldsymbol{D}''\colon\Delta\boldsymbol{\varepsilon}^0 \tag{2.53}$$

$$\frac{1}{H''} = \frac{1}{H}\left[1 + \frac{\eta\overline{F}}{H\Delta t}\left(e^{\frac{-H\Delta t}{\eta\overline{F}}} - 1\right)\right] \tag{2.54}$$

Equations (2.52-2.54) show that the convenient features of the m-AGC tangent operator derived in Aliguer et al. (2017), are also maintained in the Hardening/Softening case by simple replacing of the apparent Hardening/Softening modulus H'' with the new expression (2.54). This finding is one of the contributions of the present thesis.

Focusing now on the new expression of H'' (Eq. 2.54), one quickly notices that a singularity occurs in the limit cases $\Delta t \to 0$ or $H \to 0$, because of the presence of those variables in the denominator. The corresponding limit study, done by applying L'Hôpital's rule and Taylor series expansion, is developed in Appendix A, and leads to the following closed-form expression valid for both limit cases $\Delta t \to 0$ and $H \to 0$:

$$\left.\frac{1}{H''}\right|_{Limit} = \frac{\Delta t}{2\eta\overline{F}}\left(1 - \frac{H\Delta t}{3\eta\overline{F}}\right) \tag{2.55}$$

Equation (2.55) shows that the strict limit case of $\Delta t = 0$ would lead to $\frac{1}{H''} = 0$ therefore implying that $H'' = \infty$ which corresponds to elastic behavior. This is exactly what should be expected because for zero time there should be no visco-plastic deformation. However, this particular situation should not take place in practical calculations because in the limit situation that $\Delta t = 0$, the computer subroutines implementing the model, should identify the case as elastic behavior and not go into visco-plastic calculations. On the other hand, there is the other limit case with H/S parameter $H = 0$, for which the expression of $\frac{1}{H''}$ turns out equal to the one obtained with perfect visco-plasticity $\left(\frac{1}{H''} = \frac{\Delta t\theta}{\eta\overline{F}}\right)$ assuming that $\theta = \frac{1}{2}$ (Aliguer et al., 2017), which is a reassuring result.

2.5 Application to a fracture-based model for zero-thickness interfaces

2.5.1 Existing inviscid fracture-based model for interfaces

As already mentioned, the new energy-based softening visco-plastic model for zero-thickness interface elements is developed as an extension of an existing elastic-perfectly-viscoplastic formulation (Aliguer et al., 2017), which in turn was proposed as the basic visco-plasticity version of an existing underlying inviscid model for interfaces and cracks. This inviscid underlying model was proposed originally for the behaviour of geotechnical interfaces (Gens et al., 1989), later modified for fracture energy-based opening and development of cracks in quasi-brittle materials (concrete, rock, etc)

(Carol et al., 1997), and more recently extended to 3D and reformulated more efficiently (Caballero et al., 2008).

The fracture-based interface constitutive law, originally named *Normal/Shear Cracking Model*, is based on the theory of elasto-plasticity and it incorporates concepts of fracture mechanics and fracture energies. Its behaviour is formulated in terms of normal and shear stress components on the interface plane $\boldsymbol{\sigma}_{\mathrm{J}} = [\sigma_N, \sigma_T]^T$ and their respective relative displacements $\boldsymbol{r} = [r_N, r_T]^T$ (note that, for zero thickness interface laws the strain vector $\boldsymbol{\varepsilon}$ is replaced by the relative displacements $\boldsymbol{r}$) (Fig. 2.2).

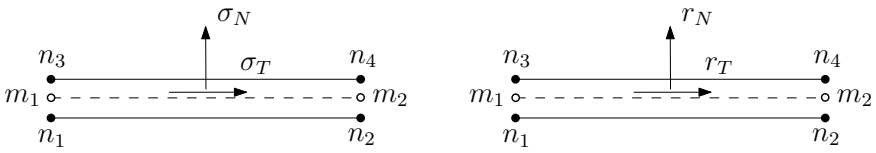

Figure 2.2: (Left) Normal and shear stress components on the interface plane and (right) their respective relative displacements.

The model is based on a hyperbolic cracking surface (Carol et al., 1997), Figure 2.3-(a). The corresponding yield (cracking) function F is defined in terms of normal and shear stresses and three geometric parameters: the strength parameters cohesion (c), uniaxial tensile strength (χ) and internal friction angle ($\tan\phi$). The algebraic expression of F has been changed in later versions of the model, the most convenient format (Caballero et al., 2008) being:

$$F\left(\boldsymbol{\sigma}_{\mathrm{J}}, \boldsymbol{p}\right) = -\left(c - \sigma_N \tan\phi\right) + \sqrt{\sigma_T^2 + \left(c - \chi \tan\phi\right)^2} \tag{2.56}$$

The Hardening/Softening laws (evolution laws of the surface geometric parameters $c, \chi, \tan\phi$) are formulated in terms of a single history variable, W^{cr}, defined as the energy spent in fracture processes. These laws, represented in Figure 2.3-(d), include as parameters the classical fracture energy in Mode I, G_f^I (pure tension) and a second mode named Mode IIa defined under shear and high compression without dilatancy, G_f^{IIa} (Fig. 2.3-(c)). The expression which describes these family of evolution curves for χ and c according to a scaling factor α is given as follows (Carol et al., 1997):

$$S\left(\xi, \alpha\right) = \left(\frac{e^{-\alpha}\xi}{1 + \left(e^{-\alpha} - 1\right)\xi}\right) \tag{2.57}$$

where $\xi = W^{cr}/G_f^I$ and $\alpha = \alpha_\chi$ for parameter χ; $\xi = W^{cr}/G_f^{IIa}$ and $\alpha = \alpha_c$ for parameter c. Note that in the particular case $\alpha = 0$, $S\left(\xi, 0\right) = \xi$ is obtained. The history variable work is defined

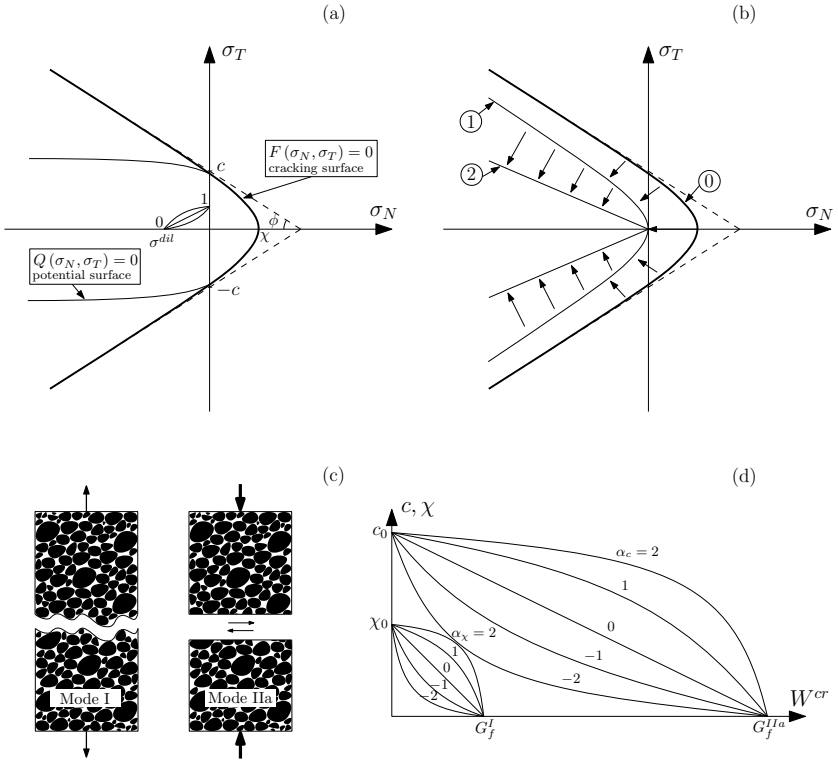

Figure 2.3: Interface model: (a) cracking surface and plastic potential, (b) evolution of cracking surface, (c) fundamental modes of fracture and (d) softening laws for c and χ.

incrementally as:

$$dW^{cr} = \begin{cases} \boldsymbol{\sigma}_{\mathrm{J}} : d\boldsymbol{r}^{cr} & \sigma_N \geq 0\,(tension) \\ (\sigma_T + \sigma_N \tan\phi)\, dr_T^{cr} & \sigma_N < 0\,(compression) \end{cases} \tag{2.58}$$

The above equations (Eq. 2.58) show that, in the case of tensile-dominated cracking, all plastic work dissipated counts towards the history variable, while in compression-shear cracking, there is a frictional part which is excluded from W^{cr}. Note that, with the definitions above, the evolution of the cracking surface is as depicted in Figure 2.3-(b): from configuration "0" with initial tensile strength χ_0 and asymptotic cohesion c_0, as the history variable reaches $W^{cr} = G_f^I$ the surface moves to configuration "1" with zero tensile strength, and as it approaches $W^{cr} = G_f^{IIa}$ the surface moves toward configuration "2" which corresponds to a pair of straight lines of residual friction

and no cohesion.

The precise evolution laws for the three fracture surface parameters $(c, \chi, \tan\phi)$ are the following (Garolera, 2017):

Tensile strength χ

As shown in Figure 2.3-(d), tensile strength decreases from χ_0 to zero as W^{cr} increases from zero to G_f^I. A family of curves is obtained by applying the scaling function $S(\xi_\chi, \alpha_\chi)$ in which $\xi_\chi = W^{cr}/G_f^I$ and $\alpha = \alpha_\chi$. The evolution expression is defined as:

$$\chi = \begin{cases} \chi_0 \left(1 - S\left(\xi_\chi, \alpha_\chi\right)\right) & W^{cr} < G_f^I \\ 0 & W^{cr} \geq G_f^I \end{cases} \tag{2.59}$$

Cohesion c

Figure 2.3-(d) also shows the evolution of c. The reduction of this parameter, though, is not defined directly but via the evolution of another parameter called "a" which represents the horizontal distance between the vertex of the hyperbola and its asymtotes, and is given by:

$$c = (\chi + a)\tan\phi \tag{2.60}$$

Note that c also evolves from its initial value to zero when $W^{cr} = G_f^{IIa}$. The scaling function in this case is defined by using parameter "a" (Fig. 2.4) as $S(\xi_a, \alpha_a)$ where $\xi_a = W^{cr}/G_f^{IIa}$ and $\alpha = \alpha_a$. The reduction of c can be then expressed as follows:

$$c = \begin{cases} c_0 \left[1 - S\left(\xi_a, \alpha_a\right) - \frac{\chi_0}{c_0}\tan\phi\left(S\left(\xi_\chi, \alpha_\chi\right) - S\left(\xi_a, \alpha_a\right)\right)\right] & W^{cr} < G_f^{IIa} \\ 0 & W^{cr} \geq G_f^{IIa} \end{cases} \tag{2.61}$$

Friction angle $\tan\phi$

The evolution of the friction angle is defined as:

$$\tan\phi = \begin{cases} \tan\phi_0 - \left(\tan\phi_0 - \tan\phi_{res}\right) S\left(\xi_\phi, \alpha_\phi\right) & W^{cr} < G_f^{IIa} \\ \tan\phi_{res} & W^{cr} \geq G_f^{IIa} \end{cases} \tag{2.62}$$

where ϕ_0 is the initial friction angle and ϕ_{res} is the residual friction angle. Therefore, $\tan\phi$ evolves from its initial value to its residual value when the final fracture surface is reached (Fig. 2.5).

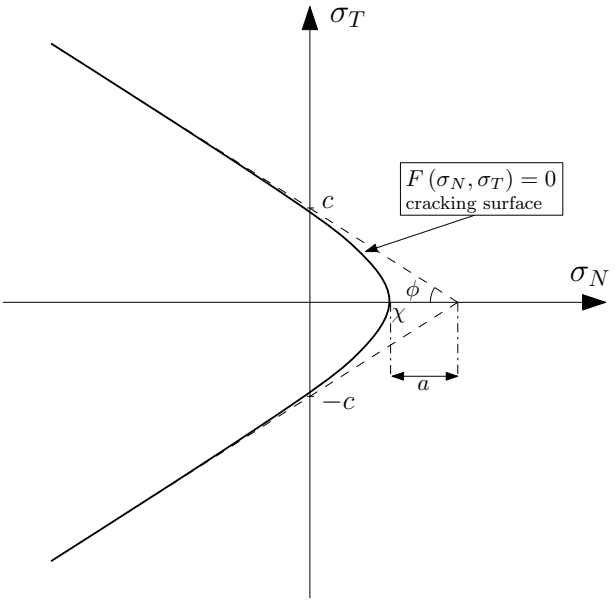

Figure 2.4: Fracture surface parameters

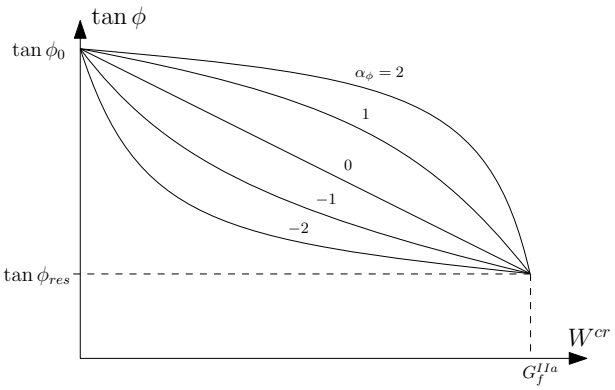

Figure 2.5: Evolution law of the friction angle.

2.5.2 New visco-plastic formulation of the fracture-based model for developing cracks

The main novelty with respect to the previous perfect visco-plastic model (Aliguer et al., 2017) is that in the current implementation the geometric parameters of the surface $\boldsymbol{p}$ (composed by $c, \chi, \tan\phi$) are assumed to evolve in an identical way as they did in the inviscid elasto-plastic model (Fig. 2.3-(d)). In addition, the history variable W^{vcr} is defined similarly to its inviscid counterpart

W^{cr} by simply replacing the plastic "strain" $\boldsymbol{r}^{cr}$ by the visco-plastic "strain" $\boldsymbol{r}^{vcr}$, i.e.:

$$dW^{vcr} = \begin{cases} \overline{\boldsymbol{\sigma}}_{\mathrm{J}} : d\boldsymbol{r}^{vcr} & \sigma_N \geq 0\,(tension) \\ (\overline{\sigma}_T + \overline{\sigma}_N \tan\phi)\, dr_T^{vcr} & \sigma_N < 0\,(compression) \end{cases} \tag{2.63}$$

In equation (2.63) it is important to emphasize two aspects. First, that the energy dissipated in the fracture process for the visco-plastic model is calculated using the stresses projected on the yield surface (instead of the visco-plastic stress that may be well outside the surface). The method used to obtain such projection is a return algorithm proposed by the authors which is based on a radial projection for tension cases and a vertical projection (parallel to the shear stress axis) for compression cases (Fig. 2.6). In tension cases, the projection of stresses is obtained

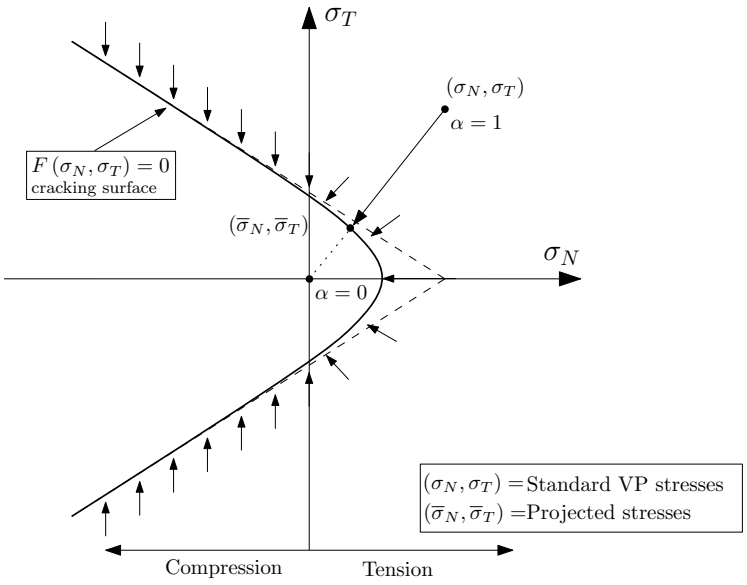

Figure 2.6: Scheme of stress projection.

by the intersection between the cracking surface equation ($F = 0$) and the straight line defined as $\overline{\sigma}_N = \alpha\sigma_N$ and $\overline{\sigma}_T = \alpha\sigma_T$. To clarify, the bar over stress components means that they are the projected stresses while the stress components without overbar are the standard visco-plastic stresses. By substituting the expressions of $\overline{\sigma}_N$ and $\overline{\sigma}_T$ just mentioned in the cracking surface equation (Eq. 2.56), one obtains:

$$-\left(c - (\alpha\sigma_N)\tan\phi\right) + \sqrt{(\alpha\sigma_T)^2 + (c - \chi\tan\phi)^2} = 0 \tag{2.64}$$

After some operations, the expression obtained can be solved using a second-degree equation (Eq. 2.65) and α has two possible solutions. The right solution for α is the one that satisfies at the same time $\alpha > 0$ and $\alpha < 1$.

$$\left(\sigma_N^2 \tan^2\phi - \sigma_T^2\right)\alpha^2 + \left(-2c\sigma_N \tan\phi\right)\alpha + \left(-\left(c - \chi\tan\phi\right)^2 + c^2\right) = 0 \tag{2.65}$$

Finally, knowing the value of α, it is possible to calculate the projected stress components as $\overline{\sigma}_N = \alpha\sigma_N$ and $\overline{\sigma}_T = \alpha\sigma_T$. Otherwise, for compression cases, the projected stresses are defined as:

$$\begin{aligned} \overline{\sigma}_N &= \sigma_N \\ \overline{\sigma}_T &= \sqrt{\left(c - \overline{\sigma}_N \tan\phi\right)^2 - \left(c - \chi\tan\phi\right)^2} \end{aligned} \tag{2.66}$$

The second remark after equation (2.63) is that, the application of the Hardening/Softening visco-plasticity, formulated in Section 2.4.2, to the fracture-based model for zero-thickness interfaces only involves replacing strains by relative displacements. In this sense, the visco-plastic strain rate can be written as:

$$\Delta\boldsymbol{r}^{vcr} = \frac{1}{H}\left[1 + \frac{\eta\overline{F}}{H\Delta t}\left(e^{\frac{-H\Delta t}{\eta\overline{F}}} - 1\right)\right]\boldsymbol{m}\otimes\boldsymbol{n}\colon\Delta\boldsymbol{\sigma}_{\mathrm{J}} + \frac{F_0}{H}\left(1 - e^{\frac{-H\Delta t}{\eta\overline{F}}}\right)\boldsymbol{m} \tag{2.67}$$

The total strain increment for interfaces is then obtained as the sum of the elastic and the visco-plastic strains ($\Delta\boldsymbol{r} = \Delta\boldsymbol{r}^{el} + \Delta\boldsymbol{r}^{vcr}$), i.e.:

$$\Delta\boldsymbol{r} = \left(\boldsymbol{C}_0 + \frac{1}{H}\left[1 + \frac{\eta\overline{F}}{H\Delta t}\left(e^{\frac{-H\Delta t}{\eta\overline{F}}} - 1\right)\right]\boldsymbol{m}\otimes\boldsymbol{n}\right)\colon\Delta\boldsymbol{\sigma}_{\mathrm{J}} + \frac{F_0}{H}\left(1 - e^{\frac{-H\Delta t}{\eta\overline{F}}}\right)\boldsymbol{m} \tag{2.68}$$

or, in the form of an expression with a compliance matrix and initial strain vector

$$\Delta\boldsymbol{r} = \boldsymbol{C}''\colon\Delta\boldsymbol{\sigma}_{\mathrm{J}} + \Delta\boldsymbol{r}^0 \tag{2.69}$$

$$\boldsymbol{C}'' = \boldsymbol{C}_0 + \frac{1}{H}\left[1 + \frac{\eta\overline{F}}{H\Delta t}\left(e^{\frac{-H\Delta t}{\eta\overline{F}}} - 1\right)\right]\boldsymbol{m}\otimes\boldsymbol{n},\ \Delta\boldsymbol{r}^0 = \frac{F_0}{H}\left(1 - e^{\frac{-H\Delta t}{\eta\overline{F}}}\right)\boldsymbol{m} \tag{2.70}$$

Again, as it was mentioned in Section 2.4.2, equation (2.68) can be rewritten using stiffness terms.

$$\Delta\boldsymbol{\sigma}_{\mathrm{J}} = \boldsymbol{D}''\colon\Delta\boldsymbol{r} + \Delta\boldsymbol{\sigma}_{\mathrm{J}}^0 \tag{2.71}$$

where $\boldsymbol{D}''$ is obtained according to equation (2.52), and $\Delta\boldsymbol{\sigma}_{\mathrm{J}}^0 = -\boldsymbol{D}''\colon\Delta\boldsymbol{r}^0$.

In previous expressions,

$$-H = \left.\frac{\partial F}{\partial \boldsymbol{p}}\right|_{\boldsymbol{\sigma}} \frac{\partial \boldsymbol{p}}{\partial \Delta W^{vcr}} \frac{\partial \Delta W^{vcr}}{\partial \Delta \boldsymbol{r}^{vcr}} : \boldsymbol{m} \tag{2.72}$$

where the derivative $\left.\frac{\partial F}{\partial \boldsymbol{p}}\right|_{\boldsymbol{\sigma}}$ has the following components:

$$\frac{\partial F}{\partial \chi} = (-\tan\phi) \cdot \frac{(c - \chi \tan\phi)}{\sqrt{\sigma_T^2 + (c - \chi \tan\phi)^2}} \tag{2.73}$$

$$\frac{\partial F}{\partial \tan\phi} = \sigma_N + \frac{(-\chi)\,(c - \chi \tan\phi)}{\sqrt{\sigma_T^2 + (c - \chi \tan\phi)^2}} \tag{2.74}$$

$$\frac{\partial F}{\partial c} = (-1) + \frac{(c - \chi \tan\phi)}{\sqrt{\sigma_T^2 + (c - \chi \tan\phi)^2}} \tag{2.75}$$

the derivatives of the three parameters (c, χ and $\tan\phi$) with respect to the history variable ΔW^{vcr} are given below (note that $S\,(\xi_*, \alpha_*)$ is the scaling function described by equation 2.57):

$$\frac{\partial \chi}{\partial \Delta W^{vcr}} = -\chi_0 \cdot \frac{S\,(\xi_\chi, \alpha_\chi)}{G_f^I} \tag{2.76}$$

$$\frac{\partial \tan\phi}{\partial \Delta W^{vcr}} = (\tan\phi_{res} - \tan\phi_0) \cdot \frac{S\,(\xi_\phi, \alpha_\phi)}{G_f^{IIa}} \tag{2.77}$$

$$\frac{\partial c}{\partial \Delta W^{vcr}} = \left(\frac{\partial a}{\partial \Delta W^{vcr}} + \frac{\partial \chi}{\partial \Delta W^{vcr}}\right) \cdot \tan\phi + (a + \chi) \cdot \frac{\partial \tan\phi}{\partial \Delta W^{vcr}} \tag{2.78}$$

where $\frac{\partial a}{\partial \Delta W^{vcr}} = -a_0 \cdot \frac{S(\xi_a, \alpha_a)}{G_f^{IIa}}$ and "a" can be considered as $a = a_0\,(1 - S\,(\xi_a, \alpha_a))$ and, finally, the derivative $\frac{\partial \Delta W^{vcr}}{\partial \Delta \boldsymbol{r}^{vcr}}$ is given by:

$$\frac{\partial \Delta W^{vcr}}{\partial \Delta \boldsymbol{r}^{vcr}} = \begin{cases} [\overline{\sigma}_N,\, \overline{\sigma}_T] & \sigma_N \geq 0\,(tension) \\ [0,\, \overline{\sigma}_T + \overline{\sigma}_N \tan\phi] & \sigma_N < 0\,(compression) \end{cases} \tag{2.79}$$

2.6 Stress-driven integration algorithm for Perzyna visco-plasticity

The numerical integration procedure developed for the new interface visco-plastic constitutive model is a generalization of the procedure described in Section 2.3.2 for perfect visco-plasticity. In that integration scheme it is assumed that the stress increment $\Delta\boldsymbol{\sigma}_{\mathrm{J}}$ (that takes place during a time increment Δt) is prescribed and the corresponding strain is calculated. As the main novelty, in this case, the geometric parameters of the yield function, $\boldsymbol{p}$ (composed by $c, \chi, \tan\phi$) are not constant, but have to be continuously updated using the softening laws in terms of W^{vcr}, which is also continuously changing. For this purpose, an iterative procedure is implemented for each time step. At the beginning of the iterative integration process for a time increment, the input data consists of the intial stress ($\boldsymbol{\sigma}_{\mathrm{J}ini}$), the initial parameters ($\boldsymbol{p}_{ini}$), the prescribed stress increment ($\Delta\boldsymbol{\sigma}_{\mathrm{J}}$) and the time increment (Δt). With this information, the value of F at the beginning of the increment $F_{ini} = F(\boldsymbol{\sigma}_{\mathrm{J}ini}, \boldsymbol{p}_{ini})$ is obtained, as well as the value of F at the end of the increment (F_{fin}) considering the stresses at the end of the increment ($\boldsymbol{\sigma}_{\mathrm{J}fin} = \boldsymbol{\sigma}_{\mathrm{J}ini} + \Delta\boldsymbol{\sigma}_{\mathrm{J}}$) and the updated parameters according to W^{vcr}.

Because visco-plastic theory allows the stress state to lie outside the yield surface, either of the two values F_{ini} and F_{fin} may take values which are negative, zero or positive which leads to having to distinguish the following cases:

a) $F_{ini} > 0$ and $F_{fin} < 0$: The stress trajectory starts outside of the yield surface and ends inside the surface. In this case, the entry point must be determined to correctly calculate the visco-plastic strain (Fig. 2.7-(a)).

b) $F_{ini} > 0$ and $F_{fin} > 0$: Both starting point and final point are outside of the yield surface which means that all the stress increment produces visco-plastic strain (Fig. 2.7-(b)).

c) $F_{ini} < 0$ and $F_{fin} < 0$: Both starting point and final point are inside of the yield surface which means that the stress state remains in the elastic zone and there is no visco-plastic strain (Fig. 2.7-(c)).

d) $F_{ini} < 0$ and $F_{fin} > 0$: In this case, the stress trajectory starts inside of the yield surface and ends outside, and therefore it is necessary to calculate the exit point to evaluate correctly the visco-plastic strain (Fig. 2.7-(d)).

As it has been mentioned above for the cases a) entry point and d) exit point, it is necessary to find the contact point (σ_N and σ_T) as an intersection between the yield surface and the stress path.

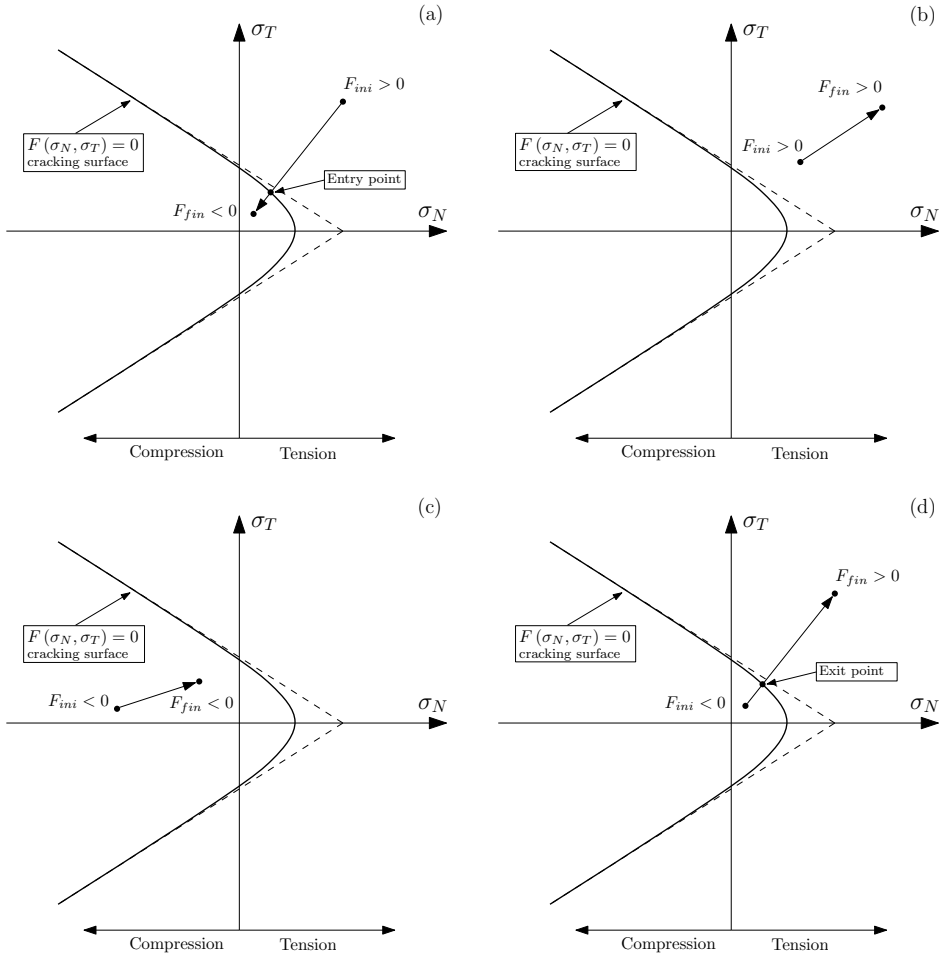

Figure 2.7: Possible stress paths during a visco-plastic increment: (a) from outside to inside of the surface: entry point, (b) always outside: visco-plastic zone, (c) always inside: elastic zone and (d) from inside to outside: exit point.

Knowing the contact point, it is possible to determine which part of the stress path belongs to the elastic zone (inside the surface) or visco-plastic zone (outside of the surface). As it is known, only the visco-plastic behavior produces changes in the history variable W^{vcr}. Conveniently, there is an closed-form solution for the problem of intersecting a line and a hyperbola defined by the following expression (Gens et al., 1989; Caballero et al., 2008):

$$F\left(\boldsymbol{\sigma}_{\mathrm{J}0} + \alpha \Delta \boldsymbol{\sigma}_{\mathrm{J}}, \boldsymbol{p}\right) = 0 \tag{2.80}$$

where $\boldsymbol{\sigma}_{\mathrm{J}0} = \boldsymbol{\sigma}_{\mathrm{J}ini}$ and α is the unknown factor to advance the stress state to the contact point

that must be real and within the range [0,1]. Developing the previous expression (Eq. 2.80), a quadratic equation for α is obtained:

$$F\left(\boldsymbol{\sigma}_{\mathrm{J}0} + \alpha\Delta\boldsymbol{\sigma}_{\mathrm{J}}, \boldsymbol{p}\right) = \gamma_2\alpha^2 + \gamma_1\alpha + \gamma_0 = 0 \tag{2.81}$$

where

$$\begin{cases} \gamma_2 = \Delta\sigma_T^2 - \Delta\sigma_N^2 \tan^2\phi \\ \gamma_1 = 2\left(\sigma_{0T}\Delta\sigma_T + \left(c - \sigma_{0N}\tan\phi\right)\Delta\sigma_N \tan\phi\right) \\ \gamma_0 = \sigma_{0T}^2 + \left(c - \chi\tan\phi\right)^2 - \left(c - \sigma_{0N}\tan\phi\right)^2 \end{cases} \tag{2.82}$$

Solving equation (2.81), two solutions are obtained for α, although only one has physical meaning depending on the case that is being studied (entry point or exit point). By considering that the function $F(\alpha) = 0$ is a 2^{nd} degree parabola, the right solution can be chosen graphically as follows:

- Case a) entry point: $F_{ini} > 0$ and $F_{fin} < 0$, the right solution is the lower value of alpha (α_{min}) (Fig. 2.8).

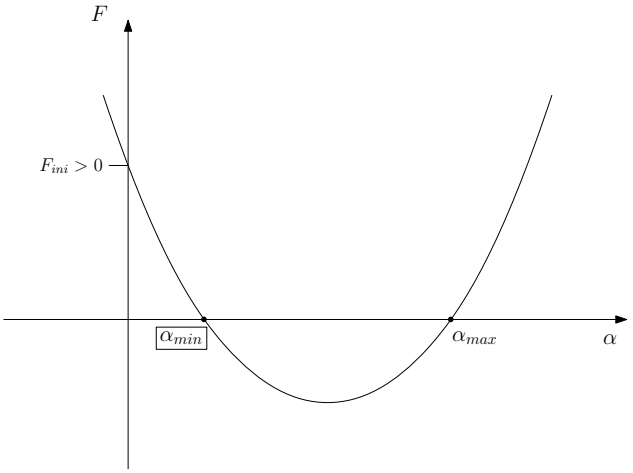

Figure 2.8: Case a) entry point where the right solution is α_{min}.

- Case d) exit point: $F_{ini} < 0$ and $F_{fin} > 0$, the right solution is the maximum alpha (α_{max}) (Fig. 2.9).

Note also that in case a), α_{min} represents the first fraction of the increment outside the surface ($F > 0$) and therefore with visco-plastic behaviour while in case d) the visco-plastic behaviour takes place in the second fraction ($1 - \alpha_{max}$) of the increment.

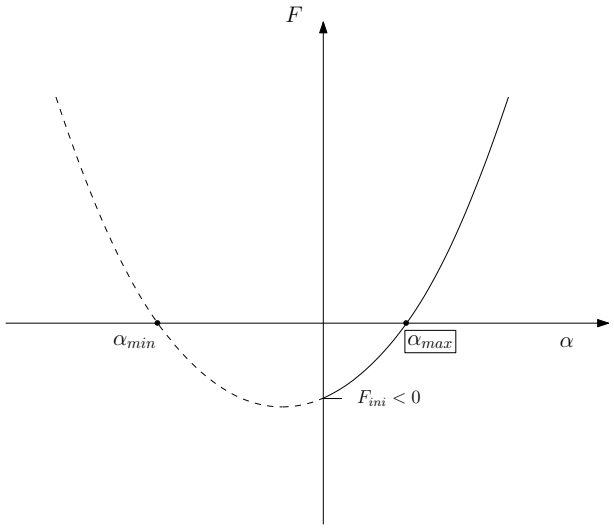

Figure 2.9: Case d) exit point where the right solution is α_{max}.

Once the fraction of the increment with visco-plastic behaviour has been determined for all cases, the next step is to calculate the corresponding visco-plastic strain in the framework of the fracture-based model for zero-thickness interfaces.

$$\Delta \boldsymbol{r}^{vcr} = \int_{t_0}^{t_1} \dot{\boldsymbol{r}}^{vcr} dt = \int_{t_0}^{t_1} \frac{1}{\eta} \frac{F\left(\boldsymbol{\sigma}_{\mathrm{J}}, \boldsymbol{p}\right)}{\overline{F}} \overline{\boldsymbol{m}}\, dt = \frac{\overline{\boldsymbol{m}}}{\eta \overline{F}} \int_{t_0}^{t_1} F\left(\boldsymbol{\sigma}_{\mathrm{J}}, \boldsymbol{p}\right) dt \tag{2.83}$$

The integral of equation (2.83) may be discretized using a generalized trapezoidal rule for the interval $\Delta t = t_1 - t_0$:

$$\Delta \boldsymbol{r}^{vcr} = \frac{\overline{\boldsymbol{m}}}{\eta \overline{F}} \left(\frac{F_{ini}\left(\boldsymbol{\sigma}_{\mathrm{J}}, \boldsymbol{p}\right) + F_{fin}\left(\boldsymbol{\sigma}_{\mathrm{J}}, \boldsymbol{p}\right)}{2} \right) \Delta t \tag{2.84}$$

where $\overline{\boldsymbol{m}}$ is the average flow rule in the visco-plastic interval, which is approximated as $\overline{\boldsymbol{m}} = (1-\gamma)\,\boldsymbol{m}_{ini} + \gamma \boldsymbol{m}_{fin}$ with $\gamma = \frac{1}{2} + \frac{1}{6}\left(\frac{F_{fin}-F_{ini}}{F_{fin}+F_{ini}}\right)$ and, therefore , $(1-\gamma) = \frac{1}{2} - \frac{1}{6}\left(\frac{F_{fin}-F_{ini}}{F_{fin}+F_{ini}}\right)$. This expression of $\overline{\boldsymbol{m}}$ is proposed in order to provide a more accurate approximation of $\boldsymbol{m}$ within the visco-plastic interval. In this context, it guarantees that if $F_{fin} > F_{ini}$ then $\boldsymbol{m}$ takes a value closer to $\boldsymbol{m}_{fin}$ while in the opposite case that $F_{fin} < F_{ini}$ then $\boldsymbol{m}$ takes a value closer to $\boldsymbol{m}_{ini}$. Finally, if $F_{fin} = F_{ini}$, one obtains $\gamma = \frac{1}{2}$, and both $\boldsymbol{m}_{ini}$ and $\boldsymbol{m}_{fin}$ have the same weight in the equation leading to $\overline{\boldsymbol{m}} = (\boldsymbol{m}_{ini} + \boldsymbol{m}_{fin})/2$. Substituting now the expression of $\overline{\boldsymbol{m}}$ into equation (2.84), leads to the final discretized equation for the visco-plastic strain:

$$\Delta \boldsymbol{r}^{vcr} = \frac{\Delta t}{2\eta \overline{F}} \left(\frac{\boldsymbol{m}_{ini} + \boldsymbol{m}_{fin}}{2} \left(F_{fin} + F_{ini}\right) + \frac{\boldsymbol{m}_{ini} - \boldsymbol{m}_{fin}}{6} \left(F_{fin} - F_{ini}\right) \right) \tag{2.85}$$

In the implementation, it is also necessary to integrate the energy dissipated in the fracture process for the visco-plastic model dW^{vcr} (Eq. 2.63). For that purpose, an average of the projected stresses ($\boldsymbol{\sigma}_{Jini}$, $\boldsymbol{\sigma}_{Jfin}$) is used. Considering all possible situations, there is a particular case of b) $F_{ini} > 0$ and $F_{fin} > 0$ (Fig. 2.7-(b)), that deserves special treatment. It is the case in which, in spite of starting and ending outside the surface,the stress trajectory crosses the yield surface (Fig. 2.10).

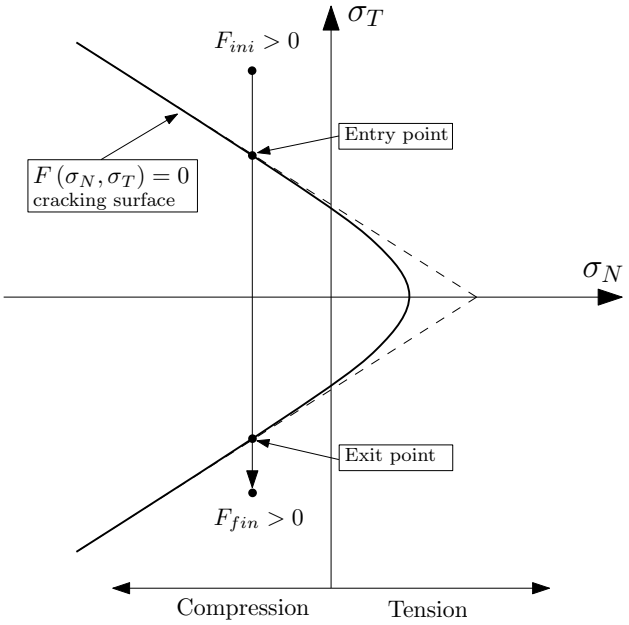

Figure 2.10: Particular case of b), crossing the yield surface.

To identify this case (Fig. 2.10), $\boldsymbol{m}_{ini}$ and $\boldsymbol{m}_{fin}$ are evaluated and the angle between them is calculated. If this angle is higher than a certain pre-established value, it is interpreted that both vectors are very different and one of them belongs to the upper part of the yield surface while the other one belongs to the lower part. Once this case is identified, a subdivision algorithm is activated to reduce the stress and time increment hoping that the final point will be inside the loading surface and the solution may be obtained using previous standard cases. If this is not the case, the subdivision is applied again until the end point falls within the loading surface.

2.7 Hydro-mechanical coupled formulation

The hydro-mechanical coupled formulation including zero-thickness interface elements has been developed and explained in detail in previous publications of the group such as Garolera (2017)

and Pérez (2018). In the present study, the FE code of the research group incorporating that formulation, has been used as the basis to develop the new approach proposed. The main aspects of the underlying H-M coupled formulation are summarized below using the formalism and notation established in Garolera (2017). The classical mechanics sign criterion is used for continuum and interfaces in which compressive stresses are negative and tensile stresses are positive. Opening relative displacements in interfaces are positive and fluid pressure in continuum and interfaces are also positive. The scheme of a boundary value problem (BVP) used in the development of the hydro-mechanical coupled formulation is shown below (Fig. 2.11).

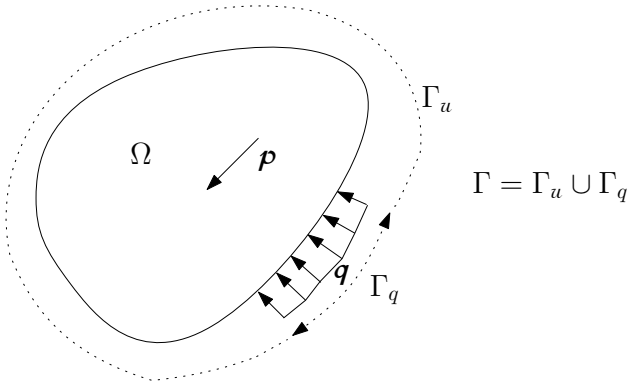

Figure 2.11: Scheme of the boundary value problem: Ω represents the volume domain, Γ is the surface domain boundary, $\boldsymbol{p}$ and $\boldsymbol{q}$ are the load terms per unit of domain volume and surface boundary, respectively (Garolera, 2017).

2.7.1 Formulation of the continuum elements

The main equations of the continuum element formulation are:

2.7.1.1 The mechanical equation

The matrix equation for the mechanical problem in a continuum finite element, takes the form:

$$\int_{\Omega} \mathbf{B}_{\mathrm{C}}^{\mathrm{T}}\, \boldsymbol{\sigma}'\, d\Omega - \mathbf{Q}_{\mathrm{C}}\, \mathbf{p}_e^f = \mathbf{f}_{\mathrm{C}}^u \tag{2.86}$$

where $\mathbf{B}_{\mathrm{C}}^{\mathrm{T}}$ is the classical FE strain to displacements or "B matrix", $\boldsymbol{\sigma}'$ is the effective stress, $\mathbf{p}_e^f$ is the vector of the element nodal fluid pressures, and $\mathbf{Q}_{\mathrm{C}}$ and $\mathbf{f}_{\mathrm{C}}^u$ are the coupling matrix and the

vector of external forces, with expressions.

$$\mathbf{Q}_{\mathrm{C}} = \int_{\Omega} \mathbf{B}_{\mathrm{C}}^{\mathrm{T}}\, \alpha_{Biot}\, \mathbf{N}^{p}\, \mathbf{m}_{\mathrm{C}}^{\mathrm{T}}\, d\Omega \tag{2.87}$$

$$\mathbf{f}_{\mathrm{C}}^{u} = \int_{\Omega} \mathbf{N}^{u\mathrm{T}} \rho\, \mathbf{g}\, d\Omega + \int_{\Gamma_q} \mathbf{N}^{u\mathrm{T}}\, \widetilde{\boldsymbol{t}}\, d\Gamma \tag{2.88}$$

In these equations, α_{Biot} is Biot's coefficient, $\mathbf{m}_{\mathrm{C}}^{\mathrm{T}}$ the identity matrix, $\mathbf{N}^{u\mathrm{T}}$ the nodal interpolation functions for displacements, ρ is the average density $\rho = (1-n)\rho_s + n\rho_f$ where ρ_s is the skeleton density and ρ_f the fluid density. Moreover, $\mathbf{g}$ is the gravity vector and $\widetilde{\boldsymbol{t}}$ is the stress traction over the part of the boundary (Γ_q) in which those tractions are prescribed.

2.7.1.2 The hydraulic equation

The matrix equation for the hydraulic problem in a continuum finite element, takes the form:

$$\mathbf{H}_{\mathrm{C}}\, \mathbf{p}_e^f + \mathbf{Q}_{\mathrm{C}}^{\mathrm{T}} \frac{\partial \mathbf{u}_e}{\partial t} + \mathbf{S}_{\mathrm{C}} \frac{\partial \mathbf{p}_e^f}{\partial t} = \mathbf{f}_{\mathrm{C}}^{p} \tag{2.89}$$

where $\mathbf{u}_e$ is the vector of element nodal displacements, and $\mathbf{H}_{\mathrm{C}}$, $\mathbf{Q}_{\mathrm{C}}$, $\mathbf{S}_{\mathrm{C}}$ and $\mathbf{f}_{\mathrm{C}}^{p}$ are, respectively, the diffusion matrix, the coupling matrix between the mechanical and hydraulic problems, the storage matrix and the element external flow ("hydraulic load") vector, with expressions:

$$\mathbf{H}_{\mathrm{C}} = \int_{\Omega} (\boldsymbol{\nabla} \mathbf{N}^{p})^{\mathrm{T}} \left(\frac{\mathbf{k}^f}{\mu^f} \right) \boldsymbol{\nabla} \mathbf{N}^{p}\, d\Omega \tag{2.90}$$

$$\mathbf{Q}_{\mathrm{C}}^{\mathrm{T}} = \int_{\Omega} \mathbf{N}^{p\mathrm{T}}\, \alpha_{Biot}\, \mathbf{m}_{\mathrm{C}}^{\mathrm{T}}\, \mathbf{B}_{\mathrm{C}}\, d\Omega \tag{2.91}$$

$$\mathbf{S}_{\mathrm{C}} = \int_{\Omega} \mathbf{N}^{p\mathrm{T}} \frac{1}{M^{Biot}}\, \mathbf{N}^{p}\, d\Omega \tag{2.92}$$

$$\mathbf{f}_{\mathrm{C}}^{p} = \int_{\Omega} (\boldsymbol{\nabla} \mathbf{N}^{p})^{\mathrm{T}} \left(\frac{\mathbf{k}^f}{\mu^f} \right) \rho^f\, \mathbf{g}\, d\Omega + \int_{\Gamma_q^f} \mathbf{N}^{p\mathrm{T}}\, \widetilde{q}^f\, d\Gamma \tag{2.93}$$

In these equations, $\mathbf{N}^{p\mathrm{T}}$ is the matrix of nodal interpolation functions for pressure, $\mathbf{k}^f$ is the hydraulic conductivity, μ^f is the dynamic viscosity, M^{Biot} is the Biot's modulus, ρ^f is the fluid density and $\widetilde{q}^f$ describes a prescribed flow, or specific discharge, on the part of the boundary with this type of prescribed boundary conditions, Γ_q^f.

2.7.2 Formulation of the zero-thickness interface elements

The main equations of the interface element formulation are:

2.7.2.1 The mechanical equation

The mechanical equation for the interface element takes the form:

$$\int_{\Omega_{\mathrm{J}}} \mathbf{B}_{\mathrm{J}}^{u\mathrm{T}}\, \boldsymbol{\sigma}'_{\mathrm{J}}\, d\Omega_{\mathrm{J}} + \mathbf{Q}_{\mathrm{J}}\, \mathbf{p}_e^f = \mathbf{f}_{\mathrm{J}}^u \tag{2.94}$$

where $\mathbf{B}_{\mathrm{J}}^{u\mathrm{T}}$ is the interface element "B matrix", $\boldsymbol{\sigma}'_{\mathrm{J}}$ is the interface effective stresses traction, $\mathbf{p}_e^f$ represents the nodal fluid pressure, $\mathbf{f}_{\mathrm{J}}^u$ is the vector of external forces for interfaces and $\mathbf{Q}_{\mathrm{J}}$ is the interface element coupling matrix, with expression:

$$\mathbf{Q}_{\mathrm{J}} = \mathbb{T}^{u\mathrm{T}} \int_{\Omega_{\mathrm{J}}} \mathbf{N}_{\mathrm{J}}^{u\mathrm{T}}\, \mathbf{R}^{\mathrm{T}}\, \alpha_{Biot}\, \mathbf{m}_{\mathrm{J}}\, \mathbf{N}_{\mathrm{J}}^{p\mathrm{T}}\, d\Omega_{\mathrm{J}}\, \mathbb{T}_L^p \tag{2.95}$$

where $\mathbb{T}^u$ is the mechanical "transport" matrix, which converts absolute nodal variables into "jumps" at the mid plane points, $\mathbf{N}_{\mathrm{J}}^u$ is the matrix of nodal shape functions for displacements, $\mathbf{R}^{\mathrm{T}}$ is the rotation matrix that transforms vector components in local (normal-tangent) orthogonal axes to global (x,y,z) axes, $\mathbf{N}_{\mathrm{J}}^p$ is the matrix of nodal shape functions for pressure, α_{Biot} is Biot's coefficient, $\mathbf{m}_{\mathrm{J}} = \begin{pmatrix} 1 & 0 & 0 \end{pmatrix}^{\mathrm{T}}$ and $\mathbb{T}_L^p$ is the "transport" matrix in terms of pressure and longitudinal flow.

2.7.2.2 The hydraulic equation

The interface element equation for hydraulic behavior consists of two contributions: the longitudinal and the transversal flow. The longitudinal flow equation is given by:

$$\mathbf{H}_{\mathrm{J}_L}^p\, \mathbf{p}_e^f + \mathbf{Q}_{\mathrm{J}}^{\mathrm{T}}\, \frac{\partial \mathbf{u}_e}{\partial t} + \mathbf{S}_{\mathrm{J}}\, \frac{\partial \mathbf{p}_e^f}{\partial t} = \mathbf{f}_{\mathrm{J}_L}^p \tag{2.96}$$

where $\mathbf{p}_e^f$ is the vector of element nodal pressure values, $\mathbf{f}_{\mathrm{J}_L}^p$ is the element longitudinal external discharge ("hydraulic load") vector, and $\mathbf{H}_{\mathrm{J}_L}^p$, $\mathbf{Q}_{\mathrm{J}}$, and $\mathbf{S}_{\mathrm{J}}$ are, respectively, the longitudinal diffusion ("stiffness) matrix , the coupling matrix between the mechanical and hydraulic problems, and the storage matrix.

The transversal flow equation is given by:

$$\mathbf{H}^{p}_{\mathrm{J}_T}\,\mathbf{p}^{f}_{e} = \mathbf{f}^{p}_{\mathrm{J}_T} \tag{2.97}$$

Combining, finally, the longitudinal and the transversal flow, with the assumption that pressure vector is the same vector $\mathbf{p}^{f}_{e}$, the final overall hydraulic interface element equation is obtained as follows:

$$\mathbf{H}_{\mathrm{J}}\,\mathbf{p}^{f}_{e} + \mathbf{Q}^{\mathrm{T}}_{\mathrm{J}}\,\frac{\partial \mathbf{u}_e}{\partial t} + \mathbf{S}_{\mathrm{J}}\,\frac{\partial \mathbf{p}^{f}_{e}}{\partial t} = \mathbf{f}^{p}_{\mathrm{J}} \tag{2.98}$$

where $\mathbf{H}_{\mathrm{J}} = \mathbf{H}^{p}_{\mathrm{J}_L} + \mathbf{H}^{p}_{\mathrm{J}_T}$ is the combined (longitudinal + transversal) diffusion matrix, $\mathbf{f}^{p}_{\mathrm{J}} = \mathbf{f}^{p}_{\mathrm{J}_L} + \mathbf{f}^{p}_{\mathrm{J}_T}$ is the combined (longitudinal + transversal) nodal discharge vector for the interface element and all the above matrices and vectors have expressions:

$$\begin{aligned}\mathbf{H}_{\mathrm{J}} = \mathbf{H}^{p}_{\mathrm{J}_L} + \mathbf{H}^{p}_{\mathrm{J}_T} = \mathbb{T}^{p\mathrm{T}}_{L}\left(\int_{\Omega_{\mathrm{J}}} \boldsymbol{\nabla}_{\mathrm{J}}\,\mathbf{N}^{p\mathrm{T}}_{\mathrm{J}}\left(\frac{T_L}{\gamma^f}\right)\boldsymbol{\nabla}_{\mathrm{J}}\,\mathbf{N}^{p}_{\mathrm{J}}\,d\Omega_{\mathrm{J}}\right)\mathbb{T}^{p}_{L} + \\ + \mathbb{T}^{p\mathrm{T}}_{T}\left(\int_{\Omega_{\mathrm{J}}} \mathbf{N}^{p\mathrm{T}}_{\mathrm{J}}\,\check{K}_t\,\mathbf{N}^{p}_{\mathrm{J}}\,d\Omega_{\mathrm{J}}\right)\mathbb{T}^{p}_{T}\end{aligned} \tag{2.99}$$

$$\mathbf{Q}^{\mathrm{T}}_{\mathrm{J}} = \mathbb{T}^{p\mathrm{T}}_{L}\left(\int_{\Omega_{\mathrm{J}}} \mathbf{N}^{p\mathrm{T}}_{\mathrm{J}}\,\alpha_{Biot}\,\mathbf{m}^{\mathrm{T}}\,\mathbf{R}\,\mathbf{N}^{u}_{\mathrm{J}}\,d\Omega_{\mathrm{J}}\right)\mathbb{T}^{u} \tag{2.100}$$

$$\mathbf{S}_{\mathrm{J}} = \mathbb{T}^{p\mathrm{T}}_{L}\left(\int_{\Omega_{\mathrm{J}}} \mathbf{N}^{p\mathrm{T}}_{\mathrm{J}}\frac{1}{M^{Biot}}\mathbf{N}^{p}_{\mathrm{J}}\,d\Omega_{\mathrm{J}}\right)\mathbb{T}^{p}_{L} \tag{2.101}$$

$$\begin{aligned}\mathbf{f}^{p}_{\mathrm{J}} = \mathbb{T}^{p\mathrm{T}}_{L}\int_{\Omega_{\mathrm{J}}} \left(\boldsymbol{\nabla}_{\mathrm{J}}\mathbf{N}^{p}_{\mathrm{J}}\right)^{\mathrm{T}}\left(-\mathrm{T}^{f}\right)\boldsymbol{\nabla}_{\mathrm{J}}z\,d\Omega_{\mathrm{J}} + \\ + \mathbb{T}^{p\mathrm{T}}_{L}\int_{\Gamma^{f}_{q}} \mathbf{N}^{p\mathrm{T}}_{\mathrm{J}}\,\widetilde{Q'}^{f}\,d\Gamma\end{aligned} \tag{2.102}$$

In the above equations, $\boldsymbol{\nabla}_{\mathrm{J}}$ is the nabla operator for the local orthogonal in-plane coordinate system on the interface mid-plane surface, T_L is the longitudinal transmissivity, γ^f is the fluid specific weight, $\mathbb{T}^{p}_{L}$ and $\mathbb{T}^{p}_{T}$ are the "transport" matrices in terms of pressure regarding longitudinal and transversal flow respectively, $\check{K}_t$ is the transverse hydraulic coefficient, M^{Biot} is Biot's modulus, α_{Biot} is Biot's coefficient, $\mathbf{m}^{\mathrm{T}} = \begin{pmatrix} 1 & 0 & 0 \end{pmatrix}^{\mathrm{T}}$, T^f is the transmissivity matrix and $\widetilde{Q'}^{f}$ is the prescribed value of the fluid pressure on the Γ^{f}_{p} boundary.

2.7.3 Time discretization and global matrix assembly

Time discretization is performed following a traditional finite difference scheme, by assuming a linear evolution of the unknowns within a time increment. The resulting time-discretized equations

are:

$$
\begin{gathered}
-\int_{\Omega} \mathbf{B}^{u\mathrm{T}}\, \boldsymbol{\sigma}'_{n+\theta}\, d\Omega + \theta\, \mathbf{Q}\, \Delta \mathbf{p}^{f}_{e\,n+1} + \mathbf{Q}\, \mathbf{p}^{f}_{e\,n} + \mathbf{f}^{u}_{n+\theta} = 0 \\
\\
\left(\mathbf{S}_{n+\theta} + \theta \Delta t_{n+1}\, \mathbf{H}_{n+\theta}\right) \Delta \mathbf{p}^{f}_{e\,n+1} + \mathbf{Q}^{\mathrm{T}}\, \Delta \mathrm{u}_{e\,n} + \\
+ \Delta t_{n+1}\, \mathbf{H}_{n+\theta}\, \mathbf{p}^{f}_{e\,n} - \Delta t_{n+1}\, \mathbf{f}^{p}_{n+\theta} = 0
\end{gathered}
\tag{2.103}
$$

Note that both continuum and interface formulations lead to similar expressions for the mechanical and hydraulic problem, the subscript "C" and "J" have been dropped. Parameter θ indicates the time at which the variable is evaluated with a range from 0 (explicit forward scheme) to 1 (implicit Backward Euler scheme).

Finally, equations (2.103) for each of the continuum and interface elements are assembled into a global system of equations representing the overall domain under analysis.

Chapter 3

Instability control methods in visco-plasticity

Contents

3.1 Introduction

Fault reactivation events may be considered as a mechanical instability phenomenon represented in the numerical analysis by a critical point on the non-linear solution path. Critical points are characterized by a snapping behavior in the structural (boundary value problem) response, and often standard numerical solution techniques such as Newton-Raphson methods are not capable of overcoming these critical points and therefore passing through them becomes one of the major

difficulties to overcome. Moreover, critical points can be classified as bifurcation points or limit points. Bifurcation points are characterized by the multiplicity of admissible solutions while limit points have only one admissible solution. Two types of limit points can be distinguished (1) load limit point when the applied load reaches a local maximum and a post-peak snap-through behavior occurs, and (2) displacement limit point when the solution path exhibits a local snap-back behavior.

Overcoming the difficulties caused by these limit points may require using special numerical procedures. If the limit point is of the first type (peak load), a standard Newton-Raphson iterative procedure may be enough to overcome this point. In contrast, if the limit point is of the second type (instability or snap-back), special techniques such as Arc-Length (AL) or Indirect Displacement Control (IDC) methods might be required. However, each method has its own peculiarities and limitations. Arc-Length method was initially proposed by Riks (1972) and Wempner (1971), followed by Ramm (1981) and then Crisfield (1981) was the first to propose a fully quadratic constraint equation which leads to a second-degree polynomial of the loading factor variation for the subsequent iteration. This constraint always exhibits two possible solutions, from which the appropriate root must be chosen. A key point in this methodology is the criterion for the selection of the proper root. Crisfield (1981) and, later, Hellweg and Crisfield (1998) tried to improve the method proposing solutions to face these numerical difficulties but in terms of numerical stability, computational efficiency and applicability the advantages and disadvantages of the Arc-Length method are still unclear. Regarding Indirect Displacement Control, this method was proposed by De Borst (1986) and is based on displacement differences which lead to a linear constraint. However, it requires an *a priori* knowledge of the expected failure zone.

Other variants of these methods are those which involve a monotonically increasing dissipation energy to solve non-linear problems. Gutiérrez (2004) developed a formulation of a simple path-following constraint based on the dissipated energy during the failure process. This methodology does not require *a priori* knowledge on the position and behavior of the failure process zone and was applied to damage models. This contribution was then extended by Verhoosel et al. (2009) to plasticity models and geometrically non-linear problems with damage. Then, May et al. (2016) proposed a new arc-length control method based on the rates of the internal and the dissipated energy. Bellora and Vescovini (2016) presented a proposal of hybrid-methods based on the combined use of geometric and dissipative constraint equations, which are updated at each step of the solution process on the basis of the damage state of the structure. This approach allows to guarantee robustness and improved computational efficiency, avoiding abrupt time-consuming transitions between the solution strategies for the dissipative and the elastic phase. More recently, Sanchez

et al. (2020) proposed a continuation method with multiple restrictions to solve the nonlinear system of equilibrium equations and overcome global convergence problems due to the sudden energy release in fracture propagation analyses. The method combines simultaneously the cylindrical Arc-Length and the dissipation-energy control methods. Then, it is applied in a linear softening damage model to simulate mixed-mode fractures. Other researchers as Zhang et al. (2021), developed a dissipation-based Arc-Length method implemented in the framework of the procedure they denote as the Global Cracking Elements Method (GCEM).

Emphasizing the contributions of MECMAT research group in this field, an alternative IDC strategy based on a prescribed increment of fracture dissipation has recently been proposed by Crusat (2018). This strategy is particularized for the elasto-plastic constitutive law developed by Carol et al. (1997) and Caballero et al. (2008) which is detailed in Section 2.5.1. Moreover, a new combined strategy between the mentioned alternative Indirect Displacement Control method based on fracture energy dissipation and the traditional cylindrical Arc-Length method was firstly developed in Crusat (2018). This was motivated by the impossibility of dissipation-based IDC strategies to follow successfully the structure equilibrium path in all cases and for all ranges of loading.

In this energy context, one of the novel path following methods proposed in this thesis constitutes a new IDC iterative method in which the constraint is based on the visco-plastic dissipation.

An alternative approach to the AL or IDC methods to solve non-linear mechanical problems with instabilities is the Dynamic Relaxation (DR) method (Papadrakakis, 1981; Underwood, 1983). The idea behind this approach is to solve the static problem as a fictitious dynamic problem, and the approach has been applied to solve a variety of engineering problems with highly non-linear behavior, such as nonlinear analyses (Frieze et al., 1978; Zhang and Yu, 1989; Golmakani and Kadkhodayan, 2011; Rezaiee-Pajand et al., 2012), buckling and post-buckling analysis (Bardet and Proubet, 1991; Pasqualino and Estefen, 2001; Ramesh and Krishnamoorthy, 1994; Rezaiee-Pajand and Alamatian, 2011), form-finding and membrane analyses (Wood, 2002; Han and Lee, 2003; Barnes et al., 2013), fracture mechanics (Kilic and Madenci, 2009, 2010), geotechnics (Dang and Meguid, 2010; Kardani et al., 2017) and dynamic analysis (Rezaiee-Pajand and Alamatian, 2008; Namadchi and Alamatian, 2016; Esmaeilzadeh and Kadkhodayan, 2019).

A strategy similar to Dynamic Relaxation but applied in quasi-static analysis in combination with visco-plastic behavior, is the Visco-plastic Relaxation (VPR) (Aliguer et al., 2017). This strategy leads to the solution of the static inviscid problem, by using a fictitious time variable governing the visco-plasticity, and applying fictitious time increments until a stationary solution is

reached.

Moreover, the VPR approach offers a way to overcome the issue of duplicity of time variables in hydro-mechanical (H-M) problems when visco-plasticity is used. In this case, the physical time is needed in the H-M problem, while visco-plasticity can be governed by a fictitious time that will start all over again from zero for each of the new physical time increments. In the H-M context, also Arc-Length strategies exhibit a conceptual limitation which favors the VPR strategy. This is because to overcome critical points AL strategies may lead to negative load factor increments (as in cases with snap-back) which, if physical time is involved, would imply a negative time increment as well, which makes no physical sense. For this reason, VPR strategy becomes more relevant for coupled H-M problems.

The content of this chapter is organized as follows: after this Introduction (Sec. 3.1), the application of the standard Newton-Raphson iterative scheme to visco-plasticity is reviewed in Section 3.2; in Section 3.3 a novel IDC method based on the time increment adjustment to obtain a certain target value of visco-plastic dissipation is proposed, and in Section 3.4 a VPR scheme is described in which a fictitious time is defined for the visco-plastic model independent of the physical time, thus making possible the combination of VPR with other physical time-governed phenomena such as fluid flow or diffusion.

3.2 Newton-Raphson iterative scheme applied to stress-driven visco-plasticity

In the case that the constitutive model is a stress-driven visco-plastic model, the FEM implementation of a Newton-Raphon (NR) iterative scheme requires of minor adjustments with respect to the standard scheme developed for traditional strain-driven constitutive models. The procedure is described in Aliguer et al. (2017) and will be only briefly summarized here.

The traditional implementation of NR scheme in the FEM is understood as a sequence of trials on the values of the nodal displacements ("iterations"), each of which requires:

1) Prior to the structural (FE-level) calculation: Evaluation of the tangential stiffness matrices and initial/residual force vectors of all elements, which are then assembled into global stiffness matrix and force vector.

2) Solution of the global (FE-level) system of linear equations to obtain nodal displacement increments for the iteration, which are then accumulated to previous values of current iterative process.

3) Post-solver calculation: verification of material and equilibrium conditions, for each Gauss point, from accumulated nodal displacements, the corresponding strain increments are obtained via "B" matrix, the constitutive subroutine is called with initial state and strain increment to obtain final stress and new stiffness matrix, the final stress is then integrated over the elements and assembled into global vector of internal forces, which is then compared to vector of (prescribed) external forces to obtain residual (unbalanced) force vector for next iteration, and also new global stiffness is formed.

Traditional strain-driven constitutive models naturally fit into this scheme, that in step 3) implies to prescribe strain increments to the constitutive model. However, stress-driven models such as the visco-plastic models considered in the present thesis, require some adaptation as explained in the paragraphs below and Figure 3.1.

The NR scheme for the stress-driven visco-plastic model developed in this thesis, is the following:

a) In the first iteration (Fig. 3.1-left) for each Gauss point in which the stress state exceeds the loading surface, the constitutive subroutine is called with the initial state ($\boldsymbol{\sigma}_{ini}^{P1}$, $\boldsymbol{\varepsilon}_{ini}^{P1}$) (point "0" in the figure) and the prescribed values of the time increment Δt, and zero stress increment $\Delta\boldsymbol{\sigma} = 0$. The subroutine then returns the corresponding final strain value, $\boldsymbol{\varepsilon}_{real}^{P1}$, (point "1") from which the strain increment may be obtained $\Delta\boldsymbol{\varepsilon}^{P1} = \boldsymbol{\varepsilon}_{real}^{P1} - \boldsymbol{\varepsilon}_{ini}^{P1}$, as well as the new stiffness $\boldsymbol{D}"^{P1}$. The value of stress drop for zero strain increment ("relaxation stress") is then computed as $\Delta\boldsymbol{\sigma}^{P1} = -\boldsymbol{D}"^{P1} : \Delta\boldsymbol{\varepsilon}^{P1}$ (point "2"). The values of $\boldsymbol{\sigma}_{ini}^{P1} + \Delta\boldsymbol{\sigma}^{P1}$ at each Gauss point are finally integrated over the elements and assembled into the global internal force vector leading to the calculation of the residual forces. In the same way, the stiffness $\boldsymbol{D}"^{P1}$ at each visco-plastic Gauss point, together with the values of initial stiffness $\boldsymbol{D}_0$ at the points in elastic state, are integrated to obtain the element stiffness matrices which are then assembled into the global stiffness matrix.

b) Same as in the strain-driven law, solution of the global (FE-level) system of linear equations leads to the nodal displacement increments for the iteration, which are then accumulated to previous values of current iterative process.

c) Post-solver calculation: for each Gauss point, from accumulated nodal displacements the corresponding total strain increments are obtained via "B" matrix. On the corresponding stress-strain diagram (Fig. 3.1-left), this means moving up on the stiffness slope, from point "2" to point "3" along that slope. This represents the final stress-strain solution of the current iteration at the Gauss point level with values ($\boldsymbol{\sigma}_{updated}^{P1}$, $\boldsymbol{\varepsilon}_{updated}^{P1}$). Now, the preparation of the second iteration

starts by calling the stress-driven constitutive law with the same initial state ($\boldsymbol{\sigma}_{ini}^{P1}$, $\boldsymbol{\varepsilon}_{ini}^{P1}$) and same prescribed values of the time increment Δt, but new values of $\Delta\boldsymbol{\sigma} = \boldsymbol{\sigma}_{updated}^{P1} - \boldsymbol{\sigma}_{ini}^{P1}$. The constitutive subroutine will return the new values of final strain that, together with the updated stress, correspond to point "4" in Figure 3.1-right, and will also return the new stiffness $\boldsymbol{D}^{"P2}$. With these values one can compute the position of the new point "5" and therefore the new values of stress to obtain the new internal force vector to calculate the new residual, as well as new stiffness, and go back to point b).

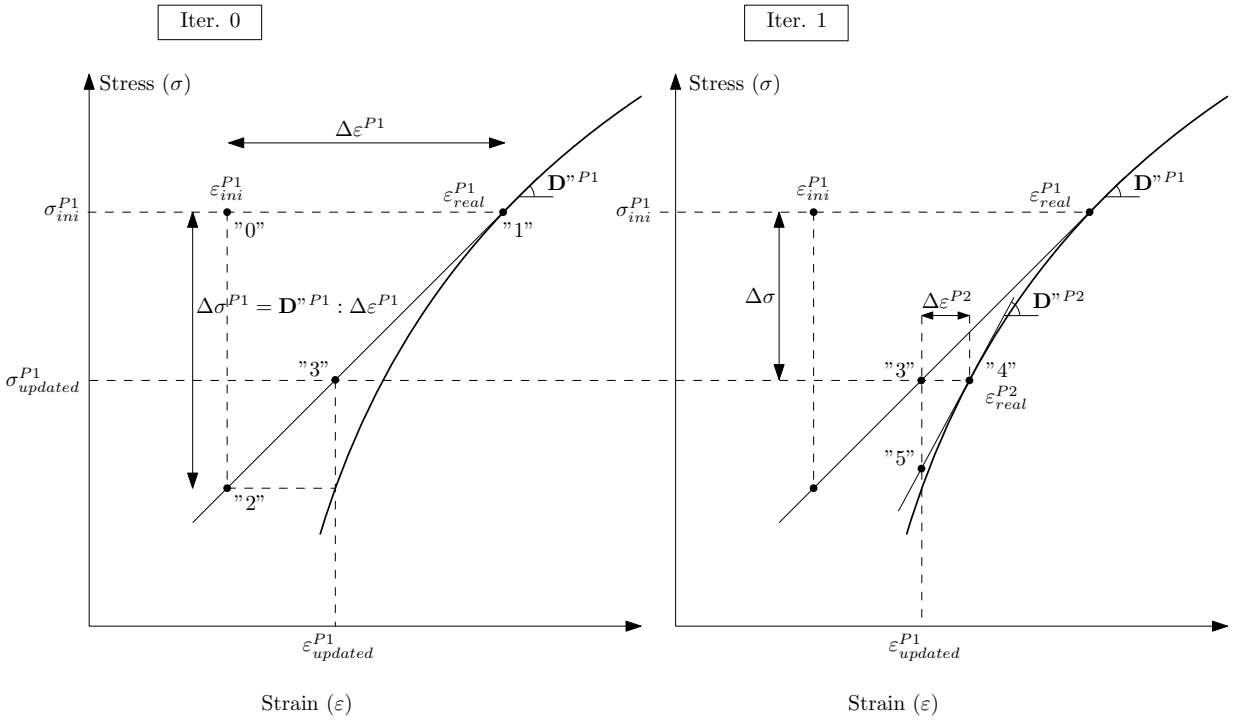

Figure 3.1: NR scheme stress-driven visco-plastic constitutive law.

3.3 Indirect displacement control based on visco-plastic dissipation

3.3.1 General formulation

In the context of a FE analysis using interface elements with the fracture-based visco-plastic model described in Chapter 2, a new indirect control iterative method has been developed in which the

constraint is based on the visco-plastic dissipation. Similar to AL and IDC methods, the loading process is divided into steps called "increments". In each of those increments, the external load factor is not known in advance, but is adjusted progressively during the iterative calculation. The total displacement increment vector (accumulated along the iterative calculation process until the current iteration k) is denoted as ${}^{k}\Delta\boldsymbol{u}$ and is composed by the displacement increment from the previous iteration $\left({}^{k-1}\Delta\boldsymbol{u}\right)$ plus the correction obtained in the current iteration $\left({}^{k}\delta\boldsymbol{u}\right)$ (Eq. 3.1).

$$ {}^{k}\Delta\boldsymbol{u} = {}^{k-1}\Delta\boldsymbol{u} + {}^{k}\delta\boldsymbol{u} \tag{3.1} $$

The correction ${}^{k}\delta\boldsymbol{u}$ is obtained by evaluating and applying on the domain the residual force vector, which in turn is calculated from the difference between external and internal force vectors. Considering visco-plasticity, this residual vector depends on both displacement and time increments (Eq. 3.2).

$$ {}^{k}\boldsymbol{\Psi}_{res}\left(\Delta\boldsymbol{u},\Delta t\right) = \Delta\boldsymbol{F}_{ext} - \Delta\boldsymbol{F}_{int} = \Delta\boldsymbol{F}_{ext} - \sum_{n.el.}\int_{V}\boldsymbol{B}^{T}\Delta\boldsymbol{\sigma}\left(\Delta\boldsymbol{u},\Delta t\right)dV \tag{3.2} $$

In the iterative scheme, it is assumed that the new residual will vanish after application of the previous residual with the corresponding Jacobians:

$$ {}^{k}\boldsymbol{\Psi}_{res}\left(\Delta\boldsymbol{u},\Delta t\right) = {}^{k-1}\boldsymbol{\Psi}_{res}\left(\Delta\boldsymbol{u},\Delta t\right) + \left.\frac{\partial^{k-1}\boldsymbol{\Psi}_{res}}{\partial\Delta\boldsymbol{u}}\right|_{\Delta t}{}^{k}\delta\boldsymbol{u} + \left.\frac{\partial^{k-1}\boldsymbol{\Psi}_{res}}{\partial\Delta t}\right|_{\Delta\boldsymbol{u}}{}^{k}\delta t = 0 \tag{3.3} $$

Note that because on the double dependence of the residual on nodal displacements and time, the Jacobian is constituted by two separate derivatives that need to be developed. First, the derivative of the residual vector with respect to displacement increment considering a constant time increment leads to the stiffness matrix of the previous iteration $\left({}^{k-1}\boldsymbol{K}\right)$ (Eq. 3.4). Second, the derivative of the residual vector with respect to time assuming a constant displacement increment, leads to the expression obtained in equation (3.5). The condition of a constant displacement increment implies that strain increment is also constant and, therefore, the derivative of the stress increment (Eq. 2.51) with respect to time can be considered as $\frac{\partial\Delta\boldsymbol{\sigma}}{\partial\Delta t} = \frac{\partial\Delta\boldsymbol{\sigma}^{0}}{\partial\Delta t} = -\boldsymbol{D}^{\text{"}}\frac{\partial\Delta\boldsymbol{\varepsilon}^{0}}{\partial\Delta t}$. Note that, as a first approach in these derivatives $\boldsymbol{D}^{\text{"}}$ has been assumed constant. But as in any Newton-type iterative procedures in which residuals are evaluated, stiffness is not essential and the possible

consequence of this assumption is that the procedure may require more iterations to converge.

$$\left.\frac{\partial^{k-1}\boldsymbol{\Psi}_{res}}{\partial\Delta\boldsymbol{u}}\right|_{\Delta t} = -\sum_{n.el.}\int_V \boldsymbol{B}^T\frac{\partial\Delta\boldsymbol{\sigma}}{\partial\Delta\boldsymbol{u}}dV = -\sum_{n.el.}\int_V \boldsymbol{B}^T\underbrace{\frac{\partial\Delta\boldsymbol{\sigma}}{\partial\Delta\boldsymbol{\varepsilon}}}_{\boldsymbol{D}"}\underbrace{\frac{\partial\Delta\boldsymbol{\varepsilon}}{\partial\Delta\boldsymbol{u}}}_{\boldsymbol{B}}dV = \\ = -\sum_{n.el.}\int_V \boldsymbol{B}^T\boldsymbol{D}"\boldsymbol{B}dV = -{}^{k-1}\boldsymbol{K} \tag{3.4}$$

$$\left.\frac{\partial^{k-1}\boldsymbol{\Psi}_{res}}{\partial\Delta t}\right|_{\Delta\boldsymbol{u}} = -\sum_{n.el.}\int_V \boldsymbol{B}^T\frac{\partial\Delta\boldsymbol{\sigma}}{\partial\Delta t}dV = -\sum_{n.el.}\int_V \boldsymbol{B}^T\left(-\boldsymbol{D}"\frac{\partial\Delta\boldsymbol{\varepsilon}^0}{\partial\Delta t}\right)dV \tag{3.5}$$

Introducing (Eqs. 3.4 and 3.5) into (Eq. 3.3), setting ${}^k\boldsymbol{\Psi}_{res} = 0$ and isolating ${}^k\delta\boldsymbol{u}$, one obtains the variation of displacements that would eliminate the residual for the following iteration, given by the following expression:

$${}^k\delta\boldsymbol{u} = \underbrace{\left({}^{k-1}\boldsymbol{K}\right)^{-1}\,{}^{k-1}\boldsymbol{\Psi}_{res}\left(\Delta\boldsymbol{u},\Delta t\right)}_{a^{II}} \underbrace{-\left({}^{k-1}\boldsymbol{K}\right)^{-1}\sum_{n.el.}\int_V \boldsymbol{B}^T\left(-\boldsymbol{D}"\frac{\partial\Delta\boldsymbol{\varepsilon}^0}{\partial\Delta t}\right)dV\,{}^k\delta t}_{a^{I}} \tag{3.6}$$

or, more concisely as ${}^k\delta\boldsymbol{u} = a^{II} + a^{Ik}\delta t$, which is similar in format to the analogous expression in the cylindrical Arc-Lenght method (Rots, 1988; Crisfield, 1991). The above equation may also be multiplied by the "B" matrix of a particular Gauss point, to obtain the expression of the corresponding strain increment, which is needed later in the formulation:

$${}^k\delta\Delta\boldsymbol{\varepsilon} = \boldsymbol{B}^k\delta\boldsymbol{u} = \boldsymbol{B}a^{II} + \boldsymbol{B}a^{Ik}\delta t \tag{3.7}$$

Knowing the expressions of ${}^k\delta\boldsymbol{u}$ and ${}^k\delta\Delta\boldsymbol{\varepsilon}$, the IDC method based on visco-plastic dissipation can be formulated. For this purpose, the increment of total visco-plastic work in the domain $\Delta\mathcal{W}^{vp}$ during the time-step is expressed as the integral of the visco-plastic dissipation per unit area of the interface (ΔW^{vp}):

$$\Delta\mathcal{W}^{vp} = \sum_{n.el.}\int_V \Delta W^{vp}\left(\Delta\boldsymbol{\sigma},\Delta t\right)dV \tag{3.8}$$

A linear approximation of the change of energy dissipation that takes place between two iterations may be obtained from the previous expression as:

$${}^k\Delta\mathcal{W}^{vp} = {}^{k-1}\Delta\mathcal{W}^{vp} + \delta\Delta\mathcal{W}^{vp} \tag{3.9}$$

$$\delta\Delta\mathcal{W}^{vp} = \sum_{n.el.}\int_V \left.\frac{\partial\Delta W^{vp}}{\partial\Delta\boldsymbol{\sigma}}\right|_{\Delta t} {}^{k}\delta\Delta\boldsymbol{\sigma}\, dV + \sum_{n.el.}\int_V \left.\frac{\partial\Delta W^{vp}}{\partial\Delta t}\right|_{\Delta\boldsymbol{\sigma}} {}^{k}\delta t\, dV \tag{3.10}$$

In the above equations, the visco-plastic stress increment $\Delta\boldsymbol{\sigma}$ is in turn a function of $\Delta\boldsymbol{\varepsilon}$ and Δt, and this is introduced via the constitutive expression:

$${}^{k}\delta\Delta\boldsymbol{\sigma} = \boldsymbol{D}^{\text{”}} : {}^{k}\delta\Delta\boldsymbol{\varepsilon} + {}^{k}\delta\Delta\boldsymbol{\sigma}^{0} = \boldsymbol{D}^{\text{”}} : {}^{k}\delta\Delta\boldsymbol{\varepsilon} + \left(-\boldsymbol{D}^{\text{”}}\delta\Delta\boldsymbol{\varepsilon}^{0} - \boldsymbol{D}^{\text{”}}\frac{\partial\Delta\boldsymbol{\varepsilon}^{0}}{\partial\Delta t}{}^{k}\delta t\right) \tag{3.11}$$

Replacing now ${}^{k}\delta\Delta\boldsymbol{\sigma}$ (Eq. 3.11) into equation (3.10), assuming that ${}^{k-1}\Delta\mathcal{W}^{vp}$ is known (total dissipation increment obtained from the constitutive subroutine values in the previous iteration) and so is ${}^{k}\Delta\mathcal{W}^{vp} = \Delta\overline{\mathcal{W}}^{vp}$ (the prescribed target value), and combining previous equations, the total visco-plastic dissipation for a given iteration may be written as:

$$\begin{aligned}\Delta\overline{\mathcal{W}}^{vp} - {}^{k-1}\Delta\mathcal{W}^{vp} = &\sum_{n.el.}\int_V \left.\frac{\partial\Delta W^{vp}}{\partial\Delta\boldsymbol{\sigma}}\right|_{\Delta t} \boldsymbol{D}^{\text{”}}\boldsymbol{B}a^{II}\, dV + \sum_{n.el.}\int_V \left.\frac{\partial\Delta W^{vp}}{\partial\Delta\boldsymbol{\sigma}}\right|_{\Delta t} \left(-\boldsymbol{D}^{\text{”}}\delta\Delta\boldsymbol{\varepsilon}^{0}\right) dV + \\ &+ \left[\sum_{n.el.}\int_V \left.\frac{\partial\Delta W^{vp}}{\partial\Delta\boldsymbol{\sigma}}\right|_{\Delta t} \boldsymbol{D}^{\text{”}}\boldsymbol{B}a^{I} dV + \sum_{n.el.}\int_V \left.\frac{\partial\Delta W^{vp}}{\partial\Delta\boldsymbol{\sigma}}\right|_{\Delta t} \left(-\boldsymbol{D}^{\text{”}}\frac{\partial\Delta\boldsymbol{\varepsilon}^{0}}{\partial\Delta t}\right) dV + \right. \\ &\left. + \sum_{n.el.}\int_V \left.\frac{\partial\Delta W^{vp}}{\partial\Delta t}\right|_{\Delta\boldsymbol{\sigma}} dV\right] {}^{k}\delta t\end{aligned} \tag{3.12}$$

Reorganizing terms in the previous equation, the final expression of ${}^{k}\delta t$ for the correction of the time increment in order to obtain the prescribed overall dissipation value, is obtained as:

$${}^{k}\delta t = \frac{\Delta\overline{\mathcal{W}}^{vp} - {}^{k-1}\Delta\mathcal{W}^{vp} - \Delta\mathcal{W}^{vp}_{II} - \sum_{n.el.}\int_V \left.\frac{\partial\Delta W^{vp}}{\partial\Delta\boldsymbol{\sigma}}\right|_{\Delta t}\left(-\boldsymbol{D}^{\text{”}}\delta\Delta\boldsymbol{\varepsilon}^{0}\right) dV}{\Delta\mathcal{W}^{vp}_{I}} \tag{3.13}$$

where

$$\begin{aligned}\Delta\mathcal{W}^{vp}_{I} = &\sum_{n.el.}\int_V \left.\frac{\partial\Delta W^{vp}}{\partial\Delta\boldsymbol{\sigma}}\right|_{\Delta t} \boldsymbol{D}^{\text{”}}\boldsymbol{B}a^{I} dV + \sum_{n.el.}\int_V \left.\frac{\partial\Delta W^{vp}}{\partial\Delta\boldsymbol{\sigma}}\right|_{\Delta t} \left(-\boldsymbol{D}^{\text{”}}\frac{\partial\Delta\boldsymbol{\varepsilon}^{0}}{\partial\Delta t}\right) dV + \\ &+ \sum_{n.el.}\int_V \left.\frac{\partial\Delta W^{vp}}{\partial\Delta t}\right|_{\Delta\boldsymbol{\sigma}} dV\end{aligned} \tag{3.14}$$

$$\Delta\mathcal{W}^{vp}_{II} = \sum_{n.el.}\int_V \left.\frac{\partial\Delta W^{vp}}{\partial\Delta\boldsymbol{\sigma}}\right|_{\Delta t} \boldsymbol{D}^{\text{”}}\boldsymbol{B}a^{II}\, dV \tag{3.15}$$

The variation of time increment (Eq. 3.13) tries to correct the difference between the work really spent in the fracture process and the target value of dissipated energy which was prescribed for the

same increment. Depending on whether the energy dissipated in the iteration is lower or higher than the prescribed energy target value, the correction may be positive or negative. However, there is a condition that always has to be fulfilled which is the time increment must always be positive.

As it may be seen in equation (3.13), ${}^{k}\delta t$ is also obtained as a linear expression with a single solution, which is an additional advantage of this procedure.

Note that, in equation (3.13), the term $\frac{\partial \Delta \boldsymbol{\varepsilon}^0}{\partial \Delta t}$ is determined by previous expressions of the visco-plastic formulation in Section 2.4.2. In that section, the initial strain expression is $\Delta \boldsymbol{\varepsilon}^0 = \frac{F_0}{H}\left(1 - e^{\frac{-H\Delta t}{\eta_F}}\right)\boldsymbol{m}$ (Eq. 2.49) which, by derivation with respect to the time increment leads to $\frac{\partial \Delta \boldsymbol{\varepsilon}^0}{\partial \Delta t} = \frac{F_0}{\eta_F} e^{\frac{-H\Delta t}{\eta_F}} \boldsymbol{m}$.

3.3.2 Application to the fracture-based interface model

According to the main purpose of this thesis, the general IDC strategy based on energy dissipation described in previous Section 3.3.1, is specified for the analysis of an elastic continuum with zero-thickness interface elements governed by the constitutive model described in Chapter 2. In order to achieve this purpose, the general expression of dissipation $\Delta \mathcal{W}^{vp}(\Delta \boldsymbol{\sigma}, \Delta t)$ in equation (3.8), must be specified for the interface model at hand, and given the way the model is defined (Chap. 2), two separate cases must be considered: (1) in terms of total dissipation (as has been presented in Sec. 3.3.1) or (2) in terms of the fracture dissipation, which only includes the part of the dissipation that has been spent in fracture processes. In the examples presented later in the thesis, the strategy has been applied always in terms of total dissipation, but in order to be general, the formulation below has been developed separately in the two cases of considering total dissipation, and in the case of considering fracture dissipation (in which case, one has to distinguish in turn two different cases; if stress is in tension or compression).

Note finally that the general notation used in Section 3.3.1 needs to be adapted to the application to interface elements, in that strain variables $\boldsymbol{\varepsilon}$ and stress variables $\boldsymbol{\sigma}$ must be replaced with the relative displacements $\boldsymbol{r}$ and stress tractions on the interface plane.

3.3.2.1 Target in terms of total dissipation

In the fracture-based interface model, the visco-plastic energy dissipation (Eq. 2.63) may be expressed as:

$$\dot{W}^{vp} = \boldsymbol{\sigma}_{\mathrm{J}}(t) \cdot \dot{\boldsymbol{r}}^{vcr} \tag{3.16}$$

As explained in Section 2.6, the implementation of the visco-plastic model for the interface

has been developed with the assumption of prescribed stress with linear variation during each increment. In accordance to that, a linear evolution is assumed for stresses with time, of the type $\boldsymbol{\sigma}_{\mathrm{J}}(t) = \boldsymbol{a} + \boldsymbol{b}t$. Combining this with the general expression of the visco-plastic strain rate in Perzyna visco-plasticity $\dot{\boldsymbol{\varepsilon}}^{vp} = \frac{1}{\eta}\frac{F(t)}{\overline{F}}\boldsymbol{m}$ (Eq. 2.45) expressed in terms of relative displacements for interfaces $\dot{\boldsymbol{r}}^{vcr}$ and the closed-form solution of the yield function (Eq. 2.44) obtained in Section 2.4.1, previous expression (3.16) may be rewritten as:

$$\begin{aligned}\dot{W}^{vp} &= (\boldsymbol{a}+\boldsymbol{b}t) : \frac{1}{\eta}\frac{F(t)}{\overline{F}}\boldsymbol{m} = \boldsymbol{a} : \frac{1}{\eta}\frac{F(t)}{\overline{F}}\boldsymbol{m} + \boldsymbol{b} : t\frac{1}{\eta}\frac{F(t)}{\overline{F}}\boldsymbol{m} = \\ &= \frac{\boldsymbol{a}:\boldsymbol{m}}{\eta\overline{F}}F(t) + \frac{\boldsymbol{b}:\boldsymbol{m}}{\eta\overline{F}}tF(t)\end{aligned} \tag{3.17}$$

Integrating in time the rate of the visco-plastic energy dissipation one obtains:

$$\Delta W^{vp} = \int_{t_0}^{t_1}\dot{W}^{vp}dt = \underbrace{\frac{\boldsymbol{a}:\boldsymbol{m}}{\eta\overline{F}}\int_{t_0}^{t_1}F(t)\,dt}_{\Delta W_a^{vp}} + \underbrace{\frac{\boldsymbol{b}:\boldsymbol{m}}{\eta\overline{F}}\int_{t_0}^{t_1}tF(t)\,dt}_{\Delta W_b^{vp}} \tag{3.18}$$

where $F(t)$ inside the integrals has to be replaced with (Eq. 2.44). For convenience, the right-hand-side has been split into two parts. Developing the first part, the following expression is obtained:

$$\Delta W_a^{vp} = \boldsymbol{a}:\boldsymbol{m}\left[\frac{F_0}{H}\left(1 - e^{\frac{-H}{\eta\overline{F}}(t_1-t_0)}\right) + \frac{(\boldsymbol{n}:\dot{\boldsymbol{\sigma}}_{\mathrm{J}})}{H}\left((t_1-t_0) + \frac{\eta\overline{F}}{H}\left(e^{\frac{-H}{\eta\overline{F}}(t_1-t_0)} - 1\right)\right)\right] \tag{3.19}$$

The second part ΔW_b^{vp}, is a little more involved and the integral is split in three parts

$$\Delta W_b^{vp} = \frac{\boldsymbol{b}:\boldsymbol{m}}{\eta\overline{F}}F_0\underbrace{\int_{t_0}^{t_1}te^{\frac{-H}{\eta\overline{F}}(t-t_0)}dt}_{Integral\ A} + \frac{\boldsymbol{b}:\boldsymbol{m}}{H}(\boldsymbol{n}:\dot{\boldsymbol{\sigma}}_{\mathrm{J}})\underbrace{\int_{t_0}^{t_1}t\,dt}_{Integral\ B} - \frac{\boldsymbol{b}:\boldsymbol{m}}{H}(\boldsymbol{n}:\dot{\boldsymbol{\sigma}}_{\mathrm{J}})\underbrace{\int_{t_0}^{t_1}te^{\frac{-H}{\eta\overline{F}}(t-t_0)}dt}_{Integral\ A} \tag{3.20}$$

Integral "A" appears twice in the equation and may be solved by parts, leading to:

$$\int_{t_0}^{t_1}te^{\frac{-H}{\eta\overline{F}}(t-t_0)}dt = \left(\frac{-\eta\overline{F}}{H}\right)\left[\left(t_1 + \frac{\eta\overline{F}}{H}\right)e^{\frac{-H}{\eta\overline{F}}(t_1-t_0)} - \left(t_0 + \frac{\eta\overline{F}}{H}\right)\right] \tag{3.21}$$

Integral "B", on its side, is pretty trivial:

$$\int_{t_0}^{t_1}t\,dt = \left[\frac{t^2}{2}\right]_{t_0}^{t_1} = \frac{t_1^2}{2} - \frac{t_0^2}{2} = \frac{t_1^2 - t_0^2}{2} \tag{3.22}$$

Once all integrals have been solved and substituted into equation (3.20), the complete expression of ΔW_b^{vp} may be obtained as:

$$\begin{aligned}\Delta W_b^{vp} = &\frac{\boldsymbol{b}:\boldsymbol{m}}{\eta\overline{F}} F_0 \left[\left(\frac{-\eta\overline{F}}{H}\right)\left(\left(t_1+\frac{\eta\overline{F}}{H}\right)e^{\frac{-H}{\eta\overline{F}}(t_1-t_0)} - \left(t_0+\frac{\eta\overline{F}}{H}\right)\right)\right] + \frac{\boldsymbol{b}:\boldsymbol{m}}{H}\left(\boldsymbol{n}:\dot{\boldsymbol{\sigma}}_{\mathrm{J}}\right)\left[\frac{t_1^2-t_0^2}{2}\right] + \\ &- \frac{\boldsymbol{b}:\boldsymbol{m}}{H}\left(\boldsymbol{n}:\dot{\boldsymbol{\sigma}}_{\mathrm{J}}\right)\left[\left(\frac{-\eta\overline{F}}{H}\right)\left(\left(t_1+\frac{\eta\overline{F}}{H}\right)e^{\frac{-H}{\eta\overline{F}}(t_1-t_0)} - \left(t_0+\frac{\eta\overline{F}}{H}\right)\right)\right]\end{aligned} \tag{3.23}$$

After some manipulation, ΔW_a^{vp} and ΔW_b^{vp} can be rewritten as:

$$\Delta W_a^{vp} = \boldsymbol{a}:\boldsymbol{m}\left[\frac{1}{H}\left(\left(F_0 - \frac{\eta\overline{F}}{H}\left(\boldsymbol{n}:\dot{\boldsymbol{\sigma}}_{\mathrm{J}}\right)\right)\left(1-e^{\frac{-H}{\eta\overline{F}}(t_1-t_0)}\right) + \left(\boldsymbol{n}:\dot{\boldsymbol{\sigma}}_{\mathrm{J}}\right)(t_1-t_0)\right)\right] \tag{3.24}$$

$$\begin{aligned}\Delta W_b^{vp} = \boldsymbol{b}:\boldsymbol{m}\frac{1}{H}&\left[\left(F_0 - \frac{\eta\overline{F}}{H}\left(\boldsymbol{n}:\dot{\boldsymbol{\sigma}}_{\mathrm{J}}\right)\right)\left(t_0+\frac{\eta\overline{F}}{H} - \left(t_1+\frac{\eta\overline{F}}{H}\right)e^{\frac{-H}{\eta\overline{F}}(t_1-t_0)}\right) + \right. \\ &\left. + \left(\boldsymbol{n}:\dot{\boldsymbol{\sigma}}_{\mathrm{J}}\right)\left(\frac{t_1^2-t_0^2}{2}\right)\right]\end{aligned} \tag{3.25}$$

In the previous equations, the two unknowns $\boldsymbol{a}$ and $\boldsymbol{b}$ have to be determined by prescribing the initial and final conditions $\boldsymbol{\sigma}_{\mathrm{J}}(t_0) = \boldsymbol{\sigma}_{\mathrm{J0}}$ and $\boldsymbol{\sigma}_{\mathrm{J}}(t_0+\Delta t) = \boldsymbol{\sigma}_{\mathrm{J0}} + \Delta\boldsymbol{\sigma}_{\mathrm{J}}$ which, after some algebra, leads to:

$$\boldsymbol{a} = \boldsymbol{\sigma}_{\mathrm{J0}} - \frac{\Delta\boldsymbol{\sigma}_{\mathrm{J}}}{\Delta t}t_0, \;\; \boldsymbol{b} = \frac{\Delta\boldsymbol{\sigma}_{\mathrm{J}}}{\Delta t} \tag{3.26}$$

Returning to equation (3.18) and replacing $\boldsymbol{a}$ and $\boldsymbol{b}$, the stress rate $\dot{\boldsymbol{\sigma}}_{\mathrm{J}} = \frac{\Delta\boldsymbol{\sigma}_{\mathrm{J}}}{\Delta t}$ and the time increment Δt, the complete visco-plastic energy dissipation expression is obtained as:

$$\begin{aligned}\Delta W^{vp} = &\frac{\boldsymbol{\sigma}_{\mathrm{J0}}:\boldsymbol{m}}{H}\left[\left(F_0 - \frac{\eta\overline{F}}{H\Delta t}\left(\boldsymbol{n}:\Delta\boldsymbol{\sigma}_{\mathrm{J}}\right)\right)\left(1-e^{\frac{-H}{\eta\overline{F}}\Delta t}\right) + \left(\boldsymbol{n}:\Delta\boldsymbol{\sigma}_{\mathrm{J}}\right)\right] + \\ &+ \frac{\Delta\boldsymbol{\sigma}_{\mathrm{J}}:\boldsymbol{m}}{H\Delta t}\left[\left(F_0 - \frac{\eta\overline{F}}{H\Delta t}\left(\boldsymbol{n}:\Delta\boldsymbol{\sigma}_{\mathrm{J}}\right)\right)\left(\frac{\eta\overline{F}}{H} - \left(\frac{\eta\overline{F}}{H}+\Delta t\right)e^{\frac{-H}{\eta\overline{F}}\Delta t}\right) + \right. \\ &\left. + \left(\boldsymbol{n}:\Delta\boldsymbol{\sigma}_{\mathrm{J}}\right)\left(\frac{\Delta t}{2}\right)\right]\end{aligned} \tag{3.27}$$

3.3.2.1.1 Derivatives of ΔW^{vp}

The derivatives of ΔW^{vp} with respect to the time increment duration and the stress increment,

are derived in Appendix B.1, and the resulting expressions are:

$$\begin{aligned}\frac{\partial \Delta W^{vp}}{\partial \Delta t} = \frac{\boldsymbol{\sigma}_{\mathrm{J}0} : \boldsymbol{m}}{H\Delta t}\left[(\boldsymbol{n} : \Delta\boldsymbol{\sigma}_{\mathrm{J}})\left(\frac{\eta\overline{F}}{H\Delta t} + \left(\frac{-\eta\overline{F}}{H\Delta t} - 1\right) e^{\frac{-H}{\eta\overline{F}}\Delta t}\right)\right] + (\boldsymbol{\sigma}_{\mathrm{J}0} + \Delta\boldsymbol{\sigma}_{\mathrm{J}}) : \boldsymbol{m}\left(\frac{F_0}{\eta\overline{F}} e^{\frac{-H}{\eta\overline{F}}\Delta t}\right) + \\ + \frac{\Delta\boldsymbol{\sigma}_{\mathrm{J}} : \boldsymbol{m}}{H\Delta t}\left[F_0\left(\frac{-\eta\overline{F}}{H\Delta t} + \left(\frac{\eta\overline{F}}{H\Delta t} + 1\right) e^{\frac{-H}{\eta\overline{F}}\Delta t}\right) + \frac{2\left(\eta\overline{F}\right)^2}{H^2\Delta t^2}(\boldsymbol{n} : \Delta\boldsymbol{\sigma}_{\mathrm{J}}) + \right. \\ \left. + \left(\frac{\eta\overline{F}}{H\Delta t}\left(\frac{-2\eta\overline{F}}{H\Delta t} - 1\right) + \left(\frac{-\eta\overline{F}}{H\Delta t} - 1\right)\right)(\boldsymbol{n} : \Delta\boldsymbol{\sigma}_{\mathrm{J}})\, e^{\frac{-H}{\eta\overline{F}}\Delta t}\right]\end{aligned} \tag{3.28}$$

$$\begin{aligned}\frac{\partial \Delta W^{vp}}{\partial \Delta\boldsymbol{\sigma}_{\mathrm{J}}} = \frac{\boldsymbol{\sigma}_{\mathrm{J}0} : \boldsymbol{m}}{H}\left[\left(\frac{\eta\overline{F}}{H\Delta t}\left(e^{\frac{-H}{\eta\overline{F}}\Delta t} - 1\right) + 1\right)\boldsymbol{n}\right] + \\ + \frac{1}{H}\left[F_0\left(\frac{\eta\overline{F}}{H\Delta t} - \left(\frac{\eta\overline{F}}{H\Delta t} + 1\right) e^{\frac{-H}{\eta\overline{F}}\Delta t}\right)\boldsymbol{m} + \right. \\ \left. + \left(\frac{\eta\overline{F}}{H\Delta t}\left(\frac{-\eta\overline{F}}{H\Delta t} + \left(\frac{\eta\overline{F}}{H\Delta t} + 1\right) e^{\frac{-H}{\eta\overline{F}}\Delta t}\right) + \frac{1}{2}\right)(\boldsymbol{m}\otimes\boldsymbol{n} + \boldsymbol{n}\otimes\boldsymbol{m}) : \Delta\boldsymbol{\sigma}_{\mathrm{J}}\right]\end{aligned} \tag{3.29}$$

3.3.2.1.2 Limit cases of derivative expressions

Equations (3.28) and (3.29) become singular in the cases of vanishing duration of the time increment, and/or perfect visco-plasticity ($\Delta t \to 0$ and/or $H \to 0$). In these limit cases, the derivatives become undefined because the expressions take an indeterminate form of the $\frac{0}{0}$ type. To solve this indetermination L'Hôpital's rule and Taylor series approximation have been applied, leading to the expressions below, which are valid for both cases $\Delta t \to 0$ and $H \to 0$. The details of this derivation can be found in Appendix B.2.

$$\begin{aligned}\left.\frac{\partial \Delta W^{vp}}{\partial \Delta t}\right|_{Limit} = \boldsymbol{\sigma}_{\mathrm{J}0} : \boldsymbol{m}\left[F_0\left(\frac{1}{\eta\overline{F}} - \frac{H\Delta t}{\left(\eta\overline{F}\right)^2}\right) + \left(\frac{1}{2\eta\overline{F}} - \frac{H\Delta t}{3\left(\eta\overline{F}\right)^2}\right)(\boldsymbol{n} : \Delta\boldsymbol{\sigma}_{\mathrm{J}})\right] + \\ + \Delta\boldsymbol{\sigma}_{\mathrm{J}} : \boldsymbol{m}\left[F_0\left(\frac{1}{2\eta\overline{F}} - \frac{2H\Delta t}{3\left(\eta\overline{F}\right)^2}\right) + \left(\frac{1}{3\eta\overline{F}} - \frac{H\Delta t}{4\left(\eta\overline{F}\right)^2}\right)(\boldsymbol{n} : \Delta\boldsymbol{\sigma}_{\mathrm{J}})\right]\end{aligned} \tag{3.30}$$

$$\begin{aligned}\left.\frac{\partial \Delta W^{vp}}{\partial \Delta\boldsymbol{\sigma}_{\mathrm{J}}}\right|_{Limit} = \boldsymbol{\sigma}_{\mathrm{J}0} : \boldsymbol{m}\left(\frac{\Delta t}{2\eta\overline{F}}\boldsymbol{n}\right) + F_0\frac{\Delta t}{2\eta\overline{F}}\boldsymbol{m} + \left(\frac{\Delta t}{3\eta\overline{F}}\right)(\boldsymbol{m}\otimes\boldsymbol{n} + \boldsymbol{n}\otimes\boldsymbol{m}) : \Delta\boldsymbol{\sigma}_{\mathrm{J}} + \\ + \boldsymbol{\sigma}_{\mathrm{J}0} : \boldsymbol{m}\left(-\frac{H\Delta t^2}{6\left(\eta\overline{F}\right)^2}\boldsymbol{n}\right) + \left(-F_0\frac{H\Delta t^2}{3\left(\eta\overline{F}\right)^2}\right)\boldsymbol{m} + \\ + \left(-\frac{H\Delta t^2}{8\left(\eta\overline{F}\right)^2}\right)(\boldsymbol{m}\otimes\boldsymbol{n} + \boldsymbol{n}\otimes\boldsymbol{m}) : \Delta\boldsymbol{\sigma}_{\mathrm{J}}\end{aligned} \tag{3.31}$$

3.3.2.2 Case of target in terms of fracture dissipation only

In the case that the target of the IDC strategy for the calculation with fracture-based interfaces is established in terms of fracture dissipation only, two cases must be distinguished: tension and compression. This is because, as explained already in Section 2.5, the dissipation takes different format in each of those situations. However, as it turns out, in tension the fracture dissipation coincides with the total dissipation, and therefore the expression would be the same as developed in the previous section. In contrast, in compression the dissipation equation is different and new expressions need to be developed.

Consequently, in this section the visco-plastic dissipation energy is going to be obtained for shear-compression cases only. In this case the work spent in the fracture process is expressed as (Eq. 2.63):

$$\dot{W}^{vcr} = \left(\sigma_T\left(t\right) + \sigma_N\left(t\right)\tan\phi\right)\cdot \dot{r}_T^{vcr} \tag{3.32}$$

Because of the stress-prescribed scheme, normal and tangential stress components may be specified as linear functions of time $\sigma_N\left(t\right) = a_N + b_N t$ and $\sigma_T\left(t\right) = a_T + b_T t$. According to the general expression for the visco-plastic strain rate (Eq. 2.12), the tangential strain rate is $\dot{r}_T^{vcr} = \frac{1}{\eta}\frac{F(t)}{\overline{F}}m_T$ and the closed-form solution for the evolution of the yield function is given by equation (2.44). Replacing those equations in (Eq. 3.32), one obtains the following expression of the fracture dissipation rate:

$$\begin{aligned}\dot{W}^{vcr} &= \left(\left(a_T + b_T t\right) + \left(a_N + b_N t\right)\tan\phi\right)\cdot\left(\frac{1}{\eta}\frac{F\left(t\right)}{\overline{F}}m_T\right) = \\ &= a_T\frac{m_T}{\eta\overline{F}}F\left(t\right) + b_T\frac{m_T}{\eta\overline{F}}tF\left(t\right) + a_N\tan\phi\frac{m_T}{\eta\overline{F}}F\left(t\right) + b_N\tan\phi\frac{m_T}{\eta\overline{F}}tF\left(t\right)\end{aligned} \tag{3.33}$$

Integrating in time the previous equation, leads to the total dissipation for the time increment:

$$\begin{aligned}\Delta W^{vcr} = \int_{t_0}^{t_1}\dot{W}^{vcr}dt = \underbrace{\left(\frac{m_T}{\eta\overline{F}}\left(a_T + a_N\tan\phi\right)\right)\int_{t_0}^{t_1}F\left(t\right)dt}_{\Delta W_a^{vcr}} + \\ + \underbrace{\left(\frac{m_T}{\eta\overline{F}}\left(b_T + b_N\tan\phi\right)\right)\int_{t_0}^{t_1}tF\left(t\right)dt}_{\Delta W_b^{vcr}}\end{aligned} \tag{3.34}$$

As it can be seen, the right-hand side of this equation is split into two parts to make the calculation of the integrals easier. Developing the first part ΔW_a^{vcr} the following expression is

obtained:

$$\begin{aligned}\Delta W_a^{vcr} = ((a_T + a_N \tan\phi)\, m_T) \left[\frac{F_0}{H}\left(1 - e^{\frac{-H}{\eta\overline{F}}(t_1-t_0)}\right) + \right. \\ \left. + \frac{(\boldsymbol{n} : \dot{\boldsymbol{\sigma}}_{\mathrm{J}})}{H}\left((t_1 - t_0) + \frac{\eta\overline{F}}{H}\left(e^{\frac{-H}{\eta\overline{F}}(t_1-t_0)} - 1\right)\right)\right]\end{aligned} \tag{3.35}$$

The development of the second term ΔW_b^{vcr} leads to the following expression:

$$\begin{aligned}\Delta W_b^{vcr} = &\left(\frac{m_T}{\eta\overline{F}}\,(b_T + b_N \tan\phi)\right) F_0 \left[\left(\frac{-\eta\overline{F}}{H}\right)\left(\left(t_1 + \frac{\eta\overline{F}}{H}\right) e^{\frac{-H}{\eta\overline{F}}(t_1-t_0)} - \left(t_0 + \frac{\eta\overline{F}}{H}\right)\right)\right] + \\ &+ ((b_T + b_N \tan\phi)\, m_T)\, \frac{(\boldsymbol{n} : \dot{\boldsymbol{\sigma}}_{\mathrm{J}})}{H}\left[\frac{t_1^2 - t_0^2}{2}\right] + \\ &- ((b_T + b_N \tan\phi)\, m_T)\, \frac{(\boldsymbol{n} : \dot{\boldsymbol{\sigma}}_{\mathrm{J}})}{H}\left[\left(\frac{-\eta\overline{F}}{H}\right)\left(\left(t_1 + \frac{\eta\overline{F}}{H}\right) e^{\frac{-H}{\eta\overline{F}}(t_1-t_0)} - \left(t_0 + \frac{\eta\overline{F}}{H}\right)\right)\right]\end{aligned} \tag{3.36}$$

After some operations, ΔW_a^{vp} and ΔW_b^{vp} may be rewritten as:

$$\begin{aligned}\Delta W_a^{vcr} = ((a_T + a_N \tan\phi)\, m_T) \left[\frac{1}{H}\left(\left(F_0 - \frac{\eta\overline{F}}{H}\,(\boldsymbol{n} : \dot{\boldsymbol{\sigma}}_{\mathrm{J}})\right)\left(1 - e^{\frac{-H}{\eta\overline{F}}(t_1-t_0)}\right) + \right.\right. \\ \left.\left. + (\boldsymbol{n} : \dot{\boldsymbol{\sigma}}_{\mathrm{J}})\,(t_1 - t_0)\right)\right]\end{aligned} \tag{3.37}$$

$$\begin{aligned}\Delta W_b^{vcr} = ((b_T + b_N \tan\phi)\, m_T)\, \frac{1}{H}\left[\left(F_0 - \frac{\eta\overline{F}}{H}\,(\boldsymbol{n} : \dot{\boldsymbol{\sigma}}_{\mathrm{J}})\right)\left(t_0 + \frac{\eta\overline{F}}{H} - \left(t_1 + \frac{\eta\overline{F}}{H}\right) e^{\frac{-H}{\eta\overline{F}}(t_1-t_0)}\right) + \right. \\ \left. + (\boldsymbol{n} : \dot{\boldsymbol{\sigma}}_{\mathrm{J}})\left(\frac{t_1^2 - t_0^2}{2}\right)\right]\end{aligned} \tag{3.38}$$

As in the Tension case which coincides with the total dissipation case (Sec. 3.3.2.1), constants a and b need to be determined. In the compression case, these parameters have to be evaluated separately for normal and tangential components as follows:

$$b_N = \frac{\Delta\sigma_N}{\Delta t},\; b_T = \frac{\Delta\sigma_T}{\Delta t} \tag{3.39}$$

$$a_N = \sigma_{N0} - \frac{\Delta\sigma_N}{\Delta t} t_0,\; a_T = \sigma_{T0} - \frac{\Delta\sigma_T}{\Delta t} t_0 \tag{3.40}$$

The expressions of a and b are then replaced in equations (Eq. 3.37) and (Eq. 3.38) and

combining those equations the visco-plastic fracture energy dissipation is obtained:

$$\begin{aligned}\Delta W^{vcr} = {} & (\sigma_{T0} + \sigma_{N0}\tan\phi)\,\frac{m_T}{H}\left[\left(F_0 - \frac{\eta\overline{F}}{H\Delta t}\,(\boldsymbol{n} : \Delta\boldsymbol{\sigma}_{\mathrm{J}})\right)\left(1 - e^{\frac{-H}{\eta\overline{F}}\Delta t}\right) + (\boldsymbol{n} : \Delta\boldsymbol{\sigma}_{\mathrm{J}})\right] + \\ & + \left(\frac{\Delta\sigma_T}{\Delta t} + \frac{\Delta\sigma_N}{\Delta t}\tan\phi\right)\frac{m_T}{H}\left[\left(F_0 - \frac{\eta\overline{F}}{H\Delta t}\,(\boldsymbol{n} : \Delta\boldsymbol{\sigma}_{\mathrm{J}})\right)\left(\frac{\eta\overline{F}}{H} - \left(\frac{\eta\overline{F}}{H} + \Delta t\right)e^{\frac{-H}{\eta\overline{F}}\Delta t}\right) + \right. \\ & \left. + (\boldsymbol{n} : \Delta\boldsymbol{\sigma}_{\mathrm{J}})\left(\frac{\Delta t}{2}\right)\right]\end{aligned} \tag{3.41}$$

3.3.2.2.1 Derivatives of ΔW^{vcr}

Comparing the final expression of ΔW^{vcr} for the total dissipation (or tension) case (Eq. 3.27) and fracture dissipation in compression case (Eq. 3.41), it can be seen that the parts limited by square brackets are the same. Therefore, the derivative with respect to time increment shown below (Eq. 3.42) is very similar to the one obtained for the tension case (Eq. 3.28). However, regarding the derivative with respect to the stress increment, it needs to be evaluated considering the normal (Eq. 3.43) and tangential (Eq. 3.44) components, which is different from the tension case. The resulting expressions are given below, and the detailed derivations are available in Appendix C.1.

$$\begin{aligned}\frac{\partial\Delta W^{vcr}}{\partial\Delta t} = {} & (\sigma_{T0} + \sigma_{N0}\tan\phi)\,\frac{m_T}{H\Delta t}\left[(\boldsymbol{n} : \Delta\boldsymbol{\sigma}_{\mathrm{J}})\left(\frac{\eta\overline{F}}{H\Delta t} + \left(\frac{-\eta\overline{F}}{H\Delta t} - 1\right)e^{\frac{-H}{\eta\overline{F}}\Delta t}\right)\right] + \\ & + (\Delta\sigma_T + \Delta\sigma_N\tan\phi)\,\frac{m_T}{H\Delta t}\left[F_0\left(\frac{-\eta\overline{F}}{H\Delta t} + \left(\frac{\eta\overline{F}}{H\Delta t} + 1\right)e^{\frac{-H}{\eta\overline{F}}\Delta t}\right) + \left(2\frac{\left(\eta\overline{F}\right)^2}{H^2\Delta t^2}\right)(\boldsymbol{n} : \Delta\boldsymbol{\sigma}_{\mathrm{J}}) + \right. \\ & \left. + \left(\frac{\eta\overline{F}}{H\Delta t}\left(\frac{-2\eta\overline{F}}{H\Delta t} - 1\right) + \left(\frac{-\eta\overline{F}}{H\Delta t} - 1\right)\right)(\boldsymbol{n} : \Delta\boldsymbol{\sigma}_{\mathrm{J}})\,e^{\frac{-H}{\eta\overline{F}}\Delta t}\right] + \\ & + ((\sigma_{T0} + \Delta\sigma_T) + (\sigma_{N0} + \Delta\sigma_N)\tan\phi)\,m_T\frac{F_0}{\eta\overline{F}}e^{\frac{-H}{\eta\overline{F}}\Delta t}\end{aligned} \tag{3.42}$$

$$\begin{aligned}\frac{\partial\Delta W^{vcr}}{\partial\Delta\sigma_N} = {} & (\sigma_{T0} + \sigma_{N0}\tan\phi)\,\frac{m_T}{H}\left[\left(\frac{\eta\overline{F}}{H\Delta t}\left(e^{\frac{-H}{\eta\overline{F}}\Delta t} - 1\right) + 1\right)n_N\right] + \\ & + \tan\phi\frac{m_T}{H}F_0\left(\frac{\eta\overline{F}}{H\Delta t} - \left(\frac{\eta\overline{F}}{H\Delta t} + 1\right)e^{\frac{-H}{\eta\overline{F}}\Delta t}\right) + \\ & + \left(\tan\phi\frac{m_T}{H}\left(n_N\Delta\sigma_N + n_T\Delta\sigma_T\right) + (\Delta\sigma_T + \Delta\sigma_N\tan\phi)\,\frac{m_T}{H}n_N\right)\cdot \\ & \cdot\left(\frac{\eta\overline{F}}{H\Delta t}\left(\frac{-\eta\overline{F}}{H\Delta t} + \left(\frac{\eta\overline{F}}{H\Delta t} + 1\right)e^{\frac{-H}{\eta\overline{F}}\Delta t}\right) + \frac{1}{2}\right)\end{aligned} \tag{3.43}$$

$$\begin{aligned}\frac{\partial \Delta W^{vcr}}{\partial \Delta \sigma_T} &= \left(\sigma_{T0} + \sigma_{N0}\tan\phi\right)\frac{m_T}{H}\left[\left(\frac{\eta\overline{F}}{H\Delta t}\left(e^{\frac{-H}{\eta\overline{F}}\Delta t} - 1\right) + 1\right)n_T\right] + \\ &+ \frac{m_T}{H}F_0\left(\frac{\eta\overline{F}}{H\Delta t} - \left(\frac{\eta\overline{F}}{H\Delta t} + 1\right)e^{\frac{-H}{\eta\overline{F}}\Delta t}\right) + \\ &+ \left(\frac{m_T}{H}\left(n_N\Delta\sigma_N + n_T\Delta\sigma_T\right) + \left(\Delta\sigma_T + \Delta\sigma_N\tan\phi\right)\frac{m_T}{H}n_T\right)\cdot \\ &\cdot\left(\frac{\eta\overline{F}}{H\Delta t}\left(\frac{-\eta\overline{F}}{H\Delta t} + \left(\frac{\eta\overline{F}}{H\Delta t} + 1\right)e^{\frac{-H}{\eta\overline{F}}\Delta t}\right) + \frac{1}{2}\right)\end{aligned} \tag{3.44}$$

3.3.2.2.2 Limit cases of derivative expressions

Concerning the limit expressions of the derivatives obtained for the compression case (Eqs. 3.42, 3.43 and 3.44) and following a similar development as in the tension case (or total dissipation case), this section shows the limit equations obtained. Details of the derivations may be found in Appendix C.2.

The limit expression of the time derivative of the visco-plastic fracture energy dissipation (Eq. 3.42) is as follows:

$$\begin{aligned}\left.\frac{\partial \Delta W^{vcr}}{\partial \Delta t}\right|_{Limit} &= \left(\sigma_{T0} + \sigma_{N0}\tan\phi\right)m_T\left[F_0\left(\frac{1}{\eta\overline{F}} - \frac{H\Delta t}{\left(\eta\overline{F}\right)^2}\right) + \left(\frac{1}{2\eta\overline{F}} - \frac{H\Delta t}{3\left(\eta\overline{F}\right)^2}\right)\left(\boldsymbol{n} : \Delta\boldsymbol{\sigma}_{\mathrm{J}}\right)\right] + \\ &+ \left(\Delta\sigma_T + \Delta\sigma_N\tan\phi\right)m_T\left[F_0\left(\frac{1}{2\eta\overline{F}} - \frac{2H\Delta t}{3\left(\eta\overline{F}\right)^2}\right) + \right. \\ &\left. + \left(\frac{1}{3\eta\overline{F}} - \frac{H\Delta t}{4\left(\eta\overline{F}\right)^2}\right)\left(\boldsymbol{n} : \Delta\boldsymbol{\sigma}_{\mathrm{J}}\right)\right]\end{aligned} \tag{3.45}$$

The limit expression of the derivative of the visco-plastic fracture energy dissipation with respect to the stress increments, both normal and tangential, are:

$$\begin{aligned}\left.\frac{\partial \Delta W^{vcr}}{\partial \Delta \sigma_N}\right|_{Limit} &= \left(\sigma_{T0} + \sigma_{N0}\tan\phi\right)m_T\left(\frac{\Delta t}{2\eta\overline{F}}n_N\right) + \left(F_0\frac{\Delta t}{2\eta\overline{F}}\right)\tan\phi m_T + \\ &+ \left(\frac{\Delta t}{3\eta\overline{F}}\right)\left(\tan\phi m_T\left(n_N\Delta\sigma_N + n_T\Delta\sigma_T\right) + \left(\Delta\sigma_T + \Delta\sigma_N\tan\phi\right)m_T n_N\right) + \\ &+ \left(\sigma_{T0} + \sigma_{N0}\tan\phi\right)m_T\left(-\frac{\Delta t^2}{6\left(\eta\overline{F}\right)^2}n_N\right)H + \left(-F_0\frac{\Delta t^2}{3\left(\eta\overline{F}\right)^2}\right)\tan\phi m_T H + \\ &+ \left(-\frac{\Delta t^2}{8\left(\eta\overline{F}\right)^2}\right)H\left(\tan\phi m_T\left(n_N\Delta\sigma_N + n_T\Delta\sigma_T\right) + \left(\Delta\sigma_T + \Delta\sigma_N\tan\phi\right)m_T n_N\right)\end{aligned} \tag{3.46}$$

$$\begin{aligned}\left.\frac{\partial \Delta W^{vcr}}{\partial \Delta \sigma_T}\right|_{Limit} &= \left(\sigma_{T0}+\sigma_{N0}\tan\phi\right) m_T \left(\frac{\Delta t}{2\eta\overline{F}} n_T\right) + \left(F_0 \frac{\Delta t}{2\eta\overline{F}}\right) m_T + \\ &+ \left(\frac{\Delta t}{3\eta\overline{F}}\right)\left(m_T\left(n_N\Delta\sigma_N + n_T\Delta\sigma_T\right) + \left(\Delta\sigma_T + \Delta\sigma_N\tan\phi\right) m_T n_T\right) \\ &+ \left(\sigma_{T0}+\sigma_{N0}\tan\phi\right) m_T \left(-\frac{\Delta t^2}{6\left(\eta\overline{F}\right)^2} n_T\right) H + \left(-F_0\frac{\Delta t^2}{3\left(\eta\overline{F}\right)^2}\right) H m_T + \\ &+ \left(-\frac{\Delta t^2}{8\left(\eta\overline{F}\right)^2}\right) H\left(m_T\left(n_N\Delta\sigma_N + n_T\Delta\sigma_T\right) + \left(\Delta\sigma_T + \Delta\sigma_N\tan\phi\right) m_T n_T\right)\end{aligned} \tag{3.47}$$

3.4 Visco-plastic Relaxation method

The second procedure developed in this thesis to overcome instability limit points, is Visco-plastic Relaxation (VPR).

In previous sections, physical visco-plasticity has been developed using physical time as a time variable. However, in some cases it may be convenient to consider a fictitious time to be used in the visco-plastic model, such as for instance if the behavior to be represented is inviscid in nature, and the fictitious time is used as an auxiliary parameter to progressively approach the solution of the inviscid non-linear problem as the fictitiuos time develops only to represent the evolution of potential instabilities within each physical time increment. This approach known as Visco-plastic Relaxation (VPR) is a particular version of the more general Dynamic Relaxation approach widely documented in the literature (Papadrakakis (1981); Underwood (1983); Zhang and Yu (1989) among others mentioned in Section 3.1). In recent years this technique has been applied to zero-thickness interface elements with perfect visco-plasticity (Aliguer et al., 2017). In this paper, a readjustment of this methodology is made to adapt it to visco-plasticity with hardening and softening.

As mentioned in Aliguer et al. (2017), Visco-plastic Relaxation is a numerical tool which makes it possible to reach a final stationary state in which the stress state at all Gauss points lies on the plastic surface. In the numerical implementation of VPR, the magnitude of the fictitious time increment is not fixed in advance, but may be readjusted over iterations. Following standard procedures, the visco-plastic integration scheme developed in Section 2.6 has been readapted as a VPR procedure with variable time increments.

The Visco-plastic Relaxation scheme can be understood as a sequence of linear calculations ("iterations"), each of which in this case corresponds to an increment of the fictitious time with visco-plastic behavior. In this way, the "iterative" process convergence may be identified with reaching stationary values in the fictitious time history. Strictly speaking, the calculation of each

time increment in visco-plasticity, by itself, could also require its own iterative process, and therefore in principle the Visco-plastic Relaxation could imply a double incremental/iterative process (fictitious time increments + iterative process within each increment). However, the implementation developed, following the scheme proposed in Aliguer et al. (2017), is based on performing the calculations in such way that a single iteration will be needed to converge for each time step. This is possible thanks to two factors: (1) using a tangential stiffness matrix for the increment that is sufficiently accurate, and (2) using the appropriate (sufficiently small) time step size for the increments. The first factor is achieved thanks to the use of the "m-AGC tangent operator" proposed in Aliguer et al. (2017), which was originally developed for perfect visco-plasticity and in the present thesis has been extended to the case of Hardening/Softening. The second factor is achieved thanks to the time-stepping algorithm implemented: for each time step, after the calculations are completed and the first solution is obtained for all variables at the end of the increment, also the residual forces are evaluated and their norm is compared to a tolerance value. If convergence is satisfied, the results of this first iteration are stored and the calculation proceeds to the following fictitious time step. But if the residual of this first iteration turns out excessive, instead of performing a second iteration the solution obtained is discarded, the time-step size is reduced and a new calculation of the increment is attempted with the smaller time-step. This strategy is complemented with the increase of the following time step in the case that the norm of the residual is smaller than a lower bound value of the tolerance. In this way it is ensured that each time step is resolved with a single calculation similar to a single iteration of the NR method, and the VPR calculation is completed with a single, -and more efficient- "iterative" process.

The process described has been represented in Figure 3.2. The left diagram corresponds to the case in which the first iteration does not satisfy the residual tolerance and the calculation has to be repeated with smaller time step size, while the right diagram corresponds to the case in which, after the increment on the left diagram has been accepted, a new time increment is performed, potentially with a different time step size.

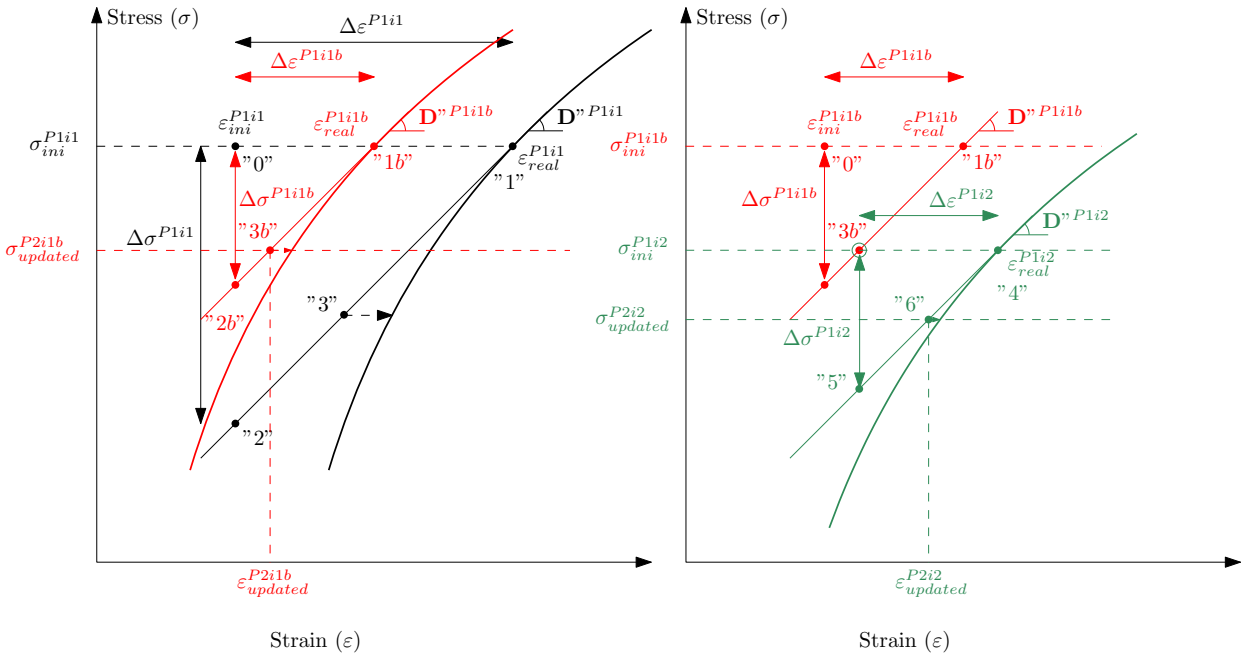

Figure 3.2: Visco-plastic relaxation scheme by iterations: (left) repeating the iteration because it does not satisfy the residual tolerance and (right) after previous iteration finally accepted a new time increments is performed.

The procedure is considered converged when the stress state is close enough to the yield surface and, consequently, the residual stress is lower than a tolerance. In addition, the algorithm shown in Appendix D is provided to describe in detail the VPR scheme.

3.5 Verification examples

Several simple examples have been considered in this section in order to verify the various formulations developed in previous sections. The results of both physical visco-plasticity and VPR approaches have been compared with those that would be obtained with the elasto-plastic constitutive law, with which they should coincide for long visco-plastic time (inviscid limit of the visco-plastic model). Iterative strategies such as Newton-Raphson (NR), Arc-Length (AL) and IDC method based on visco-plastic energy (IDC-Wvp) have been used to obtain the elasto-plastic (EP) and physical visco-plastic (VP) results. Moreover, some of these verification examples are used to verify how the VPR iterative strategy works in cases with instabilities represented by limit points in the solution path such as snap-back.

The first example is a uniaxial tension opening case, the second example is a shear-compression

sliding case with a horizontal sliding plane and constant vertical stress applied statically on the sliding plane, and the third example is another shear-compression test but now considering an interface inclined approximately 40^{o} in a rectangular block loaded vertically, which results in a normal stress on the plane that is not statically pre-determined. For each of the three cases, two sets of parameters and boundary conditions (b.c.s) have been considered, one of them leading to overall behavior with snap-back (instability), and the other not leading to such behavior.

All the examples of this section have some characteristics in common such as the numerical integration schemes used in the Finite Element analysis or the load sequence in the visco-plastic analysis. The integration rules used are: Gauss 2x2 for the continuum quadrangular elements and Trapezoidal rule with integration points at the two ends for the interface elements. Regarding the loading procedure for physical visco-plasticity analyses (which are solved using NR and IDC-Wvp iterative strategies) and VPR approaches, two alternative procedures are considered: the first one, denoted as "two-step" loading procedure, consisting of a prescribed displacement increment (applied instantaneously) followed by time increments at constant nodal displacements, while the second is a "single step" procedure in which prescribed displacements and time step are applied simultaneously.

3.5.1 Uniaxial tension opening

This first example consists of a single interface element subject to uniaxial tension (Fig. 3.3). A square continuum element ($1\,m$ x $1\,m$) has been also included in the discretization.

Regarding the constitutive model for the interface, both the elasto-plastic and visco-plastic fracture-based models described in Section 2.5, are used in the calculations. As explained before, two sets of parameters and boundary conditions have been also considered, one not leading to snap-back in the response curve and the other leading to such unstable behavior. The first set of parameters and b.c.s (not leading to snap-back), consists of displacement values directly prescribed on the interface nodes, and the following parameter values: normal and tangential elastic stiffness $K_N = K_T = 10^6\,MPa/m$, friction angle $\tan\phi = 0.7$, tensile strength $\chi = 2.0\,MPa$, cohesion $c = 2.0\,MPa$, fracture energy mode I $G_f^I = 10^{-5}\,MPa \cdot m$, fracture energy mode IIa $G_f^{IIa} = 10^{-4}\,MPa \cdot m$ and $\sigma_{dil} = 20\,MPa$ (although these two last parameters do no play a role in this case, because they are shear-related and the interface will be subject to pure tension exclusively) and, for visco-plastic calculations, viscosity $\eta = 10^6\,MPa \cdot s$.

Figure 3.4 shows the results of physical visco-plastic analysis, using both one-step and two-step loading procedures. The normal stress–normal relative displacement evolution curves are

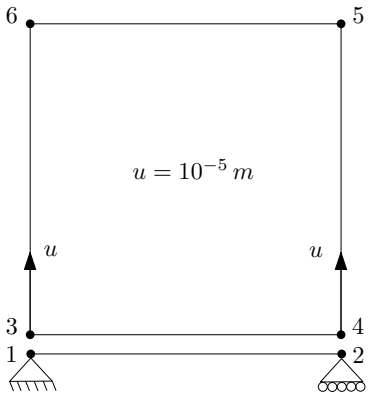

Figure 3.3: Geometry of the uniaxial tension example. Prescribed displacements are imposed on nodes 3 and 4.

represented for all calculation strategies such as EP-NR, VP-NR, VP-IDC-Wvp, VPR and also for the closed-form solution which is available for this simple example. As shown in Figure 3.4-(a), for each load step, VP-NR, VP-IDC-Wvp and VPR responses are composed by an instantaneous elastic stress increment followed by progressive relaxation as time passes, leading in the long term to the same stress value as predicted by the closed-form solution for the same relative displacement, and also very close to response obtained with the inviscid version of the interface model which is slightly shifted up with respect to the other two curves. On the other hand, Figure 3.4-(b) shows the one-step loading procedure used together with the VPR strategy. As in the previous figure, the normal stress–normal relative displacement evolution curves are shown for elasto-plasticity and visco-plastic relaxation approach, together with the closed-form solution, exhibiting great match with the closed-form solution.

The second set of parameters and b.c.s leading to snap-back (instability), for this example consist of prescribing the opening displacements to the top nodes of the continuum element (nodes 5 and 6) instead of the top interface nodes (3 and 4), while the parameters remain the same with the only exception of a slightly higher value of $G_f^I = 3.0 \cdot 10^{-5}\, MPa \cdot m$.

The results obtained using the various iterative strategies are represented in Figure 3.5 (for the two-step loading procedure in the left diagram, and for the one-step loading procedure in the right diagram). In the figure, the horizontal axis corresponds in this case to the vertical displacement of the top nodes 5 and 6, and therefore includes the deformations of both interface and continuum element.

In Figure 3.5-(a), the elastic loading steps lead to stress values higher than the ones predicted by the inviscid response, but then the time steps that follow produce a stress drop which returns

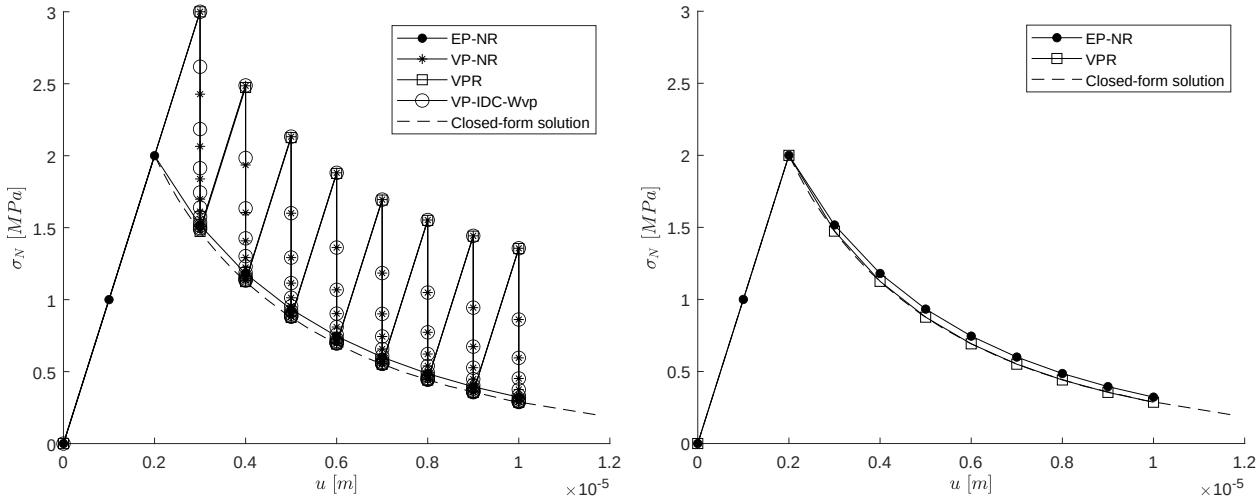

(a) Two-step loading methodology. **(b)** One-step loading methodology.

Figure 3.4: Normal stress - normal relative displacement evolution curves of the interface element.

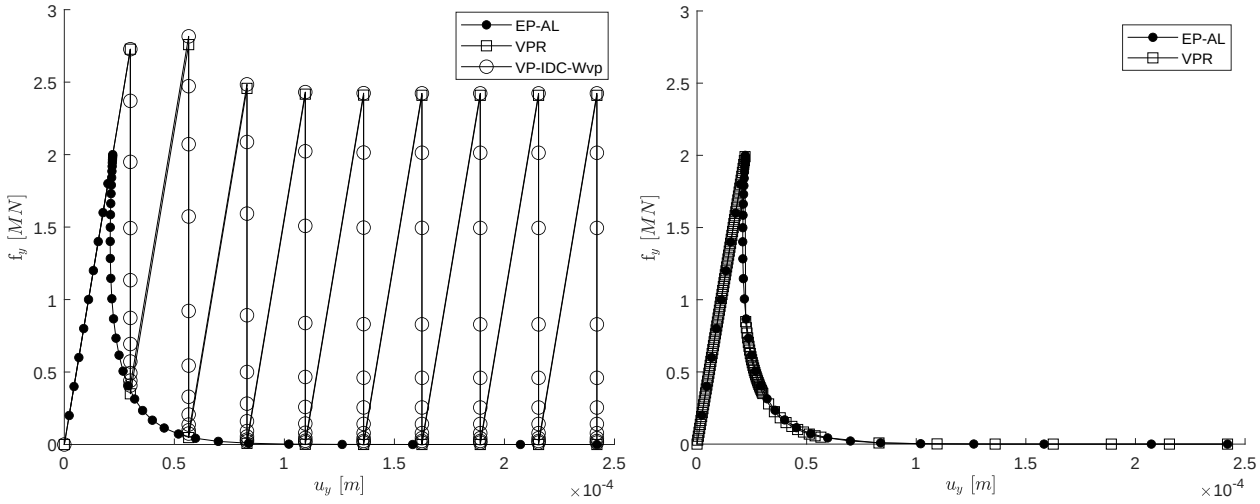

(a) Two-step loading methodology. **(b)** One-step loading methodology.

Figure 3.5: Vertical force - vertical displacement evolution curves on the top face of the continuum element.

stress values to the inviscid curve. In Figure 3.5-(b), simultaneous application of displacement and time, leads to a VPR response that always follows the inviscid curve up to the instability point. Right after that, the VPR response curve show a vertical drop skipping the snap back of the inviscid curve, until both curves meet again, and after that both curves coincide for the rest of the diagram.

This shows that the snap-back instability may be circumvented using the VPR strategy, with the fictitious time acting as a parameter that allows a transient response during the transition between stable zones of the inviscid load-displacement diagram.

3.5.2 Shear-compression sliding

The second example consists of a shear test applied on the same geometry and with the same interface constitutive parameters as the ones used in the first pure-tension example. Because the interface will be subject to shear compression in this example, the shear-related constitutive parameters G_f^{IIa} and σ_{dil} which did not play a role in the previous tension example, become relevant in this case. For the numerical calculations, the continuum is considered linear elastic with Young's modulus $E = 1.5 \cdot 10^4\, MPa$ and Poisson's ratio $\nu = 0$.

The loading sequence is shown in Figure 3.6: first a vertical load is applied on the top face of the continuum element (Fig. 3.6-left) and then horizontal displacements are prescribed to nodes 3 and 4 generating the shear effect (Fig. 3.6-right). Note that two options are also considered in this case for the application of the shear part of the loading: the "two-step" application implies successive small increments of displacement followed each of them by one or more time steps, while the "one step" consists of simultaneous application of shear displacements and time.

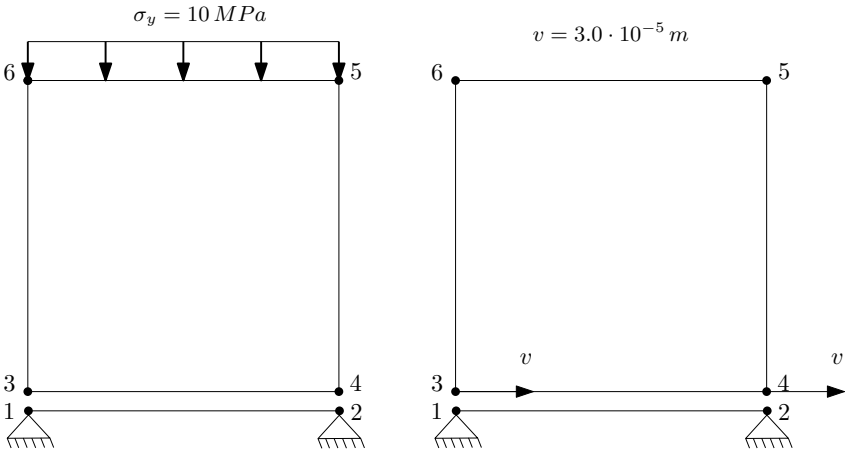

Figure 3.6: Geometry of the shear-compression sliding example: (left) an instantaneous vertical stress is applied on the top face and (right) also an instantaneous displacement is imposed on nodes 3 and 4.

Same as in the previous example, the results obtained using the "two-step" loading procedure are represented first (Fig. 3.7-(a)). This diagram shows the shear tangential relative displacement

evolution curve of the interface element for all strategies. Similar to the previous case, the results show that in the inviscid limit the physical visco-plastic (VP-NR, VP-IDC-Wvp) and VPR formulations approach nicely the predictions of the corresponding elasto-plasticity. Figure 3.7-(b), on its side, shows the results calculated using the "one-step" loading procedure.

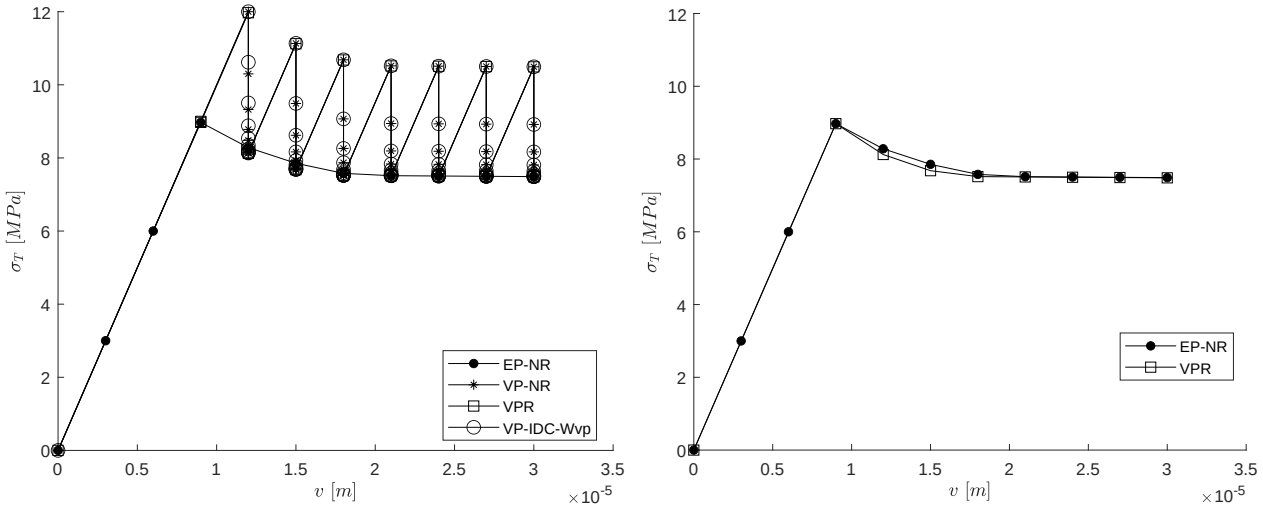

(a) Two-step loading methodology. **(b)** One-step loading methodology.

Figure 3.7: Shear stress - tangential relative displacement evolution curves of the interface element.

The case with snap-back in this example is achieved by modification of the boundary conditions, not applying the prescribed shear displacements directly on the top interface nodes, but on two additional nodes on each side of the interface, which are connected to the interface nodes by two elastic rods (springs) (Fig. 3.8). In this way, during the elastic response of the overall setup before sliding, these rods accumulate energy that is later released in the post-peak generating the snap-back response.

The continuum material is assumed linear elastic ($E = 1.5 \cdot 10^4\, MPa$ and $\nu = 0$) and the parameters used for the interface fracture-based constitutive models are: normal and tangential elastic stiffness $K_N = K_T = 10^7\, MPa/m$, friction angle $\tan\phi = 0.7$, tensile strength $\chi = 3.0\, MPa$, cohesion $c = 9.0\, MPa$, fracture energy mode I $G_f^I = 5.0 \cdot 10^{-5}\, MPa \cdot m$, fracture energy mode IIa $G_f^{IIa} = 10^{-4}\, MPa \cdot m$, normal stress to eliminate dilatation $\sigma_{dil} = 30\, MPa$ and, for visco-plastic calculations, the viscosity parameter $\eta = 10^6\, MPa \cdot s$. In addition, the rod stiffness is $EA = 6.0 \cdot 10^3\, MPa \cdot m^2$.

The results of this case are shown in Figure 3.9. The inviscid response curve shows a clear snap-

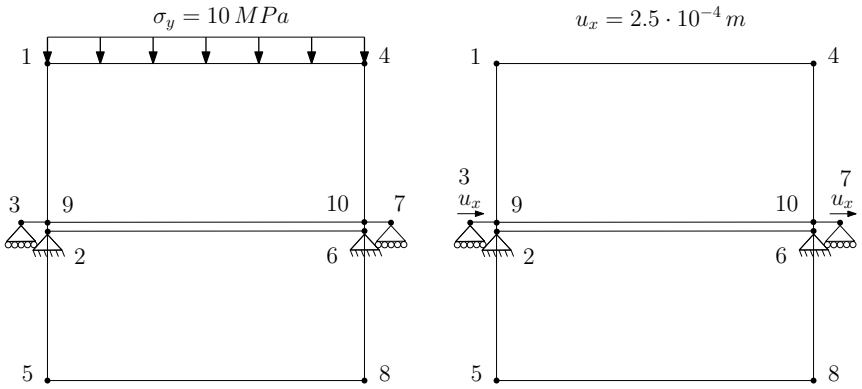

Figure 3.8: Geometry of the shear-compression additional example: (left) an instantaneous vertical stress is applied on the top face and (right) an instantaneous displacement is imposed on nodes 3 and 7.

back, and the "two step" curves obtained with the visco-plastic schemes (Fig. 3.9-(a)) reproduce a similar trend to the one observed in the pure tension example: the instantaneous loading steps lead to higher elastic stresses, while the time steps after each elastic loading brings the stresses down to the inviscid curve. The results obtained with the "one step" loading scheme and VPR, (Fig. 3.9-(b)) also reproduce well the inviscid curve in the stable parts of the diagram, and exhibits a vertical stress drop immediately after the peak, skipping the snap-back and rejoining the inviscid curve for the remainig of the test. Therefore, also in this shear-compression case the VPR scheme seems capable of by passing the instable part of the curve providing some temporary stability to the calculation while the snap-back takes place.

3.5.3 Shear-compression sliding - inclined interface element

The third and last example of this section, consists of another shear test, which adds a new degree of complexity to the previous one: the normal stress on the shear plane is not a constant value statically determined by external loading as in the previous case, but it is one more unknown of the problem. The geometric configuration of this case is shown in Figure 3.10. It consists of a single interface element inclined at approximately 40^{o} which is inserted between two continuum elements, all together configuring a rectangular domain of $2\,m$ x $3\,m$. A uniaxial compression state in the continuum elements is generated by the vertical displacements prescribed on the top face of the upper continuum element, while lateral faces remain free, and the shear-compression state on the inclined interface may be statically related to the uniaxial stress state. This relation represents a static constraint leading to a fixed proportion between normal and shear stress components on the

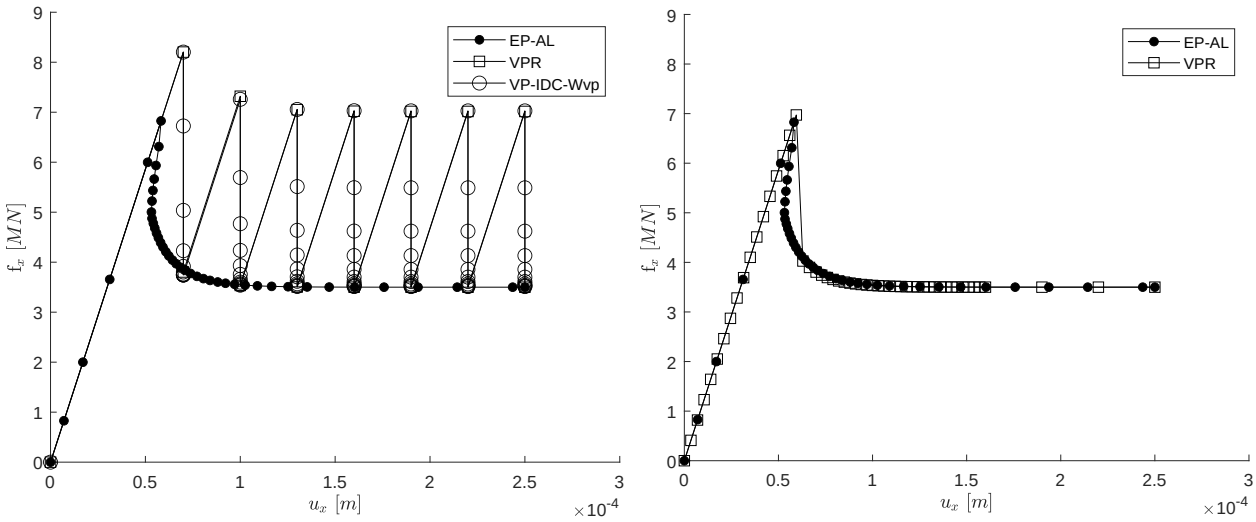

(a) Two-step loading methodology. **(b)** One-step loading methodology.

Figure 3.9: Horizontal force - horizontal displacement evolution curves plotted at node 3 of the rod element.

interface, that depends exclusively on the inclination angle. The precise values of those stresses, however, are not fixed and will evolve during the whole loading history. The loading procedures ("one step" and "two-step") are the same as in the previous examples and this case is also calculated for all strategies: EP-NR, VP-NR, VP-IDC-Wvp and VPR.

The continuum material is assumed linear elastic ($E = 1.5 \cdot 10^4\, MPa$ and $\nu = 0$) and the parameters used for both elasto-plastic and visco-plastic interface fracture-based constitutive models are: normal and tangential elastic stiffness $K_N = K_T = 10^7\, MPa/m$, friction angle $\tan\phi = 0.7$, tensile strength $\chi = 2.0\, MPa$, cohesion $c = 8.0\, MPa$, fracture energy mode I $G_f^I = 10^{-2}\, MPa \cdot m$, fracture energy mode IIa $G_f^{IIa} = 10^{-1}\, MPa \cdot m$, compression value for which dilatation vanishes $\sigma_{dil} = 20\, MPa$ and, for visco-plastic calculations, viscosity $\eta = 10^4\, MPa \cdot s$.

The results obtained for the "one-step" and "two-step" loading procedures, in terms of forces and displacements of the top nodes of specimen and the tangential stresses and relative displacements on the interface plane, are shown in Figures 3.11 and 3.12 respectively. Figure 3.11-(a) shows that force-displacement evolution curves calculated by using the various visco-plastic strategies give a good agreement with the results obtained with the elasto-plastic approach. In addition, Figure 3.11-(b) shows that the VPR response traces correctly the elasto-plastic predictions in the inviscid limit as well. Note also that in Figure 3.12, and in terms of tangential stresses and relative displacements variables, the visco-plastic response is not represented by vertical lines but by inclined

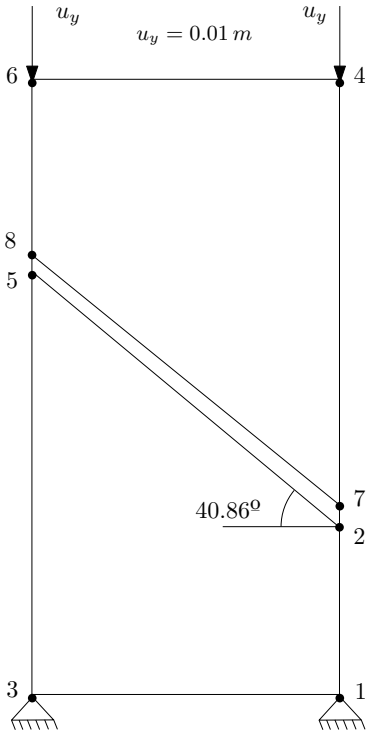

Figure 3.10: Geometry of the shear-compression sliding example. Prescribed displacements are imposed on nodes 6 and 4.

lines, which is a structural effect of the statically-indetermined character of this example. Both physical visco-plastic (VP-NR, VP-IDC-Wvp) and VPR strategies approach nicely the predictions of the corresponding inviscid elasto-plasticity.

To obtain an unstable case in this example, the fracture energy parameter values are decreased to $G_f^I = 0.006\,MPa \cdot m$ and GIIa $G_f^{IIa} = 0.06\,MPa \cdot m$, which leads to the inviscid curve with snap-back (in terms of forces and displacements of the top nodes of specimen) shown in Figure 3.13. In the figure, the results of the calculations using the various visco-plastic strategies, show that those strategies recover well the inviscid response after sufficient time has passed after each instantaneous load step (left diagram). As in previous verification examples, the right diagram in Figure 3.13-(b) shows that the VPR results follow correctly the inviscid response in the elastic range, and exhibit a post-peak vertical drop controlled by the fictitious time iteration process, until it meets the inviscid curve again for the last part of the analysis. The results of this case in terms of the shear stress and shear relative displacements on the interface plane, are represented in Figure 3.14. They generally represent the same features already mentioned for the previous figure in terms of forces and displacements, and similarly as in the previous stable case (Fig. 3.12), the stress drop

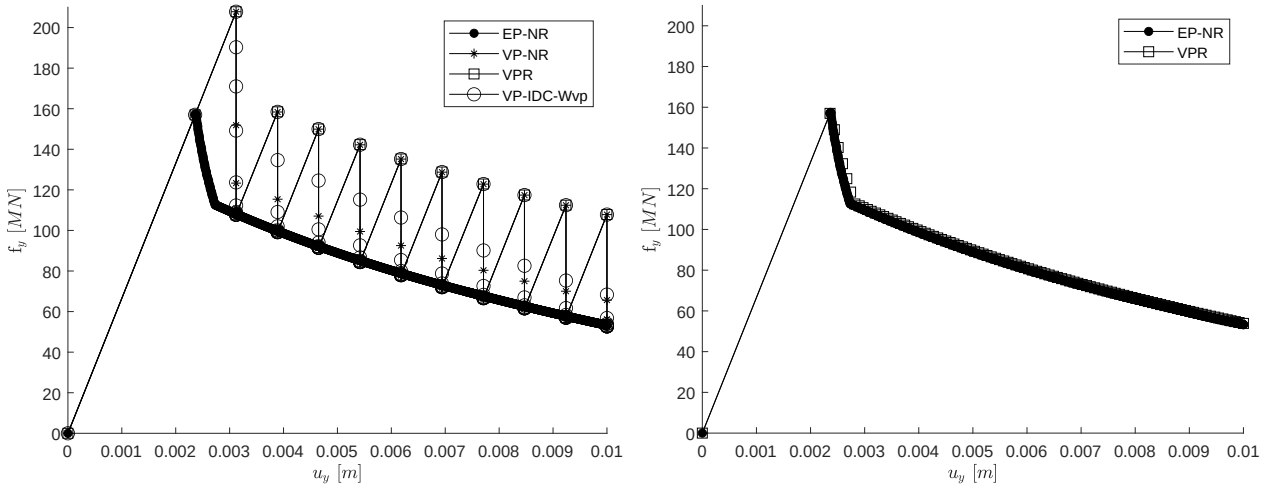

(a) Two-step loading methodology. **(b)** One-step loading methodology.

Figure 3.11: Vertical force - vertical displacement evolution curves of node 6 on the top face of the upper continuum element.

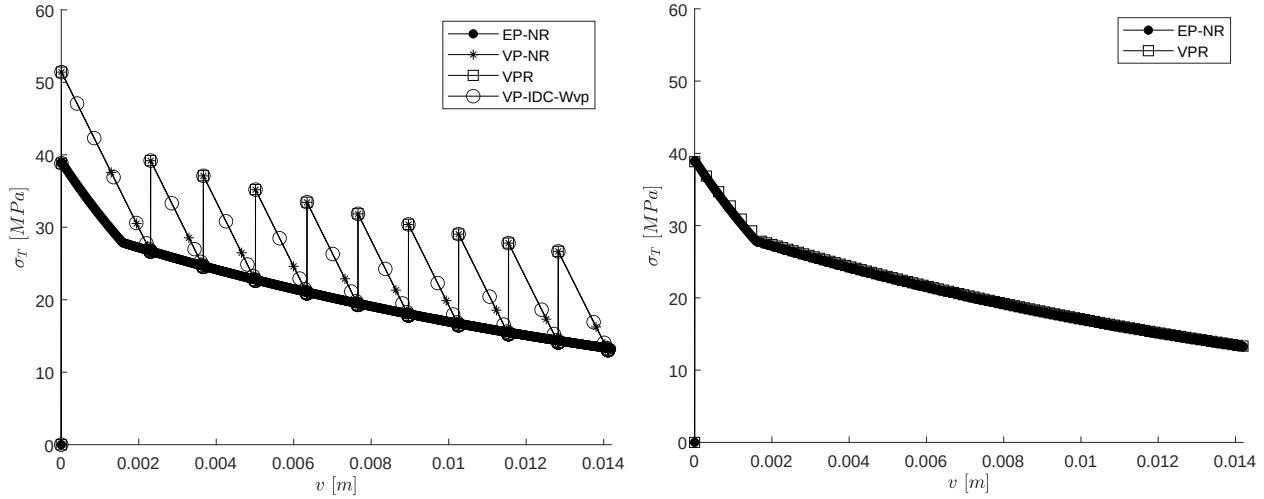

(a) Two-step loading methodology. **(b)** One-step loading methodology.

Figure 3.12: Shear stress - tangential relative displacement evolution curves of the interface element.

lines during the visco-plastic response are not vertical but exhibit a slope due to the structural effect caused by the inclined interface.

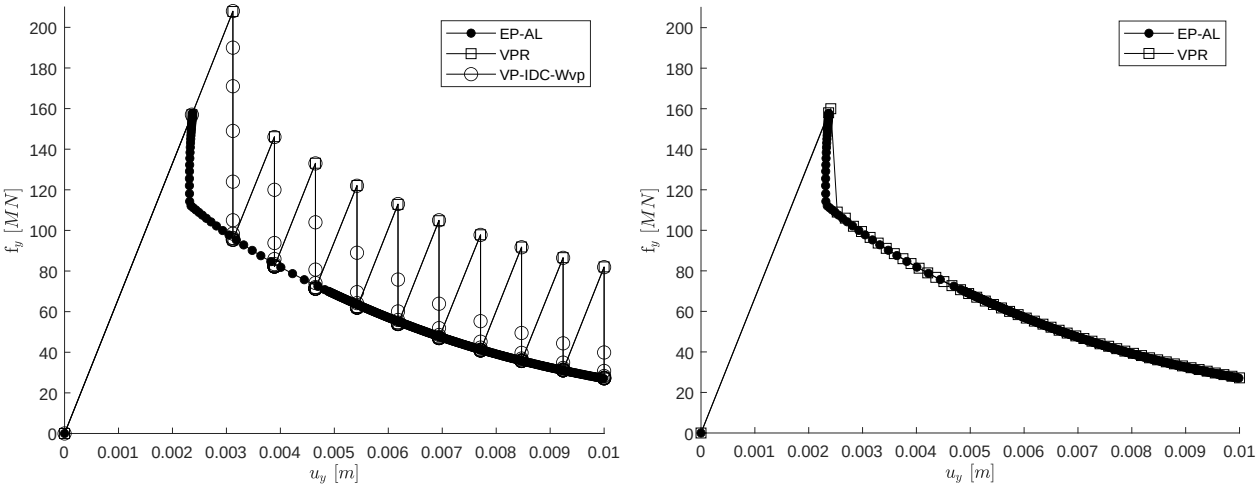

(a) Two-step loading methodology. **(b)** One-step loading methodology.

Figure 3.13: Vertical force - vertical displacement evolution curves of node 6 on the top face of the upper continuum element.

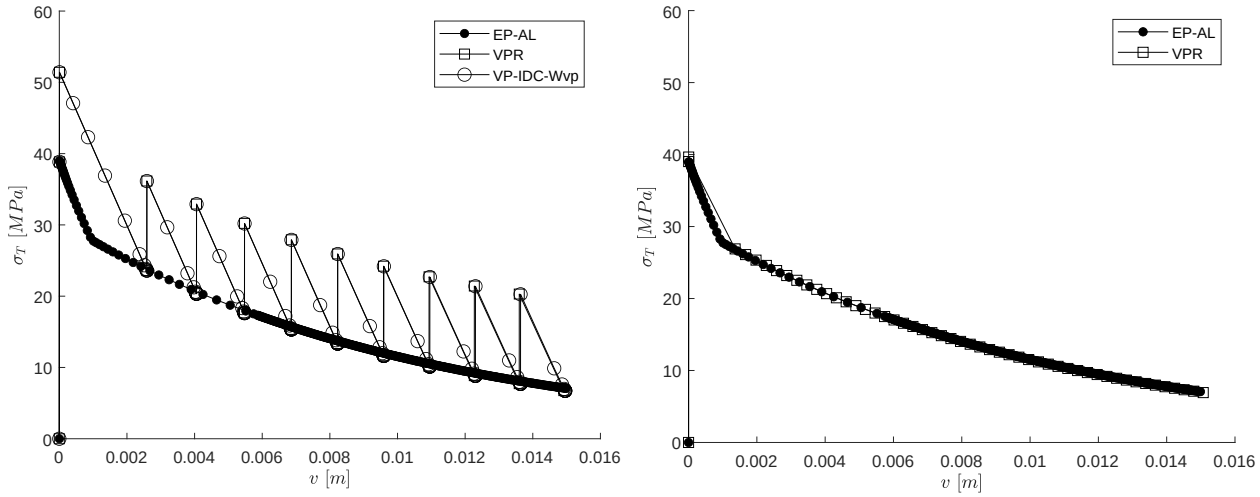

(a) Two-step loading methodology. **(b)** One-step loading methodology.

Figure 3.14: Shear stress - tangential relative displacement evolution curves of the interface element.

Chapter 4

Energy balance

Contents

4.1 Introduction

Natural seismic events are usually studied from the dynamics point of view analyzing the radiated seismic energy (E_R) as an indication of the total wave energy generated by the rapid rupture that occurs in an earthquake (Venkataraman and Kanamori, 2004). This macroscopic parameter, combined with the seismic moment (M_0), in the form of the energy – to – moment ratio E_R/M_0, is a useful tool for rapid real-time hazard assessment (Convers and Newman, 2011). Usually, these studies are based on the evaluation of the moment magnitude (M_w) and the energy magnitude (M_e) which, in turn, are linked with the seismic moment and the radiated seismic energy mentioned before. M_w is based on physical properties of the earthquake and is most appropriate for estimating the earthquake size by computing the product of rupture area times average displacement. In addition, there is another way to measure the size of an earthquake which is computing how much energy is released. In this way, M_e is more suitable for assessing the potential hazard of damage due to strong ground shaking, in other words, the earthquake strength (Bormann and Di Giacomo, 2011).

As Kanamori and Rivera explained in their article (Kanamori and Rivera, 2006), during an earthquake understanding the partitioning of energy is a key toward understanding the physics of earthquakes. In Seismology, it is considered that the potential energy stored in Earth (mainly elastic strain energy and gravitational energy) is released as radiated energy, fracture energy and thermal energy. The computation of all these energies is based on the macroscopic seismic parameters such as seismic moment and radiated energy mentioned above.

Considering this methodology for evaluating the energy released by an earthquake based on dynamics as an existing option, the approach presented in this thesis is based on Fracture Mechanics context and the evaluation of the energy balance is performed focusing on quasi-statics and considering the elastic energy released, plus all potential energy sources, and all mechanisms that can dissipate energy during a failure process.

The term "Fracture Mechanics" refers to an essential specialization within solid mechanics in which the presence of a crack is assumed and the conditions for its propagation are analyzed. In this context, it provides the tools to find quantitative relations between the crack length, the material inherent resistance to crack growth, and the stress (or other conditions) at which the crack will propagate. In this sense, and making a short review of relevant authors who contribute in this research field, Griffith (Griffith, 1921) developed his pioneering studies of fracture (in a case of purely brittle fracture) focusing on an energy-balance approach from which the total energy associated with the crack is the sum of the energy absorbed to create the new surfaces, plus the

strain energy liberated by unloading of the regions near the crack flanks. Moreover, he proposed a crack failure criterion considering the energy required to break the material bonds which after failure allow the crack growth and the associated strain energy release. With that, he was able to formulate concepts such as critical crack length and distinguish between stable and unstable crack propagation. After that, Barenblatt (Barenblatt, 1959) introduced the concept of a "cohesive zone" ahead of the apparent crack tip, in which it is necessary to spend some work to beat the cohesive stresses that oppose the opening of the crack. Other authors such as Rice and Andrews (Rice et al., 2005; Andrews, 2005) established that some energy is also expended for near and off-fault cracking associated with fault rupture. In addition, Rudnicki (1980) presents a comprehensive review of the fundamentals of fracture mechanics aimed to improving the understanding of the vast variety of earthquake-related phenomena. It is worth mentioning that during an earthquake, many additional physical processes take place near the rupture front and in the surrounding volume that contribute to the energy balance. An example of that is rock melting which is evident in exhumed faults after making geological observations. Therefore, thermal energy and latent heat should be considered in the energy balance of failure processes but, in this thesis, only mechanical and hydro-mechanical energy dissipation mechanisms have been considered.

Regarding the rock failure process, it can develop as a stable or unstable mechanism. From these two possible scenarios, the one with higher interest is the abrupt (unstable) failure of the rock mass. An uncontrolled rupture instantaneously generates unbalanced forces between the *in situ* pre-existing stresses and the rock mass undergoing failure, which in turn releases elastic energy stored in the system in the form of a seismic wave propagating to the surrounding rock mass. When this phenomenon is caused by any human activity this is known as induced seismicity.

Therefore, determining instabilities and understanding under what conditions they may or may not occur has been a huge challenge of this thesis. A key tool in order to recognize an instability is precisely performing the energy balance. As it is known, the energy balance must be fulfilled in both stable and unstable cases but this happens in a different way depending on the case: if the fracture is developed in a stable manner, the energy balance must be zero because the energy externally applied to the system is going to be completely dissipated internally by different mechanisms of dissipation such as fracture and friction (in purely mechanical processes with no fluid involved), and also by hydro-mechanical phenomena when the presence of fluid is relevant and has to be considered. If, in contrast, unstable fracture takes place, some of the energy released is going to be dissipated internally but there is a part of that energy which will be emitted in the form of seismic waves, therefore inducing an earthquake.

The energy balance is based on the law of conservation principle that states that energy can neither be created nor destroyed, only altered in form. Keeping this principle in mind, the energy released in an unstable process can be estimated by comparison between the energy supplied externally to the system plus the energy released internally by reduction of elastic stresses, with the energy dissipated through different internal processes.

Depending on the type of example, mechanical (M) or hydro-mechanical (H-M), different forms of internal dissipation energy must be considered. In purely mechanical cases dissipation is mainly caused by fracture and friction mechanisms, while in hydro-mechanical cases fluid compressibility and the dissipation associated to the fluid flow as it passes through the medium or fractures, have to be additionally considered. It must be emphasized that discontinuities are involved in all the cases mentioned, and that the different forms of dissipation related to them (mechanical, hydraulic, etc) must also be considered in the energy balance.

The purpose of this chapter is to identify the various possible mechanisms of energy release, storage or dissipation in the rock mass, in order to then be able to quantify each of those contributions. The calculation of those quantities, will be performed on the basis of the H-M calculations carried out with FE code of the research group. This has required some new developments being implemented in the code. As it was mentioned before, the first task is to identify the various energy components to be taken into account, distinguishing for that purpose between purely mechanical and hydro-mechanical coupled phenomena.

4.2 Work terms involved in the energy balance

4.2.1 Mechanical work and energy terms

4.2.1.1 General

The work W_M performed by a point load $\boldsymbol{F}$ applied on a moving point experiencing displacements $\boldsymbol{u}$ is given by the well known expressions, in incremental and total formats:

$$dW_M = \boldsymbol{F} \cdot d\boldsymbol{u},\ W_M = \int \boldsymbol{F} \cdot d\boldsymbol{u} \tag{4.1}$$

Considering, a body of volume V, and within it an infinitesimal volume element dV, which is subject to stress values $\boldsymbol{\sigma}$ and experiencing strain $\boldsymbol{\varepsilon}$, the mechanical work per unit volume w_M

performed by such stresses may be similarly expressed as:

$$dw_M = \boldsymbol{\sigma} : d\boldsymbol{\varepsilon},\ w_M = \int \boldsymbol{\sigma} : d\boldsymbol{\varepsilon}\, dV \tag{4.2}$$

In a general scenario, it is assumed that a certain part of the work performed by stresses is accumulated in the continuum medium in the form of elastic energy, while the rest may be dissipated in processes such as frictional heat, fracture of the material, or other dissipative processes. This work balance represents an elementary form of the first principle of Thermodynamics, and may be expressed as:

$$dw_M = du_e + d\mathcal{D} \tag{4.3}$$

where u_e is the elastic energy per unit volume or elastic energy density, and $\mathcal{D}$ is the energy dissipation also per unit volume. Replacing dw_M from the previous equation (4.2), one obtains:

$$du_e = \boldsymbol{\sigma} : d\boldsymbol{\varepsilon} - d\mathcal{D} \tag{4.4}$$

If the body behaves elastically, then there is no dissipation $d\mathcal{D} = 0$ and one simply has

$$du_e = \boldsymbol{\sigma} : d\boldsymbol{\varepsilon} \tag{4.5}$$

that is, all energy performed by the stresses is stored in the form of elastic energy.

4.2.1.2 Continuum elastic energy

If the body behaves according to linear elasticity $\boldsymbol{\sigma} = \boldsymbol{D} : \boldsymbol{\varepsilon}$ with constitutive stiffness $\boldsymbol{D}$ (or its inverse, $\boldsymbol{\varepsilon} = \boldsymbol{C} : \boldsymbol{\sigma}$ with constitutive compliance $\boldsymbol{C} = \boldsymbol{D}^{-1}$), one can write:

$$du_e = \boldsymbol{\sigma} : d\boldsymbol{\varepsilon} = \boldsymbol{\varepsilon} : \boldsymbol{D} : d\boldsymbol{\varepsilon},\ u_e = \int \boldsymbol{\varepsilon} : \boldsymbol{D} : d\boldsymbol{\varepsilon} = \frac{1}{2}\boldsymbol{\varepsilon} : \boldsymbol{D} : \boldsymbol{\varepsilon} = \frac{1}{2}\boldsymbol{\sigma} : \boldsymbol{C} : \boldsymbol{\sigma} \tag{4.6}$$

In the case of a 2D continuum in plane strain with isotropic linear elasticity, this expression becomes:

$$W_{e\mathrm{C}} = \int \frac{1}{2}\, \boldsymbol{\sigma} \colon \boldsymbol{C}_{\mathrm{C}} \colon \boldsymbol{\sigma}\, dV \tag{4.7}$$

where the compliance matrix for the continuum material is denoted as:

$$\boldsymbol{C}_{\mathrm{C}} = \frac{1}{E}\begin{pmatrix} 1 & -\nu & 0 & -\nu \\ -\nu & 1 & 0 & -\nu \\ 0 & 0 & 2\,(1+\nu) & 0 \\ -\nu & -\nu & 0 & 1 \end{pmatrix} \tag{4.8}$$

where E is the continuum elastic modulus and ν is the Poisson's ratio.

4.2.1.3 Interface elastic energy

Following the same structure as the continuum elastic energy, the work corresponding to the elastic energy for interface elements is computed as:

$$W_{e\mathrm{J}} = \int \frac{1}{2}\,\boldsymbol{\sigma}_{\mathrm{J}} \colon \boldsymbol{C}_{\mathrm{J}} \colon \boldsymbol{\sigma}_{\mathrm{J}}\, dS \tag{4.9}$$

The compliance matrix for interface elements is denoted as:

$$\boldsymbol{C}_{\mathrm{J}} = \begin{pmatrix} 1/K_N & 0 \\ 0 & 1/K_T \end{pmatrix} \tag{4.10}$$

where K_N and K_T are the normal and tangential interface elastic stiffness respectively.

4.2.1.4 Rod elastic energy

The elastic energy stored in a rod element subject to a constant axial force N may be calculated as follows:

$$W_{e\mathrm{R}} = \frac{1}{2}\frac{N^2}{EA}\,L = \frac{1}{2}\,K_{\mathrm{R}}\,\Delta L^2 \tag{4.11}$$

where rod stiffness is $K_{\mathrm{R}} = EA/L$ and, L and A are the rod length and cross-section area respectively, and E is the elasticity constant of the rod material (Young's modulus).

4.2.1.5 Fracture energy dissipation for interface elements

The fracture dissipation term obtained in this section is based on, the *Normal/Shear Cracking Model*, which was described in Section 2.5. That model exhibits a cracking surface defined in terms of normal and shear stresses and three geometric parameters which, in turn, vary depending on the history variable W^{cr}, the work spent (dissipated) in fracture processes. This history variable is

defined incrementally (Eq. 4.12) and its value is routinely calculated and updated for each Gauss point of every interface element in the mesh during the FE calculations. The total value of the energy dissipated in a given interface element may be calculated by integration over the element (Eq. 4.13):

$$dW^{cr} = \begin{cases} \boldsymbol{\sigma}_{\mathrm{J}} : d\boldsymbol{r}^{cr} & \sigma_N \geq 0\,(tension) \\ (\sigma_T + \sigma_N \tan\phi)\, dr_T^{cr} & \sigma_N < 0\,(compression) \end{cases} \tag{4.12}$$

$$W_{Frac}^{EP} = \int dW^{cr}\, dS \tag{4.13}$$

The above equations (4.12) are valid for (inviscid) elasto-plastic material behavior. In the case that the material is considered visco-plastic, the history variable is W^{vcr}, which is defined similarly to the previous dW^{cr} but replacing the plastic relative displacement $d\boldsymbol{r}^{cr}$ by its visco-plastic counterpart, $d\boldsymbol{r}^{vcr}$. Moreover, the visco-plastic approach requires the projection of the stresses to the yield surface to compute the energy dissipated in the fracture process.

Considering all these requirements, the fracture energy dissipation for visco-plastic cases is calculated in a similar manner as in elasto-plastic cases, by integration over the element:

$$W_{Frac}^{VP} = \int dW^{vcr}\, dS \tag{4.14}$$

4.2.1.6 Total, frictional and viscous energy dissipation for interface elements

The frictional energy dissipation for the interface in case of inviscid elasto-plastic behavior, may be simply obtained as the difference between the total energy dissipated in the interface and the fracture energies dissipated in the same interface.

The total energy dissipated may be calculated as:

$$W_{Total}^{EP} = \int \boldsymbol{\sigma}_{\mathrm{J}} : d\boldsymbol{r}^{cr}\, dS \tag{4.15}$$

Therefore, frictional dissipation in the case of inviscid behavior may be obtained as:

$$W_{Fric}^{EP} = W_{Total}^{EP} - W_{Frac}^{EP} \tag{4.16}$$

In the case of visco-plastic behavior, however, the calculation is a little more complicated because the frictional and the purely viscous parts of the interface deformation are considered jointly in the visco-plastic relative displacements term ($d\boldsymbol{r}^{vcr}$). This means that if expression (4.15) would be used directly by simply replacing the inviscid elasto-plastic deformations $d\boldsymbol{r}^{cr}$ with the visco-plastic

deformations $d\boldsymbol{r}^{vcr}$, the integral would lead to a single value including both frictional and viscous work. But it will be essential later in this study to isolate the energy dissipation due to viscous deformation, and for this purpose a decomposition of the total shear stress acting on the interface σ_T into three different parts, is considered in compression: (1) the basic friction shear stress $\sigma_{T\phi}$, (2) the additional shear stress to the inviscid failure envelope $\Delta\overline{\sigma}_T^{VP}$ and (3) the visco-plastic overstress outside of the yield surface $\Delta\sigma_T^{VP}$ (Fig. 4.1).

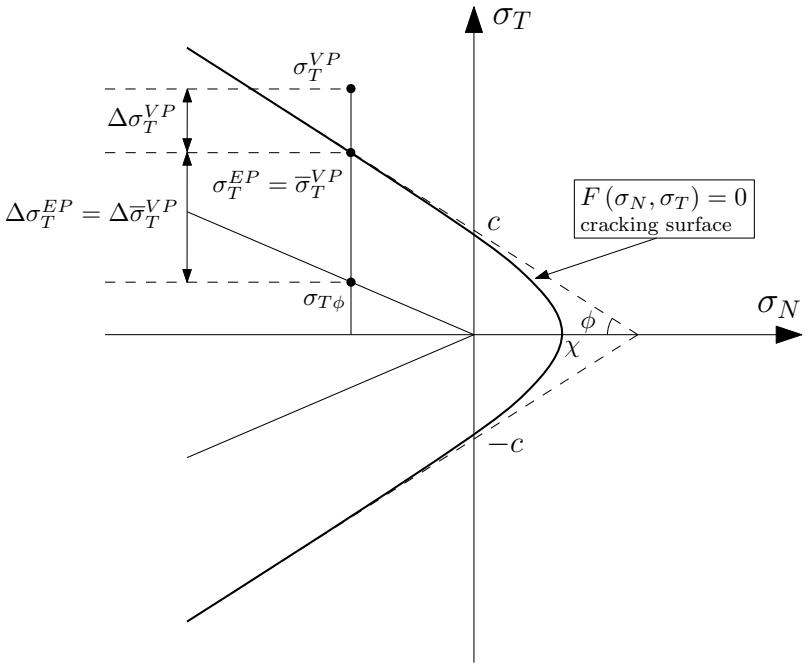

Figure 4.1: Graphical representation of the stresses used for the calculation of viscous work in compression.

By introducing this decomposition into equation (4.15), the viscous dissipation $dW^{Viscous}$ may be finally identified individually:

$$\begin{aligned} dW_{Total}^{VP} &= \boldsymbol{\sigma}_{\mathrm{J}} \colon d\boldsymbol{r}^{vcr} = \sigma_N^{VP} dr_N^{VP} + \sigma_T^{VP} dr_T^{VP} = \\ &= \sigma_N^{VP} dr_N^{VP} + \left(\underbrace{\sigma_{T\phi} + \Delta\overline{\sigma}_T^{VP}}_{\overline{\sigma}_T^{VP} = \sigma_T^{EP}} + \Delta\sigma_T^{VP} \right) dr_T^{VP} = \\ &= \underbrace{\sigma_N^{VP} dr_N^{VP} + \overline{\sigma}_T^{VP} dr_T^{VP}}_{d\overline{W}_{Total}^{VP}} + \underbrace{\Delta\sigma_T^{VP} dr_T^{VP}}_{dW^{Viscous}} \end{aligned} \tag{4.17}$$

Note that the term $d\overline{W}^{VP}_{Total}$, key to the definition of $dW^{Viscous}$, corresponds to the total work dissipated by the model if the stresses used in the calculation of work are the stresses projected on the surface instead of the real, visco-plastic stresses (usually located outside of the surface). This term may also be interpreted as the dissipation that would take place with the elasto-plastic version of the model if subject to the same relative displacement history as the VP model. And finally, one should not forget the fracture dissipation that, also in the present visco-plastic extension of the interface model is the history variable, the work dissipated in fracture processes, W^{VP}_{Frac}.

4.2.2 Hydraulic work terms

As it was mentioned in the Introduction, the energy balance for hydro-mechanical problems requires, apart from purely mechanical energy dissipation sources, the identification and formulation of all additional energy dissipation processes. The presence of fluid in a medium and also the fluid flow through it imply various additional sources of energy dissipation and storage, as described in the following sub-sections.

4.2.2.1 Energy and work principles considering fluid

Considering a body or domain made of a porous material containing a fluid, and a point of fluid injection in such body, such that in an (infinitesimal) time increment dt a volume of fluid dV is injected (therefore at a discharge rate $Q = dV/dt$) and that injection has required to apply a pressure P, the work made by the injection pump may be expressed as:

$$dW_F = P\,dV = P\,Q\,dt \tag{4.18}$$

or, in rate form:

$$\dot{W}_F = P\,Q \tag{4.19}$$

Integrating previous equations in time leads to the total work done by the point injection during a given time period:

$$W_F = \int P\,dV = \int P\,Q\,dt \tag{4.20}$$

Note that one can make a simple analogy of the previous equations with the mechanical work of a single point load, by imagining that the injection is applied by means of a cylindrical piston of cross-section A, onto which a force F is applied leading to a pressure in the fluid $P = F/A$, and the piston experiences a displacement u leading to a volume injected $dV = A\,du$. By replacing those

relations into equation (4.18) one obtains:

$$dW_F = P\,dV = \frac{F}{A}\,A\,du = F\,du \tag{4.21}$$

This shows that the work done by point fluid injection work may be assimilated to the work done by a point force (Eq. 4.1).

Considering now, a body of volume V and, within it, an infinitesimal volume element of porous material dV, which is subject to a fluid flow in its pores defined by Darcy velocity $\boldsymbol{q}$ and the field of pressure in the body being at that point the gradient of pressure is $\mathbf{grad}P$, the corresponding dissipation of energy per unit volume associated to the fluid flow through this porous medium in a time increment dt, dw_{FtC}, and the total dissipation increment in the entire domain V, dW_{FtC} may be expressed as:

$$dw_{FtC} = -\mathbf{grad}P \cdot \boldsymbol{q}\,dt,\ dW_{FtC} = \int -\mathbf{grad}P \cdot \boldsymbol{q}\,dV\,dt \tag{4.22}$$

or, dividing all equations by dt, as:

$$\dot{w}_{FtC} = -\mathbf{grad}P \cdot \boldsymbol{q},\ \dot{W}_{FtC} = \int -\mathbf{grad}P \cdot \boldsymbol{q}\,dV \tag{4.23}$$

where $\dot{w}_{FtC}$ is the dissipation rate per unit volume, and $\dot{W}_{FtC}$ is the dissipation rate for the entire domain due to the fluid flow.

Equations (4.22) have formal similarity to equations (4.2) in solid mechanics; if one substitutes $\mathbf{grad}P$ with $\boldsymbol{\sigma}$ and $\boldsymbol{q}\,dt$ with $d\boldsymbol{\varepsilon}$, the work performed by fluid flow becomes the work performed by stresses. An essential difference, however, is the destination of that work, and the subsequent balance equations. While in solid mechanics at least part of this work becomes stored in the same volume element in the form of elastic energy (or all of it in the case of linear elasticity), in the case of the fluid flow all of it becomes dissipated, no energy is stored in the fluid. Assuming small fluid velocities, this is strictly true if fluid is totally incompressible, but if the fluid is slightly compressible (only case of compressibility considered in the present thesis), energy storage in the fluid may take place if the pressure levels vary. Similar equations to (4.22 and 4.23) may be written for the fluid flow along the interface elements, and similar considerations as above in this paragraph may be also done for those elements. The specific equations for all those cases are presented in the following subsections.

4.2.2.2 Energy stored due to fluid compressibility

In the present thesis, the fluid is assumed quasi-incompressible which is the assumption normally made for liquids such as water or oil in Geomechanics studies. This means that for some purposes (such as energy storage) the fluid is assumed to exhibit some small compressibility described by a linear law, while for other purposes (for instance for the mass balance enforcement), the fluid is considered as totally incompressible. This is in a way similar to the standard (small strain, first-order) mechanical analysis of solids, in which deformations (such as displacements and strains) are calculated, but equilibrium is established in the undeformed configuration. In this context, the compressibility law for the fluid is established as:

$$\dot{P} = -M^{Biot}\,\mathrm{div}\boldsymbol{q} \tag{4.24}$$

where $\mathrm{div}\boldsymbol{q}$ represents the rate of volumetric deformation of the fluid (it measures the rate of accumulation of fluid in an elementary control volume, or difference between the amount of fluid that enters and leaves that volume in a unit time), and M^{Biot} is the Biot's Modulus, with expression (Zienkiewicz and Shiomi, 1984; Simon et al., 1984):

$$\frac{1}{M^{Biot}} = \left(\frac{\alpha_{Biot} - n}{K^s} + \frac{n}{K^f}\right) \tag{4.25}$$

where α_{Biot} is the Biot's coefficient, n is the porosity, K^s is the solid skeleton compressibility and K^f is the fluid bulk modulus.

In a volumetric extension of equation (4.19), the increase of energy storage per unit volume due to fluid compressibility, will be equal to the work performed by the pressure force, that is:

$$w_{FC} = \int -P\,\mathrm{div}\boldsymbol{q}\,dt \tag{4.26}$$

where, replacing $\mathrm{div}\boldsymbol{q}$ from equation (4.24) and resolving the integral in terms of P, one obtains the energy storage per unit volume, and the total for the domain as:

$$w_{FC} = \frac{P^2}{2M^{Biot}},\ W_{FC} = \int \frac{P^2}{2M^{Biot}}\,dV \tag{4.27}$$

In this equation, the fluid considered is that one in the pores of the continuum medium. Strictly speaking, the fluid in the fractures and the fluid in the rods would also store energy, but it is assumed that those represent a volume that is negligible in comparison to the fluid volume stored in the

continuum.

4.2.2.3 Energy dissipation rate resulting from the fluid flow in the continuum

The rate of dissipation due to the fluid flow in a continuum is given by equation (4.23). If the flow is governed by Darcy law, and in the absence of gravity effects, this means that (Darcy, 1856):

$$\boldsymbol{q} = -\boldsymbol{K}_{\mathrm{C}} \cdot \mathbf{grad} P \tag{4.28}$$

where $\boldsymbol{K}_{\mathrm{C}}$ is the hydraulic conductivity (m/s), defined as $\boldsymbol{K}_{\mathrm{C}} = k\gamma^f/\mu$ with k is the permeability (m^2), γ^f is the fluid specific weight (MN/m^3), and μ is the fluid viscosity $(MPa \cdot s)$. If Darcy equation is replaced into equation (4.23), the following expressions are obtained for dissipation rate per unit volume and for total domain volume:

$$\dot{w}_{FtC} = \mathbf{grad} P \cdot \boldsymbol{K}_{\mathrm{C}} \cdot \mathbf{grad} P, \;\; \dot{W}_{FtC} = \int \mathbf{grad} P \cdot \boldsymbol{K}_{\mathrm{C}} \cdot \mathbf{grad} P \, dV \tag{4.29}$$

4.2.2.4 Energy dissipation rate resulting from the fluid flow in the interface elements

The formulation of the fluid flow along and across zero-thickness interface elements follows previous work by Segura and Carol (2004), Segura (2007), Segura and Carol (2008a,b) and Garolera (2017).

These elements exhibit two kinds of fluid flow: longitudinal and transversal. Considering first the longitudinal flow, and assuming laminar flow, the resulting equations are very similar to Darcy flow in the continuum, with the only difference that the flow takes place on a domain which is one less dimension (a surface in 3D and a line in 2D). Equations (4.28) and (4.29) may be easily adapted to the longitudinal flow along interfaces. By doing so, and in the absence of gravity effects Darcy law (Eq. 4.28) becomes:

$$\boldsymbol{q}_{\mathrm{J}_L} = -\frac{\boldsymbol{T}_L}{\gamma^f} \cdot \mathbf{grad}_{\mathrm{J}} P \tag{4.30}$$

where $\boldsymbol{q}_{\mathrm{J}_L}$ is the fluid flow vector along the interface, integral of Darcy velocities across the interface opening (units m^2/s), with components in a local orthogonal in-plane reference system defined at each point of the interface; $\mathbf{grad}_{\mathrm{J}} P$ is the pressure gradient in the same reference system, and $\boldsymbol{T}_L$ is the longitudinal transmissivity, a 2x2 matrix in 3D (although usually assumed isotropic $\boldsymbol{T}_L = T_L \boldsymbol{I}_{2x2}$), or directly a scalar T_L in 2D, and this scalar (with units m^2/s), defined by the cubic law (Garolera, 2017), as $T_L = \gamma^f r_N^3/(12\mu)$, where r_N is the interface opening at the point, and μ the fluid viscosity. With the law (Eq. 4.30), the dissipation rate for the interface longitudinal flow,

becomes:

$$\dot{w}_{FtJ_L} = \mathbf{grad}_J P \cdot \frac{\boldsymbol{T}_L}{\gamma^f} \cdot \mathbf{grad}_J P, \; \dot{W}_{FtJ_L} = \int \mathbf{grad}_J P \cdot \frac{\boldsymbol{T}_L}{\gamma^f} \cdot \mathbf{grad}_J P \, dV \tag{4.31}$$

Regarding transversal flow, the Darcy-like equation may be expressed as (Segura and Carol, 2008a,b):

$$q_{J_T} = -\frac{K_{J_T}}{\gamma^f} \Delta P \tag{4.32}$$

where ΔP is the pressure drop across the interface opening, K_{J_T} is a transversal conductivity across the interface opening (units $1/s$), and q_{J_T} is the flow rate (units m/s). The energy dissipation rate associated to the fluid flow across the interface is:

$$\dot{w}_{FtJ_T} = \frac{K_{J_T}}{\gamma^f} \Delta P^2, \; \dot{W}_{FtJ_T} = \int \frac{K_{J_T}}{\gamma^f} \Delta P^2 \, dS \tag{4.33}$$

Note that in practical calculations it is common to assign very high values to K_{J_T}, which physically corresponds to the fluid being able to cross the discontinuity without practically any pressure losses. This causes very small pressure drops, which (being squared in the expression) in turn lead to negligible transversal dissipation rates, reason for which this term might not be taken into account in some of the examples provided later in this section.

4.2.2.5 Energy dissipation rate resulting from the fluid flow along rod elements

Rod elements are often used in the Finite Element calculations to simulate the effect of fluid pipes. If fluid flow is assumed laminar, they lead to Darcy-like flow equations similar to the ones obtained in previous sections (in 2D analysis, note the similarity of flow along rods, to the longitudinal flow along zero-thickness interfaces, except for the parameter values that reflect the out-of-plane dimensional difference although in a 2D-plane-strain analysis interfaces show up as lines, they are really surfaces and in the out-of-plane direction they occupy fully the unit thickness domain slice, while rods are really line elements physically corresponding also to a line with no dimension in the out-of-plane direction). In this context, the Darcy-like equation for a rectilinear rod, in the absence of gravity effects, may be written as:

$$q_{\mathrm{R}} = -\frac{K_{\mathrm{R}C}}{\gamma^f} \Delta P \tag{4.34}$$

where ΔP is the pressure drop between the two ends of the rod element, $K_{\mathrm{R}C}$ is the rod element conductivity (units m^2/s), and q_{R} is the flow rate (units m^3/s). The energy dissipation rate

associated to the fluid flow along the element pipe, may be expressed as:

$$\dot{W}_{Ft\mathrm{R}} = \frac{K_{\mathrm{R}C}}{\gamma^f}\Delta P^2 \tag{4.35}$$

4.3 Energy balance

The energy balance represents a form of the first principle of Thermodynamics, that requires that the net increase (or decrease) of energy stored in a body plus the energy dissipation that has taken place in the body during a certain period (W_{Int}), must be equal to the net amount of energy supplied to the body from external sources during the same period, (W_{Ext}). If considering a unit time period, the same concept may be also applied to rates, and therefore this energy balance condition may be expressed as:

$$\dot{W}_{Ext} = \dot{W}_{Int} \tag{4.36}$$

The calculation of external work may depend on the type of problem; if it is a pure mechanical problem (M) equation (4.1) for point loads (or its similar extensions for distributed surface or volume loads) would be used. If it is a hydro-mechanical (H-M) problem with fluid injection points, equation (4.21) would be also applied. Note that for the fluid the dissipation normally is given in rates, while elastic energy is expressed in total values. In any case, the application has to be consistent and all terms correspond to rates, or to the value increments over the same period of time (in the latter case, note that for fluid the calculation over a given time period would require the integration of such rate such as expressed in (Eq. 4.24)). In terms of rates, this means that:

$$\dot{W}_{Ext} = \dot{W}_M + \dot{W}_F \tag{4.37}$$

Looking now at the internal work, the more general case is considered with contributions from all the mechanical (including visco-plasticity) and fluid terms:

$$\dot{W}_{Int} = \dot{W}_{e\mathrm{C}} + \dot{W}_{e\mathrm{J}} + \dot{W}_{e\mathrm{R}} + \dot{\overline{W}}^{VP}_{Total} + \dot{W}^{Viscous} + \dot{W}_{FC} + \dot{W}_{Ft\mathrm{C}} + \dot{W}_{Ft\mathrm{J}} + \dot{W}_{Ft\mathrm{R}} \tag{4.38}$$

In the examples that follow in this Section, each term of the external work supply and energy storage and dissipation will be calculated. This will accomplish a double objective. First, it will serve as verification that the energy balance is satisfied, .i.e. that the calculation is correct and the total external work supply is equal to the sum of all the storage and dissipation terms. Second,

the study of the evolution curves of the various energy terms along the load history of simple, well understood examples, including cases with and without instability events, should make it possible to investigate whether the instability event is signaled by any of those curves, and therefore if those curves could be potentially used as indicators of instabilities occurring in more complex cases, and perhaps even quantify the energy released in such events. In particular, attention was focused on the term denoted as viscous energy dissipation, $W^{Viscous}$ in Section 4.2.1.6. This term represents the difference between the total energy dissipated by a visco-plastic interface element and its inviscid counterpart.

The verification examples considered in the paragraphs below are organized as follows: (1) mechanical examples under pure tension and shear-compression, exhibiting both stable and unstable behavior, (2) some simple hydraulic examples to check the correct calculation of the dissipation work due to the fluid flow through continuum, zero-thickness interface and rod elements. And finally, (3) more complex, hydro-mechanical problems with fluid injection with prescribed pressure and prescribed discharge.

All examples have been solved in the FE framework and the integration schemes used are Gauss 2×2 for the continuum quadrangular elements, constant rule with one central integration point for triangular continuum elements and trapezoidal rule in which the integration points are located at the two ends, for the interface elements.

4.4 Mechanical examples

Three simple examples with purely mechanical behavior are presented in this section: uniaxial tension specimen, compression-shear specimen with horizontal interface, and rectangular block loaded horizontally with an inclined discontinuity. All of them consist of a VPR analysis involving elastic loading to a peak, followed by a post-peak softening curve. Each example is repeated with two sets of parameters or loading conditions, one that generates a stable response and one that generates an unstable response. For each of those six cases, the analysis is run with Visco-plastic relaxation (VPR), and evolution curves are represented for the various energy dissipation terms obtained in the first post-peak increment, W^{VP}_{Frac}, W^{VP}_{Total} and $\overline{W}^{VP}_{Total}$, with respect to the accumulated fictitious VPR time.

4.4.1 Uniaxial tension opening

As shown in Figure 4.2, the first example consists of a single square ($1\,m$ x $1\,m$) continuum element sitting on top of a single horizontal interface element. The loading consists of a prescribed displacement applied at the top face of the continuum element (nodes 5 and 6), while the lower nodes of the interface remain fixed. This example is identical to example 1 in Chapter 3 (Sec. 3.5.1) but with slight changes in the constitutive parameters to obtain a more pronounced snap-back.

The first set of parameter values intended to produce the stable fracture propagation case, are the following: for the interface, normal and tangential elastic stiffness $K_N = K_T = 10^7\,MPa/m$, friction angle $\tan\phi = 0.7$, tensile strength $\chi = 2.0\,MPa$, cohesion $c = 2.0\,MPa$, fracture energy mode I $G_f^I = 10^{-4}\,MPa \cdot m$, fracture energy mode IIa $G_f^{IIa} = 10^{-3}\,MPa \cdot m$ and $\sigma_{dil} = 20\,MPa$ (although these two last parameters do no play a role in this case, because they are shear-related and the interface will be subject to pure tension exclusively), and for visco-plastic calculations, viscosity $\eta = 10^6\,MPa \cdot s$. For the numerical calculations, the continuum is considered linear elastic with Young's modulus $E = 10^5\,MPa$ and Poisson's ratio $\nu = 0$. On the other hand, the unstable fracture propagation case is achieved by reducing both fracture energy by a factor ten, i.e. $G_f^I = 10^{-5}\,MPa \cdot m$ and $G_f^{IIa} = 10^{-4}\,MPa \cdot m$ which leads to the snap-back.

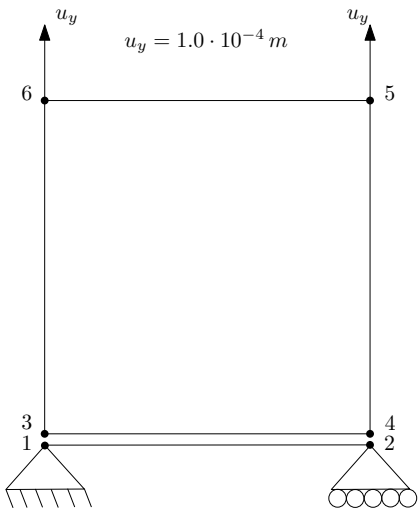

Figure 4.2: Geometry of the uniaxial tension example. Prescribed displacements are imposed on nodes 6 and 5.

The results obtained in the VPR calculation in terms of force and displacement at the top face of the continuum element, are represented in Figure 4.3, together with the results obtained using

the inviscid elasto-plastic version of the interface constitutive model (EP). In the stable case (left diagram) both VPR and EP curves coincide. However, in the unstable case, the EP curve exhibits a snap-back, while the VPR curve falls vertically from the peak, until it meets again the EP curve after the instability, to coincide for the rest of the loading case. This behavior is similar (although more pronounced in this case due to the parameter values used) to the tensile example in Section 3.5.1. As already indicated in that section, the VPR analysis provides a smooth transition across the instability event. But new considerations becomes possible as the energy dissipation terms are introduced and quantified.

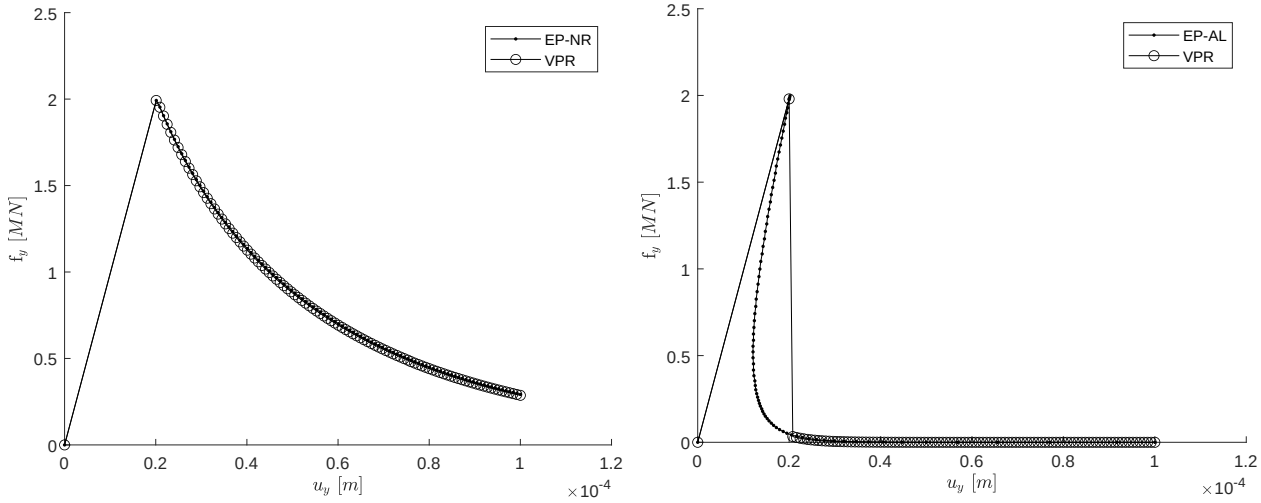

(a) Stable case **(b)** Unstable case

Figure 4.3: Load–displacement evolution curves at the top face of the continuum element for the VPR analysis. The results obtained in the same case with the inviscid elasto-plastic version of the interface model are also plotted for comparison.

The energy dissipation terms are represented in Figure 4.4 for the stable case, and Figure 4.5 for the unstable case. In each figure, the curves depict the evolution of the fracture energy dissipation W^{VP}_{Frac} (left diagram), and the total visco-plastic dissipation W^{VP}_{Total}, as well as the equivalent elasto-plastic dissipation $\overline{W}^{VP}_{Total}$ (right diagram), with respect to the accumulated fictitious VPR time during the first post-peak increment of the load history.

The curves in Figures 4.4 and 4.5 exhibit the following relevant features, one of them considered a key finding of the present thesis:

- In this uniaxial tension example, the fracture dissipation curves obtained with the visco-plastic approach (left diagrams) coincide with the dissipation curves obtained with the projected

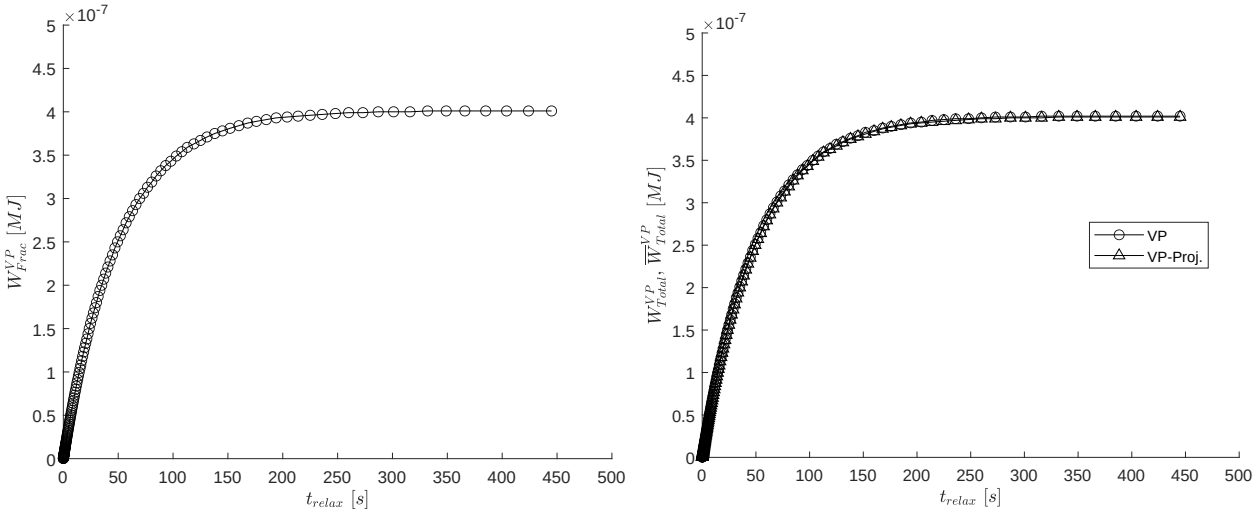

(a) W^{VP}_{Frac} **(b)** W^{VP}_{Total}, $\overline{W}^{VP}_{Total}$

Figure 4.4: (a) Fracture dissipation and (b) total dissipation obtained with visco-plastic and with projected stresses, during the first post-peak increment of the pure tension opening, stable case.

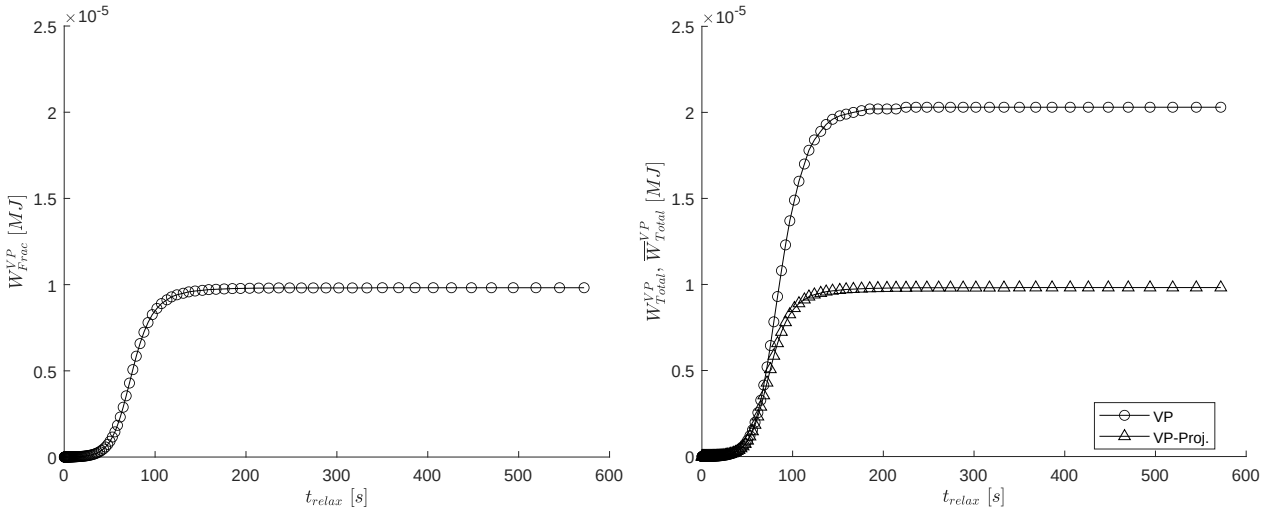

(a) W^{VP}_{Frac} **(b)** W^{VP}_{Total}, $\overline{W}^{VP}_{Total}$

Figure 4.5: (a) Fracture dissipation and (b) total dissipation obtained with visco-plastic and with projected stresses, during the first post-peak increment of the pure tension opening, unstable case.

stress (right diagrams, curve with triangles), in both stable and unstable cases. This could be expected since, in tension fracture dissipation is defined equal to total dissipation (Eq. 2.63).

- In the stable case, the total dissipation curves (right diagram, curves with circles) also coincide with the other two curves.

- In the unstable case, however, the total dissipation curve (right diagram, curve with circles), does not coincide with the other two curves, yields systematically higher values. According to equation (4.17), this difference corresponds to the term $W^{Viscous}$.

The difference observed in the unstable case, term $W^{Viscous}$, may be interpreted as the additional energy dissipated by the visco-plastic model during the instability event, that is during the transition between stable parts of the structural response. Graphically, this transition would correspond to the vertical segment of the VP curve, during which the EP curve is exhibiting the snap-back.

Therefore, the key finding of this section is that by performing a VPR analysis and evaluating and plotting the evolution of the dissipation terms W^{VP}_{Total}, and $\overline{W}^{VP}_{Total}$ (or directly the difference $W^{Viscous}$), it seems possible to identify the occurrence of a instability, and even further, the value of $W^{Viscous}$ could provide a basis for a quantitative measure of the energy released by such instability.

4.4.2 Shear-compression sliding

The configuration of the example is also similar to the second example of Chapter 3, Section 3.5.2. It consists of a shear-compression test composed by two continuum elements ($2\,m$ x $1\,m$) separated by a horizontal interface, and with two horizontal rod elements connected to the right and left of the lower nodes of the upper continuum element (Fig. 4.6). The compression effect is generated by a distributed load of $10\,MPa$ applied on the top face of the sample, and the tangential loads are applied via prescribed horizontal displacements on the free end node of the rods.

In the same way as in the previous example, the continuum material is assumed linear elastic ($E = 10^5\,MPa$ and $\nu = 0$) and the parameters used for the interface constitutive models (elasto-plastic and visco-plastic) are, in the stable case: normal and tangential elastic stiffness $K_N = K_T = 10^7\,MPa/m$, friction angle $\tan\phi = 0.7$, tensile strength $\chi = 3.0\,MPa$, cohesion $c = 9.0\,MPa$, fracture energy mode I $G_f^I = 6.0{\cdot}10^{-4}\,MPa{\cdot}m$, fracture energy mode IIa $G_f^{IIa} = 2.0{\cdot}10^{-3}\,MPa{\cdot}m$, sigma for which dilatation is suppressed $\sigma_{dil} = 30\,MPa$ and for visco-plastic calculations the viscosity $\eta = 10^6\,MPa \cdot s$. In addition, rod stiffness ($K_{\mathrm{R}} = EA/L$) is defined from the following input data: $EA = 6.0 \cdot 10^3\,MPa \cdot m^2$ and the rod length $L = 0.1\,m$. Regarding the unstable case, it can be obtained by reducing the fracture energy values to: $G_f^I = 5.0 \cdot 10^{-5}\,MPa \cdot m$, $G_f^{IIa} = 10^{-4}\,MPa \cdot m$.

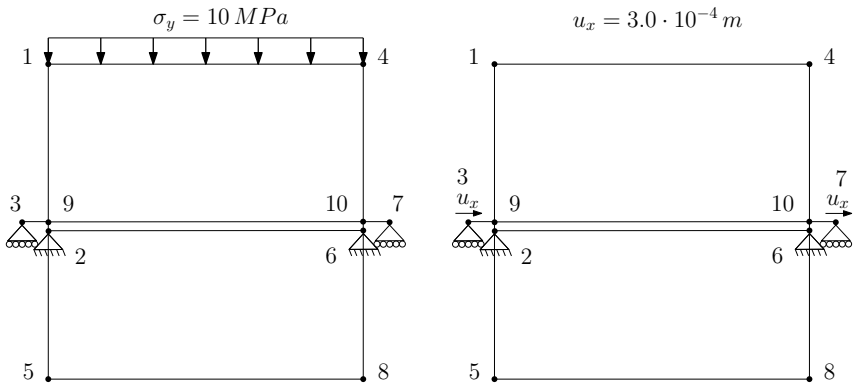

Figure 4.6: Geometry and boundary conditions of the shear-compression sliding example. (Left) Application of the vertical distributed load at the top face of the continuum element in order to generate a vertical uniaxial compression stress state and (Right) shear displacements applied through the rod elements.

The results obtained in this case with the VPR calculation are presented in Figure 4.7 below, in terms of the total horizontal force, against the horizontal displacement of the free end nodes of the rod elements, together with the results obtained using the inviscid elasto-plastic version of the interface constitutive model (EP) and iterative techniques such as NR (stable case) or AL (unstable case). Also in this example, in the stable case (left diagram) both VPR and EP curves coincide. However, in the unstable case, the EP curve exhibits a snap-back, while the VPR curve falls vertically from the peak, until it meets again the EP curve after the instability. This behavior is similar (although more pronounced in this case due to the parameter values used) to the shear-compression example in Section 3.5.2. As already indicated in that section, the VPR analysis is capable of providing a smooth transition across the instability event.

From the viewpoint of energy dissipation, the results obtained in the VPR analysis of this example for the stable case are represented in Figure 4.8 and for the unstable case in Figure 4.9. In both figures, the diagram on the left corresponds to the fracture energy dissipation, while the right diagram depicts the total dissipation obtained using the total visco-plastic stresses, or the stresses projected on the EP surface.

From the curves shown in Figures 4.8 and 4.9, some following observations can be made:

- In contrast to the previous example in tension, in this shear-compression example, the fracture dissipation curves obtained with the visco-plastic approach (left diagrams), do not coincide with the dissipation curves obtained with the projected stress (right diagrams, curve with triangles). This could be expected because compression sliding implies frictional dissipation,

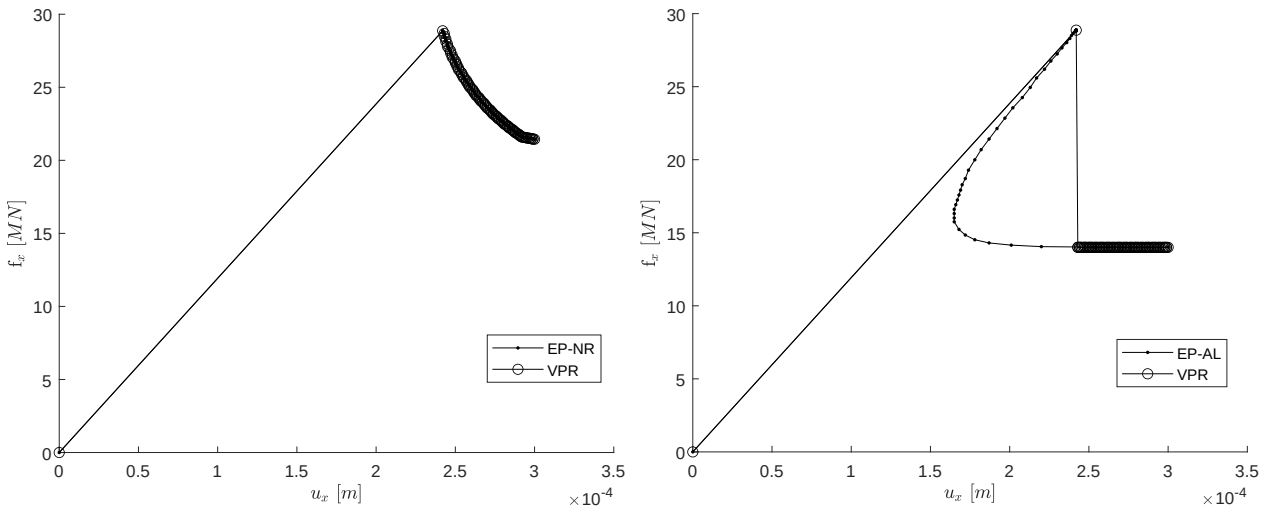

(a) Stable case **(b)** Unstable case

Figure 4.7: Horizontal force–horizontal displacement evolution curves at the end nodes of the rod elements located at both left and right sides of the domain. Elasto-plastic and visco-plastic representation.

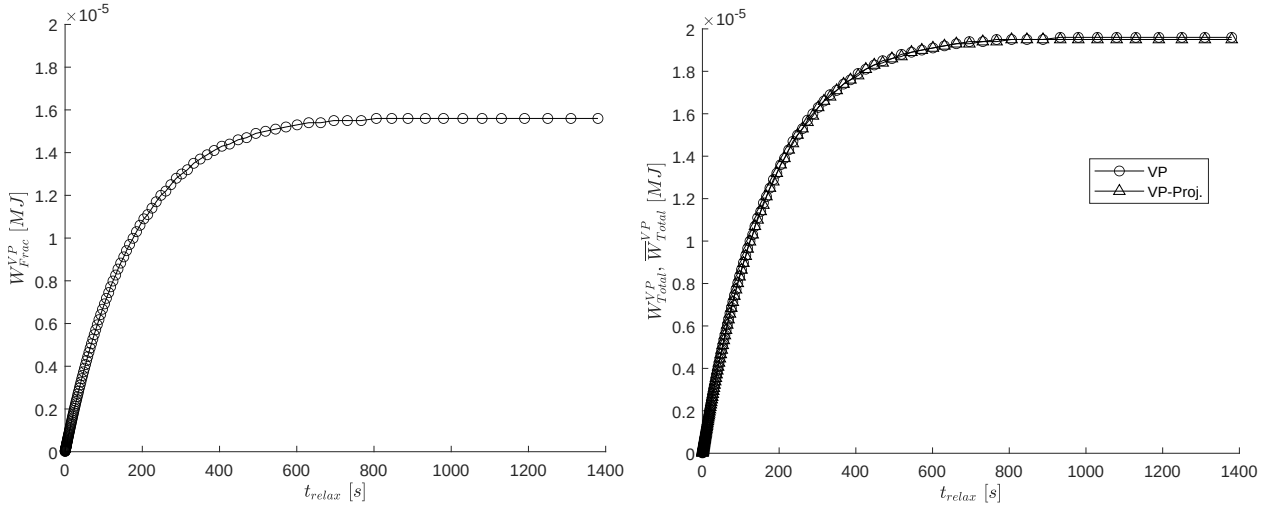

(a) W^{VP}_{Frac} **(b)** W^{VP}_{Total}, $\overline{W}^{VP}_{Total}$

Figure 4.8: (a) Fracture dissipation and (b) total dissipation obtained with visco-plastic and with projected stresses, during the first post-peak increment of the shear-compression sliding, stable case.

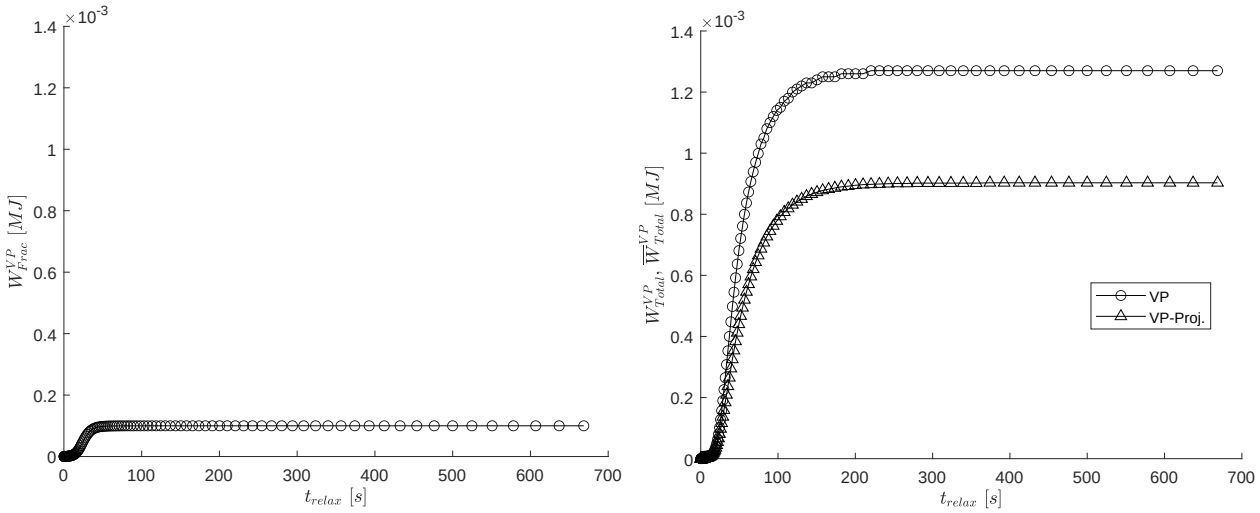

(a) W^{VP}_{Frac} **(b)** W^{VP}_{Total}, $\overline{W}^{VP}_{Total}$

Figure 4.9: (a) Fracture dissipation and (b) total dissipation obtained with visco-plastic and with projected stresses, during the first post-peak increment of the shear-compression sliding, unstable case.

that adds to the fracture dissipation to obtain the total dissipation.

- Looking only at the total dissipation (right diagrams), a similar behavior is observed as in the previous tensile example: in the stable case the total visco-plastic dissipation (curve with circles) coincides with the projected stress dissipation (curve with triangles), while in the unstable case it does not and the total visco-plastic dissipation (circles) is larger than the projected stress dissipation (triangles). This difference corresponds by definition to the viscous dissipation, that in the stable case is zero, but in the event of instability becomes positive. Therefore, also in this case the viscous dissipation could be used as an indicator of the occurrence of instabilities.

4.4.3 Shear-compression sliding with 45º inclined interface

The third example is a $10\,m$ x $10\,m$ square domain which is split diagonally by a 45º inclined interface (Fig. 4.10). This example has been calculated with a simple mesh composed of two continuum elements and one interface element. The material properties for the stable case are: continuum material with elastic modulus $E = 1.5 \cdot 10^4\,MPa$ and Poisson ratio $\nu = 0$; interface parameters (elasto-plastic and visco-plastic): normal and tangential elastic stiffness $K_N = K_T =$

$10^7\,MPa/m$, friction angle $\tan\phi = 0.7$, tensile strength $\chi = 3.0\,MPa$, cohesion $c = 9.0\,MPa$, fracture energy mode I $G_f^I = 2.0{\cdot}10^{-2}\,MPa{\cdot}m$, fracture energy mode IIa $G_f^{IIa} = 2.0{\cdot}10^{-1}\,MPa{\cdot}m$, sigma for which dilatation vanishes $\sigma_{dil} = 20\,MPa$ and, for visco-plastic calculations, viscosity $\eta = 10^4\,MPa \cdot s$. Additionally, to guarantee the existence of an instability the fracture energy values are reduced to $G_f^I = 2.0 \cdot 10^{-3}\,MPa \cdot m$ and $G_f^{IIa} = 2.0 \cdot 10^{-2}\,MPa \cdot m$. Loading is applied via increasing prescribed horizontal displacement to the left side of specimen (nodes 1 and 6).

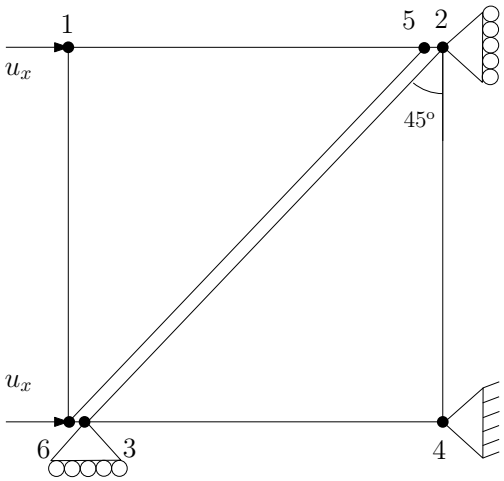

Figure 4.10: Geometry and boundary conditions of the unstable compression example with a 45º inclined interface. Simple mesh.

The results obtained with the VPR calculation are presented in Figure 4.11, in terms of the total horizontal force, against the horizontal displacement of the left side, together with the results obtained using the inviscid elasto-plastic version of the interface constitutive model (EP) using iterative NR (stable case) or AL (unstable case). Also in this example, in the stable case (left diagram) both VPR and EP curves coincide. However, in the unstable case, the EP curve exhibits a snap-back, while the VPR curve falls vertically from the peak, until it meets again the EP curve at the bottom of the diagram. This behavior is similar to previous examples analyzed and shows that, also in this statically indeterminate case, the VPR analysis is capable of providing a smooth transition across the instability event.

The energy dissipation evolution in the stable case are shown in Figure 4.12, and in the unstable case in Figure 4.13. As in previous examples, in each figure the diagram on the left corresponds to the fracture energy dissipation, while the right diagram depicts the total dissipation obtained using the total visco-plastic stresses, or the stresses projected on the EP surface.

Figures 4.12 and 4.13 exhibit similar features as previous example (Sec. 4.4.2), with fracture

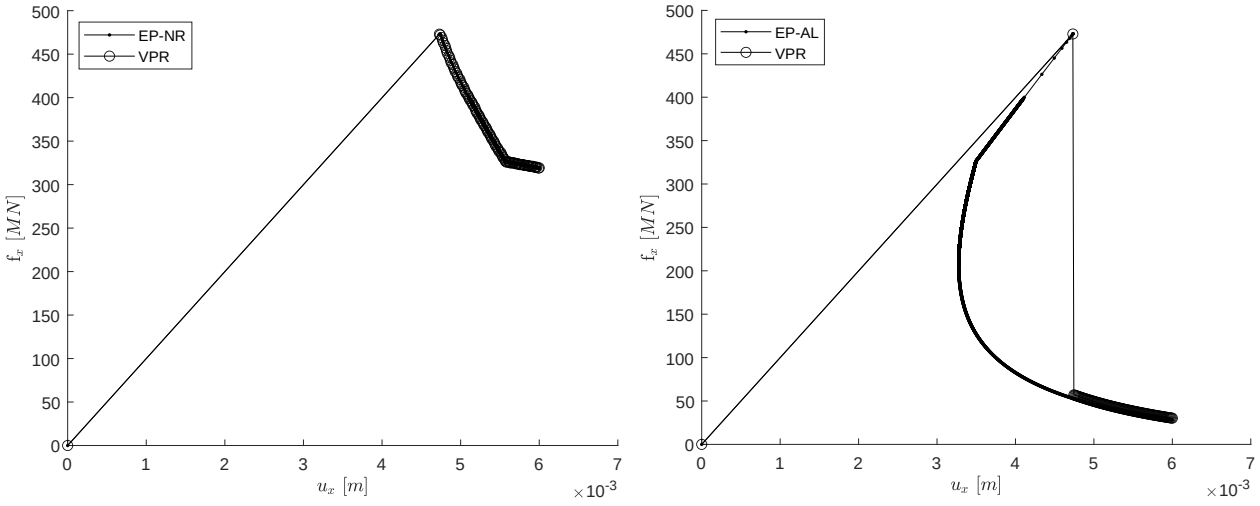

(a) Stable case **(b)** Unstable case

Figure 4.11: Horizontal force–horizontal displacement evolution curves plotted at the left side nodes of the domain. Elasto-plastic and visco-plastic representation.

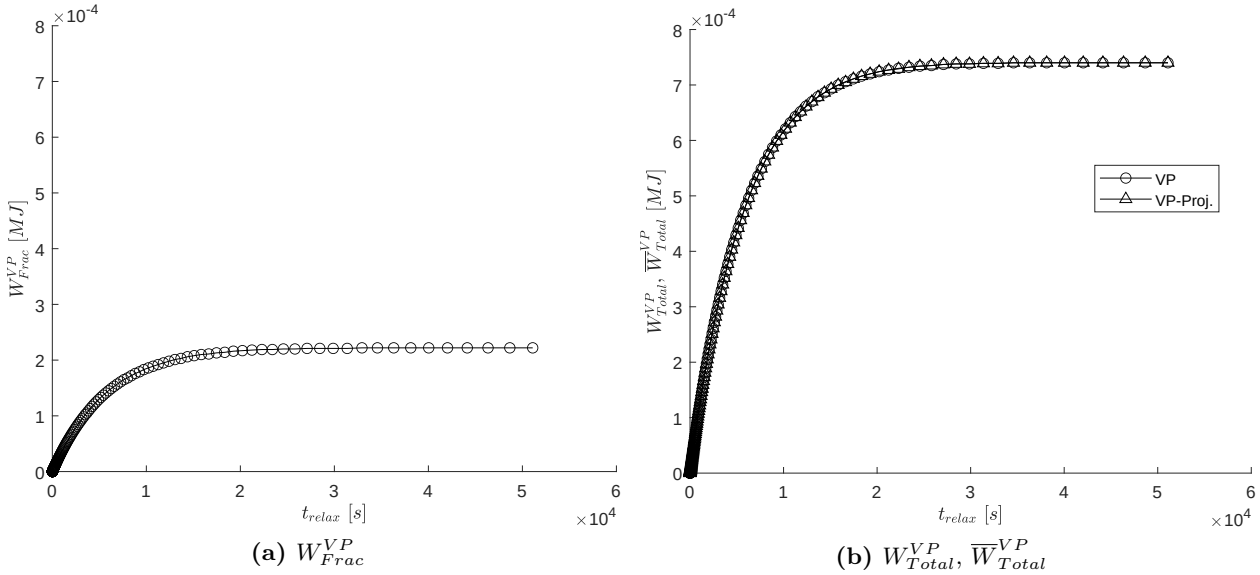

(a) W^{VP}_{Frac} **(b)** W^{VP}_{Total}, $\overline{W}^{VP}_{Total}$

Figure 4.12: (a) Fracture dissipation and (b) total dissipation obtained with visco-plastic and with projected stresses, during the first post-peak increment of the shear-compression sliding with 45º inclined interface, stable case.

dissipation lower than total dissipation due to the frictional work, and, a viscous dissipation (difference between the total visco-plastic dissipation and the total dissipation calculated using stresses

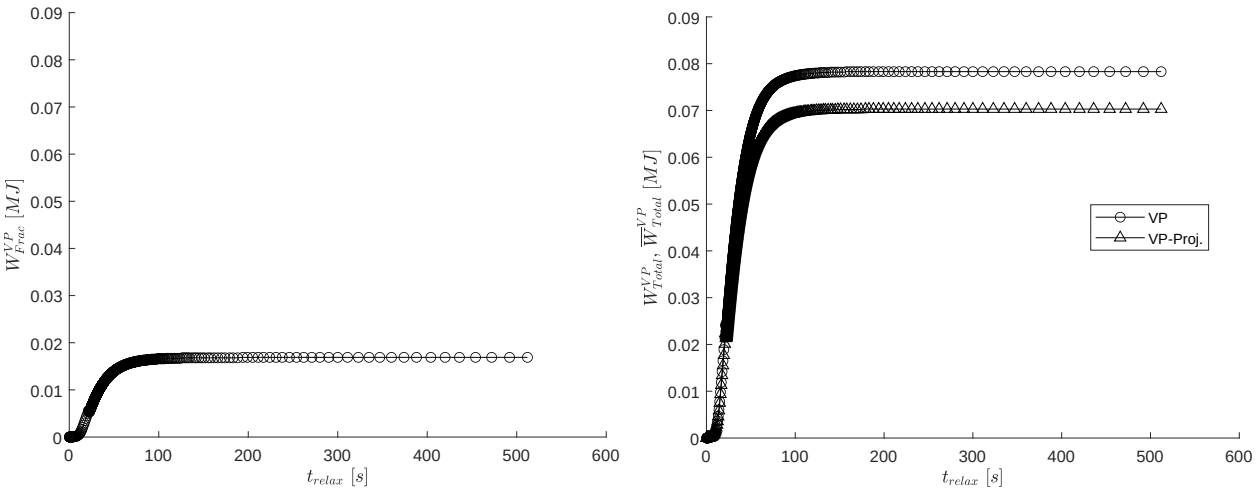

(a) W^{VP}_{Frac} **(b)** W^{VP}_{Total}, $\overline{W}^{VP}_{Total}$

Figure 4.13: (a) Fracture dissipation and (b) total dissipation obtained with visco-plastic and with projected stresses, during the first post-peak increment of the shear-compression sliding with 45^{o} inclined interface, unstable case.

projected on the EP surface) that is null in the stable case, but is non-zero in the case of instability.

4.4.4 Energy balance assessment for stable and unstable examples

This section is dedicated to the verification that the results of previous examples satisfy the energy balance $W_{Ext} = W_{Int}$ as developed in Section 4.3. According to that, the balance could include, in the most general, scenario the following terms: the continuum elastic energy ($W_{e\text{C}}$), the interface elastic energy ($W_{e\text{J}}$), the rod elastic energy ($W_{e\text{R}}$), the total visco-plastic dissipation that may be decomposed into the viscous dissipation and the projected elasto-plastic dissipation ($W^{VP}_{Total} = W^{Viscous} + \overline{W}^{VP}_{Total}$), and the latter may be in turn decomposed into the fracture dissipation plus the friction dissipation ($\overline{W}^{VP}_{Total} = W^{VP}_{Frac} + W^{VP}_{Fric}$). All these summed would lead to the total internal energy gain term W_{Int}, that should then be equal to the external supply term W_{Ext}.

In the uniaxial tension example of Section 4.4.1, the terms participating in the energy balance are the continuum elastic work ($W_{e\text{C}}$), the interface elastic work ($W_{e\text{J}}$), the fracture dissipation (W^{VP}_{Frac}) and the viscous dissipation ($W^{Viscous}$). These terms are evaluated numerically in total values (from unloaded state to end of the loading at maximum prescribed displacement equal to $10^{-4}\,m$). The external loading is calculated from the force-displacement evolution curves of Figure 4.3 by estimating the area under the curve. The results are included in Table 4.1. The figures

contained in Table 4.1 lead to the conclusion that both cases, stable and unstable, seem to satisfy the energy balance within the range of 1%.

Example 2 (Sec. 4.4.2) includes also the term of frictional dissipation (W^{VP}_{Fric}), the rod elastic energy, $W_{e\mathrm{R}}$, and the dilation negative work of the normal load, while Example 3 (Sec. 4.4.3) should also include the term of frictional dissipation. The calculations in these two cases, lead to the figures contained in Table 4.2 and Table 4.3. Those figures show that, also in those examples and for both the cases stable and unstable, the energy balance seems to be satisfied within the range of 1%.

	Stable results (MJ)	Unstable results (MJ)
$W_{e\mathrm{C}}$	$4.1082 \cdot 10^{-7}$	$4.0150 \cdot 10^{-14}$
$W_{e\mathrm{J}}$	$4.1082 \cdot 10^{-9}$	$4.0150 \cdot 10^{-16}$
W^{VP}_{Frac}	$8.5669 \cdot 10^{-5}$	$9.9995 \cdot 10^{-6}$
$W^{Viscous}$	$8.5652 \cdot 10^{-7}$	$1.0505 \cdot 10^{-5}$
W_{Int}	$8.6941 \cdot 10^{-5}$	$2.0505 \cdot 10^{-5}$
W_{Ext}	$8.6540 \cdot 10^{-5}$	$2.0368 \cdot 10^{-5}$
% Error (Ext.-Int.)	0.463%	0.673%

Table 4.1: Compilation of all work terms obtained as a result of both stable and unstable cases for uniaxial tension opening example.

As a concluding remark, it has been verified from the different examples presented in this section that the visco-plastic relaxation (VPR) strategy constitutes a tool capable of providing an estimate of the energy released in an unstable process. This achievement is of great importance to take a step forward and address more complicated examples (hydro-mechanical coupled examples) where instability can be induced by a fluid injection.

	Stable results (MJ)	Unstable results (MJ)
$W_{e\mathrm{C}}$	$6.6667 \cdot 10^{-3}$	$6.6667 \cdot 10^{-3}$
$W_{e\mathrm{J}}$	$2.1494 \cdot 10^{-5}$	$1.4900 \cdot 10^{-5}$
$W_{e\mathrm{R}}$	$1.9156 \cdot 10^{-3}$	$8.0856 \cdot 10^{-4}$
W_{Frac}^{VP}	$1.2696 \cdot 10^{-3}$	$1.9999 \cdot 10^{-4}$
W_{Fric}^{VP}	$6.6582 \cdot 10^{-4}$	$2.4097 \cdot 10^{-3}$
$W^{Viscous}$	$4.1706 \cdot 10^{-6}$	$7.3796 \cdot 10^{-4}$
W_{Dil}	$9.9662 \cdot 10^{-4}$	$1.2899 \cdot 10^{-4}$
W_{Int}	$1.1540 \cdot 10^{-2}$	$1.0976 \cdot 10^{-2}$
W_{DL}	$6.6667 \cdot 10^{-3}$	$6.6667 \cdot 10^{-3}$
W_{Ext}	$4.8828 \cdot 10^{-3}$	$4.3092 \cdot 10^{-3}$
$W_{ExtTotal}$	$1.1549 \cdot 10^{-2}$	$1.0976 \cdot 10^{-2}$
% Error (Ext.-Int.)	0.082%	0.005%

Table 4.2: Compilation of all work terms obtained as a result of both stable and unstable cases for shear-compression sliding example.

	Stable results (MJ)	Unstable results (MJ)
$W_{e\mathrm{C}}$	$5.0969 \cdot 10^{-1}$	$4.5472 \cdot 10^{-3}$
$W_{e\mathrm{J}}$	$3.6040 \cdot 10^{-4}$	$3.2153 \cdot 10^{-6}$
W_{Frac}^{VP}	$3.3816 \cdot 10^{-1}$	$2.5932 \cdot 10^{-1}$
W_{Fric}^{VP}	$7.3915 \cdot 10^{-1}$	$7.9958 \cdot 10^{-1}$
$W^{Viscous}$	$4.9332 \cdot 10^{-4}$	$1.1411 \cdot 10^{-1}$
W_{Dil}	0.0	0.0
W_{Int}	1.5879	1.1775
W_{Ext}	1.5885	1.1744
% Error (Ext.-Int.)	0.038%	0.264%

Table 4.3: Compilation of all work terms obtained as a result of both stable and unstable cases for shear-compression sliding example with 45^{o} inclined interface.

4.5 Hydraulic examples

In this section some examples are presented in order to verify the energy balance in the case of fluid flow through the continuum, interface and rod elements ($W_{Fluid} = W_{FtC} + W_{FtJ} + W_{FtR}$) and, additionally, the energy term due to the compressibility of the fluid in the continuous medium, W_{FC}.

4.5.1 Fluid compressibility

The work due to the fluid compressibility can be easily checked with a simple example consisting of a single square continuum element ($1\,m$ x $1\,m$), with the displacements of the four corners of the domain completely fixed. Regarding the hydraulic boundary conditions, in a first step pressure is increased from zero to $1.0\,MPa$ ($\Delta P = 1.0\,MPa$) during a time increment of duration $\Delta t = 0.001\,s$ at the four corners of the domain and in a second step of the same duration, the nodal pressure is removed ($\Delta P = -1.0\,MPa$) (Figures 4.14 and 4.15).

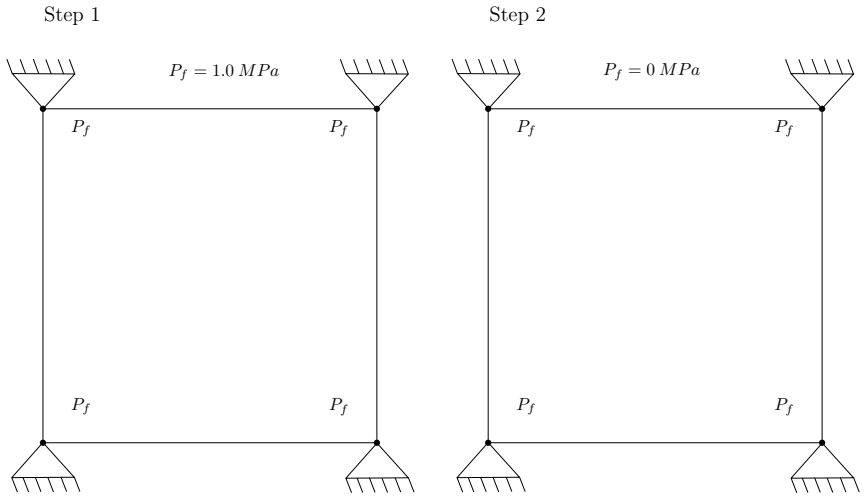

Figure 4.14: Geometry of the simple example for fluid compressibility verification. The mechanical and hydraulic boundary conditions are specified for each step.

It is assumed that the fluid injected is water and its characteristic parameters are: density $\rho = 10^{-3}\,kT/m^3$, fluid bulk modulus $K^f = 3000\,MPa$ and viscosity $\mu = 10^{-9}\,MPa \cdot s$. Moreover, the hydraulic properties of continuum are: hydraulic conductivity $K_C = 10^{-6}\,m/s$, skeleton compressibility $K^s = 3600\,MPa$, Biot's coefficient alpha $\alpha_{Biot} = 1.0$ and porosity $n = 0.2$.

With the values above, the value of the total energy stored due to fluid compressibility at the end of step 1, may be obtained in closed form. With the values of α_{Biot}, n, K^s and K^f, the Biot

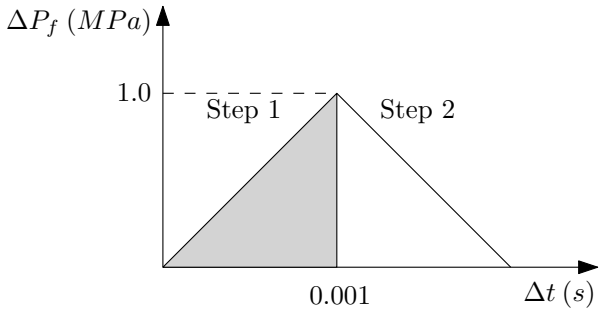

Figure 4.15: Prescribed fluid pressure versus time.

modulus (Eq. 4.25) is obtained as $M^{Biot} = 3461.54\,MPa$, and with this value and $P = 1.0\,MPa$ the specific energy per unit volume in the element (Eq. 4.27) is obtained and then multiplied by the element volume of $1\,m^3$, leading to the final value of $W_{FC} = 1.444 \cdot 10^{-9}\,MJ$. This value represents the "internal work" W_{Int} in this case.

This value may be then compared to the FE results. Among those results is the fluid nodal discharge ("reaction") that corresponds to the nodes with prescribed pressure, and is $Q = 7.222 \cdot 10^{-2}\,m^3/s$. With this value, the external work supply W_{Ext} may be computed, according to expression in equation (4.20). Because the nodal discharge Q is constant during the increment, it can be extracted out of the integral, which finally contains only the prescribed pressure. Because the pressure is increased as a ramp during the time increment $\Delta t = 0.001\,s$, the integral corresponds to the area under the mentioned ramp (gray triangular area of Figure 4.15) and, the external work due to the pressure imposed on the four corner nodes turns out as:

$$W_{Ext} = 4 \int Q\,P\,dt = 4\,Q \int P\,dt = 4 \cdot 7.222 \cdot 10^{-2} \frac{0.001 \cdot 1.0}{2} = 1.444 \cdot 10^{-4}\,MJ \tag{4.39}$$

value which coincides with the theoretical work computed earlier.

In the second step of the same duration as Step 1, the pressure previously imposed on the 4 corner nodes of the domain is removed which implies that the fluid nodal discharge is exactly the same as in Step1 but in the opposite way, $Q = -7.222 \cdot 10^{-2}\,m^3/s$, leading to a external work value also expressed in the opposite way as the one obtained in Step1. Note that considering both steps, the initial state is recovered at the end of the calculation.

$$W_{Ext} = 4 \int Q\,P\,dt = 4\,Q \int P\,dt = 4 \cdot -7.222 \cdot 10^{-2} \frac{0.001 \cdot 1.0}{2} = -1.444 \cdot 10^{-4}\,MJ \tag{4.40}$$

4.5.2 Dissipation due to the fluid flow through the continuum and interfaces

This example is a purely hydraulic case intended to check the dissipation of the fluid through the interfaces and the continuum medium. The geometry is composed by a square domain ($10\,m$ x $10\,m$) crossed horizontally and vertically by four interface elements which divide the domain into four continuum elements, as depicted in Figure 4.16.

As in the previous case, the fluid is assumed to be water and its properties are: density $\rho = 10^{-3}\,kT/m^3$, the fluid bulk modulus $K^f = 3000\,MPa$ and viscosity $\mu = 10^{-9}\,MPa \cdot s$. Moreover, the hydraulic properties of continuum are: hydraulic conductivity $K_C = 10^{-9}\,m/s$, skeleton compressibility $K^s = 3600\,MPa$, Biot's coefficient alpha $\alpha_{Biot} = 1.0$ and finally, the hydraulic properties of the interfaces are: longitudinal transmissivity $T_L = 10^{-10}\,m^2/s$, and transversal conductivity $K_t = 1.0\,s^{-1}$. The boundary conditions consist of prescribed pressure values at the points in which the interfaces intersect the boundary, which are at the center of each of the four domain edges, while the rest of the boundary is free boundary (no flow). The prescribed pressure values are of $0.5\,MPa$ at the point on the left edge, and zero at the points on the other three edges (Fig. 4.16). The analysis is run in steady state, which means that all flow magnitudes obtained will have the meaning of rates.

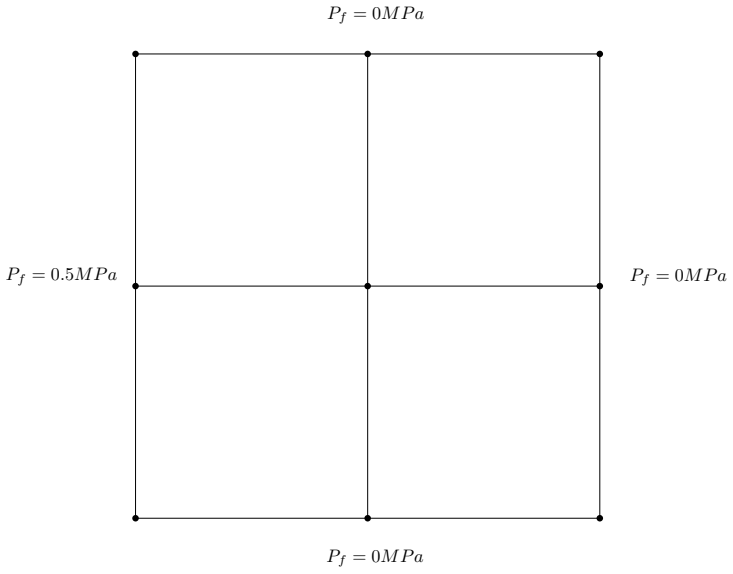

Figure 4.16: Geometry and hydraulic boundary conditions that allows to verify the work due to the fluid dissipation through the continuum and interfaces.

The results of the analysis in terms of fluid pressure and flow rate along the interfaces, are

shown in Figure 4.17. The figure shows that pressure is maximum at injection point and decays radially in all directions; along interface lines pressure decays to some reduced value at the central node and from there to zero at the other three boundary points. Flow along interfaces is relatively low due to the low transmissivity is compared to the continuum permeability. As expected, the sum of discharges at the three exit points with prescribed zero pressure is equal to the inflow at injection point.

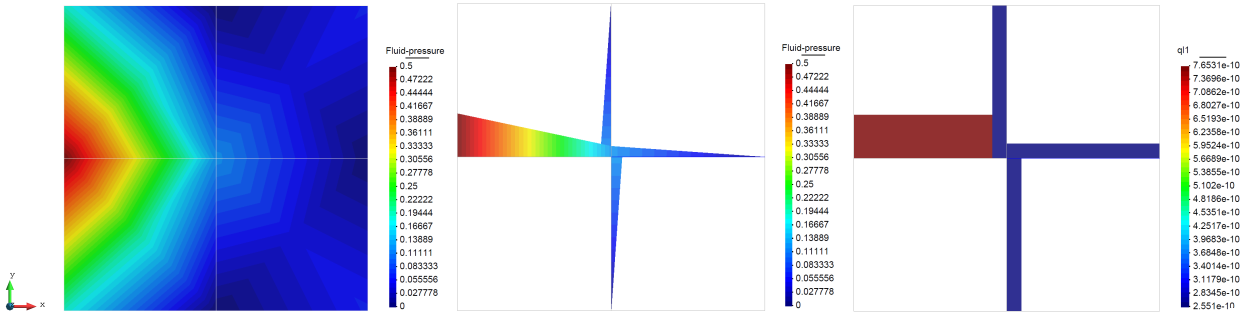

(a) **(b)** **(c)**

Figure 4.17: Results of the second flow example: (a) pressure field in the domain, (b) pressure profiles along interface elements and (c) flow rate along interface elements.

In purely hydraulic problems, the external work consists of the work associated to external fluid injections or extractions (W_F). In this case, the fluid can enter or leave the domain only along the four points with prescribed pressure values, and therefore the calculation of the work of injection/extraction has to be performed at those four points. As it was introduced in Section 4.2.2, equation (4.19) gives the expression to compute the injection work from the discharge rate and the pressure value. The discharge rate is obtained from the finite element calculation as the "reactions" that correspond to the four points (eight nodes because of the interface double nodes) with prescribed pressure values, $Q = 5.81634 \cdot 10^{-8}\, m^3/s$ and the pressure gradient $\nabla P = (0 - 0.5)\ MPa$.

Steady state is considered for this example which means that inflows and outflows are perfectly balanced as it is shown in Figure 4.17. Therefore, the injection work per unit of time can be calculated as:

$$W_F = Q \cdot \nabla P = -5.81634 \cdot 10^{-8} \cdot (0 - 0.5) = 2.908167 \cdot 10^{-8} \left(\frac{MJ}{s} \right) \tag{4.41}$$

The other part of the energy balance verification corresponds to the fluid dissipation through the

continuum (W_{FtC}, Eq. 4.29) and the interfaces (W_{FtJ}, Eq. 4.31). The corresponding expressions were implemented in the finite element code and the code provides as outputs these values: $W_{FtC} = 2.8699 \cdot 10^{-8}\, MJ/s$ and $W_{FtJ} = 3.82653 \cdot 10^{-10}\, MJ/s$. Adding both values $W_{Fluid} = 2.9081653 \cdot 10^{-8}\, MJ/s$, it can be seen that the total (W_{Fluid}) coincides with the external injection work (W_F), therefore the hydraulic energy balance is fulfilled.

4.5.3 Dissipation due to the fluid flow through the rod elements, and basic H-M coupling

This example has been chosen with the intention of verifying the calculation of the fluid flow and associated dissipation along rod elements, and also this is the first example with a very basic type of coupling between flow and mechanical behavior. The geometry and boundary conditions of this example are depicted in Figure 4.18. As seen in the figure, two $1\,m$ x $1\,m$ continuum elements are separated by an interface and two rods are connected on the left and right sides, to the lower nodes of the interface element. Regarding material properties, the continuum is assumed linear elastic ($E = 10^3\, MPa$ and $\nu = 0$) and it is considered that it does not intervene in terms of flow since hydraulic conductivity and Biot's coefficient are assumed zero. In contrast, the interface has a pure hydraulic behavior, with zero normal and tangential stiffness $K_N = K_T = 0$, but non-zero longitudinal transmissivity $T_L = 5.0 \cdot 10^{-6}\, m^2/s$ and transversal conductivity $K_t = 1.0\, s^{-1}$. Finally, the rod parameters are: stiffness $K_{\mathrm{R}} = EA/L$ (although it does not play a role) is obtained from $EA = 10^3\, MPa \cdot m^2$ and rod length $L = 1.0\, m$, while rod conductivity is $K_{\mathrm{R}C} = 5.0 \cdot 10^{-6}\, m^2/s$. As in previous examples, the fluid is assumed to be water.

As pressure is prescribed to the end external nodes of the rods (while the interface nodes have initial zero pressure) the fluid goes into the interface and forces it to open. This opening starts compressing the upper continuum element, which acts as a spring, opposing that opening, and increasing the fluid pressure in the interface. The result is that the opening of the interface is progressively slowing down until reaching an asymptotic state of equilibrium in which the vertical compressive stress in the upper continuum element is equal to the prescribed fluid pressure. Due to its conceptual simplicity, the problem can be solved in closed form and analytical expressions can be obtained for all system variables such as the pressure gradient in the contact point between the rod element and the continuum, the volume of fluid entering the interface and the fluid dissipation through the rods.

The analytical developments are detailed in Appendix E, and the resulting expressions for the relevant variables are:

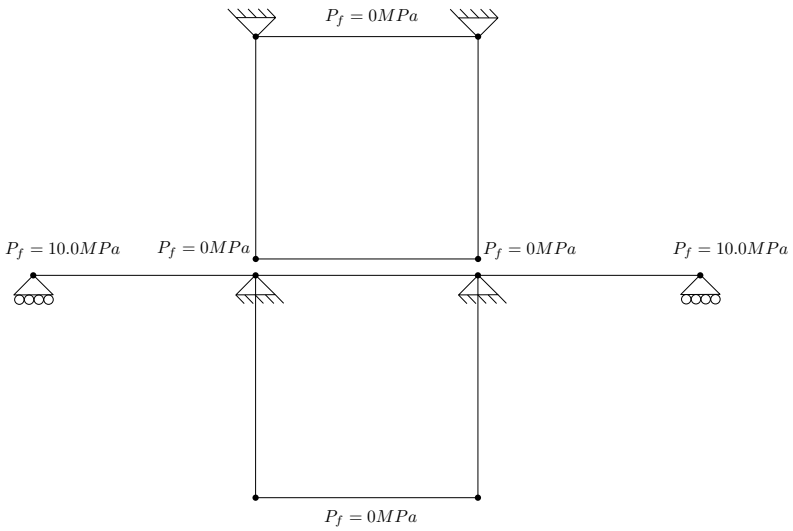

Figure 4.18: Geometry and boundary conditions of the third flow example.

- Pressure in the contact point rod-continuum:

$$P = P_0 \left(1 - e^{-kt}\right) \tag{4.42}$$

where $k = 2K_{\mathrm{R}C}\frac{E}{L}$ being L the height of the upper continuum element and $K_{\mathrm{R}C}$ the rod conductivity.

- Total fluid volume entering the interface:

$$V = \frac{L}{E} P_0 \left(1 - e^{-kt}\right) \tag{4.43}$$

- Fluid dissipation along the rods:

$$W_{Ft\mathrm{R}} = \frac{K_{\mathrm{R}C}}{\gamma^f}\left[P_0^2\left(t + \frac{2}{k}e^{-kt} - \frac{1}{2k}e^{-2kt}\right) + P_0^2\, t - 2P_0^2\left(t + \frac{1}{k}e^{-kt}\right)\right] + \frac{K_{\mathrm{R}C}}{\gamma^f}\frac{P_0^2}{2k} \tag{4.44}$$

Knowing the closed-form expressions mentioned above (Eq. 4.44 plus elastic energy of the continuum, Eq. 4.6) a direct comparison can be made with the results obtained in the numerical calculation. This is done in Figure 4.19 showing very good agreement between theoretical and numerical values for both energy terms of fluid dissipation along rods $W_{Ft\mathrm{R}}$ and elastic energy in the continuum elements $W_{e\mathrm{C}}$.

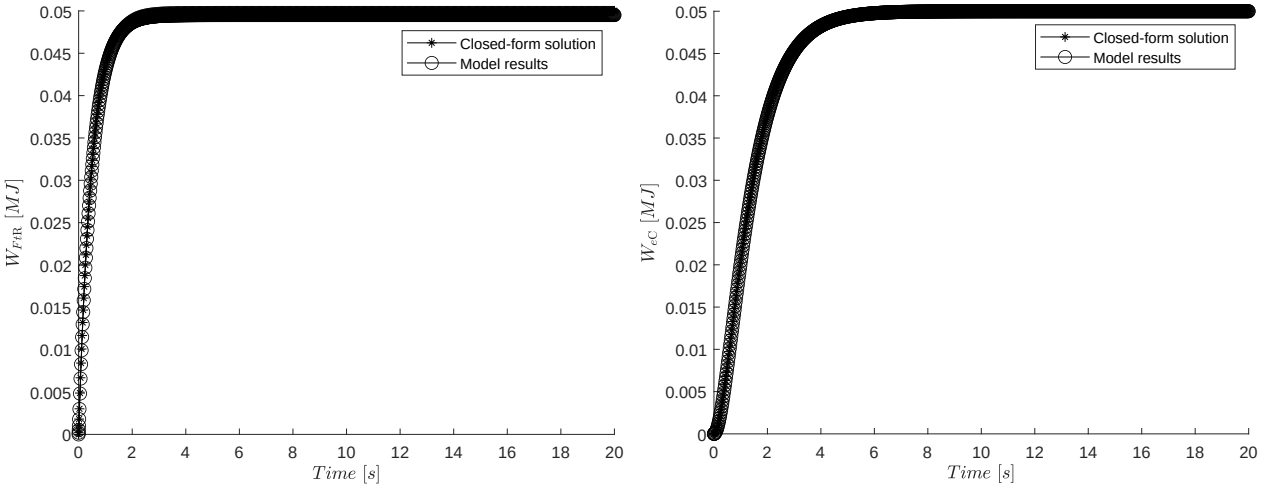

(a) W_{FtR} **(b)** W_{eC}

Figure 4.19: Comparison between closed-form and numerical results for both W_{FtR} and W_{eC} work terms.

Performing the energy balance at the end of the calculation, the external work W_{Ext} corresponds to the work generated by the fluid injection (W_F, Eq. 4.20) at the free ends of the rod elements. In this case it is calculated considering that is a constant value $P(t) = P_0 = 10\,MPa$ and can go out of the integral and that the final volume of fluid that has entered the interface through both rods for infinite time according to equation 4.43 is $V(t = \infty) = 0.01\,m^3$, which leads to:

$$W_{Ext} = W_F = \int Q\,P\,dt = \int P\,dV = P_0 \int dV = P_0 V\,(t) = 10 \cdot 0.01 = 0.1\,MJ \tag{4.45}$$

On the other hand, the internal work may be calculated as:

$$W_{Int} = W_{FtR} + W_{eC} = 0.05\,(MJ) + 0.05\,(MJ) = 0.1\,MJ \tag{4.46}$$

which confirms that the energy balance $W_{Ext} = W_{Int}$ is satisfied. As equation (4.46) shows, the internal work in this case involves only two terms because, in this case, the dissipation generated by the flow through the interface is zero since the same volume of fluid enters through both ends of the interface and, therefore, there is no pressure gradient.

4.6 Hydro-mechanical coupled examples

Once it has been verified that the energy balance is fulfilled in various types of examples and it is guaranteed that the different work terms implemented in the FE code of the research group are calculated correctly, the next step is to consider simple hydro-mechanical cases in which an instability can be induced by a fluid injection and quantify the energy released in the unstable process.

The mentioned fluid injection can be performed both by prescribing a pressure value or prescribing a flow discharge. The first two examples presented in this section develop an instability by prescribing pressure while the third one reaches the instability by prescribed discharge.

All the cases analyzed in this section have been chosen to involve shear-compression stress states on the discontinuity plane, this is the most common type of failure that corresponds to the reactivation of discontinuities by fluid injection.

Regarding the methodology used to calculate, these examples have been run with visco-plasticity combined with VPR iterative strategy.

4.6.1 Instability induced by imposing fluid pressure

4.6.1.1 Unstable Shear-compression sliding imposing pressure

The first example consists of the same geometry, boundary conditions and material properties as the purely mechanical compression unstable case studied in Section 4.4.2. The difference is in the way of inducing the instability, here it is induced by the effect of a fluid injection (rather than by the effect of applying additional displacements in the end nodes of each rod element). Figure 4.20 shows the geometry and the sequence of load steps that have been defined to calculate this case:

- Step 1: A vertical distributed load is applied on the top face of the domain which generates the compression effect.
- Step 2: A horizontal displacement is prescribed to the free end nodes of each rod. The imposed displacement is such that brings the interface to a stress state just before the peak of the force-displacement curve.
- Step 3: A pressure increment is prescribed to the interface nodes to reduce effective stress and induce the instability.
- Step 4: After the instability has taken place, a new increment of prescribed displacements is

applied again to the free end nodes of each rod in order to complete the force-displacement curve of this test, while maintaining the prescribed pressure values of the previous step.

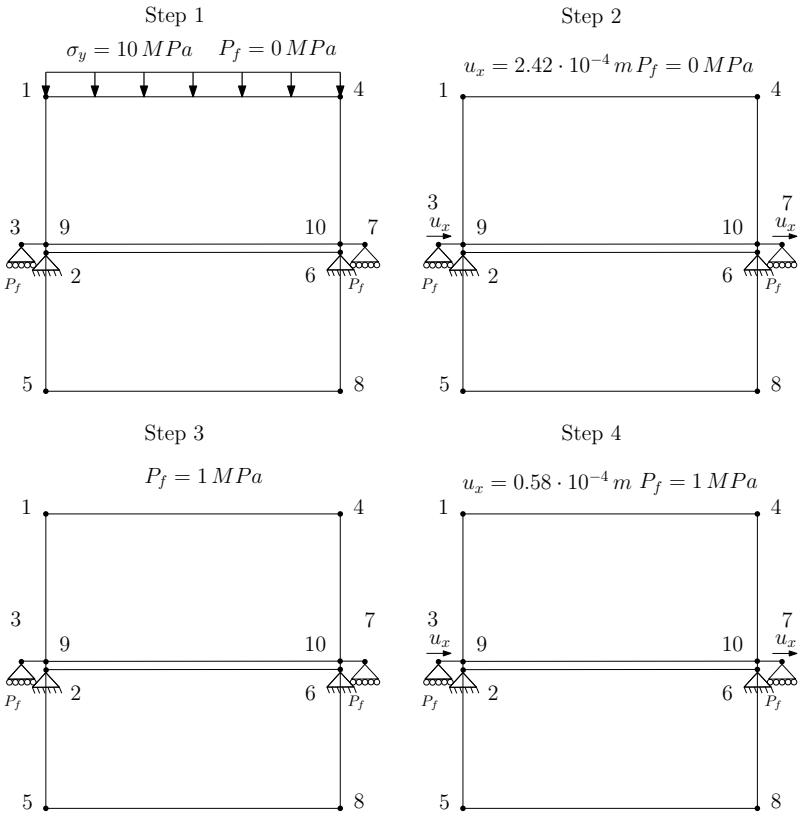

Figure 4.20: Geometry and boundary conditions of the unstable shear-compression example with prescribed pressure.

As in hydraulic cases, the fluid is assumed to be water and its properties are: density $\rho = 10^{-3}\,kT/m^3$, fluid bulk modulus $K^f = 3000\,MPa$ and viscosity $\mu = 10^{-9}\,MPa \cdot s$. Moreover, the hydraulic properties of the continuum are: Biot's coefficient $\alpha_{Biot} = 0$, hydraulic conductivity $K_{\mathrm{C}} = 10^{-10}\,m/s$, and skeleton compressibility $K^s = 3600\,MPa$, (although the latter parameters will be irrelevant in this case since $\alpha_{Biot} = 0$ and the boundary conditions prevent any flow into the continuum elements); hydraulic properties of interfaces are: longitudinal transmissivity $T_L = 10^{-6}\,m^2/s$, transversal conductivity $K_t = 1.0\,s^{-1}$ and finally, the rod conductivity $K_{\mathrm{RC}} = 5.0 \cdot 10^{-6}\,m^2/s$.

Figure 4.21 represents the structural H-M force-displacement curve obtained with the visco-plastic approach ("VPR-HM" curve), together with the similar curves that had been obtained with

the mechanical-only study of the same case in Section 4.4.2 using elasto-plasticity and Arc-Length ("EP-M" curve) leading to a snap-back, and VPR ("VPR-M" curve) leading to a vertical drop across the snap-back and then joining the EP curve for the tail part of the diagram (Fig. 4.7-(b)). It can be seen in the figure that the current curve coincides well with the VPR-M curve except that, after the instability has taken place, the hydro-mechanical curve drops to a lower residual value than the inviscid curve. This is due to the decrease of the effective normal stresses by the effect of the fluid pressure, which leads to a lower residual shear stress (note that this H-M example cannot be calculated directly by using elasto-plasticity combined with Arc-Length iterative method leading to snap-back because in H-M problems the time involved is the physical time, and negative displacement increments implied in the snap back would mean negative time increment which makes no physical sense).

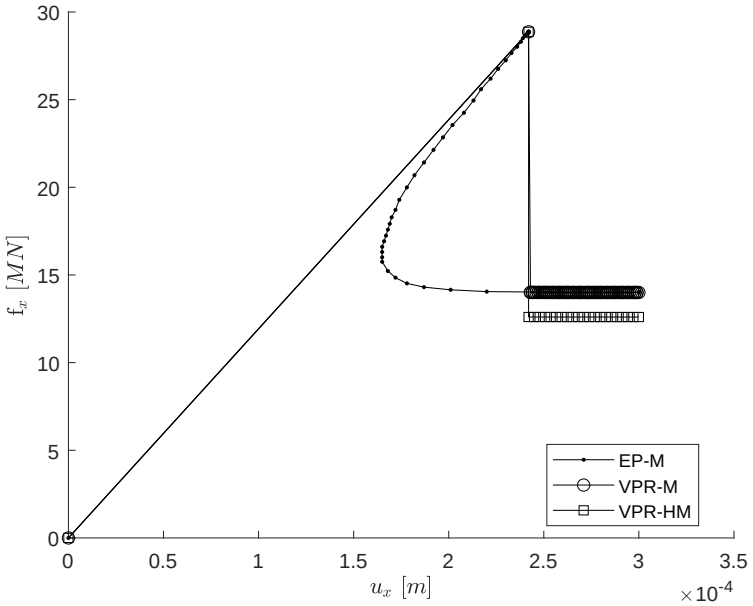

Figure 4.21: Representation of the structural force-displacement curves for EP and VP-VPR mechanical problem together with the curve obtained with VP-VPR method considering the hydro-mechanical problem.

Once the instability has taken place in a fictitious time step of the VPR calculation (in this case the first one), the evolution of the various energy dissipations in the interface element during that fictitious time step, have been plotted as introduced in Section 4.4.2, (Fig. 4.9). In Figure 4.22 the left diagram depicts the fracture energy dissipation while the right diagram presents the total visco-plastic dissipation and the dissipation obtained using the stresses projected on the yield

surface. Same as in Section 4.4.2 a clear difference is observed between the curves represented in the right diagram. This difference corresponds to the viscous dissipation which can be considered as an indicator of the occurrence of the instability, and may be eventually used to quantify the magnitude of energy released during the instability event.

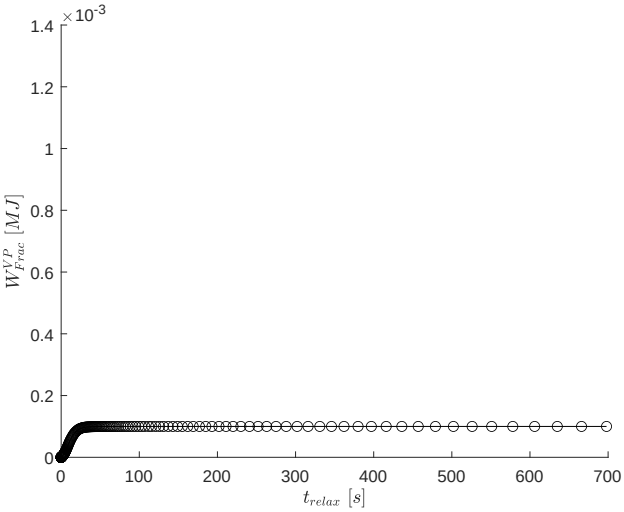

(a) W^{VP}_{Frac}

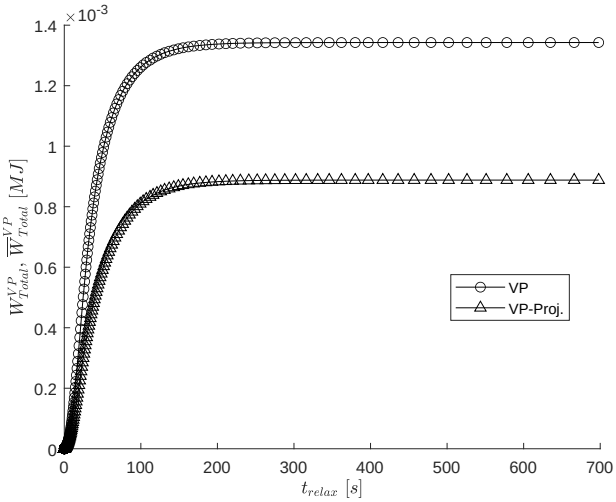

(b) W^{VP}_{Total}, $\overline{W}^{VP}_{Total}$

Figure 4.22: (a) Fracture dissipation and (b) total dissipation obtained with the visco-plastic stress and with projected stresses, during the first post-peak increment of the shear-compression sliding where the instability is induced by fluid pressure.

In the present example and also in previous ones, the point along the loading history in which the instability can occur is known *a priori*, since all these examples exhibit a clear peak in the force-displacement diagrams followed by steep softening. However, in a more complex case the point along the loading history at which the instability can occur may be unknown and to obtain it may be one more objective of the analysis. One way to do it is to plot the curves of evolution with the load history variable (physical time in the case of transient H-M analysis, or loading factor in the case of time-independent mechanical analysis), of the two VPR dissipations involved: the total VP dissipation W^{VP}_{Total}, and the VP dissipation using the projected stresses $\overline{W}^{VP}_{Total}$. This has been done in the current example, and the resulting curves are depicted in Figure 4.23.

In the Figure 4.23, one can see that the curves first remain with zero values during the elastic loading until the time $t = 0.1\,s$ when the peak is attained. At that time the curves exhibit a sudden jump coinciding with the initiation of the interface sliding, and from there on they continue growing more gradually till the end of the time analyzed. The jump clearly corresponds to the vertical drop

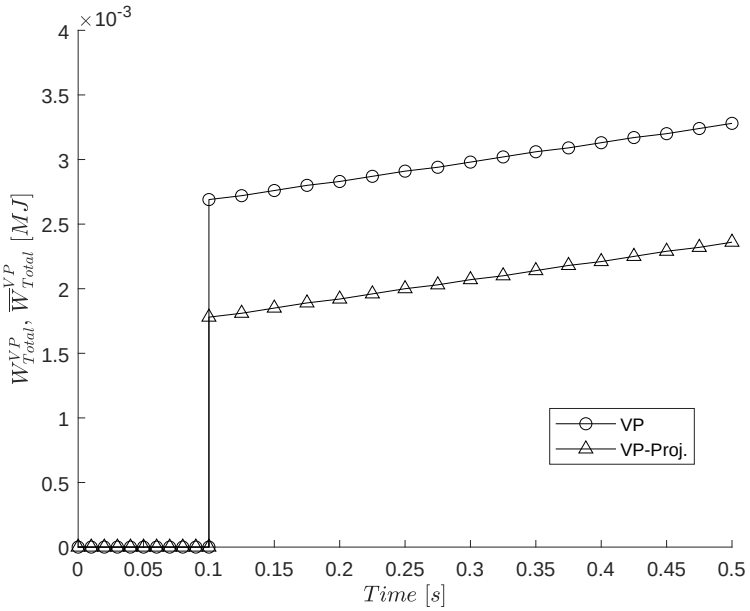

Figure 4.23: Evolution with physical time, of the total VP dissipation calculated with total VP stresses, W^{VP}_{Total}, and with the stresses projected on the loading surface, $\overline{W}^{VP}_{Total}$.

of the force-displacement diagram in Figure 4.21, therefore to the dissipation occurring while the VPR calculation bypasses the instability. Essential in this graph is not only the jump itself, but the fact that the jump is of a different magnitude for the two curves represented, indicating not only the time of occurrence of the unstable event, but also the magnitude of it in terms of the energy the VP model has dissipated during the unstable transition $W^{Viscous} = W^{VP}_{Total} - \overline{W}^{VP}_{Total}$.

With the purpose of verification, finally, Table 4.4 shows the values of all individual components of the energy dissipation and storage balance for the present example at the end of the simulation, including the released energy ($W^{Viscous} = W^{VP}_{Total} - \overline{W}^{VP}_{Total}$). It is reassuring to verify that the overall error in the energy balance is lower than 1%.

Note that one of the components of this balance is the negative external work of the applied vertical load due to the interface dilatancy during shear sliding, which can be calculated using the vertical displacement variation of the top nodes. This value is $u_y = 7.0232 \cdot 10^{-6}\, m$ in this case, and therefore, W_{Dil} is calculated as:

$$W_{Dil} = u_y \cdot f_y = 7.0232 \cdot 10^{-6} \cdot (10 \cdot 2) = 1.4046 \cdot 10^{-4}\, MJ \tag{4.47}$$

On the other hand, the elastic energy stored in both rod elements can be calculated using

Unstable HM results (MJ)	
$W_{e\mathrm{C}}$	$6.6667 \cdot 10^{-3}$
$W_{e\mathrm{J}}$	$1.2069 \cdot 10^{-5}$
$W_{e\mathrm{R}}$	$6.6150 \cdot 10^{-4}$
W^{VP}_{Frac}	$2.0000 \cdot 10^{-4}$
W^{VP}_{Fric}	$2.3069 \cdot 10^{-3}$
$W^{Viscous}$	$9.1941 \cdot 10^{-4}$
W_{FC}	$2.1111 \cdot 10^{-5}$
W_{Dil}	$1.4046 \cdot 10^{-4}$
W_{Int}	$1.0928 \cdot 10^{-2}$
W_{DL}	$6.6667 \cdot 10^{-3}$
W_{Ext}	$4.2237 \cdot 10^{-3}$
$W_{ExtTotal}$	$1.0890 \cdot 10^{-2}$
% Error (Ext.-Int.)	0.3464%

Table 4.4: Compilation of all work and energy terms obtained as a result of visco-plastic calculations for the unstable shear-compression example for which instability is induced by imposing pressure.

equation (4.11) and here $K_{\mathrm{R}} = 60000\, MPa \cdot m$.

Finally, just need to know the horizontal displacements experienced by each rod which are provided by the model: $\delta u_x = 1.05 \cdot 10^{-4}\, m$. Therefore, $W_{e\mathrm{R}}$ is calculated as:

$$W_{e\mathrm{R}} = \frac{1}{2} \cdot 60000 \cdot \left(1.05 \cdot 10^{-4}\right)^2 = 3.3075 \cdot 10^{-4}\, MJ \tag{4.48}$$

$$W_{e\mathrm{R}(2rods)} = 3.3075 \cdot 10^{-4} \cdot 2 = 6.615 \cdot 10^{-4}\, MJ \tag{4.49}$$

4.6.1.2 Unstable Shear-compression sliding of inclined interface by imposing fluid pressure

As an step forward to represent more realistic cases, the second example in this section is a square domain crossed by an inclined interface. Specifically, the geometry is the same as used in the third

example of mechanical-only behavior, Section 4.4.3 (Fig. 4.10), which consists of a $10\,m$ x $10\,m$ square domain which is split in half by a 45^{o} inclined interface. This example has been calculated first with a simple mesh composed of two continuum elements and one interface element (as in Sec. 4.4.3), but it has also been calculated with a finer mesh (Fig. 4.24). As it was expected, the results obtained with both meshes are the same but performing the refined mesh example is useful in order to check the methodology VPR in more complicated cases. This is important since a refined mesh will be necessary in cases where the instability would be induced by injection of a fluid flow (prescribed discharge instead of prescribed pressure).

The material properties that guarantee the existence of an instability are:

- The continuum material is assumed linear elastic with $E = 1.5 \cdot 10^4\,MPa$ and $\nu = 0$.
- The parameter values used for the interface constitutive models (elasto-plastic and visco-plastic) are: normal and tangential elastic stiffness $K_N = K_T = 10^7\,MPa/m$, friction angle $\tan\phi = 0.7$, tensile strength $\chi = 3.0\,MPa$, cohesion $c = 9.0\,MPa$, fracture energy mode I $G_f^I = 2.0 \cdot 10^{-3}\,MPa \cdot m$, fracture energy mode IIa $G_f^{IIa} = 2.0 \cdot 10^{-2}\,MPa \cdot m$, sigma dilatation $\sigma_{dil} = 20\,MPa$ and for visco-plastic calculations the viscosity $\eta = 10^4\,MPa \cdot s$.

Moreover, the hydraulic properties are:

- Water is the fluid injected: density $\rho = 10^{-3}\,kT/m^3$, bulk modulus $K^f = 3000\,MPa$ and viscosity $\mu = 10^{-9}\,MPa \cdot s$.
- Hydraulic properties of continuum: hydraulic conductivity $K_{\text{C}} = 10^{-3}\,m/s$, skeleton compressibility $K^s = 3600\,MPa$, Biot's coefficient $\alpha_{Biot} = 1.0$.
- Hydraulic properties of interfaces: longitudinal transmissivity according to cubic law ($T_L = \gamma^f r_N^3/(12\mu)$, specified in Section 4.2.2.4), with minimum value $T_{L,min} = 10^{-14}\,m^2/s$, and transversal conductivity $K_t = 1.0\,s^{-1}$.

As in the previous example, the loading procedure followed to induce the instability consists of prescribing increasing displacements (this time in the horizontal direction), until the peak of the load-displacement diagram is reached, and then prescribing a uniform fluid pressure of value $0.1\,MPa$ on the whole domain to trigger the instability. Finally, after the instability has taken place, the rest of the displacements are prescribed until the end of the calculation ($u_x = 0.006\,m$).

The results of the calculation are represented in Figures 4.25, 4.26 and 4.27. In Figure 4.25, the load-displacement curves obtained with VPR considering the single element mesh and the refined

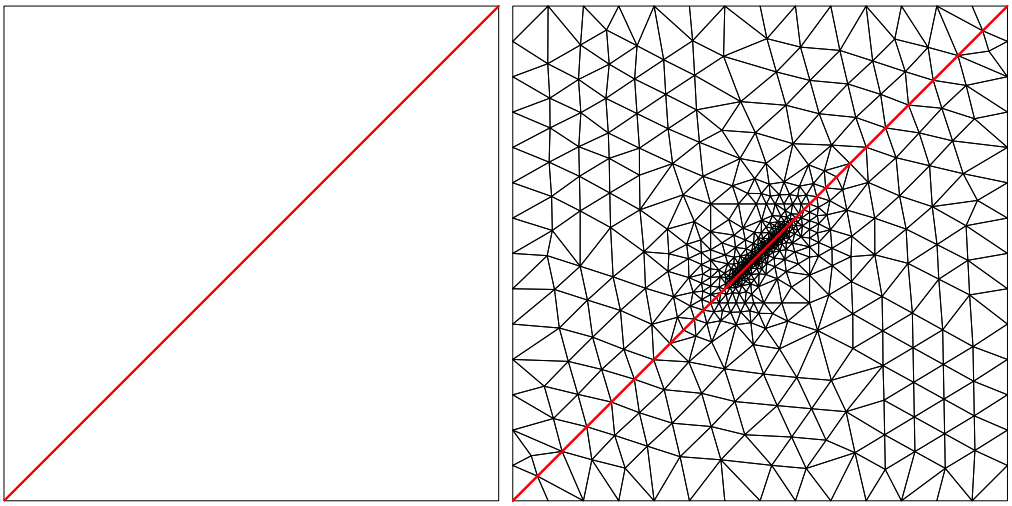

(a) Simple mesh **(b)** Refined mesh

Figure 4.24: Unstable shear-compression example with a 45º inclined interface. (a) Simple mesh and (b) refined mesh.

mesh have been plotted together with the inviscid results previously obtained in Section 4.4.3 using elasto-plasticity with Arc-Length and showing a clear snap-back (curves "EP-AL-M", in dashed red lines) and VPR showing a vertical fall from the peak to meet again the previous curve after the snap-back (curves "VPR-M", in dashed blue lines and curves "VPR-HM", in black lines). The overall figure shows that: (1) the VPR approach is successful in bypassing the mechanical instability also in a coupled H-M calculation, (2) the same calculations performed with the one-element mesh and the refined mesh are coincident, which could be expected given the uniform fields in this case, but it is reassuring in view of the calculations to be performed in following sections with refined meshes and non-uniform fields; and (3) the VPR-HM curves follow exactly their mechanical only counterpart in the elastic ascending branch and during the vertical fall, but at the end of it they land on a slightly lower residual curve. Similar to the previous example, this difference may be interpreted by the effect or fluid pressure that reduces effective normal stress on the interface and therefore also its shear capacity, leading to a lower curve in the H-M calculations. However, the effect is less pronounced in this case than in previous example due to the smaller magnitude of the fluid pressure prescribed ($0.1\,MPa$ instead of $1\,MPa$, ten times lower).

In Figure 4.26 the evolution curves of visco-plastic energy dissipation with physical time, are represented with the aim of identifying the time of occurrence of the instability. As in previous subsection, two curves are represented, one for the total visco-plastic dissipation W^{VP}_{Total}, and the

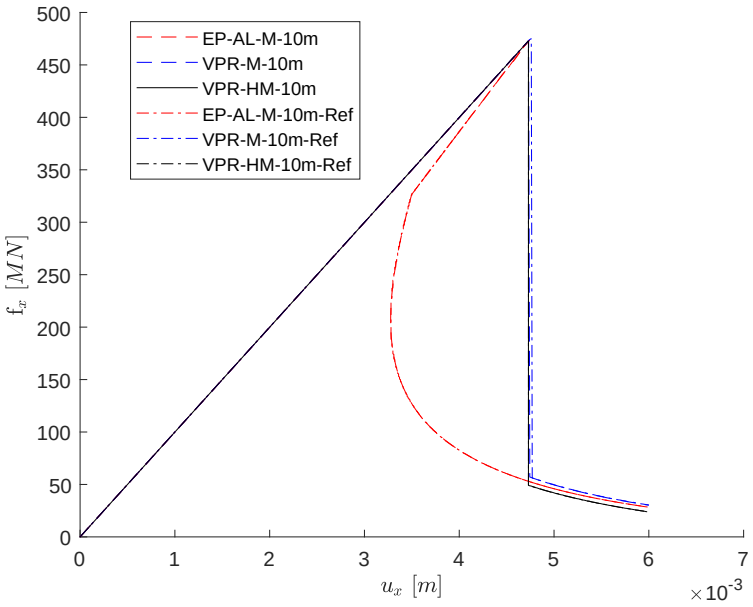

Figure 4.25: Horizontal force-horizontal displacement curves for the domain of ten square meters, discretized using a simple mesh and using a refined mesh.

other for the visco-plastic dissipation calculated using the stresses projected on the loading surface $\overline{W}^{VP}_{Total}$. As it can be seen in the Figure 4.26, the curves are both zero until the peak of the load-displacement curve and then at $t = 0.1\,s$ make a jump to two different values, therefore signaling clearly that the instability has emerged at that time, and providing a quantitative magnitude of the energy dissipated by the VP model to stabilize the event, $W^{Viscous} = W^{VP}_{Total} - \overline{W}^{VP}_{Total}$.

In Figure 4.27, the evolution of the fracture dissipation W^{VP}_{Frac} (history variable of the VP model) is represented as a function of the fictitious time developing within the load increment of the instability (left diagram), and similar curves are plotted for magnitudes W^{VP}_{Total} and $\overline{W}^{VP}_{Total}$.

This example has been also used to verify additional relevant aspects of the FEM approach used, such as the size/scale effect of the absolute model dimensions.

It is well known that the use of zero-thickness interfaces with a constitutive law based on fracture mechanics principles (as the one used in this thesis), automatically brings size-scale effect into the overall FEM representation, effect that otherwise (with only continuum elements in the mesh) would not be present except is special regularization techniques would be used (Crusat, 2018). To show that size/scale effect is embedded in the present model, the mechanical analysis of this example (no fluid flow) is repeated by scaling down homotetically the overall mesh by a factor 2 and a factor 4, that is, reducing the domain dimensions from 10 to 5 and then 2.5 m. For each of

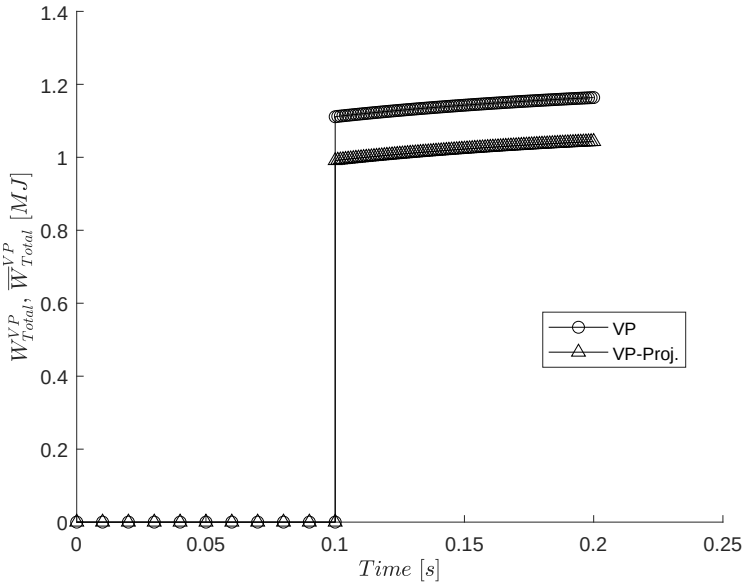

Figure 4.26: Evolution with physical time, of the total VP dissipation calculated with total VP stresses, W^{VP}_{Total}, and with the stresses projected on the loading surface, $\overline{W}^{VP}_{Total}$.

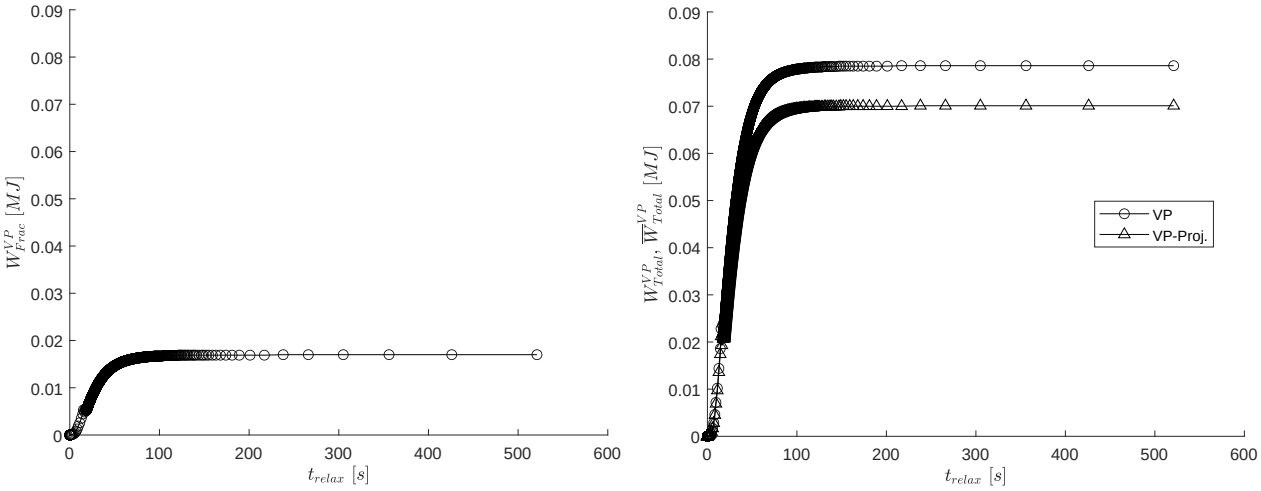

(a) W^{VP}_{Frac} **(b)** W^{VP}_{Total}, $\overline{W}^{VP}_{Total}$

Figure 4.27: (a) Fracture dissipation and (b) total dissipation obtained with the visco-plastic stress and with projected stresses.

those additional dimensions, the same three analysis as previously shown in Figure 4.25 have been carried out.

The following figures show the results of those calculations in terms of horizontal force-horizontal

displacement (Fig. 4.28) and horizontal stress-horizontal displacement (Fig. 4.29) along the left side of the square domain. Note that fracture initiation along the interface is subject to the same stress criterion in all cases, and therefore also the peak value of the horizontal stress in the continuum and the horizontal stress acting along the vertical side of the domain, should be the same for the three geometries (Fig. 4.29). In contrast, the total horizontal force should increase as the model size also increases, as observed in Figure 4.28. From the viewpoint of deformations, the displacement applied is the same for all three cases but the dimensions are different, which means that strain will be larger for the smaller domain sizes. All of the above leads to the curves in Figures 4.28 and 4.29, which show the following conclusions:

1. In terms of stress-displacement diagrams, larger domains lead to softer elastic stiffness, but same peak stress values.

2. In terms of force-displacement curves, the larger domains lead to same stiffness but higher peak loads.

3. And, most important for the purpose of the present thesis: the larger the domain the more pronounced the snap-back and, therefore, the vertical drop of the VPR model to bypass the snap-back will also be more marked, which may be associated to larger amount of energy released during the instability.

The latter conclusion agrees well with the arguments for mechanical size/scale effect in brittle failure, based on the so called "dimensional mismatch" inherent to many physical processes including quasi-brittle fracture (Bažant and Planas, 1998). The argument is based on assuming similar domain geometry (including fracture length), same material parameters (including fracture energy), and same stress state, but different domain sizes. In that context the elastic energy available to be released, that corresponds to a certain region around the crack extension, grows with the cube of the size (in 3D, or area in 2D) while energy expenditure for fracture propagation, which is per unit area of new crack, will grow only with the square of the size (in 3D, or linearly in 2D) Therefore there is a dimensional mismatch which causes that, for the same stress conditions and similar geometries, the availability of energy per unit area of new crack is proportionally larger for the larger geometries.

Finally, Table 4.5 shows the values of all individual components of the energy dissipation and storage balance for the present example at the end of the simulation considering both simple and refined meshes, including the released energy ($W^{Viscous} = W^{VP}_{Total} - \overline{W}^{VP}_{Total}$). As in previous cases,

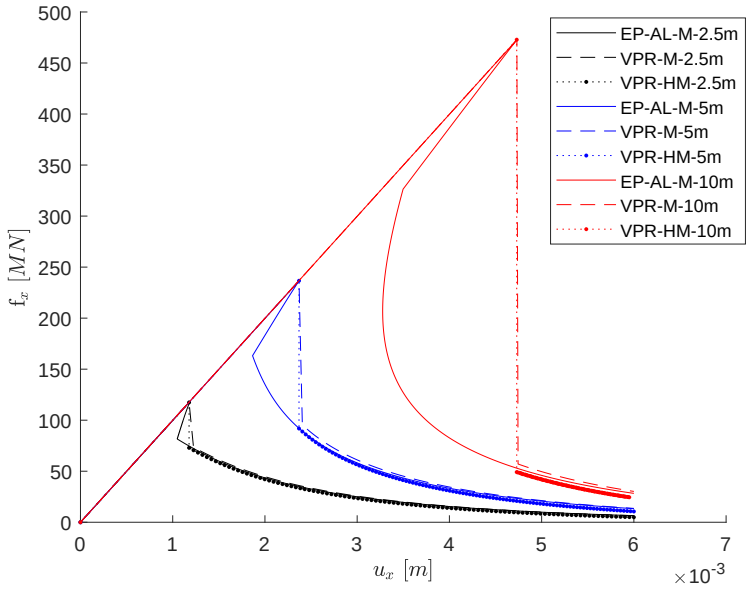

Figure 4.28: Horizontal force-horizontal displacement curves for different dimensions of the domain. Simple mesh.

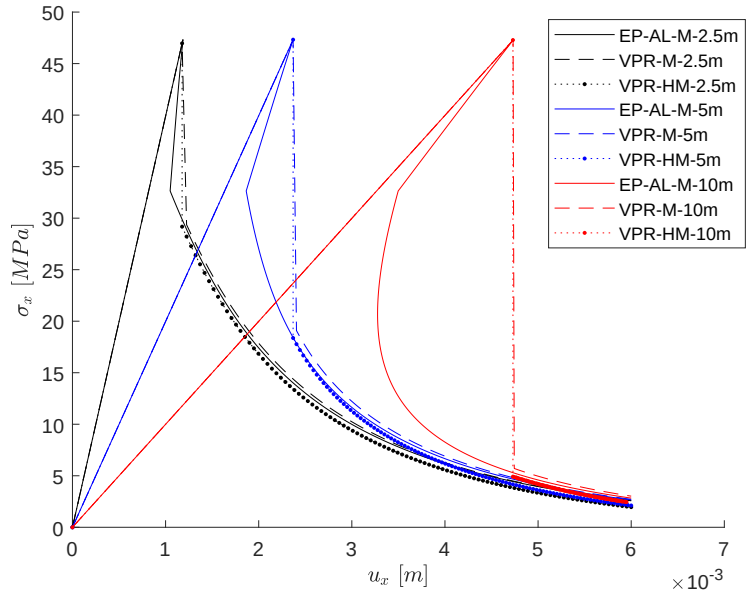

Figure 4.29: Horizontal stress-horizontal displacement curves for different dimensions of the domain. Simple mesh.

it is reassuring to verify that the overall error in the energy balance obtained with both kind of meshes is lower than 1%.

	Simple mesh results (MJ)	Refined mesh results (MJ)
W_{eC}	$2.7628 \cdot 10^{-3}$	$2.6080 \cdot 10^{-3}$
W_{eJ}	$1.9536 \cdot 10^{-6}$	$1.8441 \cdot 10^{-6}$
W^{VP}_{Frac}	$2.5890 \cdot 10^{-1}$	$2.5942 \cdot 10^{-1}$
W^{VP}_{Fric}	$7.8460 \cdot 10^{-1}$	$7.8585 \cdot 10^{-1}$
$W^{Viscous}$	$1.2080 \cdot 10^{-1}$	$1.2081 \cdot 10^{-1}$
W_{FC}	$4.2917 \cdot 10^{-5}$	$1.4417 \cdot 10^{-4}$
W_{Dil}	0.0	0.0
W_{Int}	1.1671	1.1688
W_{Ext}	1.1613	1.1628
% Error (Ext.-Int.)	0.499%	0.518%

Table 4.5: Compilation of all work terms obtained as a result of calculating the unstable shear-compression sliding example with 45^{o} inclined interface considering both simple and refined meshes. Instability induced by imposing fluid pressure.

4.6.2 Instability induced by fluid injection with prescribed discharge

Inducing an instability imposing a fluid flow injected at a single injection point requires the use of a refined mesh such as the one shown in the previous section (Fig. 4.24, right diagram). The example described in the present section, consists of that same mesh geometry considering both quadratic continuum and interface elements.

This example tries to simulate an injection process at a certain depth ($1000\,m$) and, for this purpose, an initial stress state needs to be defined. The vertical stress is assumed equal to the self-weight of the column of material above the domain to study. Therefore, considering a rock density value of $\rho_s = 2500\,kg/m^3$ which implies a specific weight of $\gamma_s = 24500\,N/m^3$ and the corresponding vertical stress at $1000\,m$ depth is $\sigma_y = 24.5\,MPa$. In the same way, the existing initial fluid pressure at $1000\,m$ depth is $p_f = 9.7\,MPa$ (considering $\rho_w = 997\,kg/m^3$).

On the other hand, the horizontal stress value has been selected in such a way that the interface elements are subject a stress state close to the peak of resistance of the model. To determine that horizontal stress value requires knowing vertical stress and the set of parameter values which define the constitutive behavior of interfaces (detailed below) and enforcing that the yield surface defined

by equation (2.56) is equal to zero ($F = 0$). As a result, the horizontal stress which satisfies this condition is $\sigma_x = 116.096\,MPa$.

The domain of this example has dimensions $25\,m$ x $25\,m$ and is divided in half by its diagonal, along which a line of zero-thickness interface elements are inserted. The injection point is located in the middle of the fracture plane (center of the domain) (Fig. 4.30). In order to consider heterogeneities that may exist along a natural fracture plane (for instance if that plane crosses different geological layers), three zones with different sets of interface properties have been defined with a symmetrical distribution side and side of the injection point. The main difference between the mentioned sets of parameters are the cohesion and friction angle values. In the zone closest to the injection point both cohesion and friction angle are the lowest and they progressively increase in the zones which are farer from the injection point and closer to the domain boundary. The material properties values assumed are:

- The continuum material is assumed linear elastic: $E = 1.5 \cdot 10^4\,MPa$ and $\nu = 0$.
- The parameters used for the interface constitutive models: normal and tangential elastic stiffness $K_N = K_T = 10^7\,MPa/m$, friction angle $\tan\phi = 0.7$, tensile strength $\chi = 0.00001\,MPa$, fracture energy mode I $G_f^I = 10^{-5}\,MPa \cdot m$, fracture energy mode IIa $G_f^{IIa} = 10^{-4}\,MPa \cdot m$, sigma for which dilatancy vanishes $\sigma_{dil} = 20\,MPa$ and the viscosity $\eta = 10^4\,MPa \cdot s$. Regarding the cohesion, the values used are $c_L = 3.7\,MPa$, $c_{L_n} = 5.0\,MPa$ and $c_{L_f} = 10.0\,MPa$, where the subscripts indicate the corresponding section of the fracture in which each cohesion value is defined (see Figure 4.30). Additionally, in order to increase the resistance of the L_n and L_f sections the friction angle also takes progressively increasing values for each zone as it gets farer from the injection point and closer to the boundary, from 35^{o} near the injection point to 40^{o} and 43^{o} in L_n and L_f respectively.

Moreover, the hydraulic properties are:

- The fluid injected is assumed to be water, with parameters: density $\rho = 0.997 \cdot 10^{-3}\,kT/m^3$, fluid bulk modulus $K^f = 3000\,MPa$ and viscosity $\mu = 10^{-9}\,MPa \cdot s$.
- The hydraulic properties of continuum: hydraulic conductivity $K_{\text{C}} = 10^{-6}\,m/s$, skeleton compressibility $K^s = 3600\,MPa$, Biot's coefficient $\alpha_{Biot} = 1.0$.
- The hydraulic properties of interfaces: longitudinal transmissivity according to cubic law ($T_L = \gamma^f r_N^3/(12\mu)$, specified in Section 4.2.2.4), with minimum value $T_{L,min} = 10^{-14}\,m^2/s$, and transversal conductivity $K_t = 1.0\,s^{-1}$.

Some comments are in order with respect to the loads and boundary conditions shown in Figure 4.30. First these conditions must allow the movement of the upper wedge while keeping the lower wedge fixed and, second, the distributed loads applied on the top and left faces of the domain are meant to represent the initial stress state applied over the entire domain.

The procedure to generate the instability is quite simple because the initial stress state is defined already at critical (failure) conditions: once the initial stress has been applied, a new load step is defined consisting of a fluid injection applied at the central point of the interface line with final discharge value $Q = 0.002\, m^3/s$. This discharge value is prescribed progressively ("ramp" from zero to Q) during a short time increment $\Delta t = 0.01\, s$. As the injection progresses, the increase of pore pressure leads to a decrease of the effective stresses in the vicinity of the injection point and the instability is triggered. The motivation for defining such a short time increment for the ramp ($\Delta t = 0.01\, s$) and then splitting it into 10 increments, is to be able to detect more precisely when the instability occurs.

The results obtained are depicted in Figures 4.31 to 4.39. In Figure 4.31, the evolution with physical time is represented of the shear stress in the neighborhood of the injection point. The curve shows a sharp drop of the shear stress in the third increment. This may be a sign indicating an instability. In order to confirm this, the magnitudes of the total visco-plastic work W^{VP}_{Total} and the total projected visco-plastic work $\overline{W}^{VP}_{Total}$ have been represented as a function of injection time (right diagram in Fig. 4.32). As it can be seen in the figure, initially the two curves are coincident, but in the third increment they exhibit a jump of different magnitude. As it has been already pointed out in previous sections, this has been proposed to be an indicator of instability, which would confirm that in this example the instability takes place in time increment No. 3 of the loading sequence.

In order to reconfirm that the criterion previously established for identifying the instability is also valid in an injection case, the calculation has been repeated for a stable case and a similar diagram has been represented. The new, stable case has been obtained with the same parameters except the fracture energy values that have been increased various orders of magnitude to $G^I_f = 1.0\, MPa \cdot m$, and $G^{IIa}_f = 10.0\, MPa \cdot m$. With these values of the fracture energies, the interface should behave as elastic-perfectly visco-plastic, i.e. no softening. And, effectively, when the evolution of the energy dissipation terms W^{VP}_{Total} and $\overline{W}^{VP}_{Total}$ are plotted (left diagram of Fig. 4.32), the resulting curves turn out smooth (no jumps) and identical, which is interpreted as this case not exhibiting any instability and, by comparison, reconfirming that curves in Figure 4.32-(b) do exhibit the instability taking place in increment No.3.

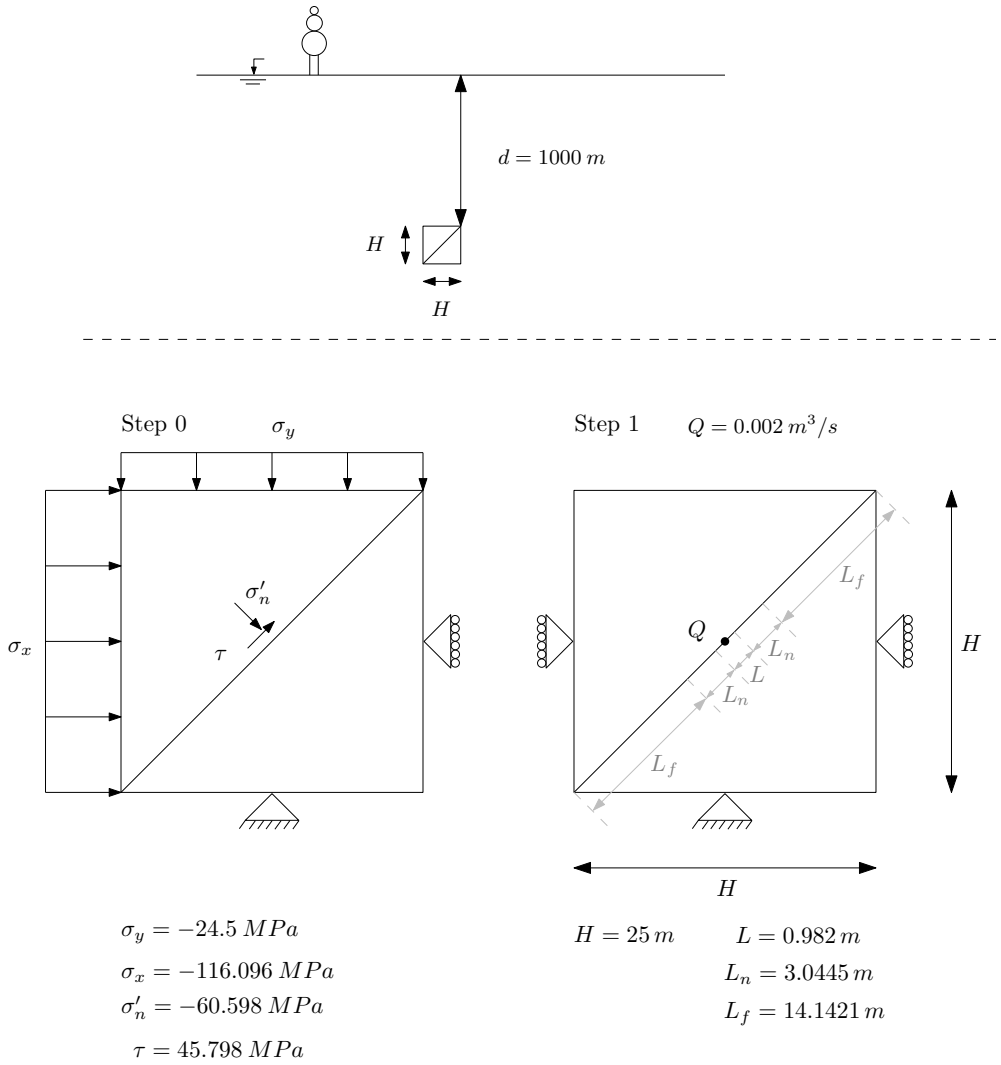

Figure 4.30: Geometry and boundary conditions of the H-M shear-compression unstable case with instability is induced by fluid injection.

A second point worth to be discussed is the magnitude of the difference between the two curves of Figure 4.32-(b). The FE model shows that the length affected by the instability constitutes 2.8% of the total length of the interface line that makes up the entire fracture, therefore the difference between the curves shown in the graphic 4.32-(b) is also small.

On the other hand, energy balance has been also checked in this example. The effects of both the initial stress state and the fluid injection ($W_F = (\overline{QP})\Delta t$ measured at the injection point, with $\overline{QP}$ the average value of the product QP during the increment) have to be considered as an

external work and this must coincide with the work due to the remaining final stress state plus the work due to the different internal dissipation mechanisms. Therefore, as can be seen in Table 4.6 the energy balance is fulfilled.

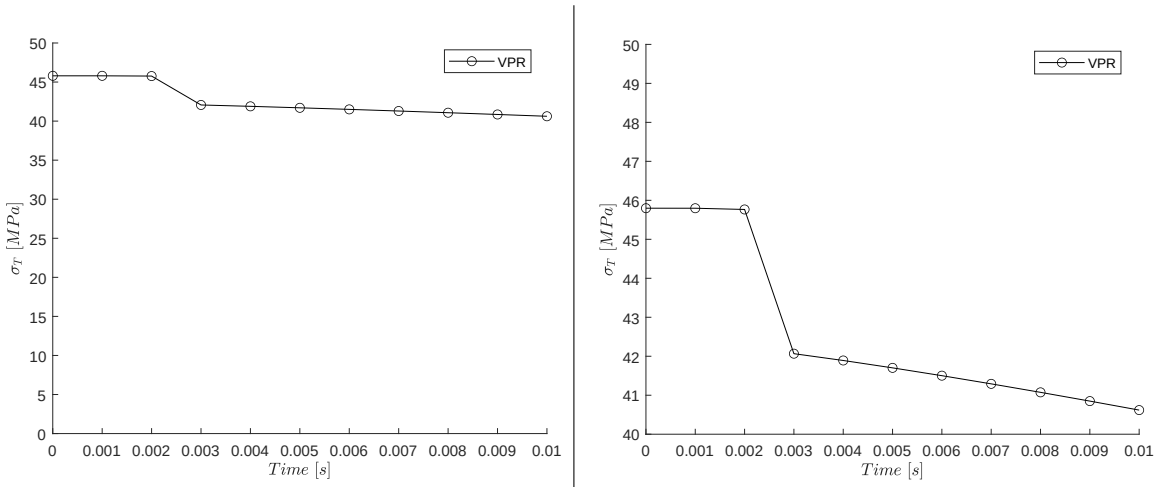

(a) General representation **(b)** Detail representation

Figure 4.31: (a) Representation of the shear stress- injection time in the injection point located in the center of the fracture. (b) The same representation giving more detail of the moment when the instability occurs.

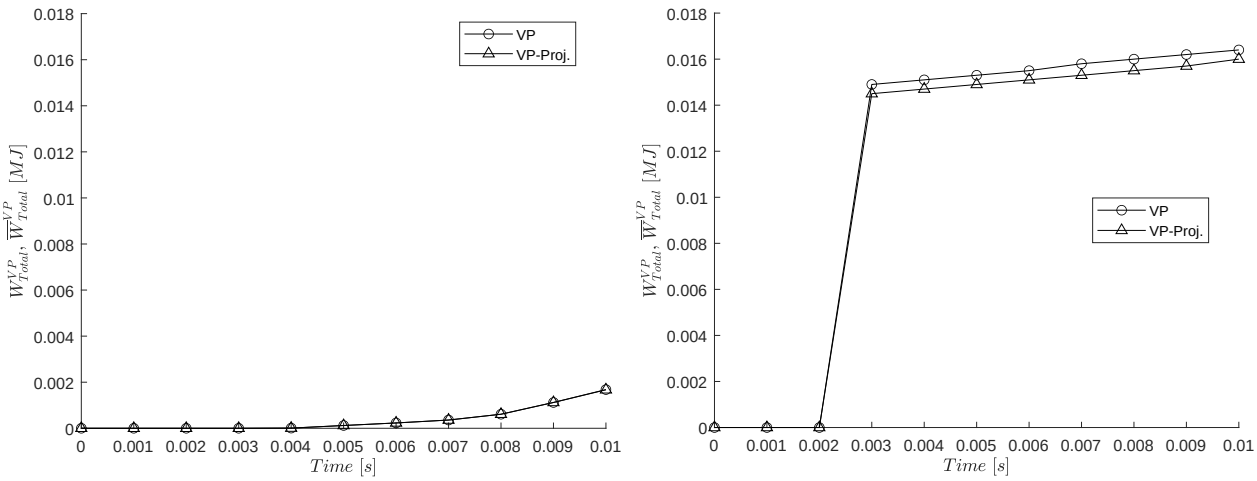

(a) Stable case **(b)** Unstable case

Figure 4.32: Representation of the total visco-plastic work and total projected visco-plastic work with time injection.

	W_{Ext} (MJ)	W_{Int} (MJ)
W_{eC}	$2.4040 \cdot 10^{+2}$	$2.4038 \cdot 10^{+2}$
W_{eJ}	$1.0199 \cdot 10^{-2}$	$1.0174 \cdot 10^{-2}$
W^{VP}_{Frac}	$--$	$1.2234 \cdot 10^{-4}$
$W^{Viscous}$	$--$	$4.5158 \cdot 10^{-4}$
W_{Fric}	$--$	$1.5849 \cdot 10^{-2}$
W_{FC}	8.4790	8.4767
W_F	$3.0208 \cdot 10^{-4}$	$--$
$\sum$	$2.4889 \cdot 10^{+2}$	$2.4888 \cdot 10^{+2}$
% Error (Ext.-Int.)	0.0016%	

Table 4.6: Compilation of all work terms obtained as a result of calculating the unstable shear-compression sliding example with 45^{o} inclined interface considering both simple and refined meshes. Instability induced by imposing fluid pressure.

These results are very important because they demonstrate the ability of the VPR methodology proposed in this thesis to calculate unstable cases, establish criteria to detect an instability and quantify the energy released in these processes. In turn, it is envisaged that in futures research this released energy may be related to the magnitude of the subsequent earthquake.

Aside from the instability indicators already discussed, the results of this example may be represented in conventional diagrams or contour plots, which is done in Figures 4.33 to 4.39.

Figure 4.33 depicts the tangential relative displacement (slip) along the discontinuity, both in the initial state (left diagram, no slip) and in the final state after the injection ramp, in which a highly localized zone may be observed along the part of the discontinuity zone with lowest mechanical parameters.

Figure 4.34 depicts the evolution of the elastic energy density in the continuum, with the uniform distribution that corresponds to the initial stress state on the left diagram, and the resulting state after the end of the injection ramp. As shown in the figure, a reduction in elastic energy is observed around the slipped area. The area affected by the instability evolves from an energy value of $0.38464\,MJ$ in the initial state to approximately $0.31\,MJ$ in the final state. This energy differential is invested in dissipation mechanisms mentioned in this chapter including the energy released. Moreover, note that two energy accumulation regions can be seen at both ends of the

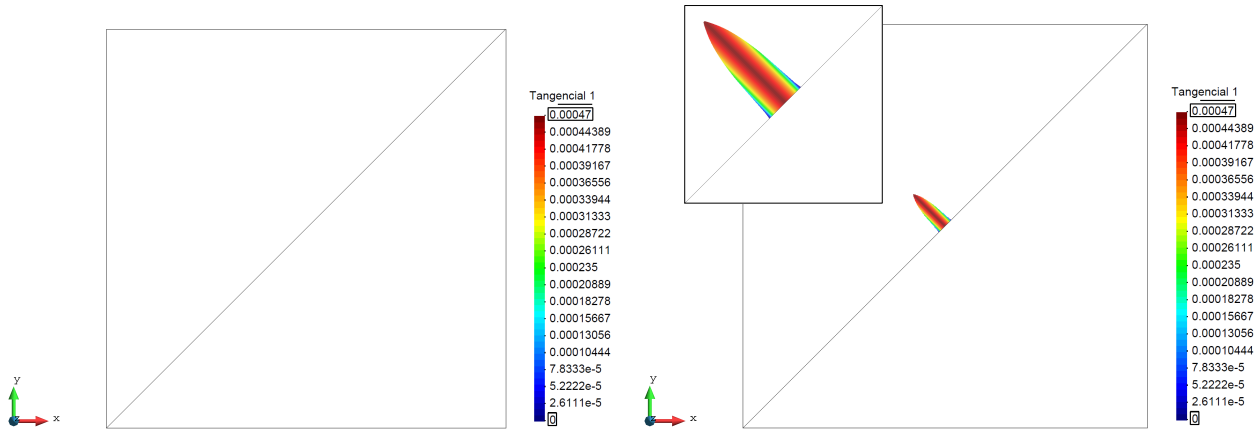

(a) Initial state **(b)** Final state

Figure 4.33: (a) Tangential relative displacement along the discontinuity in the initial state. (b) Tangential relative displacement along the discontinuity in the final state.

slipped area. It can be explained by the fact that those regions represent transition points in the discontinuity in which the interface resistance goes from the weakest central zone to a more resistant outer zone.

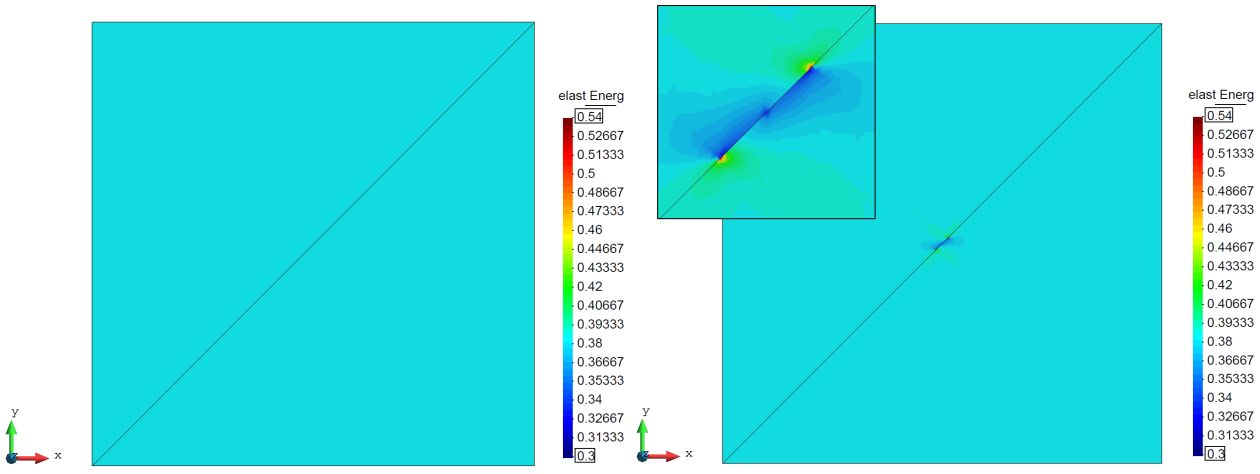

(a) Initial state **(b)** Final state

Figure 4.34: (a) Continuum elastic energy in the initial state. (b) Continuum elastic energy in the final state.

Figures 4.35 and 4.36 represent the evolution of horizontal and vertical effective stresses of the continuum from initial to final state. In the figure it can be seen that horizontal effective

stresses experience a decrease in their maximum values after the fracture process (σ_x decreases from $-106.4\,MPa$ to $-95.399\,MPa$) (Fig. 4.35), while vertical effective stresses increase its maximum values (σ_y increases from $-14.8\,MPa$ to $-25.785\,MPa$) (Fig. 4.36). The shear-compression fracture mechanism, with horizontal stress much greater than the vertical stress, produces a sliding of the upper part of the central region (surrounding the injection point) in the positive X and Y directions obtaining as a result the evolution of effective stresses mentioned above.

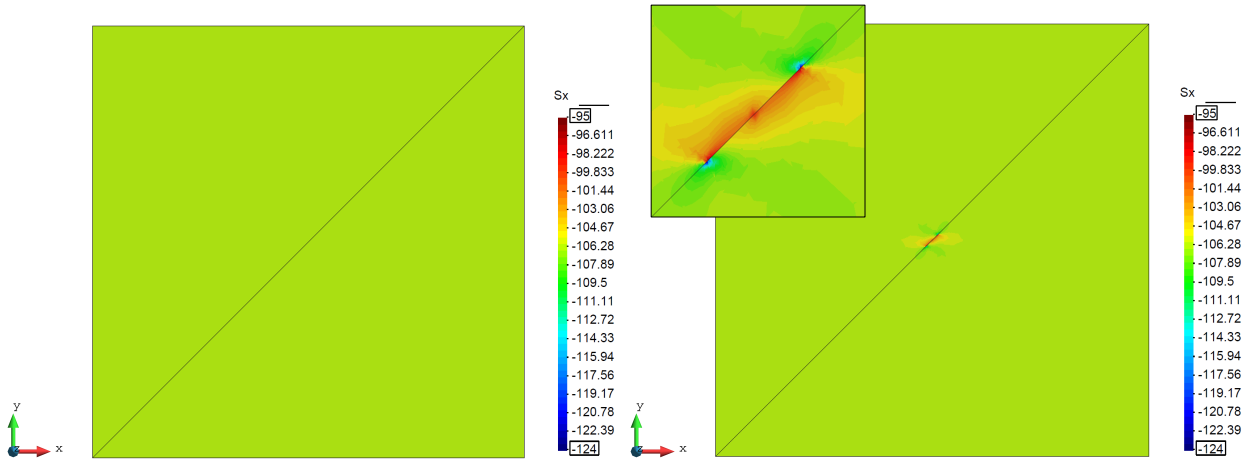

(a) Initial state **(b)** Final state

Figure 4.35: (a) Continuum horizontal effective stress in the initial state. (b) Continuum horizontal effective stress in the final state.

Figure 4.37 depicts the interface internal variable defined by the fracture dissipation divided by the parameter fracture energy in mode I (W^{cr}/G_f^I). The plot shows that the fractured area corresponding to the interface section with lowest parameters becomes completely degraded when the instability occurs. As the legend shows, almost all this area achieves a value of $W^{cr}/G_f^I = 10$ which is the maximum since, according to the input parameters used, $G_f^{IIa} = 10 \cdot G_f^I$. This means that the part of the interface which has experienced slip, has undergone the maximum level of degradation which is possible in this constitutive model.

Normal and shear effective stress distribution along the discontinuity are represented in Figure 4.38 and Figure 4.39, respectively. In the initial state, normal effective stress has a homogeneous distribution along the discontinuity with the value corresponding to the initial stress state ($\sigma_N = -60.598\,MPa$, the minus sign indicates compression) while, in the final state, the stress distribution shows a minimum at the injection point ($\sigma_N = -58.011\,MPa$) due to the fluid pressure effect. In the same way, shear stress evolves from the initial homogeneous distribution with a value of

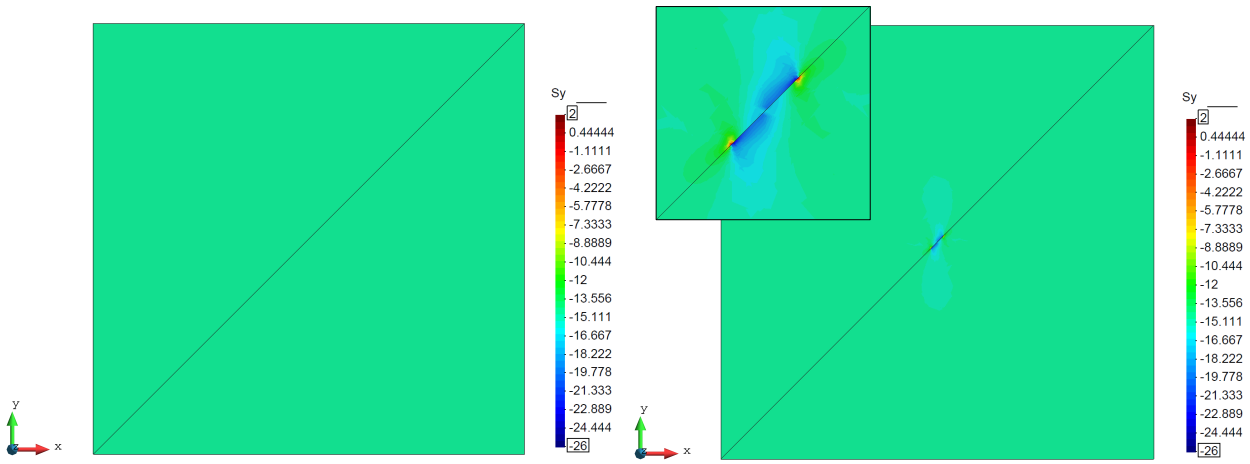

(a) Initial state **(b)** Final state

Figure 4.36: (a) Continuum vertical effective stress in the initial state. (b) Continuum vertical effective stress in the final state.

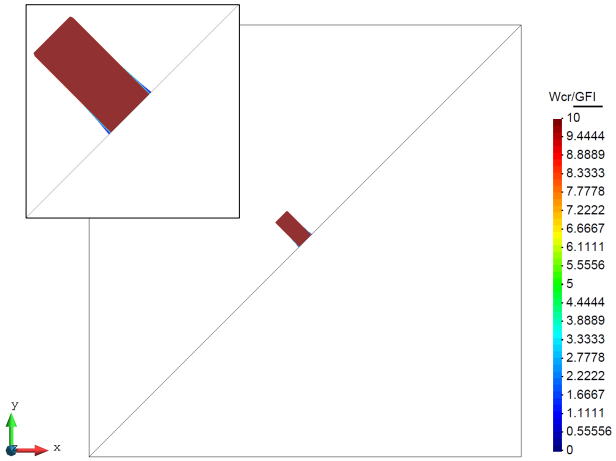

Figure 4.37: Distribution of W^{cr}/G_f^I along the discontinuity

$\sigma_T = 45.798\,MPa$, to a more complex distribution in the final state, which includes a maximum just at the limit of the slip zone, and a reduction in the area affected by fracture slip reaching a minimum at the injection point itself ($\sigma_T = 40.619\,MPa$).

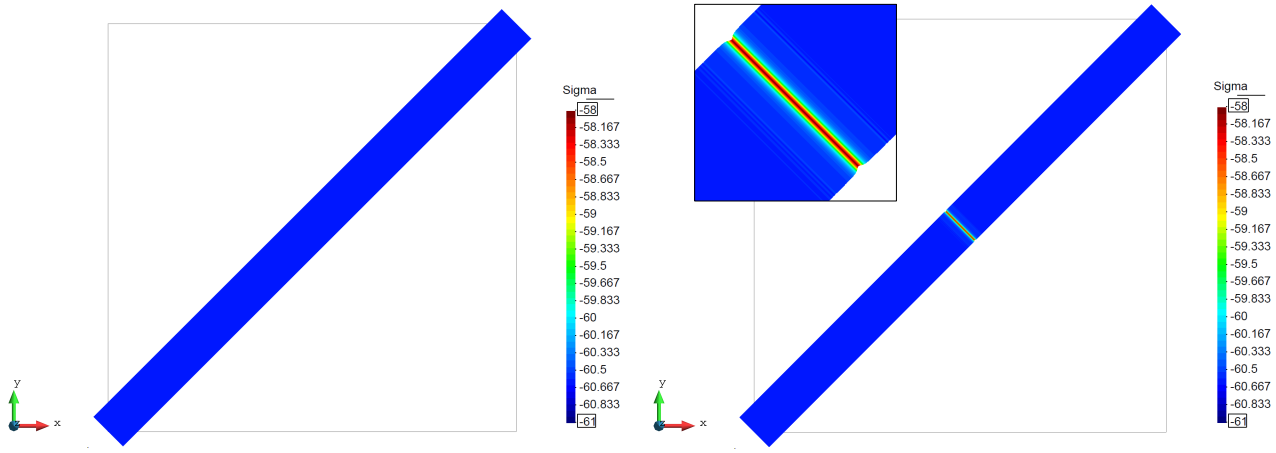

(a) Initial state **(b)** Final state

Figure 4.38: (a) Normal effective stress along the discontinuity in the initial state. (b) Normal effective stress along the discontinuity in the final state.

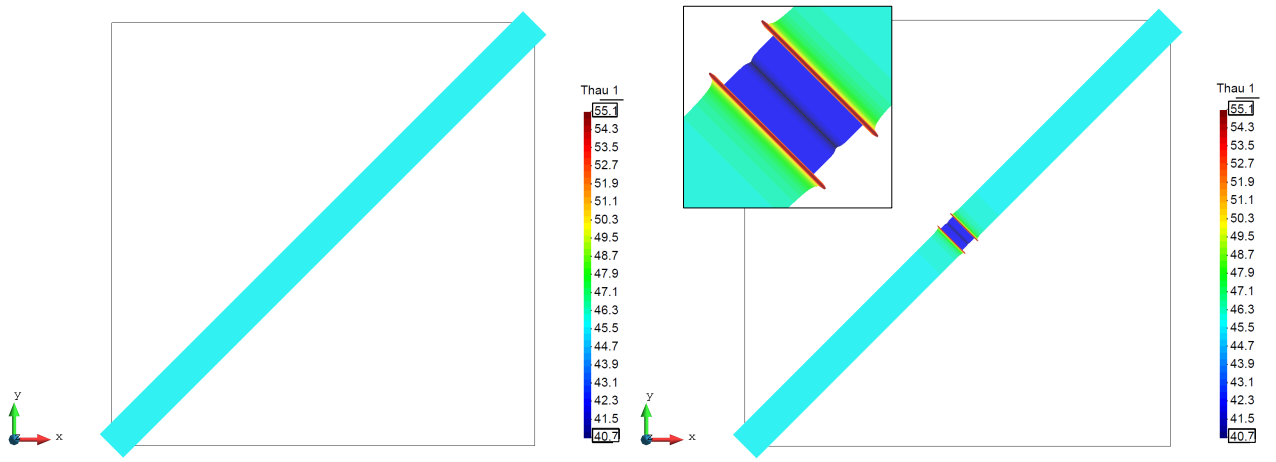

(a) Initial state **(b)** Final state

Figure 4.39: (a) Shear stress along the discontinuity in the initial state. (b) Shear stress along the discontinuity in the final state.

Chapter 5

Summary, conclusions and future research

Contents

5.1 Summary

The main objective of this thesis was to propose a procedure to tackle fault reactivation problems from a quasi-static point of view, and therefore without the need to address the full dynamics problem. In order to accomplish this target, a methodology based on visco-plasticity (Chapter 2) combined with different numerical iterative strategies (Chapter 3) has been proposed to solve the mechanical or hydro-mechanical problem including the case of mechanical instabilities. In this sense, a strategy based on various energy indicators has been devised to identify the occurrence of such instabilities, which in practice may be associated to seismic reactivation events (Chapter 4). Moreover, the strategy developed it is not only capable of signaling the occurrence of the instability but also quantifying the energy released during such event, which is an additional important achievement.

As a starting point, in Chapter 2, an energy-based softening visco-plastic model of the Perzyna type for zero-thickness interface elements has been developed, using a stress-prescribed integration algorithm in a FE framework. This model is an extension of the perfect visco-plastic model for interfaces previously developed by Aliguer et al. (2017) which has been adapted to hardening and softening. In turn, these visco-plastic versions of the constitutive law for interfaces are based on the original elasto-plastic fracture-based interface constitutive law (Carol et al., 1997). An important finding of the new extended version of the visco-plastic interface constitutive law is that the convenient *m-AGC* tangent operator proposed in the original perfectly visco-plastic model, is maintained also for the new Hardening/Softening version. From that expression, some limit cases have had to be considered and limit expressions evaluated in order to avoid numerical problems.

The visco-plastic approach was required as a previous step to the development of instability control methods described in Chapter 3. First of all, a new Indirect Displacement Control method based on the visco-plastic dissipation was proposed (IDC-Wvp) and second, a Visco-plastic Relaxation (VPR) was rethought and implemented in the FE code of the research group. And is in the context of the instability control methods when it becomes more clear why using visco-plastic constitutive models. Time is a parameter which, by physical definition, must be always positive and monotonously increasing. If inviscid constitutive models are used for the analysis, the strategies to overcome an instability of the snap-back type, such as AL or IDC, in general may imply a temporary decrease of the load factor and therefore be incompatible with analysis in which the loading factor is directly or indirectly related to physical time. In contrast, strategies based on visco-plasticity have been shown to be able to bypass the instability without the need to decrease the load factor, and therefore they would avoid this conceptual problem.

Regarding instability control methods, the first proposal of this thesis has been the IDC-Wvp strategy. As presented in Chapter 3 and its corresponding appendices, this method has required considerable developments since, once more, some limit cases of the derivative terms involved in the procedure had to be considered. As a result, IDC-Wvp was successfully tested by calculating some simple verification examples which correspond to academic examples that represent different fracture mechanisms that can occur in a geomechanical scenario.

The mentioned verifications were performed in purely mechanical cases but, when coupled hydro-mechanical cases were considered, it was realized that the IDC-Wvp strategy was not well adapted to hydro-mechanical problems. The reason for that has to do with the time variable. As already explained, IDC-Wvp uses the physical time as a variable of the visco-plastic approach to overcome the instabilities and therefore this time needs to be free to evolve for that purpose, but

hydro-mechanical coupled examples require physical time being linked to the fluid flow, i.e. to define the fluid injection time or the amount of time that fluid pressure is going to be applied. This creates a conflict, since the same time parameter cannot be used simultaneously in two different processes. This conflict may be overcome with Visco-plastic Relaxation (VPR) since it involves two different types of time: physical and fictitious. In VPR, physical time is used to define the characteristics of fluid injection or pressure while fictitious time is reserved to visco-plasticity. Another advantage of this method is the automatic control on the fictitious time increment. This method has been also verified by running the same validation examples as with IDC-Wvp. All developments mentioned above have been implemented in the Finite Element code of the research group, which has the capability of solving purely mechanical and also hydro-mechanical problems.

An essential part of this thesis has also been the energy balance assessment described in Chapter 4. Identifying the different energy storage and dissipation terms that may be involved in both purely mechanical and hydro-mechanical cases, has made it possible to verify the energy balance in each example. Moreover, a criterion based on energy dissipation has been proposed to differentiate between stable and unstable fracture propagation cases, and identify the occurrence of mechanical instabilities that may be associated to seismic reactivation events. In the case of instability, the methodology developed also leads to a quantification of the amount of energy released in an instability which is an essential achievement since it could be directly related to the magnitude of the earthquake that would be generated.

In this context, once the criterion to distinguish between stable and unstable fracture propagation was well established, hydro-mechanical coupled examples in which instability is induced by the effects of the fluid have been analyzed. These include cases with prescribed pressure along the interfaces, and with prescribed discharge at a point of fluid injection. In the last example presented, the discontinuity has been assumed to have different zones with different properties, as it would correspond for instance to a fracture intersecting various geological layers. In the case analyzed, the injection point is located within the weakest of those zones and the unstable propagation reaches the limits of the zone, stopping at the points of transition to higher strength zones.

5.2 Conclusions

From the work developed and the results obtained, the following conclusions can be drawn:

5.2.1 General conclusions

- A general procedure based on FEM with interface elements equipped with a fracture-based visco-plastic constitutive model and the VPR approach has been developed for identifying the occurrence of mechanical instabilities which may be associated to fault reactivation events caused by either human activities or natural factors.

- The procedure developed not only seems capable of identifying those events, but also offering a quantitative estimate of the energy released during the event, which may be eventually related to the seismic event magnitude.

- The studies on visco-plasticity with hardening and softening which have been needed to develop the procedures above, have also led to additional potentially useful results in various areas such as the new *m-AGC* tangent stiffness tensor, and a new IDC iterative strategy based on a target of visco-plastic energy dissipation.

- The proposals raised in this thesis can serve as a basis for new developments such as considering additional energy terms, for example, those derived from thermal effects which are involved in fault reactivation processes, or suggest technical recommendations in order to prevent that an instability occurs and avoid damage.

5.2.2 Specific conclusions

Specific conclusions with regard to visco-plasticity (Chapter 2)

- The new energy-based softening visco-plastic constitutive law for interface elements which has been proposed using a stress-prescribed integration algorithm in a FE framework, is capable of representing well the interface behavior showing very good agreement between the visco-plastic response and the elasto-plastic response in the inviscid limit.

- A closed-form solution of the yield function evolution at a point of the interface as a function of time has been developed as a necessary ingredient of the *m-AGC* tangent operator. This is a great advantage of this approach because it eliminates the need of inverting the compliance tensor numerically at each Gauss point for each iteration, as is common for some existing integration schemes for visco-plastic models. This tangent operator may be considered an extension of the similar one obtained with the perfect visco-plastic model for interfaces previously developed by Aliguer et al. (2017).

- Also, the indeterminations of the Hardening/Softening modulus H'' which is part of the m-AGC tangent expression have been analyzed in order to avoid numerical problems in limit cases and provide a robust methodology.

- The stress-driven integration algorithm proposed in this thesis is capable of evaluating all visco-plastic cases that can occur in a time increment. All possible stress trajectories which lead to cross (or not) the yield surface are considered and this contributes to give robustness to the constitutive law.

- The methodology proposed in this chapter has been implemented in the FE code of the research group and adapted to the hydro-mechanical formulation in order to calculate hydro-mechanical problems. Different H-M cases have been run with satisfactory results which ensure the proper functioning of the proposed methodology.

Specific conclusions with regard to iterative strategies (Chapter 3)

- The new Indirect Displacement Control (IDC) method based on the visco-plastic dissipation has been developed as a general method valid for any Hardening/Softening visco-plastic model, and then it has been specified for the analysis of an elastic continuum with zero-thickness interface elements governed by a visco-plastic constitutive model. This iterative strategy is successful in stable and unstable problems when physical time is used as a controlling magnitude that makes it possible to reach the inviscid equilibrium path after sufficient time has passed.

- In order to be more general, in the case of interface elements, two different approaches have been proposed such as the energy target of the method may be specified in terms of total dissipation or in terms of fracture dissipation. Developing this iterative strategy as general as possible makes it possible to calculate wider range of cases and choose the most optimal option in each case.

- The developments of the new IDC-Wvp method involve the previously mentioned closed-form solution of the yield function which implies the existence of indeterminations in some limit cases. All these indeterminations have been solved in order to avoid numerical problems and provide a robust iterative strategy.

- The Visco-plastic Relaxation (VPR) iterative strategy, has been implemented in the Finite Element code of the research group. An advantage of this method is that it implicitly introduces

a second type of time, the fictitious viso-plastic time, which is additional and independent of the physical time (or loading factor) already present in any non-linear calculation. Thanks to this implementation, it becomes possible to properly calculate stable and unstable cases in which the material behavior is inviscid, both in mechanical and hydro-mechanical problems.

- These iterative strategies combined with the energy-based softening visco-plastic model presented in Chapter 2 have been verified by calculating different simple academic examples which represent different geomechanical fracture mechanisms. The results show that the response obtained with all calculation strategies considering visco-plasticity proposed in this thesis (VP-NR, VP-IDC-Wvp and VPR) match in the long term the elasto-plastic response as was expected.

Specific conclusions with regard to the examples of application (Chapter 4)

- The methodology developed for instability detection has been tested in both mechanical and hydro-mechanical scenarios where the instability may be induced by mechanical loads or by the effects of the fluid respectively. The results obtained in all cases calculated considering both scenarios show that VPR analysis is capable of determining when the instability occurs and quantifying the energy released. These results seem consistent in all cases calculated which seems to indicate the validity of the method proposed in this thesis.

- Additionally, the results obtained with the last hydro-mechanical example where the instability is induced by imposing a fluid flow injected at a single point of the interface line show the evolution of all the problem variables such as the tangential relative displacement along the discontinuity, the elastic energy density in the continuum, the stress state in the continuum and along the interface, etc. thus providing an overview of the effects of the instability on both the continuum and the discontinuity. From those results it can be concluded that the instability is a phenomenon in which a reduction of elastic energy of the continuum around the slipped area provides the energy needed in the fracture and visco-plastic dissipation mechanisms taking place at the interface.

- When the instability occurs, the fracture is observed to propagate in a sudden way over the length of the weaker zone of the interface, and it only stops at the limits of this zone where the interface strength parameters are higher. Once the fracture is initiated, its propagation over the weak interface zone is uncontrollable, that is, even if the action that triggered the

instability, i.e. the fluid injection in this case, is stopped, the propagation will continue to the limits of the weak interface zone.

5.3 Future Research

This thesis has opened a wide range of possibilities of future research. The most relevant of them are highlighted below:

Relation between energy released and earthquake magnitude

As has already been mentioned, the methodology proposed in this thesis is capable to estimate the energy released in an unstable fault reactivation process. But the relevant information from the Engineering viewpoint would be the magnitude of the potential earthquake, and for this purpose it would be essential to relate the amount of energy released with the corresponding magnitude of the generated earthquake.

In this context, it is necessary to link both research fields Fracture Mechanics from which the energy assessment presented in this work is proposed and Seismology which relates the earthquake's released energy with seismic radiated waves. One way to do it may be considering the seismic approach following the Gutenberg-Richter magnitude-energy relation (Gutenberg and Richter, 1956).

Additionally, note that the energy approach presented in this work is evaluated in a 2D plane-strain scenario while earthquakes are 3D phenomena, therefore the effect of depth in Z direction has to be considered. It is assumed that in Z direction the slipped fault length must be the same as in XY plane. Therefore, the released energy calculated in the 2D scenario has to be multiplied by the slipped fault length in Z direction.

Going deeper in this research line requires to consider an earthquake as a complex energy conversion process. When an earthquake occurs, much of the available local energy is used to power the earthquake fracture growth, generating seismic waves which radiate outward and are detected by seismographs and producing heat. This last consequence leads to propose the following future research work.

THM coupling

It is well known that when two fault surfaces slide against other at fast slip rates, the asperities may reach temperatures in excess of 1500^{o}C, lowering the fault friction. Some experiments performed by Goldsby and Tullis (2011) revealed that in these situations heat is generated so quickly at the

contacts that temperatures can spike enough to melt most rock types associated with earthquakes. Note that the extremely high temperatures are due to the fact that there is simply no time for the heat to get difussed away from the heat source, which causes a decrease of the friction coefficient. Moreover, their experiments showed that the friction stays low as long as the slip rate remains fast and the friction immediately increases when slip slows down and there is enough time for heat to diffuse away.

Considering the importance of both the effect of heat itself as well as its influence in friction during an earthquake, it makes sense to evaluate these cases from a Thermo-Hydro-Mechanical coupling viewpoint. In this sense, the currently implemented methodology should be reformulated considering the thermal approach and the corresponding energy dissipation terms due to thermal effects.

Extension to 3D

The extension to 3D is essential in order to represent as realistically as possible fault reactivation events and, also, to more accurately estimate the energy released which leads to determine the magnitude of the consequent earthquake.

The purpose of this line of development is to be able to calculate real cases of fault reactivation where different geomechanical data were available and compare the results of the model with real measurements taken *in-situ*.

Sensitivity analysis

In order to propose a methodology as general as possible, it would be suitable to evaluate various cases with different geometries, material properties, initial stresses, fluid conditions, etc. to determine under what conditions a fault reactivation is most likely to occur. Moreover, once unstable conditions are stablished the minimum and maximum magnitude of the earthquakes that could be generated.

This type of analysis can be very useful in preventing fault reactivation events and avoid undesirable damage. In this context, the last future research line exposes the importance of designing an action protocol for this type of events.

Preventive technical recommendations

When a likely induced fault reactivation is detected, it would be desirable to suggest technical recommendations based on modeling results which contribute to prevent these phenomena. Giving

an example, in cases where reactivations are induced by injection/extraction of fluid, studying the behavior of the model under different injection conditions (by means of a previously mentioned sensitivity analysis) it would lead to determine under which conditions the model behaves in a stable or unstable way and adapt the injection accordingly.

This is intended to avoid extreme events that could cause great damage.

References

Alassi, H. T. (2008). *Modeling reservoir geomechanics using discrete element method: application to reservoir monitoring*. PhD thesis, Norwegian University of Science and Technology (NTNU).

Aliguer, I., Carol, I., and Sture, S. (2017). Stress-driven integration strategies and m-AGC tangent operator for Perzyna viscoplasticity and viscoplastic relaxation: application to geomechanical interfaces. *International journal for numerical and analytical methods in geomechanics*, 41(6):918–939.

Andrews, D. (2005). Rupture dynamics with energy loss outside the slip zone. *Journal of Geophysical Research: Solid Earth*, 110(B1).

Bardet, J. and Proubet, J. (1991). Adaptative dynamic relaxation for statics of granular materials. *Computers & structures*, 39(3-4):221–229.

Barenblatt, G. I. (1959). The formation of equilibrium cracks during brittle fracture. general ideas and hypotheses. axially-symmetric cracks. *Journal of applied mathematics and mechanics*, 23(3):622–636.

Barnes, M. R., Adriaenssens, S., and Krupka, M. (2013). A novel torsion/bending element for dynamic relaxation modeling. *Computers & Structures*, 119:60–67.

Bažant, Z. P. and Planas, J. (1998). *Fracture and Size Effect in Concrete and Other Quasibrittle Materials*. CRC Press.

Bellora, D. and Vescovini, R. (2016). Hybrid geometric-dissipative arc-length methods for the quasi-static analysis of delamination problems. *Computers & Structures*, 175:123–133.

Bennett, T. J., Marshall, M. E., Barker, B. W., and Murphy, J. R. (1994). Characteristics of Rockbursts for Use in Seismic Discrimination. Technical report, MAXWELL LABS INC SAN DIEGO CA.

Bormann, P. and Di Giacomo, D. (2011). The moment magnitude Mw and the energy magnitude Me: common roots and differences. *Journal of Seismology*, 15(2):411–427.

Caballero, A. (2005). *3D meso-mechanical numerical analysis of concrete fracture using interface elements*. PhD thesis, Universitat Politècnica de Catalunya (UPC), Barcelona.

Caballero, A., Garolera, D., Carol, I., and Gens, A. (2009). Viscoplastic multilaminate model for jointed rock with stress-prescribed using a stress-prescribed LEGI scheme. In *Proceedings of the Int. Conf. on Rock Joints and Jointed Rock Masses*, pages 1–8.

Caballero, A., Willam, K., and Carol, I. (2008). Consistent tangent formulation for 3D interface modeling of cracking/fracture in quasi-brittle materials. *Computer Methods in Applied Mechanics and Engineering*, 197(33-40):2804–2822.

Carol, I., Prat, P. C., and López, C. M. (1997). Normal/shear cracking model: application to discrete crack analysis. *Journal of engineering mechanics*, 123(8):765–773.

Carosio, A., Willam, K., and Etse, G. (2000). On the consistency of viscoplastic formulations. *International Journal of Solids and Structures*, 37(48-50):7349–7369.

Cesca, S., Grigoli, F., Heimann, S., González, A., Buforn, E., Maghsoudi, S., Blanch, E., and Dahm, T. (2014). The 2013 September–October seismic sequence offshore Spain: a case of seismicity triggered by gas injection? *Geophysical Journal International*, 198(2):941–953.

Convers, J. and Newman, A. (2011). Global evaluation of large earthquake energy from 1997 through mid-2010. *Journal of Geophysical Research: Solid Earth*, 116(B8).

Cook, N. G. W., Hoek, E., Pretorius, J., Ortlepp, W., and Salamon, M. (1966). Rock mechanics applied to study of rockbursts. *Journal of the Southern African Institute of Mining and Metallurgy*, 66(10):435–528.

Crisfield, M. A. (1981). A fast incremental/iterative solution procedure that handles "snap-through". In *Computational methods in nonlinear structural and solid mechanics*, volume 13(1/3), pages 55–62. Elsevier.

Crisfield, M. A. (1991). *Nonlinear finite element analysis of solids and structures*, volume 1. John Wiley & Sons.

Crusat, L. (2018). *Numerical modeling of cracking along non-preestablished paths*. PhD thesis, Doctoral thesis, Universitat Politècnica de Catalunya, Barcelona.

Dang, H. K. and Meguid, M. A. (2010). Evaluating the performance of an explicit dynamic relaxation technique in analyzing non-linear geotechnical engineering problems. *Computers and Geotechnics*, 37(1-2):125–131.

Darcy, H. (1856). *Les fontaines publiques de la ville de Dijon: Exposition et application des principes à suivre et des formules à employer dans les questions de distribution d'eau: Ouvrage terminé par un appendice relatif aux fournitures d'eau de plusieurs villes, au filtrage des eaux et à la fabrication des tuyaux de fonte, de plomb, de tôle et de bitume*, volume 2. V. Dalmont.

De Borst, R. (1986). *Non-linear analysis of frictional materials*. PhD thesis, Delft University of Technology, The Netherlands.

De Francisco, M. (2021). *Elementos junta/interfase mortar con nudos no coincidentes. Aplicación al análisis de discontinuidades y contactos en geomecánica*. PhD thesis, Doctoral thesis, Universitat Politècnica de Catalunya, Barcelona.

Detournay, E. (2016). Mechanics of hydraulic fractures. *Annual review of fluid mechanics*, 48:311–339.

Detournay, E. and Garagash, D. (2003). The near-tip region of a fluid-driven fracture propagating in a permeable elastic solid. *Journal of Fluid Mechanics*, 494:1–32.

Durrheim, R., Anderson, R., Cichowicz, A., Ebrahim-Trolloped, R., Hubert, G., Kijko, A., McGarr, A., Ortlepp, W., and Van der Merwe, N. (2006). The risks to miners, mines, and the public posed by large seismic events in the gold mining districts of South Africa. In *Proceedings of the 3rd International Seminar on Deep and High Stress Mining, J. Hadjigeorgiou and M. Grenon (eds)*. Université Laval, Quebec City, Canada, Section 30.

Duvaut, G. and Lions, J. (1972). Les inéquations en mécanique et en physique. 1972. *Dunod, Paris*.

Engdahl, E. R. (1972). Seismic effects of the MILROW and CANNIKIN nuclear explosions. *Bulletin of the Seismological Society of America*, 62(6):1411–1423.

Esmaeilzadeh, M. and Kadkhodayan, M. (2019). Dynamic analysis of stiffened bi-directional functionally graded plates with porosities under a moving load by dynamic relaxation method with kinetic damping. *Aerospace Science and Technology*, 93:105333.

Foulger, G. R., Wilson, M. P., Gluyas, J. G., Julian, B. R., and Davies, R. J. (2018). Global review of human-induced earthquakes. *Earth-Science Reviews*, 178:438–514.

Frieze, P., Hobbs, R., and Dowling, P. (1978). Application of dynamic relaxation to the large deflection elasto-plastic analysis of plates. *Computers & Structures*, 8(2):301–310.

Gaite, B., Ugalde, A., Villaseñor, A., and Blanch, E. (2016). Improving the location of induced earthquakes associated with an underground gas storage in the Gulf of Valencia (Spain). *Physics of the Earth and Planetary Interiors*, 254:46–59.

Garolera, D. (2017). *Zero-thickness interface elements in petroleum geomechanics: sand production and hydraulic fracture*. PhD thesis, Universitat Politècnica de Catalunya (UPC), Barcelona.

Gens, A., Carol, I., and Alonso, E. E. (1989). An interface element formulation for the analysis of soil-reinforcement interaction. *Computers and Geotechnics*, 7:133–151.

Gibowicz, S. and Kijko, A. (1994). An Introduction to Mining Seismology, Acad. Press.

Glowacka, E. and Nava, F. (1996). Major earthquakes in Mexicali Valley, Mexico, and fluid extraction at Cerro Prieto geothermal field. *Bulletin of the Seismological Society of America*, 86(1A):93–105.

Goldsby, D. L. and Tullis, T. E. (2011). Flash heating leads to low frictional strength of crustal rocks at earthquake slip rates. *Science*, 334(6053):216–218.

Golmakani, M. and Kadkhodayan, M. (2011). Nonlinear bending analysis of annular FGM plates using higher-order shear deformation plate theories. *Composite Structures*, 93(2):973–982.

González, P. J., Tiampo, K. F., Palano, M., Cannavó, F., and Fernández, J. (2012). The 2011 Lorca earthquake slip distribution controlled by groundwater crustal unloading. *Nature Geoscience*, 5(11):821–825.

Goodman, R. E., Taylor, R. L., and Brekke, T. L. (1968). A model for the mechanics of jointed rock. *Journal of the soil mechanics and foundations division*, 94(3):637–659.

Griffith, A. A. (1921). The phenomena of rupture and flow in solids. *Philosophical transactions of the royal society of london. Series A, containing papers of a mathematical or physical character*, 221(582-593):163–198.

Gupta, H. K. (2002). A review of recent studies of triggered earthquakes by artificial water reservoirs with special emphasis on earthquakes in Koyna, India. *Earth-Science Reviews*, 58(3-4):279–310.

Gutenberg, B. and Richter, C. F. (1956). Magnitude and energy of earthquakes. *Annali di Geofisica*, 9(1):1–15.

Gutiérrez, M. A. (2004). Energy release control for numerical simulations of failure in quasi-brittle solids. *Communications in Numerical Methods in Engineering*, 20(1):19–29.

Han, S.-E. and Lee, K.-S. (2003). A study of the stabilizing process of unstable structures by dynamic relaxation method. *Computers & Structures*, 81(17):1677–1688.

Haseganu, E. and Steigmann, D. (1994). Analysis of partly wrinkled membranes by the method of dynamic relaxation. *Computational Mechanics*, 14(6):596–614.

Hawkes, C., McLellan, P., and Bachu, S. (2005). Geomechanical factors affecting geological storage of CO2 in depleted oil and gas reservoirs. *Journal of Canadian Petroleum Technology*, 44(10):52–61.

Heeres, O. M., Suiker, A. S., and de Borst, R. (2002). A comparison between the Perzyna viscoplastic model and the consistency viscoplastic model. *European Journal of Mechanics-A/Solids*, 21(1):1–12.

Hellweg, H.-B. and Crisfield, M. (1998). A new arc-length method for handling sharp snap-backs. *Computers & Structures*, 66(5):704–709.

Hughes, T. J. and Taylor, R. L. (1978). Unconditionally stable algorithms for quasi-static elasto/visco-plastic finite element analysis. *Computers & Structures*, 8(2):169–173.

Husen, S., Kissling, E., and von Deschwanden, A. (2012). Induced seismicity during the construction of the Gotthard Base Tunnel, Switzerland: hypocenter locations and source dimensions. *Seismol*, 16:195–213.

Idiart, A. E. (2009). *Coupled analysis of degradation processes in concrete specimens at the meso-level*. PhD thesis, Universitat Politècnica de Catalunya (UPC), Barcelona.

Ju, J. (1990). Consistent tangent moduli for a class of viscoplasticity. *Journal of Engineering Mechanics*, 116(8):1764–1779.

Kanamori, H. and Rivera, L. (2006). *Energy partitioning during an earthquake. In: Abercrombie, R., McGarr, A., Kanamori, H., Di Toro, G. (Eds.), Earthquakes: Radiated Energy and the Physics of Faulting. Geophysical Monograph Series*, volume 170. American Geophysical Union.

Kardani, O., Nazem, M., Kardani, M., and Sloan, S. (2017). On the application of the maximum entropy meshfree method for elastoplastic geotechnical analysis. *Computers and Geotechnics*, 84:68–77.

Keranen, K. M., Savage, H. M., Abers, G. A., and Cochran, E. S. (2013). Potentially induced earthquakes in Oklahoma, USA: Links between wastewater injection and the 2011 Mw 5.7 earthquake sequence. *Geology*, 41(6):699–702.

Kilic, B. and Madenci, E. (2009). Structural stability and failure analysis using peridynamic theory. *International Journal of Non-Linear Mechanics*, 44(8):845–854.

Kilic, B. and Madenci, E. (2010). An adaptive dynamic relaxation method for quasi-static simulations using the peridynamic theory. *Theoretical and Applied Fracture Mechanics*, 53(3):194–204.

Klose, C. D. (2012). Evidence for anthropogenic surface loading as trigger mechanism of the 2008 Wenchuan earthquake. *Environmental Earth Sciences*, 66(5):1439–1447.

Knoll, P. (1990). The fluid-induced tectonic rockburst of March 13, 1989 in the Werra potash mining district of the GDR (first results). *Gerlands Beiträge zur Geophysik*, 99(3):239–245.

Lecampion, B., Desroches, J., Jeffrey, R. G., and Bunger, A. P. (2017). Experiments versus theory for the initiation and propagation of radial hydraulic fractures in low-permeability materials. *Journal of Geophysical Research: Solid Earth*, 122(2):1239–1263.

Li, T., Cai, M., and Cai, M. (2007). A review of mining-induced seismicity in China. *International Journal of Rock Mechanics and Mining Sciences*, 44(8):1149–1171.

Liaudat, J. (2018). *Experimental and numerical study of the effect of stress on ASR expansions in concrete*. PhD thesis, Universitat Politècnica de Catalunya (UPC), Barcelona.

López, C. M. (1999). *Análisis microestructural de la fractura del hormigón utilizando elementos finitos tipo junta. Aplicación a diferentes hormigones*. PhD thesis, Universitat Politècnica de Catalunya (UPC), Barcelona.

Lorefice, R., Etse, G., and Carol, I. (2008). Viscoplastic approach for rate-dependent failure analysis of concrete joints and interfaces. *International Journal of Solids and Structures*, 45(9):2686–2705.

Majer, E. L. and Peterson, J. E. (2007). The impact of injection on seismicity at The Geysers, California Geothermal Field. *International Journal of Rock Mechanics and Mining Sciences*, 44(8):1079–1090.

Martínez, A. (2020). *Estudio numérico del ataque ácido por CO2 en cementos de pozos de petróleo sellados*. PhD thesis, Universitat Politècnica de Catalunya (UPC), Barcelona.

May, S., Vignollet, J., and de Borst, R. (2016). A new arc-length control method based on the rates of the internal and the dissipated energy. *Engineering Computations*.

McDonald, A. J. (1982). *Seismicity of the Witwatersrand basin*. PhD thesis, University of the Witwatersrand, Johannesburg, South Africa.

McGarr, A. (1991). On a possible connection between three major earthquakes in California and oil production. *Bulletin of the Seismological Society of America*, 81(3):948–970.

McGarr, A., Simpson, D., Seeber, L., and Lee, W. (2002). Case histories of induced and triggered seismicity. *International Geophysics Series*, 81(A):647–664.

McKeown, F. and Dickey, D. (1969). Fault displacements and motion related to nuclear explosions. *Bulletin of the Seismological Society of America*, 59(6):2253–2269.

Moeck, I., Kwiatek, G., and Zimmermann, G. (2009). Slip tendency analysis, fault reactivation potential and induced seismicity in a deep geothermal reservoir. *Journal of Structural Geology*, 31(10):1174–1182.

Namadchi, A. H. and Alamatian, J. (2016). Explicit dynamic analysis using dynamic relaxation method. *Computers & Structures*, 175:91–99.

Neves, M. C., Paiva, L. T., and Luis, J. (2009). Software for slip-tendency analysis in 3D: A plug-in for Coulomb. *Computers & Geosciences*, 35(12):2345–2352.

Nicholson, C. and Wesson, R. L. (1992). Triggered earthquakes and deep well activities. *Pure and applied Geophysics*, 139(3):561–578.

Papadrakakis, M. (1981). A method for the automatic evaluation of the dynamic relaxation parameters. *Computer methods in applied mechanics and engineering*, 25(1):35–48.

Pasqualino, I. and Estefen, S. (2001). A nonlinear analysis of the buckle propagation problem in deepwater pipelines. *International journal of solids and structures*, 38(46-47):8481–8502.

Pérez, A. (2018). *Thm coupling with large advection in fractured rock masses using zero-thickness interface elements*. PhD thesis, Universitat Politècnica de Catalunya (UPC), Barcelona.

Perić, D. (1993). On a class of constitutive equations in viscoplasticity: formulation and computational issues. *International journal for numerical methods in engineering*, 36(8):1365–1393.

Perzyna, P. (1966). Fundamental problems in viscoplasticity. In *Advances in applied mechanics*, volume 9, pages 243–377. Elsevier.

Ponthot, J.-P. (1995). Radial return extensions for visco-plasticity and lubricated friction. In *Proceedings of International Conference on Structural Mechanics and Reactor Technology SMIRT-13*, pages 711–722. IASMiRT, Porto Alegre, Brazil.

Ponthot, J.-P. (2002). Unified stress update algorithms for the numerical simulation of large deformation elasto-plastic and elasto-viscoplastic processes. *International Journal of Plasticity*, 18(1):91–126.

Prat, P., Gens, A., Carol, I., Ledesma, A., and Gili, J. (1993). Drac: A computer software for the analysis of rock mechanics problems. *Application of computer methods in rock mechanics. Shaanxi Science and Technology Press, Xian, China*, pages 1361–1368.

Ramesh, G. and Krishnamoorthy, C. (1994). Inelastic post-buckling analysis of truss structures by dynamic relaxation method. *International journal for numerical methods in engineering*, 37(21):3633–3657.

Ramm, E. (1981). Strategies for tracing the nonlinear response near limit points. In *Nonlinear finite element analysis in structural mechanics*, pages 63–89. Springer, Berlin, Heidelberg.

Rezaiee-Pajand, M. and Alamatian, J. (2008). Nonlinear dynamic analysis by dynamic relaxation method. *Structural engineering and mechanics: An international journal*, 28(5):549–570.

Rezaiee-Pajand, M. and Alamatian, J. (2011). Automatic dr structural analysis of snap-through and snap-back using optimized load increments. *Journal of Structural Engineering*, 137(1):109–116.

Rezaiee-Pajand, M., Sarafrazi, S. R., and Rezaiee, H. (2012). Efficiency of dynamic relaxation methods in nonlinear analysis of truss and frame structures. *Computers & Structures*, 112:295–310.

Rice, J. R., Sammis, C. G., and Parsons, R. (2005). Off-fault secondary failure induced by a dynamic slip pulse. *Bulletin of the Seismological Society of America*, 95(1):109–134.

Riks, E. (1972). The application of newton's method to the problem of elastic stability. *Journal of Applied Mechanics*, 39:1060–1066.

Rinaldi, A. P., Vilarrasa, V., Rutqvist, J., and Cappa, F. (2015). Fault reactivation during CO2 sequestration: Effects of well orientation on seismicity and leakage. *Greenhouse Gases: Science and Technology*, 5(5):645–656.

Rodríguez, M. (2020). *Análisis numérico termo-mecánico y termo-higrométrico del hormigón expuesto a altas temperaturas*. PhD thesis, Universitat Politècnica de Catalunya (UPC), Barcelona.

Rots, J. G. (1988). *Computational modeling of concrete fracture*. PhD thesis, Technische Universiteit Delft.

Rudnicki, J. W. (1980). Fracture mechanics aplied to the earth's crust. *Annual Review of Earth and Planetary Sciences*, 8:489.

Rutqvist, J., Rinaldi, A. P., Cappa, F., Jeanne, P., Mazzoldi, A., Urpi, L., Guglielmi, Y., and Vilarrasa, V. (2016). Fault activation and induced seismicity in geological carbon storage–lessons learned from recent modeling studies. *Journal of Rock Mechanics and Geotechnical Engineering*, 8(6):789–804.

Sanchez, E. C. M., Muñoz, L. F. P., and Roehl, D. (2020). Discrete fracture propagation analysis using a robust combined continuation method. *International Journal of Solids and Structures*, 193:405–417.

Schultz, R., Stern, V., Novakovic, M., Atkinson, G., and Gu, Y. J. (2015). Hydraulic fracturing and the Crooked Lake sequences: Insights gleaned from regional seismic networks. *Geophysical Research Letters*, 42(8):2750–2758.

Schwer, L. E. (1994). Viscoplastic augmentation of the smooth cap model. *Nuclear engineering and design*, 150(2-3):215–223.

Seeber, L., Armbruster, J. G., Kim, W.-Y., Barstow, N., and Scharnberger, C. (1998). The 1994 Cacoosing Valley earthquakes near Reading, Pennsylvania: A shallow rupture triggered by quarry unloading. *Journal of Geophysical Research: Solid Earth*, 103(B10):24505–24521.

Segall, P. and Fitzgerald, S. D. (1998). A note on induced stress changes in hydrocarbon and geothermal reservoirs. *Tectonophysics*, 289(1-3):117–128.

Segall, P., Grasso, J.-R., and Mossop, A. (1994). Poroelastic stressing and induced seismicity near the Lacq gas field, southwestern France. *Journal of Geophysical Research: Solid Earth*, 99(B8):15423–15438.

Segura, J. M. (2007). *Coupled HM analysis using zero-thickness interface elements with double nodes*. PhD thesis, Universitat Politècnica de Catalunya (UPC), Barcelona.

Segura, J. M. and Carol, I. (2004). On zero-thickness interface elements for diffusion problems. *International journal for numerical and analytical methods in geomechanics*, 28(9):947–962.

Segura, J. M. and Carol, I. (2008a). Coupled HM analysis using zero-thickness interface elements with double nodes. Part I: Theoretical model. *International journal for numerical and analytical methods in geomechanics*, 32(18):2083–2101.

Segura, J. M. and Carol, I. (2008b). Coupled HM analysis using zero-thickness interface elements with double nodes. Part II: Verification and application. *International Journal for Numerical and Analytical Methods in Geomechanics*, 32(18):2103–2123.

Sherman, J. and Morrison, W. J. (1950). Adjustment of an inverse matrix corresponding to a change in one element of a given matrix. *The Annals of Mathematical Statistics*, 21(1):124–127.

Simo, J., Kennedy, J., and Govindjee, S. (1988). Non-smooth multisurface plasticity and viscoplasticity. Loading/unloading conditions and numerical algorithms. *International Journal for Numerical Methods in Engineering*, 26(10):2161–2185.

Simon, B., Zienkiewicz, O., and Paul, D. (1984). An analytical solution for the transient response of saturated porous elastic solids. *International Journal for Numerical and analytical methods in Geomechanics*, 8(4):381–398.

Simpson, D. W. and Leith, W. (1985). The 1976 and 1984 Gazli, USSR, earthquakes—Were they induced? *Bulletin of the Seismological Society of America*, 75(5):1465–1468.

Soltanzadeh, H. and Hawkes, C. D. (2008). Semi-analytical models for stress change and fault reactivation induced by reservoir production and injection. *Journal of Petroleum Science and Engineering*, 60(2):71–85.

Soltanzadeh, H. and Hawkes, C. D. (2009). Assessing fault reactivation tendency within and surrounding porous reservoirs during fluid production or injection. *International Journal of Rock Mechanics and Mining Sciences*, 46(1):1–7.

Stark, M. (1990). Imaging injected water in The Geysers reservoir using microearthquake data. *Geothermal Resources Council Trans*, 14:1697–1704.

Streit, J. and Hillis, R. (2002). Estimating fluid pressures that can induce reservoir failure during hydrocarbon depletion. In *SPE/ISRM Rock Mechanics Conference*. OnePetro.

Underwood, P. (1983). Dynamic relaxation computational methods for transient analysis, vol. 1, 245–265.

Van Eck, T., Goutbeek, F., Haak, H., and Dost, B. (2006). Seismic hazard due to small-magnitude, shallow-source, induced earthquakes in The Netherlands. *Engineering geology*, 87(1-2):105–121.

Van Wees, J., Buijze, L., Van Thienen-Visser, K., Nepveu, M., Wassing, B., Orlic, B., and Fokker, P. (2014). Geomechanics response and induced seismicity during gas field depletion in The Netherlands. *Geothermics*, 52:206–219.

Venkataraman, A. and Kanamori, H. (2004). Observational constraints on the fracture energy of subduction zone earthquakes. *Journal of Geophysical Research: Solid Earth*, 109(B5).

Verdon, J. P., Kendall, J.-M., Stork, A. L., Chadwick, R. A., White, D. J., and Bissell, R. C. (2013). Comparison of geomechanical deformation induced by megatonne-scale CO2 storage at Sleipner, Weyburn, and In Salah. *Proceedings of the National Academy of Sciences*, 110(30):E2762–E2771.

Verhoosel, C. V., Remmers, J. J., and Gutiérrez, M. A. (2009). A dissipation-based arc-length method for robust simulation of brittle and ductile failure. *International journal for numerical methods in engineering*, 77(9):1290–1321.

Vidal-Gilbert, S., Nauroy, J.-F., and Brosse, E. (2009). 3D geomechanical modelling for CO2 geologic storage in the Dogger carbonates of the Paris Basin. *International Journal of Greenhouse Gas Control*, 3(3):288–299.

Vilarrasa, V., Bolster, D., Olivella, S., and Carrera, J. (2010). Coupled hydromechanical modeling of CO2 sequestration in deep saline aquifers. *International Journal of Greenhouse Gas Control*, 4(6):910–919.

Vilarrasa, V., Makhnenko, R., and Gheibi, S. (2016). Geomechanical analysis of the influence of CO2 injection location on fault stability. *Journal of Rock Mechanics and Geotechnical Engineering*, 8(6):805–818.

Walters, R. J., Zoback, M. D., Baker, J. W., and Beroza, G. C. (2015). Characterizing and responding to seismic risk associated with earthquakes potentially triggered by fluid disposal and hydraulic fracturing. *Seismological Research Letters*, 86(4):1110–1118.

Wang, W., Sluys, L., and De Borst, R. (1997). Viscoplasticity for instabilities due to strain softening and strain-rate softening. *International Journal for Numerical Methods in Engineering*, 40(20):3839–3864.

Wempner, G. A. (1971). Discrete approximations related to nonlinear theories of solids. *International Journal of Solids and Structures*, 7(11):1581–1599.

Wood, R. (2002). A simple technique for controlling element distortion in dynamic relaxation form-finding of tension membranes. *Computers & Structures*, 80(27-30):2115–2120.

Yeck, W. L., Hayes, G. P., McNamara, D. E., Rubinstein, J. L., Barnhart, W. D., Earle, P. S., and Benz, H. M. (2017). Oklahoma experiences largest earthquake during ongoing regional wastewater injection hazard mitigation efforts. *Geophysical Research Letters*, 44(2):711–717.

Yoon, J. S., Zimmermann, G., Zang, A., and Stephansson, O. (2015). Discrete element modeling of fluid injection–induced seismicity and activation of nearby fault. *Canadian Geotechnical Journal*, 52(10):1457–1465.

Zang, A., Majer, E., and Bruhn, D. (2014). Analysis of induced seismicity in geothermal operations. *Geothermics*, 52.

Zeppilli, D., Pouya, A., Zhu, C., Shi, X.-C., and Xu, H. (2021). Numerical analysis of injection-induced fault reactivation using hydro-mechanical coupled finite element model with cohesive zone elements. *Geomechanics and Geophysics for Geo-Energy and Geo-Resources*, 7(3):1–21.

Zhang, L. and Yu, T. (1989). Modified adaptive dynamic relaxation method and its application to elastic-plastic bending and wrinkling of circular plates. *Computers & structures*, 33(2):609–614.

Zhang, Y., Gartrell, A., Underschultz, J., and Dewhurst, D. (2009). Numerical modelling of strain localisation and fluid flow during extensional fault reactivation: Implications for hydrocarbon preservation. *Journal of Structural Geology*, 31(3):315–327.

Zhang, Y., Huang, J., Yuan, Y., and Mang, H. A. (2021). Cracking elements method with a dissipation-based arc-length approach. *Finite Elements in Analysis and Design*, 195:103573.

Zienkiewicz, O. and Cormeau, I. (1974). Visco-plasticity—plasticity and creep in elastic solids—a unified numerical solution approach. *International Journal for Numerical Methods in Engineering*, 8(4):821–845.

Zienkiewicz, O. and Shiomi, T. (1984). Dynamic behaviour of saturated porous media; the generalized biot formulation and its numerical solution. *International journal for numerical and analytical methods in geomechanics*, 8(1):71–96.

Zoback, M. D. (2007). *Reservoir geomechanics*. Cambridge university press.

Appendices

Appendix A

Limit cases of $\frac{1}{H''}$ when Δt or H tend to zero

This appendix is focused on the developments of both limit cases $\Delta t \to 0$ and $H \to 0$ of the equation $f = \frac{1}{H''}$. As a reminder, the original expression of $\frac{1}{H''}$ is given below.

$$\frac{1}{H''} = \frac{1}{H}\left[1 + \frac{\eta\overline{F}}{H\Delta t}\left(e^{\frac{-H\Delta t}{\eta\overline{F}}} - 1\right)\right] \tag{A.1}$$

A.1 Case $\Delta t \to 0$

By slightly developing the equation (A.1), it can be seen that there is only a part that depends on the time increment ($f(\Delta t)$).

$$\frac{1}{H"} = \frac{1}{H}\left[1 + \frac{\eta\overline{F}}{H\Delta t}\left(e^{\frac{-H\Delta t}{\eta\overline{F}}} - 1\right)\right] = \frac{1}{H} + \underbrace{\frac{\eta\overline{F}}{H^2\Delta t}\left(e^{\frac{-H\Delta t}{\eta\overline{F}}} - 1\right)}_{f(\Delta t)} \tag{A.2}$$

Applying the Taylor series approximation $\left(\sum_{n=0}^{\infty} \frac{f^{(n)}(a)}{n!}(x-a)^n\right)$ and analyzing the first term, the expression takes an indeterminate form of the $\frac{0}{0}$ type as follows:

$$f(\Delta t) = \frac{\eta\overline{F}}{H^2\Delta t}\left(e^{\frac{-H\Delta t}{\eta\overline{F}}} - 1\right) = \frac{\eta\overline{F}e^{\frac{-H\Delta t}{\eta\overline{F}}} - \eta\overline{F}}{H^2\Delta t} \overset{\Delta t=0}{=} \frac{0}{0} \tag{A.3}$$

Then, the limit solution of this first term $f(\Delta t = 0)$ is obtained applying the L'Hôpital's rule

$\left(lim_{x\to 0}\frac{q(x)}{g(x)} = lim_{x\to 0}\frac{q'(x)}{g'(x)}\right)$:

$$f(\Delta t) = \frac{\eta\overline{F}e^{\frac{-H\Delta t}{\eta\overline{F}}} - \eta\overline{F}}{H^2\Delta t} \overset{L'Hôpital}{=} \frac{\cancel{\eta\overline{F}}\frac{-H}{\cancel{\eta\overline{F}}}e^{\frac{-H\Delta t}{\eta\overline{F}}}}{H^2} = \frac{-e^{\frac{-H\Delta t}{\eta\overline{F}}}}{H} = \frac{-1}{H}e^{\frac{-H\Delta t}{\eta\overline{F}}} \tag{A.4}$$

$$f(\Delta t = 0) = \frac{-1}{H} \tag{A.5}$$

The second term of the Taylor series approximation requires the first derivative with respect to Δt, $f'(\Delta t)$, and, as it can be seen in the following expression, it takes an indeterminate form again when Δt tends to zero:

$$\begin{aligned} f'(\Delta t) &= \frac{\left(\cancel{\eta\overline{F}}\frac{-H}{\cancel{\eta\overline{F}}}e^{\frac{-H\Delta t}{\eta\overline{F}}}\right)H^2\Delta t - \left(\eta\overline{F}e^{\frac{-H\Delta t}{\eta\overline{F}}} - \eta\overline{F}\right)H^2}{\left(H^2\Delta t\right)^2} = \\ &= \frac{-H\Delta te^{\frac{-H\Delta t}{\eta\overline{F}}} - \eta\overline{F}e^{\frac{-H\Delta t}{\eta\overline{F}}} + \eta\overline{F}}{H^2\Delta t^2} \overset{\Delta t=0}{=} \frac{0}{0} \end{aligned} \tag{A.6}$$

In the same way, the L'Hôpital's rule is applied:

$$f'(\Delta t) = \frac{-H\Delta te^{\frac{-H\Delta t}{\eta\overline{F}}} - \eta\overline{F}e^{\frac{-H\Delta t}{\eta\overline{F}}} + \eta\overline{F}}{H^2\Delta t^2} \overset{L'Hôpital}{=} \frac{\frac{H^2}{\eta\overline{F}}e^{\frac{-H\Delta t}{\eta\overline{F}}} - \frac{H^3\Delta t}{\left(\eta\overline{F}\right)^2}e^{\frac{-H\Delta t}{\eta\overline{F}}}}{2H^2} \tag{A.7}$$

$$f'(\Delta t = 0) = \frac{1}{2\eta\overline{F}} \tag{A.8}$$

Finally, developing the third term of the Taylor series approximation, which requires the second derivative with respect to Δt, $f''(\Delta t)$, an indeterminate form is also obtained:

$$\begin{aligned} f''(\Delta t) = &\frac{\left(-He^{\frac{-H\Delta t}{\eta\overline{F}}} + (\cancel{H}H\Delta t)\cdot\frac{\cancel{H}}{\eta\overline{F}}e^{\frac{-H\Delta t}{\eta\overline{F}}} + \left(\cancel{\eta\overline{F}}\right)\cdot\frac{\cancel{H}}{\cancel{\eta\overline{F}}}e^{\frac{-H\Delta t}{\eta\overline{F}}}\right)H^2\Delta t^2}{\left(H^2\Delta t^2\right)^2} + \\ &- \frac{\left(-H\Delta te^{\frac{-H\Delta t}{\eta\overline{F}}} - \eta\overline{F}e^{\frac{-H\Delta t}{\eta\overline{F}}} + \eta\overline{F}\right)H^2 2\Delta t}{\left(H^2\Delta t^2\right)^2} = \\ &= \frac{\frac{H^2\Delta t^2}{\eta\overline{F}}e^{\frac{-H\Delta t}{\eta\overline{F}}} + 2H\Delta te^{\frac{-H\Delta t}{\eta\overline{F}}} + 2\eta\overline{F}e^{\frac{-H\Delta t}{\eta\overline{F}}} - 2\eta\overline{F}}{H^2\Delta t^3} \overset{\Delta t=0}{=} \frac{0}{0} \end{aligned} \tag{A.9}$$

The procedure followed is the same as in the previous developments applying the L'Hôpital's

rule.

$$f''(\Delta t) = \frac{\frac{H^2\Delta t^2}{\eta\overline{F}}e^{\frac{-H\Delta t}{\eta\overline{F}}} + 2H\Delta t e^{\frac{-H\Delta t}{\eta\overline{F}}} + 2\eta\overline{F}e^{\frac{-H\Delta t}{\eta\overline{F}}} - 2\eta\overline{F}}{H^2\Delta t^3} \overset{L'Hôpital}{=} \frac{-\frac{2H^3}{\left(\eta\overline{F}\right)^2}e^{\frac{-H\Delta t}{\eta\overline{F}}} + \frac{H^4 2\Delta t}{\left(\eta\overline{F}\right)^3}e^{\frac{-H\Delta t}{\eta\overline{F}}} + \frac{H^4 2\Delta t}{\left(\eta\overline{F}\right)^3}e^{\frac{-H\Delta t}{\eta\overline{F}}} - \frac{H^5\Delta t^2}{\left(\eta\overline{F}\right)^4}e^{\frac{-H\Delta t}{\eta\overline{F}}}}{6H^2} \tag{A.10}$$

$$f''(\Delta t = 0) = \frac{-H}{3\left(\eta\overline{F}\right)^2} \tag{A.11}$$

Grouping the limit expressions obtained for each term of the Taylor series approximation when $\Delta t \to 0$ (Eqs. A.5, A.8 and A.11), the following complete limit expression is obtained:

$$\frac{1}{H"} = \frac{1}{\cancel{H}} + \left[\frac{-\cancel{1}}{\cancel{H}} + \frac{1}{2\eta\overline{F}}\frac{\Delta t}{1!} - \frac{H}{3\left(\eta\overline{F}\right)^2}\frac{\Delta t^2}{2!}\right] = \frac{\Delta t}{2\eta\overline{F}} - \frac{H\Delta t^2}{2\cdot 3\left(\eta\overline{F}\right)^2} \tag{A.12}$$

Rearranging the previous equation (Eq. A.12) the following one is obtained:

$$\left.\frac{1}{H"}\right|_{Limit} = \frac{\Delta t}{2\eta\overline{F}}\left(1 - \frac{H\Delta t}{3\eta\overline{F}}\right) \tag{A.13}$$

From equation (A.13) it can be deduced that if $\Delta t = 0$ then $\frac{1}{H"} = 0$ and this implies that $H" = \infty$. This particular case shouldn't happen because it is known that in the limit situation when $\Delta t = 0$, the visco-plastic strain tends to zero and visco-plasticity tends to elasticity.

A verification test has been performed to assess the behavior of the closed-form solution near the limit zone $\Delta t = 0$ and ensure that it provides better results. The following graphic shows (Fig. A.1) a comparison between the original (Eq. A.1) and the limit expression (Eq. A.13). Moreover, the values of the parameters used such as $\overline{F} = 1.4$, $\eta = 10^6\, MPa{\cdot}s$ and $H = -183884.6850\, MPa$ come from the pure tension example with softening found in the verification examples section (Sec. 3.5.1).

A.2 Case $H \to 0$

The other limit case occurs when $H \to 0$. In contrast to the previous limit case, as it can be seen in equation (A.14), the entire equation depends on H, which is going to be called $f(H)$.

$$\frac{1}{H"} = \frac{1}{H}\left[1 + \frac{\eta\overline{F}}{H\Delta t}\left(e^{\frac{-H\Delta t}{\eta\overline{F}}} - 1\right)\right] = \frac{1}{H} + \frac{\eta\overline{F}}{H^2\Delta t}\left(e^{\frac{-H\Delta t}{\eta\overline{F}}} - 1\right) = \underbrace{\frac{H\Delta t + \eta\overline{F}e^{\frac{-H\Delta t}{\eta\overline{F}}} - \eta\overline{F}}{H^2\Delta t}}_{f(H)} \tag{A.14}$$

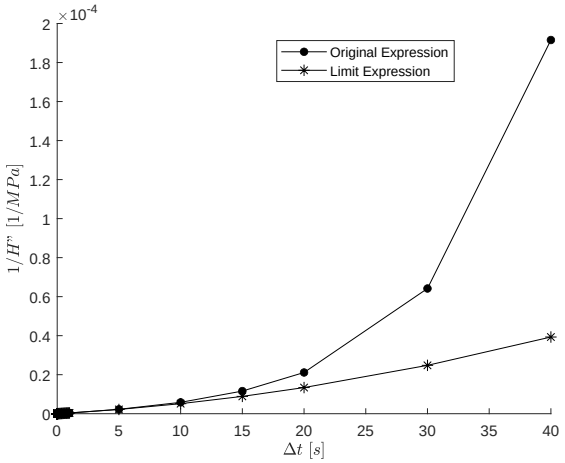

(a) Limit case $\Delta t \to 0$: Evolution of $\frac{1}{H''}$ over time.

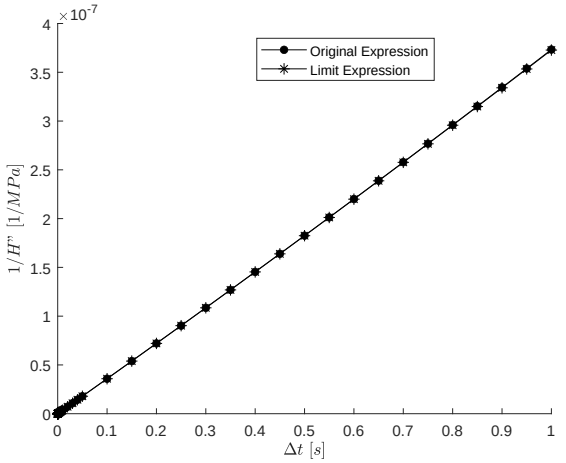

(b) Limit case $\Delta t \to 0$: Evolution of $\frac{1}{H''}$ in the first moments of time.

Figure A.1: Representation of both original and limit expressions for $\Delta t \to 0$ limit case.

As in the previous limit case, the limit solution is going to be obtained using the Taylor series approximation. Note that the first term $f(H)$ becomes an indeterminate form $\frac{0}{0}$ when $H = 0$:

$$f(H) = \frac{H\Delta t + \eta\overline{F} e^{\frac{-H\Delta t}{\eta\overline{F}}} - \eta\overline{F}}{H^2\Delta t} \overset{H=0}{=} \frac{0}{0} \tag{A.15}$$

Then, the application of the L'Hôpital's rule is required and the limit expression of the first term of the Taylor series approximation is obtained as follows:

$$f(H) = \frac{H\Delta t + \eta\overline{F} e^{\frac{-H\Delta t}{\eta\overline{F}}} - \eta\overline{F}}{H^2\Delta t} \overset{L'Hôpital}{=} \frac{\Delta t}{2\eta\overline{F}} e^{\frac{-H\Delta t}{\eta\overline{F}}} \tag{A.16}$$

$$f(H=0) = \frac{\Delta t}{2\eta\overline{F}} \tag{A.17}$$

The second term of the Taylor series approximation needs the first derivative with respect to H, $f'(H)$, and again an indeterminate form is obtained when $H = 0$ is considered.

$$\begin{aligned} f'(H) &= \frac{\left(\Delta t + \eta\overline{F} \cdot \frac{-\Delta t}{\eta\overline{F}} e^{\frac{-H\Delta t}{\eta\overline{F}}}\right) H^2\Delta t - \left(H\Delta t + \eta\overline{F} e^{\frac{-H\Delta t}{\eta\overline{F}}} - \eta\overline{F}\right) 2H\Delta t}{\left(H^2\Delta t\right)^2} = \\ &= \frac{-H\Delta t e^{\frac{-H\Delta t}{\eta\overline{F}}} - H\Delta t - 2\eta\overline{F} e^{\frac{-H\Delta t}{\eta\overline{F}}} + 2\eta\overline{F}}{H^3\Delta t} \overset{H=0}{=} \frac{0}{0} \end{aligned} \tag{A.18}$$

After applying the L'Hôpital's rule, the limit expression of this term may be reached as a result of the following development.

$$f'(H) = \frac{-H\Delta t e^{\frac{-H\Delta t}{\eta\overline{F}}} - H\Delta t - 2\eta\overline{F}e^{\frac{-H\Delta t}{\eta\overline{F}}} + 2\eta\overline{F}}{H^3\Delta t} \overset{L'Hôpital}{=} \frac{-\frac{\Delta t^3}{(\eta\overline{F})^2}e^{\frac{-H\Delta t}{\eta\overline{F}}} + \frac{H\Delta t^4}{(\eta\overline{F})^3}e^{\frac{-H\Delta t}{\eta\overline{F}}}}{6\Delta t} \tag{A.19}$$

$$f'(H=0) = \frac{-\Delta t^2}{6\left(\eta\overline{F}\right)^2} \tag{A.20}$$

Keeping the limit expressions previously obtained for each term of the Taylor series (Eqs. A.17 and A.20) together, the complete limit equation may be written as:

$$\frac{1}{H"} = \frac{\Delta t}{2\eta\overline{F}} + \frac{-\Delta t^2}{6\left(\eta\overline{F}\right)^2}\frac{H}{1!} = \frac{\Delta t}{2\eta\overline{F}}\left(1 - \frac{H\Delta t}{3\eta\overline{F}}\right) \tag{A.21}$$

Note that, this limit expression is exactly the same as the one obtained for the limit case considering $\Delta t = 0$. For verification purposes, a comparison between the original expression (Eq. A.1) and the limit expression (Eq. A.21) has been performed and the results are shown in the graphics below (Fig. A.2). The parameters used are $\overline{F} = 1.4$, $\eta = 10^6\, MPa{\cdot}s$ and $\Delta t = 1.0\, s$ that come from the pure tension example with softening found in the verification examples section (Sec. 3.5.1).

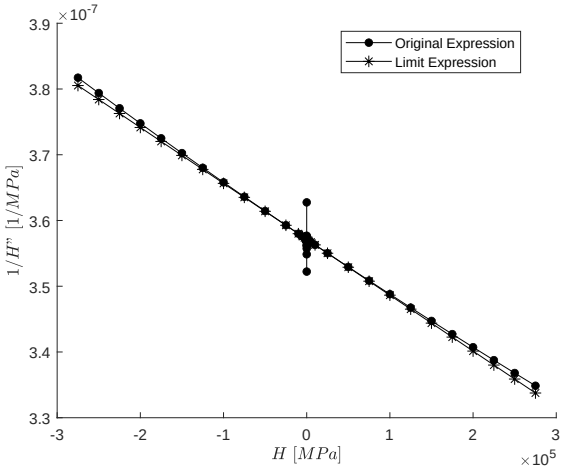

(a) Limit case $H \to 0$: Evolution of $\frac{1}{H''}$ along H.

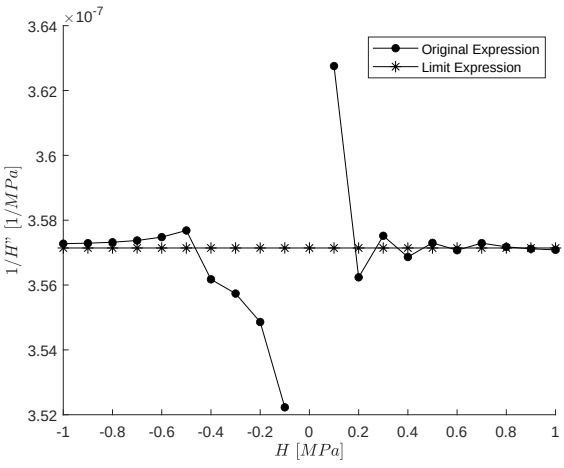

(b) Limit case $H \to 0$: Evolution of $\frac{1}{H''}$ in the near zero H values.

Figure A.2: Representation of both original and limit expressions for $H \to 0$ limit case.

To conclude, the limit expression obtained in both cases $\Delta t \to 0$ and H$\to$ 0 is the same (Eq. A.21). In addition, if perfect visco-plasticicity is considered, which means $H = 0$, the following expression is obtained:

$$\frac{1}{H"} = \frac{\Delta t}{2\eta\overline{F}} \tag{A.22}$$

It is reassuring to verify that this expression matches the one obtained by Aliguer et al. (2017), $\frac{1}{H"} = \frac{\theta\Delta t}{\eta\overline{F}}$ considering $\theta = \frac{1}{2}$.

Appendix B

IDC-Wvp: Target in terms of total dissipation

This appendix contains two parts: (1) the developments of the derivatives of ΔW^{vp} (Eq. 3.27) with respect to the time increment duration and the stress increment and (2) the description of how to obtain the limit expressions of those derivatives when the limit cases $\Delta t \to 0$ and $H \to 0$ are considered.

B.1 Derivatives of ΔW^{vp}

For convenience, the right-hand-side of ΔW^{vp} (Eq. 3.27) has been split into two parts in order to develop the derivatives with respect to the time increment duration and to the stress increment:

$$\begin{aligned}\Delta W^{vp} = &\underbrace{\frac{\boldsymbol{\sigma}_{\mathrm{J}0} : \boldsymbol{m}}{H}\left[\left(F_0 - \frac{\eta\overline{F}}{H\Delta t}\left(\boldsymbol{n} : \Delta\boldsymbol{\sigma}_{\mathrm{J}}\right)\right)\left(1 - e^{\frac{-H}{\eta\overline{F}}\Delta t}\right) + \left(\boldsymbol{n} : \Delta\boldsymbol{\sigma}_{\mathrm{J}}\right)\right]}_{Part\,A} + \\ &+ \underbrace{\frac{\Delta\boldsymbol{\sigma}_{\mathrm{J}} : \boldsymbol{m}}{H\Delta t}\left[\left(F_0 - \frac{\eta\overline{F}}{H\Delta t}\left(\boldsymbol{n} : \Delta\boldsymbol{\sigma}_{\mathrm{J}}\right)\right)\left(\frac{\eta\overline{F}}{H} - \left(\frac{\eta\overline{F}}{H} + \Delta t\right)e^{\frac{-H}{\eta\overline{F}}\Delta t}\right) + \right.}_{Part\,B} \\ &\underbrace{\left. + \left(\boldsymbol{n} : \Delta\boldsymbol{\sigma}_{\mathrm{J}}\right)\left(\frac{\Delta t}{2}\right)\right]}_{Part\,B}\end{aligned} \tag{B.1}$$

B.1.1 Derivative of ΔW^{vp} with respect to the time increment

Developing the derivative of ΔW^{vp} with respect to the time increment of the first part ($Part\,A$), note that this part is further divided into different derivative terms for convenience:

$$Part\,A = \frac{\boldsymbol{\sigma}_{\mathrm{J0}} : \boldsymbol{m}}{H}\left[F_0 \underbrace{-F_0 e^{\frac{-H}{\eta\overline{F}}\Delta t}}_{deriv.1A_t} \underbrace{-\frac{\eta\overline{F}}{H\Delta t}\left(\boldsymbol{n} : \Delta\boldsymbol{\sigma}_{\mathrm{J}}\right)}_{deriv.2A_t} \underbrace{+\frac{\eta\overline{F}}{H\Delta t}\left(\boldsymbol{n} : \Delta\boldsymbol{\sigma}_{\mathrm{J}}\right) e^{\frac{-H}{\eta\overline{F}}\Delta t}}_{deriv.3A_t} + \left(\boldsymbol{n} : \Delta\boldsymbol{\sigma}_{\mathrm{J}}\right)\right] \tag{B.2}$$

where

$$deriv.1A_t : \ \frac{\partial}{\partial\Delta t}\frac{\boldsymbol{\sigma}_{\mathrm{J0}} : \boldsymbol{m}}{H}\left(-F_0 e^{\frac{-H}{\eta\overline{F}}\Delta t}\right) = \frac{F_0}{\eta\overline{F}}\left(\boldsymbol{\sigma}_{\mathrm{J0}} : \boldsymbol{m}\right) e^{\frac{-H}{\eta\overline{F}}\Delta t} \tag{B.3}$$

$$deriv.2A_t : \ \frac{\partial}{\partial\Delta t}\frac{\boldsymbol{\sigma}_{\mathrm{J0}} : \boldsymbol{m}}{H}\left(-\frac{\eta\overline{F}}{H\Delta t}\left(\boldsymbol{n} : \Delta\boldsymbol{\sigma}_{\mathrm{J}}\right)\right) = \frac{\boldsymbol{\sigma}_{\mathrm{J0}} : \boldsymbol{m}}{H}\frac{\eta\overline{F}}{H\Delta t^2}\left(\boldsymbol{n} : \Delta\boldsymbol{\sigma}_{\mathrm{J}}\right) \tag{B.4}$$

$$\begin{aligned} deriv.3A_t : \ &\frac{\partial}{\partial\Delta t}\frac{\boldsymbol{\sigma}_{\mathrm{J0}} : \boldsymbol{m}}{H}\left(\frac{\eta\overline{F}}{H\Delta t}\left(\boldsymbol{n} : \Delta\boldsymbol{\sigma}_{\mathrm{J}}\right) e^{\frac{-H}{\eta\overline{F}}\Delta t}\right) = \\ &= \frac{\boldsymbol{\sigma}_{\mathrm{J0}} : \boldsymbol{m}}{H}\left(\boldsymbol{n} : \Delta\boldsymbol{\sigma}_{\mathrm{J}}\right)\left(\frac{-\eta\overline{F}}{H\Delta t^2} - \frac{1}{\Delta t}\right) e^{\frac{-H}{\eta\overline{F}}\Delta t} \end{aligned} \tag{B.5}$$

In the same way, the second part ($Part\,B$) is split in several derivative terms:

$$\begin{aligned} Part\,B = \frac{\Delta\boldsymbol{\sigma}_{\mathrm{J}} : \boldsymbol{m}}{H}\Bigg[&\underbrace{F_0\frac{\eta\overline{F}}{H\Delta t}}_{deriv.1B_t} \underbrace{-F_0\frac{\eta\overline{F}}{H\Delta t}e^{\frac{-H}{\eta\overline{F}}\Delta t}}_{deriv.2B_t} \underbrace{-F_0 e^{\frac{-H}{\eta\overline{F}}\Delta t}}_{deriv.3B_t} \underbrace{-\frac{\left(\eta\overline{F}\right)^2}{H^2\Delta t^2}\left(\boldsymbol{n} : \Delta\boldsymbol{\sigma}_{\mathrm{J}}\right)}_{deriv.4B_t} + \\ &+ \underbrace{\frac{\left(\eta\overline{F}\right)^2}{H^2\Delta t^2}\left(\boldsymbol{n} : \Delta\boldsymbol{\sigma}_{\mathrm{J}}\right) e^{\frac{-H}{\eta\overline{F}}\Delta t}}_{deriv.5B_t} + \underbrace{\frac{\eta\overline{F}}{H\Delta t}\left(\boldsymbol{n} : \Delta\boldsymbol{\sigma}_{\mathrm{J}}\right) e^{\frac{-H}{\eta\overline{F}}\Delta t}}_{deriv.6B_t} + \left(\boldsymbol{n} : \Delta\boldsymbol{\sigma}_{\mathrm{J}}\right)\left(\frac{1}{2}\right)\Bigg] \end{aligned} \tag{B.6}$$

where

$$deriv.1B_t : \ \frac{\partial}{\partial\Delta t}\frac{\Delta\boldsymbol{\sigma}_{\mathrm{J}} : \boldsymbol{m}}{H}\left(F_0\frac{\eta\overline{F}}{H\Delta t}\right) = \frac{\Delta\boldsymbol{\sigma}_{\mathrm{J}} : \boldsymbol{m}}{H}\left(F_0\frac{-\eta\overline{F}}{H\Delta t^2}\right) \tag{B.7}$$

$$deriv.2B_t : \ \frac{\partial}{\partial\Delta t}\frac{\Delta\boldsymbol{\sigma}_{\mathrm{J}} : \boldsymbol{m}}{H}\left(-F_0\frac{\eta\overline{F}}{H\Delta t}e^{\frac{-H}{\eta\overline{F}}\Delta t}\right) = \frac{\Delta\boldsymbol{\sigma}_{\mathrm{J}} : \boldsymbol{m}}{H}F_0\left[\frac{\eta\overline{F}}{H\Delta t^2} + \frac{1}{\Delta t}\right] e^{\frac{-H}{\eta\overline{F}}\Delta t} \tag{B.8}$$

$$deriv.3B_t : \ \frac{\partial}{\partial\Delta t}\frac{\Delta\boldsymbol{\sigma}_{\mathrm{J}} : \boldsymbol{m}}{H}\left(-F_0 e^{\frac{-H}{\eta\overline{F}}\Delta t}\right) = \frac{F_0}{\eta\overline{F}}\left(\Delta\boldsymbol{\sigma}_{\mathrm{J}} : \boldsymbol{m}\right) e^{\frac{-H}{\eta\overline{F}}\Delta t} \tag{B.9}$$

$$deriv.4B_t : \ \frac{\partial}{\partial\Delta t}\frac{\Delta\boldsymbol{\sigma}_{\mathrm{J}} : \boldsymbol{m}}{H}\left(-\frac{\left(\eta\overline{F}\right)^2}{H^2\Delta t^2}\left(\boldsymbol{n} : \Delta\boldsymbol{\sigma}_{\mathrm{J}}\right)\right) = \frac{\Delta\boldsymbol{\sigma}_{\mathrm{J}} : \boldsymbol{m}}{H}\left(2\frac{\left(\eta\overline{F}\right)^2}{H^2\Delta t^3}\right)\left(\boldsymbol{n} : \Delta\boldsymbol{\sigma}_{\mathrm{J}}\right) \tag{B.10}$$

$$deriv.5B_t: \frac{\partial}{\partial \Delta t}\frac{\Delta\boldsymbol{\sigma}_{\mathrm{J}}:\boldsymbol{m}}{H}\left(\frac{\left(\eta\overline{F}\right)^2}{H^2\Delta t^2}\left(\boldsymbol{n}:\Delta\boldsymbol{\sigma}_{\mathrm{J}}\right)e^{\frac{-H}{\eta\overline{F}}\Delta t}\right)= \\ =\frac{\Delta\boldsymbol{\sigma}_{\mathrm{J}}:\boldsymbol{m}}{H}\left(\frac{\eta\overline{F}}{H\Delta t^2}\left(\frac{-2\eta\overline{F}}{H\Delta t}-1\right)\left(\boldsymbol{n}:\Delta\boldsymbol{\sigma}_{\mathrm{J}}\right)e^{\frac{-H}{\eta\overline{F}}\Delta t}\right) \tag{B.11}$$

$$deriv.6B_t: \frac{\partial}{\partial \Delta t}\frac{\Delta\boldsymbol{\sigma}_{\mathrm{J}}:\boldsymbol{m}}{H}\left(\frac{\eta\overline{F}}{H\Delta t}\left(\boldsymbol{n}:\Delta\boldsymbol{\sigma}_{\mathrm{J}}\right)e^{\frac{-H}{\eta\overline{F}}\Delta t}\right)= \\ =\frac{\Delta\boldsymbol{\sigma}_{\mathrm{J}}:\boldsymbol{m}}{H}\left(\left(\frac{-\eta\overline{F}}{H\Delta t^2}-\frac{1}{\Delta t}\right)\left(\boldsymbol{n}:\Delta\boldsymbol{\sigma}_{\mathrm{J}}\right)e^{\frac{-H}{\eta\overline{F}}\Delta t}\right) \tag{B.12}$$

Once all derivatives have been solved and by regrouping both parts $Part\,A$ and $Part\,B$, the complete expression of the derivative of ΔW^{vp} with respect to time increment is obtained as:

$$\frac{\partial\Delta W^{vp}}{\partial\Delta t}=\frac{\boldsymbol{\sigma}_{\mathrm{J0}}:\boldsymbol{m}}{H\Delta t}\left[\left(\boldsymbol{n}:\Delta\boldsymbol{\sigma}_{\mathrm{J}}\right)\left(\frac{\eta\overline{F}}{H\Delta t}+\left(\frac{-\eta\overline{F}}{H\Delta t}-1\right)e^{\frac{-H}{\eta\overline{F}}\Delta t}\right)\right]+\left(\boldsymbol{\sigma}_{\mathrm{J0}}+\Delta\boldsymbol{\sigma}_{\mathrm{J}}\right):\boldsymbol{m}\left(\frac{F_0}{\eta\overline{F}}e^{\frac{-H}{\eta\overline{F}}\Delta t}\right)+ \\ +\frac{\Delta\boldsymbol{\sigma}_{\mathrm{J}}:\boldsymbol{m}}{H\Delta t}\left[F_0\left(\frac{-\eta\overline{F}}{H\Delta t}+\left(\frac{\eta\overline{F}}{H\Delta t}+1\right)e^{\frac{-H}{\eta\overline{F}}\Delta t}\right)+\frac{2\left(\eta\overline{F}\right)^2}{H^2\Delta t^2}\left(\boldsymbol{n}:\Delta\boldsymbol{\sigma}_{\mathrm{J}}\right)+\right. \\ \left.+\left(\frac{\eta\overline{F}}{H\Delta t}\left(\frac{-2\eta\overline{F}}{H\Delta t}-1\right)+\left(\frac{-\eta\overline{F}}{H\Delta t}-1\right)\right)\left(\boldsymbol{n}:\Delta\boldsymbol{\sigma}_{\mathrm{J}}\right)e^{\frac{-H}{\eta\overline{F}}\Delta t}\right] \tag{B.13}$$

B.1.2 Derivative of ΔW^{vp} with respect to the stress increment

The derivatives with respect to the stress increment of the first part of ΔW^{vp} ($Part\,A$) are detailed below:

$$Part\,A=\frac{\boldsymbol{\sigma}_{\mathrm{J0}}:\boldsymbol{m}}{H}\left[F_0-F_0e^{\frac{-H}{\eta\overline{F}}\Delta t}\underbrace{-\frac{\eta\overline{F}}{H\Delta t}\left(\boldsymbol{n}:\Delta\boldsymbol{\sigma}_{\mathrm{J}}\right)}_{deriv.1A_s}\underbrace{+\frac{\eta\overline{F}}{H\Delta t}\left(\boldsymbol{n}:\Delta\boldsymbol{\sigma}_{\mathrm{J}}\right)e^{\frac{-H}{\eta\overline{F}}\Delta t}}_{deriv.2A_s}+\underbrace{\left(\boldsymbol{n}:\Delta\boldsymbol{\sigma}_{\mathrm{J}}\right)}_{deriv.3A_s}\right] \tag{B.14}$$

where

$$deriv.1A_s:\ \frac{\partial}{\partial\Delta\boldsymbol{\sigma}_{\mathrm{J}}}\frac{\boldsymbol{\sigma}_{\mathrm{J0}}:\boldsymbol{m}}{H}\left(-\frac{\eta\overline{F}}{H\Delta t}\left(\boldsymbol{n}:\Delta\boldsymbol{\sigma}_{\mathrm{J}}\right)\right)=\frac{\boldsymbol{\sigma}_{\mathrm{J0}}:\boldsymbol{m}}{H}\left(-\frac{\eta\overline{F}}{H\Delta t}\boldsymbol{n}\right) \tag{B.15}$$

$$deriv.2A_s:\ \frac{\partial}{\partial\Delta\boldsymbol{\sigma}_{\mathrm{J}}}\frac{\boldsymbol{\sigma}_{\mathrm{J0}}:\boldsymbol{m}}{H}\left(\frac{\eta\overline{F}}{H\Delta t}\left(\boldsymbol{n}:\Delta\boldsymbol{\sigma}_{\mathrm{J}}\right)e^{\frac{-H}{\eta\overline{F}}\Delta t}\right)=\frac{\boldsymbol{\sigma}_{\mathrm{J0}}:\boldsymbol{m}}{H}\left(\frac{\eta\overline{F}}{H\Delta t}e^{\frac{-H}{\eta\overline{F}}\Delta t}\boldsymbol{n}\right) \tag{B.16}$$

$$deriv.3A_s:\ \frac{\partial}{\partial\Delta\boldsymbol{\sigma}_{\mathrm{J}}}\frac{\boldsymbol{\sigma}_{\mathrm{J0}}:\boldsymbol{m}}{H}\left(\boldsymbol{n}:\Delta\boldsymbol{\sigma}_{\mathrm{J}}\right)=\frac{\boldsymbol{\sigma}_{\mathrm{J0}}:\boldsymbol{m}}{H}\boldsymbol{n} \tag{B.17}$$

Developing the derivatives with respect to the stress increment of the second part ($Part\,B$), the

following expressions may be obtained:

$$Part\,B = \frac{\Delta\boldsymbol{\sigma}_{\mathrm{J}} : \boldsymbol{m}}{H} \Bigg[\underbrace{F_0 \frac{\eta\overline{F}}{H\Delta t}}_{deriv.1B_s} \underbrace{-F_0 \frac{\eta\overline{F}}{H\Delta t} e^{\frac{-H}{\eta\overline{F}}\Delta t}}_{deriv.2B_s} \underbrace{-F_0 e^{\frac{-H}{\eta\overline{F}}\Delta t}}_{deriv.3B_s} \underbrace{-\frac{\left(\eta\overline{F}\right)^2}{H^2\Delta t^2} \left(\boldsymbol{n} : \Delta\boldsymbol{\sigma}_{\mathrm{J}}\right)}_{deriv.4B_s} + \\ + \underbrace{\frac{\left(\eta\overline{F}\right)^2}{H^2\Delta t^2} \left(\boldsymbol{n} : \Delta\boldsymbol{\sigma}_{\mathrm{J}}\right) e^{\frac{-H}{\eta\overline{F}}\Delta t}}_{deriv.5B_s} + \underbrace{\frac{\eta\overline{F}}{H\Delta t} \left(\boldsymbol{n} : \Delta\boldsymbol{\sigma}_{\mathrm{J}}\right) e^{\frac{-H}{\eta\overline{F}}\Delta t}}_{deriv.6B_s} + \underbrace{\left(\boldsymbol{n} : \Delta\boldsymbol{\sigma}_{\mathrm{J}}\right) \left(\frac{1}{2}\right)}_{deriv.7B_s} \Bigg] \tag{B.18}$$

where

$$deriv.1B_s : \ \frac{\partial}{\partial\Delta\boldsymbol{\sigma}_{\mathrm{J}}} \frac{\Delta\boldsymbol{\sigma}_{\mathrm{J}} : \boldsymbol{m}}{H} \left(F_0 \frac{\eta\overline{F}}{H\Delta t}\right) = \frac{\boldsymbol{m}}{H} \left(F_0 \frac{\eta\overline{F}}{H\Delta t}\right) \tag{B.19}$$

$$deriv.2B_s : \ \frac{\partial}{\partial\Delta\boldsymbol{\sigma}_{\mathrm{J}}} \frac{\Delta\boldsymbol{\sigma}_{\mathrm{J}} : \boldsymbol{m}}{H} \left(-F_0 \frac{\eta\overline{F}}{H\Delta t} e^{\frac{-H}{\eta\overline{F}}\Delta t}\right) = \frac{\boldsymbol{m}}{H} \left(-F_0 \frac{\eta\overline{F}}{H\Delta t} e^{\frac{-H}{\eta\overline{F}}\Delta t}\right) \tag{B.20}$$

$$deriv.3B_s : \ \frac{\partial}{\partial\Delta\boldsymbol{\sigma}_{\mathrm{J}}} \frac{\Delta\boldsymbol{\sigma}_{\mathrm{J}} : \boldsymbol{m}}{H} \left(-F_0 e^{\frac{-H}{\eta\overline{F}}\Delta t}\right) = \frac{\boldsymbol{m}}{H} \left(-F_0 e^{\frac{-H}{\eta\overline{F}}\Delta t}\right) \tag{B.21}$$

$$deriv.4B_s : \ \frac{\partial}{\partial\Delta\boldsymbol{\sigma}_{\mathrm{J}}} \frac{\Delta\boldsymbol{\sigma}_{\mathrm{J}} : \boldsymbol{m}}{H} \left(-\frac{\left(\eta\overline{F}\right)^2}{H^2\Delta t^2} \left(\boldsymbol{n} : \Delta\boldsymbol{\sigma}_{\mathrm{J}}\right)\right) = \frac{-1}{H} \frac{\left(\eta\overline{F}\right)^2}{H^2\Delta t^2} \left(\boldsymbol{m}\otimes\boldsymbol{n} + \boldsymbol{n}\otimes\boldsymbol{m}\right) : \Delta\boldsymbol{\sigma}_{\mathrm{J}} \tag{B.22}$$

$$deriv.5B_s : \frac{\partial}{\partial\Delta\boldsymbol{\sigma}_{\mathrm{J}}} \frac{\Delta\boldsymbol{\sigma}_{\mathrm{J}} : \boldsymbol{m}}{H} \left(\frac{\left(\eta\overline{F}\right)^2}{H^2\Delta t^2} \left(\boldsymbol{n} : \Delta\boldsymbol{\sigma}_{\mathrm{J}}\right) e^{\frac{-H}{\eta\overline{F}}\Delta t}\right) = \tag{B.23}$$
$$= \frac{1}{H} \frac{\left(\eta\overline{F}\right)^2}{H^2\Delta t^2} e^{\frac{-H}{\eta\overline{F}}\Delta t} \left(\boldsymbol{m}\otimes\boldsymbol{n} + \boldsymbol{n}\otimes\boldsymbol{m}\right) : \Delta\boldsymbol{\sigma}_{\mathrm{J}}$$

$$deriv.6B_s : \frac{\partial}{\partial\Delta\boldsymbol{\sigma}_{\mathrm{J}}} \frac{\Delta\boldsymbol{\sigma}_{\mathrm{J}} : \boldsymbol{m}}{H} \left(\frac{\eta\overline{F}}{H\Delta t} \left(\boldsymbol{n} : \Delta\boldsymbol{\sigma}_{\mathrm{J}}\right) e^{\frac{-H}{\eta\overline{F}}\Delta t}\right) = \tag{B.24}$$
$$= \frac{1}{H} \frac{\eta\overline{F}}{H\Delta t} e^{\frac{-H}{\eta\overline{F}}\Delta t} \left(\boldsymbol{m}\otimes\boldsymbol{n} + \boldsymbol{n}\otimes\boldsymbol{m}\right) : \Delta\boldsymbol{\sigma}_{\mathrm{J}}$$

$$deriv.7B_s : \ \frac{\partial}{\partial\Delta\boldsymbol{\sigma}_{\mathrm{J}}} \frac{\Delta\boldsymbol{\sigma}_{\mathrm{J}} : \boldsymbol{m}}{H} \left(\left(\boldsymbol{n} : \Delta\boldsymbol{\sigma}_{\mathrm{J}}\right) \left(\frac{1}{2}\right)\right) = \frac{1}{2H} \left(\boldsymbol{m}\otimes\boldsymbol{n} + \boldsymbol{n}\otimes\boldsymbol{m}\right) : \Delta\boldsymbol{\sigma}_{\mathrm{J}} \tag{B.25}$$

Considering all derivative expressions of both parts *Part A* and *Part B*, the resulting expression of the derivative of ΔW^{vp} with respect to the stress increment is:

$$\begin{aligned}\frac{\partial \Delta W^{vp}}{\partial \Delta \boldsymbol{\sigma}_{\mathrm{J}}} = \frac{\boldsymbol{\sigma}_{\mathrm{J0}} : \boldsymbol{m}}{H} \left[\left(\frac{\eta \overline{F}}{H \Delta t} \left(e^{\frac{-H}{\eta \overline{F}} \Delta t} - 1 \right) + 1 \right) \boldsymbol{n} \right] + \\ + \frac{1}{H} \left[F_0 \left(\frac{\eta \overline{F}}{H \Delta t} - \left(\frac{\eta \overline{F}}{H \Delta t} + 1 \right) e^{\frac{-H}{\eta \overline{F}} \Delta t} \right) \boldsymbol{m} + \right. \\ \left. + \left(\frac{\eta \overline{F}}{H \Delta t} \left(\frac{-\eta \overline{F}}{H \Delta t} + \left(\frac{\eta \overline{F}}{H \Delta t} + 1 \right) e^{\frac{-H}{\eta \overline{F}} \Delta t} \right) + \frac{1}{2} \right) (\boldsymbol{m} \otimes \boldsymbol{n} + \boldsymbol{n} \otimes \boldsymbol{m}) : \Delta \boldsymbol{\sigma}_{\mathrm{J}} \right]\end{aligned} \tag{B.26}$$

B.2 Limit cases of derivative expressions

As already mentioned in section 3.3.2.1.2, the derivatives of the visco-plastic dissipation with respect to the time increment (Eq. B.13) and the stress increment (Eq. B.26) become undefined because the expressions take an indeterminate form of the $\frac{0}{0}$ type when $\Delta t \to 0$ and/or $H \to 0$. Solving this indetermination requires the use of L'Hôpital's rule and Taylor series approximation $\left(\sum_{n=0}^{\infty} \frac{f^{(n)}(a)}{n!} (x-a)^n \right)$. From now on, note that f denotes the corresponding derivative expression in each case.

These developments are very extensive since L'Hôpital's rule must be applied several times to solve the indetermination and, therefore, to be concise the resulting expression of each term of the Taylor series approximation is presented in the following sections for each limit case evaluated.

B.2.1 Limit cases of $\frac{\partial \Delta W^{vp}}{\partial \Delta t}$ when Δt or H tend to zero

This section is dedicated to develop both limit cases $\Delta t \to 0$ and $H \to 0$ of the equation $f = \frac{\partial \Delta W^{vp}}{\partial \Delta t}$ (Eq. B.13).

B.2.1.1 Case $\Delta t \to 0$

The resulting expression of the first term of the Taylor series when $f(\Delta t \to 0)$ is:

$$f(\Delta t \to 0) = \boldsymbol{\sigma}_{\mathrm{J0}} : \boldsymbol{m} \left[\frac{F_0}{\eta \overline{F}} + \frac{(\boldsymbol{n} : \Delta \boldsymbol{\sigma}_{\mathrm{J}})}{2 \eta \overline{F}} \right] + \Delta \boldsymbol{\sigma}_{\mathrm{J}} : \boldsymbol{m} \left[\frac{F_0}{2 \eta \overline{F}} + \frac{(\boldsymbol{n} : \Delta \boldsymbol{\sigma}_{\mathrm{J}})}{3 \eta \overline{F}} \right] \tag{B.27}$$

In the same way, the development of the second term of the Taylor series approximation requires the first derivative of equation B.13 with respect to Δt, $f'(\Delta t)$, and the limit expression when

$\Delta t \to 0$ is presented below:

$$
\begin{aligned}
f'(\Delta t) = \frac{\boldsymbol{\sigma}_{J0} : \boldsymbol{m}}{H\Delta t^3}\Bigg(&-F_0\Delta t^3\frac{H^2}{\left(\eta\overline{F}\right)^2}e^{\frac{-H}{\eta\overline{F}}\Delta t} + \Delta t^2\left(\boldsymbol{n} : \Delta\boldsymbol{\sigma}_J\right)\frac{H}{\eta\overline{F}}e^{\frac{-H}{\eta\overline{F}}\Delta t} + 2\Delta t\left(\boldsymbol{n} : \Delta\boldsymbol{\sigma}_J\right)e^{\frac{-H}{\eta\overline{F}}\Delta t} + \\
&-2\frac{\eta\overline{F}}{H}\left(\boldsymbol{n} : \Delta\boldsymbol{\sigma}_J\right) + 2\frac{\eta\overline{F}}{H}\left(\boldsymbol{n} : \Delta\boldsymbol{\sigma}_J\right)e^{\frac{-H}{\eta\overline{F}}\Delta t}\Bigg) + \\
+\frac{\Delta\boldsymbol{\sigma}_J : \boldsymbol{m}}{H\Delta t^4}\Bigg(&-F_0\Delta t^4\frac{H^2}{\left(\eta\overline{F}\right)^2}e^{\frac{-H}{\eta\overline{F}}\Delta t} + \Delta t^3\left(\boldsymbol{n} : \Delta\boldsymbol{\sigma}_J\right)\frac{H}{\eta\overline{F}}e^{\frac{-H}{\eta\overline{F}}\Delta t} + \\
&- F_0\Delta t^3\frac{H}{\eta\overline{F}}e^{\frac{-H}{\eta\overline{F}}\Delta t} + 3\Delta t^2\left(\boldsymbol{n} : \Delta\boldsymbol{\sigma}_J\right)e^{\frac{-H}{\eta\overline{F}}\Delta t} + 2F_0\Delta t\frac{\eta\overline{F}}{H} - 2F_0\Delta t\frac{\eta\overline{F}}{H}e^{\frac{-H}{\eta\overline{F}}\Delta t} + \\
&- 2F_0\Delta t^2e^{\frac{-H}{\eta\overline{F}}\Delta t} - 6\frac{\eta\overline{F}}{H}\left(\boldsymbol{n} : \Delta\boldsymbol{\sigma}_J\right)\frac{\eta\overline{F}}{H} + 6\frac{\eta\overline{F}}{H}\left(\boldsymbol{n} : \Delta\boldsymbol{\sigma}_J\right)\frac{\eta\overline{F}}{H}e^{\frac{-H}{\eta\overline{F}}\Delta t} + \\
&+6\frac{\eta\overline{F}}{H}\Delta t\left(\boldsymbol{n} : \Delta\boldsymbol{\sigma}_J\right)e^{\frac{-H}{\eta\overline{F}}\Delta t}\Bigg)
\end{aligned}
\tag{B.28}
$$

$$
f'(\Delta t \to 0) = \boldsymbol{\sigma}_{J0} : \boldsymbol{m}\left[-\frac{F_0H}{\left(\eta\overline{F}\right)^2} - \frac{\left(\boldsymbol{n} : \Delta\boldsymbol{\sigma}_J\right)H}{3\left(\eta\overline{F}\right)^2}\right] + \Delta\boldsymbol{\sigma}_J : \boldsymbol{m}\left[-\frac{2F_0H}{3\left(\eta\overline{F}\right)^2} - \frac{\left(\boldsymbol{n} : \Delta\boldsymbol{\sigma}_J\right)H}{4\left(\eta\overline{F}\right)^2}\right] \tag{B.29}
$$

From these expressions (Eqs. B.27 and B.29), the resulting limit equation of $\frac{\partial\Delta W^{vp}}{\partial\Delta t}$ when $\Delta t \to 0$ may be written as:

$$
\begin{aligned}
\left.\frac{\partial\Delta W^{vp}}{\partial\Delta t}\right|_{Limit} = \boldsymbol{\sigma}_{J0} : \boldsymbol{m}&\left[F_0\left(\frac{1}{\eta\overline{F}} - \frac{H\Delta t}{\left(\eta\overline{F}\right)^2}\right) + \left(\frac{1}{2\eta\overline{F}} - \frac{H\Delta t}{3\left(\eta\overline{F}\right)^2}\right)\left(\boldsymbol{n} : \Delta\boldsymbol{\sigma}_J\right)\right] + \\
+\Delta\boldsymbol{\sigma}_J : \boldsymbol{m}&\left[F_0\left(\frac{1}{2\eta\overline{F}} - \frac{2H\Delta t}{3\left(\eta\overline{F}\right)^2}\right) + \left(\frac{1}{3\eta\overline{F}} - \frac{H\Delta t}{4\left(\eta\overline{F}\right)^2}\right)\left(\boldsymbol{n} : \Delta\boldsymbol{\sigma}_J\right)\right]
\end{aligned}
\tag{B.30}
$$

In addition, this limit equation (Eq. B.30) may be verified graphically in the near $\Delta t = 0$ zone. The following graphics (Fig. B.1) show a comparison between the original (Eq. B.13) and the limit (Eq. B.30) equations. The parameters used are $\overline{F} = 1.4$, $\eta = 10^6\ MPa{\cdot}s$, $H = -183884.6850\ MPa$, $\boldsymbol{n} = \begin{pmatrix} 0.7 \\ 0 \end{pmatrix}$, $\boldsymbol{m} = \begin{pmatrix} 0.7 \\ 0 \end{pmatrix}$, $\boldsymbol{\sigma}_{J0} = \begin{pmatrix} 3.0 \\ 0 \end{pmatrix} MPa$, $\Delta\boldsymbol{\sigma}_J = \begin{pmatrix} -0.35709822 \\ 0 \end{pmatrix} MPa$ and $F_0 = 0.7$ taken from the pure tension example with softening found in the verification examples section (Sec. 3.5.1).

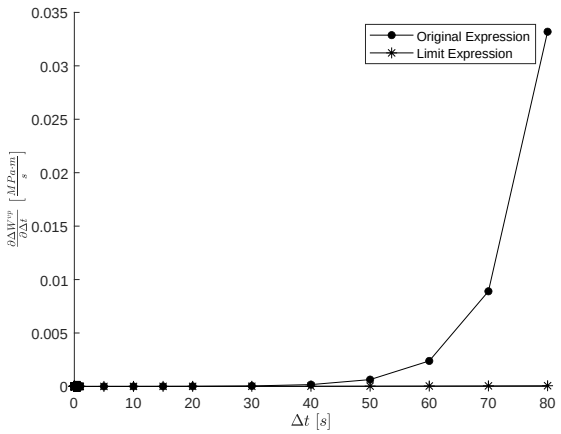

(a) Limit case $\Delta t \to 0$: Evolution of $\frac{\partial \Delta W^{vp}}{\partial \Delta t}$ over time.

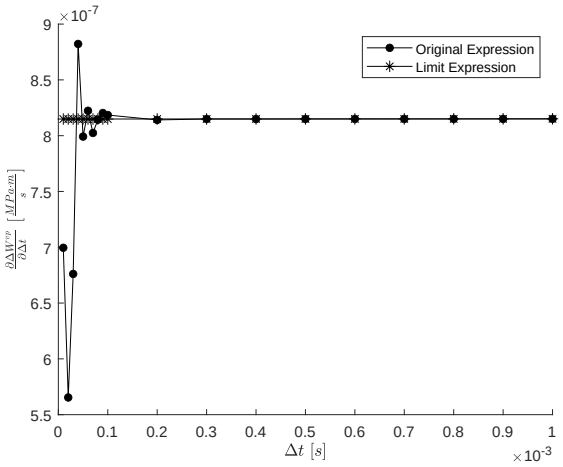

(b) Limit case $\Delta t \to 0$: Evolution of $\frac{\partial \Delta W^{vp}}{\partial \Delta t}$ in the first moments of time.

Figure B.1: Representation of both original and limit expressions $\left(\frac{\partial \Delta W^{vp}}{\partial \Delta t}\right)$ for $\Delta t \to 0$ limit case.

B.2.1.2 Case $H \to 0$

The other limit case is when $H \to 0$ and the procedure performed is the same as in the previous limit case. The resulting expression of the first term of the Taylor series approximation $f\,(H \to 0)$ obtained from applying L'Hôpital's development is shown below:

$$f\,(H \to 0) = \boldsymbol{\sigma}_{\mathrm{J}0} : \boldsymbol{m} \left[\frac{F_0}{\eta \overline{F}} + \frac{(\boldsymbol{n} : \Delta \boldsymbol{\sigma}_{\mathrm{J}})}{2\eta \overline{F}} \right] + \Delta \boldsymbol{\sigma}_{\mathrm{J}} : \boldsymbol{m} \left[\frac{F_0}{2\eta \overline{F}} + \frac{(\boldsymbol{n} : \Delta \boldsymbol{\sigma}_{\mathrm{J}})}{3\eta \overline{F}} \right] \tag{B.31}$$

The limit expression of the second term of the Taylor series approximation, which includes the first derivative of equation B.13 with respect to H, $f'\,(H)$, is also obtained after some calculations:

$$
\begin{aligned}
f'(H) = \frac{\boldsymbol{\sigma}_{J0} : \boldsymbol{m}}{H^3 \Delta t^2} \Bigg(& -F_0 H^3 \frac{\Delta t^3}{\left(\eta \overline{F}\right)^2} e^{\frac{-H}{\eta \overline{F}} \Delta t} + H^2 \frac{\Delta t^2}{\eta \overline{F}} \left(\boldsymbol{n} : \Delta \boldsymbol{\sigma}_J\right) e^{\frac{-H}{\eta \overline{F}} \Delta t} + \\
& + 2 \Delta t H \left(\boldsymbol{n} : \Delta \boldsymbol{\sigma}_J\right) e^{\frac{-H}{\eta \overline{F}} \Delta t} - 2 \eta \overline{F} \left(\boldsymbol{n} : \Delta \boldsymbol{\sigma}_J\right) + 2 \eta \overline{F} \left(\boldsymbol{n} : \Delta \boldsymbol{\sigma}_J\right) e^{\frac{-H}{\eta \overline{F}} \Delta t} \Bigg) + \\
& + \frac{\Delta \boldsymbol{\sigma}_J : \boldsymbol{m}}{H^4 \Delta t^3} \Bigg(-F_0 H^4 \frac{\Delta t^4}{\left(\eta \overline{F}\right)^2} e^{\frac{-H}{\eta \overline{F}} \Delta t} + \left(\boldsymbol{n} : \Delta \boldsymbol{\sigma}_J\right) H^3 \frac{\Delta t^3}{\eta \overline{F}} e^{\frac{-H}{\eta \overline{F}} \Delta t} + \\
& - F_0 H^3 \frac{\Delta t^3}{\eta \overline{F}} e^{\frac{-H}{\eta \overline{F}} \Delta t} + 3 \left(\boldsymbol{n} : \Delta \boldsymbol{\sigma}_J\right) H^2 \Delta t^2 e^{\frac{-H}{\eta \overline{F}} \Delta t} + 2 F_0 H \Delta t \eta \overline{F} - 2 F_0 H \Delta t \eta \overline{F} e^{\frac{-H}{\eta \overline{F}} \Delta t} + \\
& - 2 F_0 H^2 \Delta t^2 e^{\frac{-H}{\eta \overline{F}} \Delta t} - 6 \left(\eta \overline{F}\right)^2 \left(\boldsymbol{n} : \Delta \boldsymbol{\sigma}_J\right) + 6 \left(\eta \overline{F}\right)^2 \left(\boldsymbol{n} : \Delta \boldsymbol{\sigma}_J\right) e^{\frac{-H}{\eta \overline{F}} \Delta t} + \\
& + 6 \eta \overline{F} H \left(\boldsymbol{n} : \Delta \boldsymbol{\sigma}_J\right) \Delta t e^{\frac{-H}{\eta \overline{F}} \Delta t} \Bigg)
\end{aligned}
\tag{B.32}
$$

$$
f'(H \to 0) = \boldsymbol{\sigma}_{J0} : \boldsymbol{m} \left[-\frac{F_0 \Delta t}{\left(\eta \overline{F}\right)^2} - \frac{\left(\boldsymbol{n} : \Delta \boldsymbol{\sigma}_J\right) \Delta t}{3 \left(\eta \overline{F}\right)^2} \right] + \Delta \boldsymbol{\sigma}_J : \boldsymbol{m} \left[-\frac{2 F_0 \Delta t}{3 \left(\eta \overline{F}\right)^2} - \frac{\left(\boldsymbol{n} : \Delta \boldsymbol{\sigma}_J\right) \Delta t}{4 \left(\eta \overline{F}\right)^2} \right] \tag{B.33}
$$

The resulting limit expression when $H \to 0$ is composed by grouping equations (B.31 and B.33). Fortunately, the limit expression deduced for both cases $\Delta t \to 0$ and $H \to 0$ is exactly the same (Eq. B.30). For verification purposes, a graphic comparison between the original (Eq. B.13) and the limit (Eq. B.30) expressions has been performed (Fig. B.2). The parameters used in this case are the same as those used for the previous case $\Delta t \to 0$ (Sec. B.2.1.1) only substituting the H parameter by $\Delta t = 1.0\, s$.

B.2.2 Limit cases of $\frac{\partial \Delta W^{vp}}{\partial \Delta \sigma_J}$ when Δt or H tend to zero

The other derivative that must be evaluated considering both limit cases $\Delta t \to 0$ and $H \to 0$ is $\frac{\partial \Delta W^{vp}}{\partial \Delta \boldsymbol{\sigma}_J}$. The original equation of this derivative is given by equation (B.26).

B.2.2.1 Case $\Delta t \to 0$

Following the same procedure outlined for $\frac{\partial \Delta W^{vp}}{\partial \Delta t}$ in the previous section B.2.1, the $\Delta t \to 0$ limit case is analyzed first. Note that, in this case, the first term of the Taylor series approximation $f(\Delta t \to 0)$ leads to a zero value: $f = \frac{\partial \Delta W^{vp}}{\partial \Delta \boldsymbol{\sigma}_J}(\Delta t = 0) = 0$.

The second Taylor's term requires the first derivative of equation (B.26) with respect to Δt,

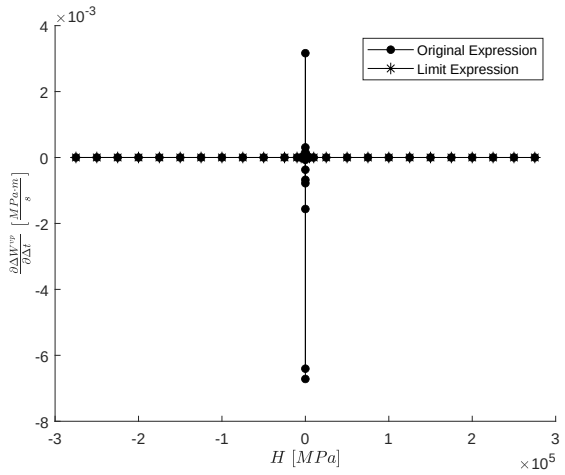

(a) Limit case $H \to 0$: Evolution of $\frac{\partial \Delta W^{vp}}{\partial \Delta t}$ along H.

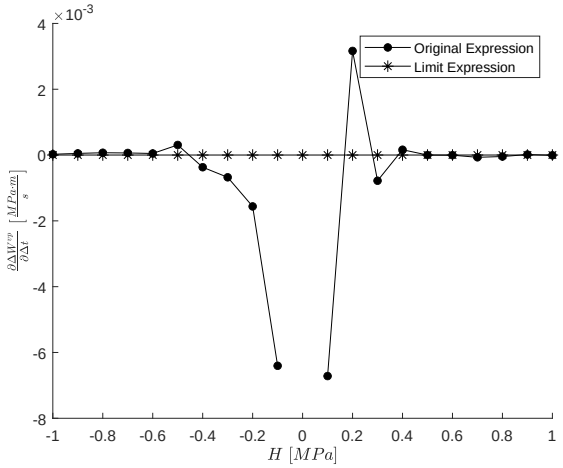

(b) Limit case $H \to 0$: Evolution of $\frac{\partial \Delta W^{vp}}{\partial \Delta t}$ in the near zero H values.

Figure B.2: Representation of both original and limit expressions $\left(\frac{\partial \Delta W^{vp}}{\partial \Delta t}\right)$ for $H \to 0$ limit case.

$f'(\Delta t)$, and the resulting expression when $(\Delta t \to 0)$ is given below:

$$
\begin{aligned}
f'(\Delta t) = \frac{\boldsymbol{\sigma}_{\mathrm{J0}} : \boldsymbol{m}}{H\Delta t^2} \Bigg(\Bigg(-\Delta t e^{\frac{-H}{\eta \overline{F}}\Delta t} - \frac{\eta \overline{F}}{H} e^{\frac{-H}{\eta \overline{F}}\Delta t} + \frac{\eta \overline{F}}{H} \Bigg) \boldsymbol{n} \Bigg) + \\
+ \frac{1}{H\Delta t^3} \Bigg[\Bigg(F_0 \Delta t^3 \frac{H}{\eta \overline{F}} e^{\frac{-H}{\eta \overline{F}}\Delta t} - F_0 \Delta t \frac{\eta \overline{F}}{H} + F_0 \Delta t \frac{\eta \overline{F}}{H} e^{\frac{-H}{\eta \overline{F}}\Delta t} + F_0 \Delta t^2 e^{\frac{-H}{\eta \overline{F}}\Delta t} \Bigg) \boldsymbol{m} + \\
+ \Bigg(-\Delta t^2 e^{\frac{-H}{\eta \overline{F}}\Delta t} + \frac{2\left(\eta \overline{F}\right)^2}{H^2} - \frac{2\left(\eta \overline{F}\right)^2}{H^2} e^{\frac{-H}{\eta \overline{F}}\Delta t} - 2\frac{\eta \overline{F}}{H} \Delta t e^{\frac{-H}{\eta \overline{F}}\Delta t} \Bigg) \\
(\boldsymbol{m} \otimes \boldsymbol{n} + \boldsymbol{n} \otimes \boldsymbol{m}) : \Delta \boldsymbol{\sigma} \Bigg]
\end{aligned}
\tag{B.34}
$$

$$
f'(\Delta t \to 0) = \boldsymbol{\sigma}_0 : \boldsymbol{m} \left[\frac{1}{2\eta \overline{F}} \boldsymbol{n} \right] + \left(\frac{F_0}{2\eta \overline{F}} \right) \boldsymbol{m} + \left(\frac{1}{3\eta \overline{F}} \right) (\boldsymbol{m} \otimes \boldsymbol{n} + \boldsymbol{n} \otimes \boldsymbol{m}) : \Delta \boldsymbol{\sigma} \tag{B.35}
$$

In this case, due to the first Taylor's term being zero, it is suitable to develop a third additional Taylor's term to obtain a better approximation. For this reason, the second derivative with respect to Δt, $f''(\Delta t)$, is also presented below (Eq. B.36) together with its limit equation (B.37):

$$\begin{aligned} f''(\Delta t) = \frac{\boldsymbol{\sigma}_{J0} : \boldsymbol{m}}{H\Delta t^3}\left(\left(\Delta t^2 \frac{H}{\eta\overline{F}} e^{\frac{-H}{\eta\overline{F}}\Delta t} + 2\Delta t e^{\frac{-H}{\eta\overline{F}}\Delta t} + 2\frac{\eta\overline{F}}{H} e^{\frac{-H}{\eta\overline{F}}\Delta t} - 2\frac{\eta\overline{F}}{H}\right)\boldsymbol{n}\right) + \\ + \frac{1}{H\Delta t^4}\left[\left(-F_0\Delta t^4 \frac{H^2}{\left(\eta\overline{F}\right)^2} e^{\frac{-H}{\eta\overline{F}}\Delta t} - F_0\Delta t^3 \frac{H}{\eta\overline{F}} e^{\frac{-H}{\eta\overline{F}}\Delta t} + 2F_0\Delta t \frac{\eta\overline{F}}{H} + \right.\right. \\ \left. -2F_0\Delta t \frac{\eta\overline{F}}{H} e^{\frac{-H}{\eta\overline{F}}\Delta t} - 2F_0\Delta t^2 e^{\frac{-H}{\eta\overline{F}}\Delta t}\right)\boldsymbol{m} + \\ + \left(\Delta t^3 \frac{H}{\eta\overline{F}} e^{\frac{-H}{\eta\overline{F}}\Delta t} + 3\Delta t^2 e^{\frac{-H}{\eta\overline{F}}\Delta t} - 6\frac{\left(\eta\overline{F}\right)^2}{H^2} + \right. \\ \left.\left. + 6\frac{\left(\eta\overline{F}\right)^2}{H^2} e^{\frac{-H}{\eta\overline{F}}\Delta t} + 6\frac{\eta\overline{F}}{H}\Delta t e^{\frac{-H}{\eta\overline{F}}\Delta t}\right)(\boldsymbol{m}\otimes\boldsymbol{n} + \boldsymbol{n}\otimes\boldsymbol{m}) : \Delta\boldsymbol{\sigma}_J\right] \end{aligned} \tag{B.36}$$

$$\begin{aligned} f''(\Delta t \to 0) = \boldsymbol{\sigma}_{J0} : \boldsymbol{m}\left[-\frac{H}{3\left(\eta\overline{F}\right)^2}\boldsymbol{n}\right] + \left(-2F_0\frac{H}{3\left(\eta\overline{F}\right)^2}\right)\boldsymbol{m} + \\ + \left(-\frac{H}{4\left(\eta\overline{F}\right)^2}\right)(\boldsymbol{m}\otimes\boldsymbol{n} + \boldsymbol{n}\otimes\boldsymbol{m}) : \Delta\boldsymbol{\sigma}_J \end{aligned} \tag{B.37}$$

Regrouping the limit expressions of the Taylor series approximation terms (Eqs. B.35 and B.37), the complete limit expression of $\frac{\partial\Delta W^{vp}}{\partial\Delta\boldsymbol{\sigma}_J}$ when $\Delta t \to 0$ is:

$$\begin{aligned} \left.\frac{\partial\Delta W^{vp}}{\partial\Delta\boldsymbol{\sigma}_J}\right|_{Limit} = \boldsymbol{\sigma}_{J0} : \boldsymbol{m}\left(\frac{\Delta t}{2\eta\overline{F}}\boldsymbol{n}\right) + F_0\frac{\Delta t}{2\eta\overline{F}}\boldsymbol{m} + \left(\frac{\Delta t}{3\eta\overline{F}}\right)(\boldsymbol{m}\otimes\boldsymbol{n} + \boldsymbol{n}\otimes\boldsymbol{m}) : \Delta\boldsymbol{\sigma}_J + \\ + \boldsymbol{\sigma}_{J0} : \boldsymbol{m}\left(-\frac{H\Delta t^2}{6\left(\eta\overline{F}\right)^2}\boldsymbol{n}\right) + \left(-F_0\frac{H\Delta t^2}{3\left(\eta\overline{F}\right)^2}\right)\boldsymbol{m} + \\ + \left(-\frac{H\Delta t^2}{8\left(\eta\overline{F}\right)^2}\right)(\boldsymbol{m}\otimes\boldsymbol{n} + \boldsymbol{n}\otimes\boldsymbol{m}) : \Delta\boldsymbol{\sigma}_J \end{aligned} \tag{B.38}$$

As has been done before, the limit expression (Eq. B.38) is graphically verified in the near $\Delta t = 0$ zone. The following graphics (Fig. B.3) show a comparison between the original equation (Eq. B.26) and the limit one (Eq. B.38). The parameters used are $\overline{F} = 1.4$, $\eta = 10^6\, MPa{\cdot}s$, $H = -183884.6850\, MPa$, $\boldsymbol{n} = \begin{pmatrix} 0.7 \\ 0 \end{pmatrix}$, $\boldsymbol{m} = \begin{pmatrix} 0.7 \\ 0 \end{pmatrix}$, $\boldsymbol{\sigma}_{J0} = \begin{pmatrix} 3.0 \\ 0 \end{pmatrix} MPa$,

$\Delta\boldsymbol{\sigma}_{\mathrm{J}} = \begin{pmatrix} -0.35709822 \\ 0 \end{pmatrix} MPa$ and $F_0 = 0.7$ taken from the pure tension example with softening found in the verification examples section (Sec. 3.5.1).

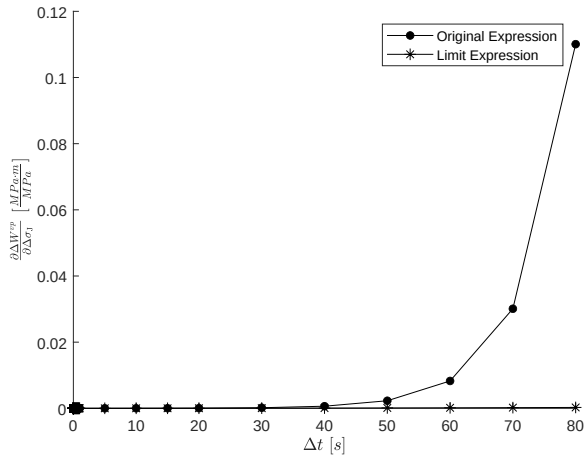

(a) Limit case $\Delta t \to 0$: Evolution of $\frac{\partial \Delta W^{vp}}{\partial \Delta \boldsymbol{\sigma}_{\mathrm{J}}}$ over time.

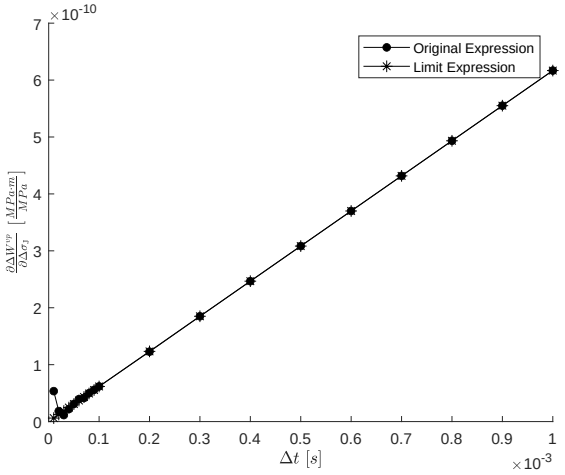

(b) Limit case $\Delta t \to 0$: Evolution of $\frac{\partial \Delta W^{vp}}{\partial \Delta \boldsymbol{\sigma}_{\mathrm{J}}}$ in the first moments of time.

Figure B.3: Representation of both original and limit expressions $\left(\frac{\partial \Delta W^{vp}}{\partial \Delta \boldsymbol{\sigma}_{\mathrm{J}}}\right)$ for $\Delta t \to 0$ limit case.

B.2.2.2 Case $H \to 0$

The other limit case analyzed for $\frac{\partial \Delta W^{vp}}{\partial \Delta \boldsymbol{\sigma}_{\mathrm{J}}}$ is when H tends to zero. In this sense, the development of the Taylor series approximation is required and the resulting expression of the first term is presented below:

$$f\left(H \to 0\right) = \boldsymbol{\sigma}_{\mathrm{J}0} : \boldsymbol{m}\left(\frac{\Delta t}{2\eta\overline{F}}\boldsymbol{n}\right) + \left(F_0\frac{\Delta t}{2\eta\overline{F}}\right)\boldsymbol{m} + \left(\frac{\Delta t}{3\eta\overline{F}}\right)\left(\boldsymbol{m}\otimes\boldsymbol{n} + \boldsymbol{n}\otimes\boldsymbol{m}\right) : \Delta\boldsymbol{\sigma}_{\mathrm{J}} \tag{B.39}$$

The second Taylor's term requires the first derivative of equation (B.26) with respect to H, $f'\left(H\right)$, and the limit expression of this term when $H \to 0$ is also shown below:

$$
\begin{aligned}
f'(H) = \frac{\boldsymbol{\sigma}_{J0} : \boldsymbol{m}}{H^3} \Bigg(& -He^{\frac{-H}{\eta\overline{F}}\Delta t}\boldsymbol{n} - 2\frac{\eta\overline{F}}{\Delta t}e^{\frac{-H}{\eta\overline{F}}\Delta t}\boldsymbol{n} + 2\frac{\eta\overline{F}}{\Delta t}\boldsymbol{n} - H\boldsymbol{n}\Bigg) + \\
& + \frac{1}{H^4}\Bigg[\Bigg(H^3F_0\frac{\Delta t}{\eta\overline{F}}e^{\frac{-H}{\eta\overline{F}}\Delta t} - 2HF_0\frac{\eta\overline{F}}{\Delta t} + 2HF_0\frac{\eta\overline{F}}{\Delta t}e^{\frac{-H}{\eta\overline{F}}\Delta t} + 2H^2F_0e^{\frac{-H}{\eta\overline{F}}\Delta t}\Bigg)\boldsymbol{m} + \\
& + \Bigg(-H^2e^{\frac{-H}{\eta\overline{F}}\Delta t} + 3\frac{\left(\eta\overline{F}\right)^2}{\Delta t^2} - 3\frac{\left(\eta\overline{F}\right)^2}{\Delta t^2}e^{\frac{-H}{\eta\overline{F}}\Delta t} \\
& -3H\frac{\eta\overline{F}}{\Delta t}e^{\frac{-H}{\eta\overline{F}}\Delta t} - \frac{1}{2}H^2\Bigg)(\boldsymbol{m}\otimes\boldsymbol{n} + \boldsymbol{n}\otimes\boldsymbol{m}) : \Delta\boldsymbol{\sigma}_J\Bigg]
\end{aligned}
\tag{B.40}
$$

$$
\begin{aligned}
f'(H\to 0) = \boldsymbol{\sigma}_{J0} : \boldsymbol{m}\left(-\frac{\Delta t^2}{6\left(\eta\overline{F}\right)^2}\boldsymbol{n}\right) + \left(-F_0\frac{\Delta t^2}{3\left(\eta\overline{F}\right)^2}\right)\boldsymbol{m} + \\
+ \left(-\frac{\Delta t^2}{8\left(\eta\overline{F}\right)^2}\right)(\boldsymbol{m}\otimes\boldsymbol{n} + \boldsymbol{n}\otimes\boldsymbol{m}) : \Delta\boldsymbol{\sigma}_J
\end{aligned}
\tag{B.41}
$$

Note that, by regrouping the limit expressions corresponding to each term of the Taylor series approximation, the complete limit expression obtained for the $H \to 0$ case is exactly the same that the one deduced for the $\Delta t \to 0$ case (Eq. B.38). For verification purposes, a graphic comparison between the original (Eq. B.26) and limit (Eq. B.38) expressions has been performed (Fig. B.4). The parameters used in this case are the same as those used for the previous case $\Delta t \to 0$ (Sec. B.2.2.1) only substituting the H parameter by $\Delta t = 1.0\,s$.

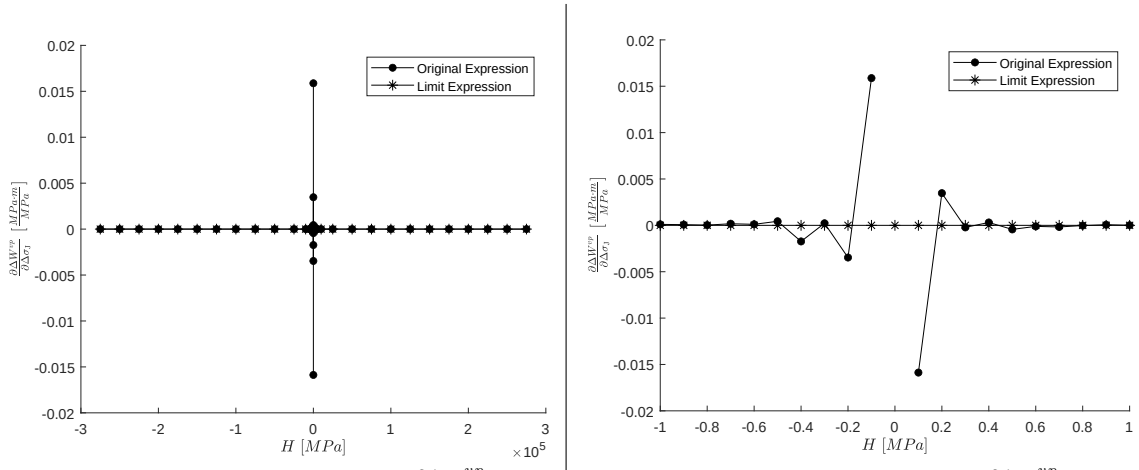

(a) Limit case $H \to 0$: Evolution of $\frac{\partial\Delta W^{vp}}{\partial\Delta\boldsymbol{\sigma}_J}$ along H.

(b) Limit case $H \to 0$: Evolution of $\frac{\partial\Delta W^{vp}}{\partial\Delta\boldsymbol{\sigma}_J}$ in the near zero H values.

Figure B.4: Representation of both original and limit expressions $\left(\frac{\partial\Delta W^{vp}}{\partial\Delta\boldsymbol{\sigma}_J}\right)$ for $H \to 0$ limit case.

Appendix C

IDC-Wvp: Case of target in terms of fracture dissipation

Similar to what was done in Appendix B, the developments of the derivatives with respect to the time increment and stress increment ($\frac{\partial \Delta W^{vcr}}{\partial \Delta t}$ and $\frac{\partial \Delta W^{vcr}}{\partial \Delta \boldsymbol{\sigma}_{\mathrm{J}}}$) together with the corresponding limit expressions, considering firstly $\Delta t \to 0$ and then $H \to 0$, are detailed in this appendix when only fracture dissipation target is considered (Eq. 3.41).

C.1 Derivatives of ΔW^{vcr}

Once more, for convenience, the right-hand-side of ΔW^{vcr} (Eq. 3.41) has been divided into two parts in order to develop the derivatives with respect to the time increment duration and to the stress increment:

$$\begin{aligned}\Delta W^{vcr} = & \underbrace{\left(\sigma_{T0} + \sigma_{N0}\tan\phi\right)\frac{m_T}{H}\left[\left(F_0 - \frac{\eta\overline{F}}{H\Delta t}\left(\boldsymbol{n} : \Delta\boldsymbol{\sigma}_{\mathrm{J}}\right)\right)\left(1 - e^{\frac{-H}{\eta\overline{F}}\Delta t}\right) + \left(\boldsymbol{n} : \Delta\boldsymbol{\sigma}_{\mathrm{J}}\right)\right]}_{Part\,C} + \\ & + \underbrace{\left(\frac{\Delta\sigma_T}{\Delta t} + \frac{\Delta\sigma_N}{\Delta t}\tan\phi\right)\frac{m_T}{H}\left[\left(F_0 - \frac{\eta\overline{F}}{H\Delta t}\left(\boldsymbol{n} : \Delta\boldsymbol{\sigma}_{\mathrm{J}}\right)\right)\left(\frac{\eta\overline{F}}{H} - \left(\frac{\eta\overline{F}}{H} + \Delta t\right)e^{\frac{-H}{\eta\overline{F}}\Delta t}\right) + \right.}_{Part\,D} \\ & \underbrace{\left. + \left(\boldsymbol{n} : \Delta\boldsymbol{\sigma}_{\mathrm{J}}\right)\left(\frac{\Delta t}{2}\right)\right]}_{Part\,D}\end{aligned} \tag{C.1}$$

C.1.1 Derivative of ΔW^{vcr} with respect to the time increment

Developing the derivative with respect to the time increment of the first part ($Part\,C$), note that this part is further divided into different derivative terms for convenience and to facilitate calculations:

$$Part\,C = (\sigma_{T0} + \sigma_{N0}\tan\phi)\,\frac{m_T}{H}\left[F_0\underbrace{-F_0 e^{\frac{-H}{\eta\overline{F}}\Delta t}}_{deriv.1C_t}\underbrace{-\frac{\eta\overline{F}}{H\Delta t}\,(\boldsymbol{n}:\Delta\boldsymbol{\sigma}_{\mathrm{J}})}_{deriv.2C_t} + \underbrace{+\frac{\eta\overline{F}}{H\Delta t}\,(\boldsymbol{n}:\Delta\boldsymbol{\sigma}_{\mathrm{J}})\,e^{\frac{-H}{\eta\overline{F}}\Delta t}}_{deriv.3C_t} + (\boldsymbol{n}:\Delta\boldsymbol{\sigma}_{\mathrm{J}})\right] \tag{C.2}$$

where

$$deriv.1C_t:\ \frac{\partial}{\partial\Delta t}\,(\sigma_{T0} + \sigma_{N0}\tan\phi)\,\frac{m_T}{H}\left(-F_0 e^{\frac{-H}{\eta\overline{F}}\Delta t}\right) = (\sigma_{T0} + \sigma_{N0}\tan\phi)\,m_T\frac{F_0}{\eta\overline{F}}e^{\frac{-H}{\eta\overline{F}}\Delta t} \tag{C.3}$$

$$\begin{aligned} deriv.2C_t:\ &\frac{\partial}{\partial\Delta t}\,(\sigma_{T0} + \sigma_{N0}\tan\phi)\,\frac{m_T}{H}\left(-\frac{\eta\overline{F}}{H\Delta t}\,(\boldsymbol{n}:\Delta\boldsymbol{\sigma}_{\mathrm{J}})\right) = \\ &= (\sigma_{T0} + \sigma_{N0}\tan\phi)\,\frac{m_T}{H}\frac{\eta\overline{F}}{H\Delta t^2}\,(\boldsymbol{n}:\Delta\boldsymbol{\sigma}_{\mathrm{J}}) \end{aligned} \tag{C.4}$$

$$\begin{aligned} deriv.3C_t:\ &\frac{\partial}{\partial\Delta t}\,(\sigma_{T0} + \sigma_{N0}\tan\phi)\,\frac{m_T}{H}\left(\frac{\eta\overline{F}}{H\Delta t}\,(\boldsymbol{n}:\Delta\boldsymbol{\sigma}_{\mathrm{J}})\,e^{\frac{-H}{\eta\overline{F}}\Delta t}\right) = \\ &= (\sigma_{T0} + \sigma_{N0}\tan\phi)\,\frac{m_T}{H}\left(\frac{-\eta\overline{F}}{H\Delta t^2} - \frac{1}{\Delta t}\right)(\boldsymbol{n}:\Delta\boldsymbol{\sigma}_{\mathrm{J}})\,e^{\frac{-H}{\eta\overline{F}}\Delta t} \end{aligned} \tag{C.5}$$

The second part of the ΔW^{vcr} expression ($Part\,D$) is composed, in turn, of several parts detailed below:

$$\begin{aligned} Part\,D = (\Delta\sigma_T + \Delta\sigma_N\tan\phi)\,\frac{m_T}{H}\Bigg[&\underbrace{F_0\frac{\eta\overline{F}}{H\Delta t}}_{deriv.1D_t}\underbrace{-F_0\frac{\eta\overline{F}}{H\Delta t}e^{\frac{-H}{\eta\overline{F}}\Delta t}}_{deriv.2D_t}\underbrace{-F_0 e^{\frac{-H}{\eta\overline{F}}\Delta t}}_{deriv.3D_t}\underbrace{-\frac{\left(\eta\overline{F}\right)^2}{H^2\Delta t^2}\,(\boldsymbol{n}:\Delta\boldsymbol{\sigma}_{\mathrm{J}})}_{deriv.4D_t} + \\ &+\underbrace{\frac{\left(\eta\overline{F}\right)^2}{H^2\Delta t^2}\,(\boldsymbol{n}:\Delta\boldsymbol{\sigma}_{\mathrm{J}})\,e^{\frac{-H}{\eta\overline{F}}\Delta t}}_{deriv.5D_t} + \underbrace{\frac{\eta\overline{F}}{H\Delta t}\,(\boldsymbol{n}:\Delta\boldsymbol{\sigma}_{\mathrm{J}})\,e^{\frac{-H}{\eta\overline{F}}\Delta t}}_{deriv.6D_t} + (\boldsymbol{n}:\Delta\boldsymbol{\sigma}_{\mathrm{J}})\left(\frac{1}{2}\right)\Bigg] \end{aligned} \tag{C.6}$$

where

$$deriv.1D_t : \frac{\partial}{\partial \Delta t}\left(\Delta\sigma_T + \Delta\sigma_N \tan\phi\right)\frac{m_T}{H}\left(F_0\frac{\eta\overline{F}}{H\Delta t}\right) = \\ = \left(\Delta\sigma_T + \Delta\sigma_N \tan\phi\right)\frac{m_T}{H}\left(F_0\frac{-\eta\overline{F}}{H\Delta t^2}\right) \tag{C.7}$$

$$deriv.2D_t : \frac{\partial}{\partial \Delta t}\left(\Delta\sigma_T + \Delta\sigma_N \tan\phi\right)\frac{m_T}{H}\left(-F_0\frac{\eta\overline{F}}{H\Delta t}e^{\frac{-H}{\eta\overline{F}}\Delta t}\right) = \\ = \left(\Delta\sigma_T + \Delta\sigma_N \tan\phi\right)\frac{m_T}{H}F_0\left[\frac{\eta\overline{F}}{H\Delta t^2} + \frac{1}{\Delta t}\right]e^{\frac{-H}{\eta\overline{F}}\Delta t} \tag{C.8}$$

$$deriv.3D_t : \frac{\partial}{\partial \Delta t}\left(\Delta\sigma_T + \Delta\sigma_N \tan\phi\right)\frac{m_T}{H}\left(-F_0 e^{\frac{-H}{\eta\overline{F}}\Delta t}\right) = \\ = \left(\Delta\sigma_T + \Delta\sigma_N \tan\phi\right)m_T\left(\frac{F_0}{\eta\overline{F}}e^{\frac{-H}{\eta\overline{F}}\Delta t}\right) \tag{C.9}$$

$$deriv.4D_t : \frac{\partial}{\partial \Delta t}\left(\Delta\sigma_T + \Delta\sigma_N \tan\phi\right)\frac{m_T}{H}\left(-\frac{\left(\eta\overline{F}\right)^2}{H^2\Delta t^2}\left(\boldsymbol{n} : \Delta\boldsymbol{\sigma}_{\mathrm{J}}\right)\right) = \\ = \left(\Delta\sigma_T + \Delta\sigma_N \tan\phi\right)\frac{m_T}{H}\left(2\frac{\left(\eta\overline{F}\right)^2}{H^2\Delta t^3}\right)\left(\boldsymbol{n} : \Delta\boldsymbol{\sigma}_{\mathrm{J}}\right) \tag{C.10}$$

$$deriv.5D_t : \frac{\partial}{\partial \Delta t}\left(\Delta\sigma_T + \Delta\sigma_N \tan\phi\right)\frac{m_T}{H}\left(\frac{\left(\eta\overline{F}\right)^2}{H^2\Delta t^2}\left(\boldsymbol{n} : \Delta\boldsymbol{\sigma}_{\mathrm{J}}\right)e^{\frac{-H}{\eta\overline{F}}\Delta t}\right) = \\ = \left(\Delta\sigma_T + \Delta\sigma_N \tan\phi\right)\frac{m_T}{H}\left(\frac{\eta\overline{F}}{H\Delta t^2}\left(\frac{-2\eta\overline{F}}{H\Delta t} - 1\right)\left(\boldsymbol{n} : \Delta\boldsymbol{\sigma}_{\mathrm{J}}\right)e^{\frac{-H}{\eta\overline{F}}\Delta t}\right) \tag{C.11}$$

$$deriv.6D_t : \frac{\partial}{\partial \Delta t}\left(\Delta\sigma_T + \Delta\sigma_N \tan\phi\right)\frac{m_T}{H}\left(\frac{\eta\overline{F}}{H\Delta t}\left(\boldsymbol{n} : \Delta\boldsymbol{\sigma}_{\mathrm{J}}\right)e^{\frac{-H}{\eta\overline{F}}\Delta t}\right) = \\ = \left(\Delta\sigma_T + \Delta\sigma_N \tan\phi\right)\frac{m_T}{H}\left(\left(\frac{-\eta\overline{F}}{H\Delta t^2} - \frac{1}{\Delta t}\right)\left(\boldsymbol{n} : \Delta\boldsymbol{\sigma}_{\mathrm{J}}\right)e^{\frac{-H}{\eta\overline{F}}\Delta t}\right) \tag{C.12}$$

Once all derivatives have been solved and by regrouping both parts $Part\,C$ and $Part\,D$, the complete expression of the derivative of ΔW^{vcr} with respect to time increment is obtained as:

$$\begin{aligned}\frac{\partial \Delta W^{vcr}}{\partial \Delta t} &= (\sigma_{T0} + \sigma_{N0}\tan\phi)\,\frac{m_T}{H\Delta t}\left[(\boldsymbol{n} : \Delta\boldsymbol{\sigma}_{\mathrm{J}})\left(\frac{\eta\overline{F}}{H\Delta t} + \left(\frac{-\eta\overline{F}}{H\Delta t} - 1\right)e^{\frac{-H}{\eta\overline{F}}\Delta t}\right)\right] + \\ &+ (\Delta\sigma_T + \Delta\sigma_N\tan\phi)\,\frac{m_T}{H\Delta t}\left[F_0\left(\frac{-\eta\overline{F}}{H\Delta t} + \left(\frac{\eta\overline{F}}{H\Delta t} + 1\right)e^{\frac{-H}{\eta\overline{F}}\Delta t}\right) + \left(2\frac{\left(\eta\overline{F}\right)^2}{H^2\Delta t^2}\right)(\boldsymbol{n} : \Delta\boldsymbol{\sigma}_{\mathrm{J}}) + \right. \\ &\left. + \left(\frac{\eta\overline{F}}{H\Delta t}\left(\frac{-2\eta\overline{F}}{H\Delta t} - 1\right) + \left(\frac{-\eta\overline{F}}{H\Delta t} - 1\right)\right)(\boldsymbol{n} : \Delta\boldsymbol{\sigma}_{\mathrm{J}})\,e^{\frac{-H}{\eta\overline{F}}\Delta t}\right] + \\ &+ ((\sigma_{T0} + \Delta\sigma_T) + (\sigma_{N0} + \Delta\sigma_N)\tan\phi)\,m_T\frac{F_0}{\eta\overline{F}}e^{\frac{-H}{\eta\overline{F}}\Delta t}\end{aligned} \tag{C.13}$$

C.1.2 Derivative of ΔW^{vcr} with respect to the stress increment

The derivatives with respect to the stress increment of the first part of ΔW^{vcr} ($Part\,C$) are detailed below. Note that, in this case, the product $(\boldsymbol{n} : \Delta\boldsymbol{\sigma}_{\mathrm{J}})$ is performed by distinguishing between normal and tangential stress components as follows:

$$\begin{aligned}Part\,C = (\sigma_{T0} + \sigma_{N0}\tan\phi)\,\frac{m_T}{H}\Bigg[&F_0 - F_0 e^{\frac{-H}{\eta\overline{F}}\Delta t}\underbrace{-\frac{\eta\overline{F}}{H\Delta t}\left(n_N\Delta\sigma_N + n_T\Delta\sigma_T\right)}_{deriv.1C_s} + \\ &\underbrace{+\frac{\eta\overline{F}}{H\Delta t}\left(n_N\Delta\sigma_N + n_T\Delta\sigma_T\right)e^{\frac{-H}{\eta\overline{F}}\Delta t}}_{deriv.2C_s}\underbrace{+\left(n_N\Delta\sigma_N + n_T\Delta\sigma_T\right)}_{deriv.3C_s}\Bigg]\end{aligned} \tag{C.14}$$

where

$$\begin{aligned}deriv.1C_s :\ &\frac{\partial}{\partial\Delta\sigma_N}(\sigma_{T0} + \sigma_{N0}\tan\phi)\,\frac{m_T}{H}\left(-\frac{\eta\overline{F}}{H\Delta t}\left(n_N\Delta\sigma_N + n_T\Delta\sigma_T\right)\right) = \\ &= (\sigma_{T0} + \sigma_{N0}\tan\phi)\,\frac{m_T}{H}\left(-\frac{\eta\overline{F}}{H\Delta t}n_N\right)\end{aligned} \tag{C.15}$$

$$\begin{aligned}deriv.1C_s :\ &\frac{\partial}{\partial\Delta\sigma_T}(\sigma_{T0} + \sigma_{N0}\tan\phi)\,\frac{m_T}{H}\left(-\frac{\eta\overline{F}}{H\Delta t}\left(n_N\Delta\sigma_N + n_T\Delta\sigma_T\right)\right) = \\ &= (\sigma_{T0} + \sigma_{N0}\tan\phi)\,\frac{m_T}{H}\left(-\frac{\eta\overline{F}}{H\Delta t}n_T\right)\end{aligned} \tag{C.16}$$

$$deriv.2C_s: \frac{\partial}{\partial \Delta\sigma_N}\left(\sigma_{T0}+\sigma_{N0}\tan\phi\right)\frac{m_T}{H}\left(\frac{\eta\overline{F}}{H\Delta t}\left(n_N\Delta\sigma_N+n_T\Delta\sigma_T\right)e^{\frac{-H}{\eta\overline{F}}\Delta t}\right)= \\ =\left(\sigma_{T0}+\sigma_{N0}\tan\phi\right)\frac{m_T}{H}\left(\frac{\eta\overline{F}}{H\Delta t}e^{\frac{-H}{\eta\overline{F}}\Delta t}n_N\right) \tag{C.17}$$

$$deriv.2C_s: \frac{\partial}{\partial \Delta\sigma_T}\left(\sigma_{T0}+\sigma_{N0}\tan\phi\right)\frac{m_T}{H}\left(\frac{\eta\overline{F}}{H\Delta t}\left(n_N\Delta\sigma_N+n_T\Delta\sigma_T\right)e^{\frac{-H}{\eta\overline{F}}\Delta t}\right)= \\ =\left(\sigma_{T0}+\sigma_{N0}\tan\phi\right)\frac{m_T}{H}\left(\frac{\eta\overline{F}}{H\Delta t}e^{\frac{-H}{\eta\overline{F}}\Delta t}n_T\right) \tag{C.18}$$

$$deriv.3C_s: \frac{\partial}{\partial \Delta\sigma_N}\left(\sigma_{T0}+\sigma_{N0}\tan\phi\right)\frac{m_T}{H}\left(n_N\Delta\sigma_N+n_T\Delta\sigma_T\right)= \\ =\left(\sigma_{T0}+\sigma_{N0}\tan\phi\right)\frac{m_T}{H}n_N \tag{C.19}$$

$$deriv.3C_s: \frac{\partial}{\partial \Delta\sigma_T}\left(\sigma_{T0}+\sigma_{N0}\tan\phi\right)\frac{m_T}{H}\left(n_N\Delta\sigma_N+n_T\Delta\sigma_T\right)= \\ =\left(\sigma_{T0}+\sigma_{N0}\tan\phi\right)\frac{m_T}{H}n_T \tag{C.20}$$

Developing the derivatives of the second part of ΔW^{vcr} $(Part\,D)$ with respect to both normal and tangential stress components, the following expressions are obtained:

$$Part\,D=\left(\Delta\sigma_T+\Delta\sigma_N\tan\phi\right)\frac{m_T}{H}\left[\underbrace{F_0\frac{\eta\overline{F}}{H\Delta t}}_{deriv.1D_s}\underbrace{-F_0\frac{\eta\overline{F}}{H\Delta t}e^{\frac{-H}{\eta\overline{F}}\Delta t}}_{deriv.2D_s}\underbrace{-F_0e^{\frac{-H}{\eta\overline{F}}\Delta t}}_{deriv.3D_s}+\right. \\ \underbrace{-\frac{\left(\eta\overline{F}\right)^2}{H^2\Delta t^2}\left(n_N\Delta\sigma_N+n_T\Delta\sigma_T\right)}_{deriv.4D_s}+\underbrace{\frac{\left(\eta\overline{F}\right)^2}{H^2\Delta t^2}\left(n_N\Delta\sigma_N+n_T\Delta\sigma_T\right)e^{\frac{-H}{\eta\overline{F}}\Delta t}}_{deriv.5D_s}+ \\ \left.\underbrace{+\frac{\eta\overline{F}}{H\Delta t}\left(n_N\Delta\sigma_N+n_T\Delta\sigma_T\right)e^{\frac{-H}{\eta\overline{F}}\Delta t}}_{deriv.6D_s}\underbrace{+\left(n_N\Delta\sigma_N+n_T\Delta\sigma_T\right)\left(\frac{1}{2}\right)}_{deriv.7Ds}\right] \tag{C.21}$$

where

$$deriv.1D_s: \frac{\partial}{\partial \Delta\sigma_N}\left(\Delta\sigma_T+\Delta\sigma_N\tan\phi\right)\frac{m_T}{H}\left(F_0\frac{\eta\overline{F}}{H\Delta t}\right)=\tan\phi\frac{m_T}{H}\left(F_0\frac{\eta\overline{F}}{H\Delta t}\right) \tag{C.22}$$

$$deriv.1D_s: \frac{\partial}{\partial \Delta\sigma_T}\left(\Delta\sigma_T+\Delta\sigma_N\tan\phi\right)\frac{m_T}{H}\left(F_0\frac{\eta\overline{F}}{H\Delta t}\right)=1\cdot\frac{m_T}{H}\left(F_0\frac{\eta\overline{F}}{H\Delta t}\right) \tag{C.23}$$

$$deriv.2D_s: \frac{\partial}{\partial \Delta\sigma_N}\left(\Delta\sigma_T + \Delta\sigma_N \tan\phi\right)\frac{m_T}{H}\left(-F_0\frac{\eta\overline{F}}{H\Delta t}e^{\frac{-H}{\eta\overline{F}}\Delta t}\right) = \\ = \tan\phi\frac{m_T}{H}\left(-F_0\frac{\eta\overline{F}}{H\Delta t}e^{\frac{-H}{\eta\overline{F}}\Delta t}\right) \tag{C.24}$$

$$deriv.2D_s: \frac{\partial}{\partial \Delta\sigma_T}\left(\Delta\sigma_T + \Delta\sigma_N \tan\phi\right)\frac{m_T}{H}\left(-F_0\frac{\eta\overline{F}}{H\Delta t}e^{\frac{-H}{\eta\overline{F}}\Delta t}\right) = \\ = 1\cdot\frac{m_T}{H}\left(-F_0\frac{\eta\overline{F}}{H\Delta t}e^{\frac{-H}{\eta\overline{F}}\Delta t}\right) \tag{C.25}$$

$$deriv.3D_s: \frac{\partial}{\partial \Delta\sigma_N}\left(\Delta\sigma_T + \Delta\sigma_N \tan\phi\right)\frac{m_T}{H}\left(-F_0 e^{\frac{-H}{\eta\overline{F}}\Delta t}\right) = \tan\phi\frac{m_T}{H}\left(-F_0 e^{\frac{-H}{\eta\overline{F}}\Delta t}\right) \tag{C.26}$$

$$deriv.3D_s: \frac{\partial}{\partial \Delta\sigma_T}\left(\Delta\sigma_T + \Delta\sigma_N \tan\phi\right)\frac{m_T}{H}\left(-F_0 e^{\frac{-H}{\eta\overline{F}}\Delta t}\right) = 1\cdot\frac{m_T}{H}\left(-F_0 e^{\frac{-H}{\eta\overline{F}}\Delta t}\right) \tag{C.27}$$

$$deriv.4D_s: \frac{\partial}{\partial \Delta\sigma_N}\left(\Delta\sigma_T + \Delta\sigma_N \tan\phi\right)\frac{m_T}{H}\left(-\frac{\left(\eta\overline{F}\right)^2}{H^2\Delta t^2}\left(n_N\Delta\sigma_N + n_T\Delta\sigma_T\right)\right) = \\ = \tan\phi\frac{m_T}{H}\left(-\frac{\left(\eta\overline{F}\right)^2}{H^2\Delta t^2}\left(n_N\Delta\sigma_N + n_T\Delta\sigma_T\right)\right) + \\ + \left(\Delta\sigma_T + \Delta\sigma_N \tan\phi\right)\frac{m_T}{H}\left(-\frac{\left(\eta\overline{F}\right)^2}{H^2\Delta t^2}n_N\right) \tag{C.28}$$

$$deriv.4D_s: \frac{\partial}{\partial \Delta\sigma_T}\left(\Delta\sigma_T + \Delta\sigma_N \tan\phi\right)\frac{m_T}{H}\left(-\frac{\left(\eta\overline{F}\right)^2}{H^2\Delta t^2}\left(n_N\Delta\sigma_N + n_T\Delta\sigma_T\right)\right) = \\ = 1\cdot\frac{m_T}{H}\left(-\frac{\left(\eta\overline{F}\right)^2}{H^2\Delta t^2}\left(n_N\Delta\sigma_N + n_T\Delta\sigma_T\right)\right) + \\ + \left(\Delta\sigma_T + \Delta\sigma_N \tan\phi\right)\frac{m_T}{H}\left(-\frac{\left(\eta\overline{F}\right)^2}{H^2\Delta t^2}n_T\right) \tag{C.29}$$

$$deriv.5D_s: \frac{\partial}{\partial \Delta\sigma_N}\left(\Delta\sigma_T + \Delta\sigma_N \tan\phi\right)\frac{m_T}{H}\left(\frac{\left(\eta\overline{F}\right)^2}{H^2\Delta t^2}\left(n_N\Delta\sigma_N + n_T\Delta\sigma_T\right)e^{\frac{-H}{\eta\overline{F}}\Delta t}\right) = \\ = \tan\phi\frac{m_T}{H}\left(\frac{\left(\eta\overline{F}\right)^2}{H^2\Delta t^2}\left(n_N\Delta\sigma_N + n_T\Delta\sigma_T\right)e^{\frac{-H}{\eta\overline{F}}\Delta t}\right) + \\ + \left(\Delta\sigma_T + \Delta\sigma_N \tan\phi\right)\frac{m_T}{H}\left(\frac{\left(\eta\overline{F}\right)^2}{H^2\Delta t^2}n_N\, e^{\frac{-H}{\eta\overline{F}}\Delta t}\right) \tag{C.30}$$

$$deriv.5D_s: \frac{\partial}{\partial \Delta\sigma_T}\left(\Delta\sigma_T + \Delta\sigma_N \tan\phi\right)\frac{m_T}{H}\left(\frac{\left(\eta\overline{F}\right)^2}{H^2\Delta t^2}\left(n_N\Delta\sigma_N + n_T\Delta\sigma_T\right)e^{\frac{-H}{\eta\overline{F}}\Delta t}\right) =$$
$$= 1\cdot\frac{m_T}{H}\left(\frac{\left(\eta\overline{F}\right)^2}{H^2\Delta t^2}\left(n_N\Delta\sigma_N + n_T\Delta\sigma_T\right)e^{\frac{-H}{\eta\overline{F}}\Delta t}\right) + \tag{C.31}$$
$$+ \left(\Delta\sigma_T + \Delta\sigma_N\tan\phi\right)\frac{m_T}{H}\left(\frac{\left(\eta\overline{F}\right)^2}{H^2\Delta t^2}n_T\, e^{\frac{-H}{\eta\overline{F}}\Delta t}\right)$$

$$deriv.6D_s: \frac{\partial}{\partial \Delta\sigma_N}\left(\Delta\sigma_T + \Delta\sigma_N \tan\phi\right)\frac{m_T}{H}\left(\frac{\eta\overline{F}}{H\Delta t}\left(n_N\Delta\sigma_N + n_T\Delta\sigma_T\right)e^{\frac{-H}{\eta\overline{F}}\Delta t}\right) =$$
$$= \tan\phi\frac{m_T}{H}\left(\frac{\eta\overline{F}}{H\Delta t}\left(n_N\Delta\sigma_N + n_T\Delta\sigma_T\right)e^{\frac{-H}{\eta\overline{F}}\Delta t}\right) + \tag{C.32}$$
$$+ \left(\Delta\sigma_T + \Delta\sigma_N\tan\phi\right)\frac{m_T}{H}\left(\frac{\eta\overline{F}}{H\Delta t}n_N\, e^{\frac{-H}{\eta\overline{F}}\Delta t}\right)$$

$$deriv.6D_s: \frac{\partial}{\partial \Delta\sigma_T}\left(\Delta\sigma_T + \Delta\sigma_N \tan\phi\right)\frac{m_T}{H}\left(\frac{\eta\overline{F}}{H\Delta t}\left(n_N\Delta\sigma_N + n_T\Delta\sigma_T\right)e^{\frac{-H}{\eta\overline{F}}\Delta t}\right) =$$
$$= 1\cdot\frac{m_T}{H}\left(\frac{\eta\overline{F}}{H\Delta t}\left(n_N\Delta\sigma_N + n_T\Delta\sigma_T\right)e^{\frac{-H}{\eta\overline{F}}\Delta t}\right) + \tag{C.33}$$
$$+ \left(\Delta\sigma_T + \Delta\sigma_N\tan\phi\right)\frac{m_T}{H}\left(\frac{\eta\overline{F}}{H\Delta t}n_T\, e^{\frac{-H}{\eta\overline{F}}\Delta t}\right)$$

$$deriv.7D_s: \frac{\partial}{\partial \Delta\sigma_N}\left(\Delta\sigma_T + \Delta\sigma_N \tan\phi\right)\frac{m_T}{H}\left(\left(n_N\Delta\sigma_N + n_T\Delta\sigma_T\right)\left(\frac{1}{2}\right)\right) = \tag{C.34}$$
$$= \tan\phi\frac{m_T}{2H}\left(n_N\Delta\sigma_N + n_T\Delta\sigma_T\right) + \left(\Delta\sigma_T + \Delta\sigma_N\tan\phi\right)\frac{m_T}{2H}n_N$$

$$deriv.7D_s: \frac{\partial}{\partial \Delta\sigma_T}\left(\Delta\sigma_T + \Delta\sigma_N \tan\phi\right)\frac{m_T}{H}\left(\left(n_N\Delta\sigma_N + n_T\Delta\sigma_T\right)\left(\frac{1}{2}\right)\right) = \tag{C.35}$$
$$= 1\cdot\frac{m_T}{2H}\left(n_N\Delta\sigma_N + n_T\Delta\sigma_T\right) + \left(\Delta\sigma_T + \Delta\sigma_N\tan\phi\right)\frac{m_T}{2H}n_T$$

Considering all derivatives of both parts $Part\,C$ and $Part\,D$, the resulting expressions of the derivatives of ΔW^{vcr} with respect to the normal and tangential terms of the stress increment are:

$$\frac{\partial \Delta W^{vcr}}{\partial \Delta\sigma_N} = \left(\sigma_{T0} + \sigma_{N0}\tan\phi\right)\frac{m_T}{H}\left[\left(\frac{\eta\overline{F}}{H\Delta t}\left(e^{\frac{-H}{\eta\overline{F}}\Delta t} - 1\right) + 1\right)n_N\right] +$$
$$+ \tan\phi\frac{m_T}{H}F_0\left(\frac{\eta\overline{F}}{H\Delta t} - \left(\frac{\eta\overline{F}}{H\Delta t} + 1\right)e^{\frac{-H}{\eta\overline{F}}\Delta t}\right) + \tag{C.36}$$
$$+ \left(\tan\phi\frac{m_T}{H}\left(n_N\Delta\sigma_N + n_T\Delta\sigma_T\right) + \left(\Delta\sigma_T + \Delta\sigma_N\tan\phi\right)\frac{m_T}{H}n_N\right)\cdot$$
$$\cdot\left(\frac{\eta\overline{F}}{H\Delta t}\left(\frac{-\eta\overline{F}}{H\Delta t} + \left(\frac{\eta\overline{F}}{H\Delta t} + 1\right)e^{\frac{-H}{\eta\overline{F}}\Delta t}\right) + \frac{1}{2}\right)$$

$$\begin{aligned}\frac{\partial \Delta W^{vcr}}{\partial \Delta \sigma_T} = &\left(\sigma_{T0} + \sigma_{N0}\tan\phi\right)\frac{m_T}{H}\left[\left(\frac{\eta\overline{F}}{H\Delta t}\left(e^{\frac{-H}{\eta\overline{F}}\Delta t} - 1\right) + 1\right)n_T\right] + \\ &+ \frac{m_T}{H}F_0\left(\frac{\eta\overline{F}}{H\Delta t} - \left(\frac{\eta\overline{F}}{H\Delta t} + 1\right)e^{\frac{-H}{\eta\overline{F}}\Delta t}\right) + \\ &+ \left(\frac{m_T}{H}\left(n_N\Delta\sigma_N + n_T\Delta\sigma_T\right) + \left(\Delta\sigma_T + \Delta\sigma_N\tan\phi\right)\frac{m_T}{H}n_T\right)\cdot \\ &\cdot\left(\frac{\eta\overline{F}}{H\Delta t}\left(\frac{-\eta\overline{F}}{H\Delta t} + \left(\frac{\eta\overline{F}}{H\Delta t} + 1\right)e^{\frac{-H}{\eta\overline{F}}\Delta t}\right) + \frac{1}{2}\right)\end{aligned} \tag{C.37}$$

C.2 Limit cases of derivative expressions

As was mentioned in the previous Appendix B, the derivatives of the visco-plastic fracture dissipation with respect to the time increment (Eq. C.13) and the normal and tangential components of the stress increment (Eqs. C.36 and C.37 respectively) become undefined because the expressions take an indeterminate form of the $\frac{0}{0}$ type when $\Delta t \to 0$ and/or $H \to 0$. Solving this indetermination requires the use of L'Hôpital's rule and Taylor series approximation $\left(\sum_{n=0}^{\infty}\frac{f^{(n)}(a)}{n!}(x-a)^n\right)$. From now on, note that f denotes the corresponding derivative expression in each case.

These developments are very extensive since L'Hôpital's rule must be applied several times to solve the indetermination and, therefore, to be concise the resulting expression of each term of the Taylor series approximation is presented in the following sections for each limit case evaluated.

C.2.1 Limit cases of $\frac{\partial \Delta W^{vcr}}{\partial \Delta t}$ when Δt or H tend to zero

This section is dedicated to develop both limit cases $\Delta t \to 0$ and $H \to 0$ of the equation $f = \frac{\partial \Delta W^{vcr}}{\partial \Delta t}$ (Eq. C.13).

C.2.1.1 Case $\Delta t \to 0$

Analyzing the $\Delta t \to 0$ limit case, the resulting expression of the first term of the Taylor series approximation $f\left(\Delta t \to 0\right)$ is shown below:

$$\begin{aligned}f\left(\Delta t \to 0\right) = &\left(\sigma_{T0} + \sigma_{N0}\tan\phi\right)m_T\left[\frac{F_0}{\eta\overline{F}} + \frac{\left(\boldsymbol{n} : \Delta\boldsymbol{\sigma}_{\mathrm{J}}\right)}{2\eta\overline{F}}\right] + \\ &+ \left(\Delta\sigma_T + \Delta\sigma_N\tan\phi\right)m_T\left[\frac{F_0}{2\eta\overline{F}} + \frac{\left(\boldsymbol{n} : \Delta\boldsymbol{\sigma}_{\mathrm{J}}\right)}{3\eta\overline{F}}\right]\end{aligned} \tag{C.38}$$

At this point in the developments of the limit cases and after carrying out the necessary checks, it can be seen that the only difference between both expressions (1) considering the total visco-

plastic dissipation (or tension cases) and (2) considering the visco-plastic fracture dissipation only which corresponds to compression cases, is that $\boldsymbol{\sigma}_{\mathrm{J}0} : \boldsymbol{m}$ and $\Delta\boldsymbol{\sigma}_{\mathrm{J}} : \boldsymbol{m}$ in tension cases are replaced by $(\sigma_{T0} + \sigma_{N0}\tan\phi)\, m_T$ and $(\Delta\sigma_T + \Delta\sigma_N \tan\phi)\, m_T$ in compression cases respectively. Therefore, once the limit expressions have been obtained for tension cases it is easy to make the analogy between both types of cases and to obtain the limit expressions for compression cases doing the replacement mentioned before. Taking advantage of that, the second Taylor's term is obtained easily as:

$$\begin{aligned} f'\left(\Delta t \to 0\right) = {} & \left(\sigma_{T0} + \sigma_{N0}\tan\phi\right) m_T \left[-\frac{F_0 H}{\left(\eta\overline{F}\right)^2} - \frac{\left(\boldsymbol{n} : \Delta\boldsymbol{\sigma}_{\mathrm{J}}\right) H}{3\left(\eta\overline{F}\right)^2}\right] + \\ & + \left(\Delta\sigma_T + \Delta\sigma_N \tan\phi\right) m_T \left[-\frac{2F_0 H}{3\left(\eta\overline{F}\right)^2} - \frac{\left(\boldsymbol{n} : \Delta\boldsymbol{\sigma}_{\mathrm{J}}\right) H}{4\left(\eta\overline{F}\right)^2}\right] \end{aligned} \tag{C.39}$$

The complete limit expression of $\frac{\partial \Delta W^{vcr}}{\partial \Delta t}$ when $\Delta t \to 0$ regrouping the limit expressions of the first two terms of the Taylor series approximation (Eqs. C.38 and C.39) is shown below:

$$\begin{aligned} \left.\frac{\partial \Delta W^{vcr}}{\partial \Delta t}\right|_{Limit} = {} & \left(\sigma_{T0} + \sigma_{N0}\tan\phi\right) m_T \left[F_0\left(\frac{1}{\eta\overline{F}} - \frac{H\Delta t}{\left(\eta\overline{F}\right)^2}\right) + \left(\frac{1}{2\eta\overline{F}} - \frac{H\Delta t}{3\left(\eta\overline{F}\right)^2}\right)\left(\boldsymbol{n} : \Delta\boldsymbol{\sigma}_{\mathrm{J}}\right)\right] + \\ & + \left(\Delta\sigma_T + \Delta\sigma_N \tan\phi\right) m_T \left[F_0\left(\frac{1}{2\eta\overline{F}} - \frac{2H\Delta t}{3\left(\eta\overline{F}\right)^2}\right) + \left(\frac{1}{3\eta\overline{F}} - \frac{H\Delta t}{4\left(\eta\overline{F}\right)^2}\right)\left(\boldsymbol{n} : \Delta\boldsymbol{\sigma}_{\mathrm{J}}\right)\right] \end{aligned} \tag{C.40}$$

For shear-compression cases, limit expressions are also verified graphically in the Δt near zero zone. As in the previous appendix (App. B), the following graphics show a comparison between the original equation (Eq. C.13) and the limit one (Eq. C.40) of $\frac{\partial \Delta W^{vcr}}{\partial \Delta t}$ when $\Delta t \to 0$ (Fig. C.1). The parameters used for this case are $\overline{F} = 1.4$, $\eta = 10^6\, MPa \cdot s$, $H = -486810.3209\, MPa$, $\boldsymbol{n} = \begin{pmatrix} 0.7 \\ 0.998422 \end{pmatrix}, \boldsymbol{m} = \begin{pmatrix} 0.339414 \\ 0.998422 \end{pmatrix}, \boldsymbol{\sigma}_{\mathrm{J}0} = \begin{pmatrix} -10 \\ 11.9999 \end{pmatrix} MPa, \Delta\boldsymbol{\sigma}_{\mathrm{J}} = \begin{pmatrix} 0 \\ -1.65245 \end{pmatrix} MPa$ and $F_0 = 3.0149898$ taken from the shear-compression example with softening (Sec. 3.5.2).

C.2.1.2 Case $H \to 0$

The other limit case is when $H \to 0$ and the procedure performed is the same as in the previous limit case (Sec. C.2.1.1). Taking advantage of the aforementioned similarities between the limit

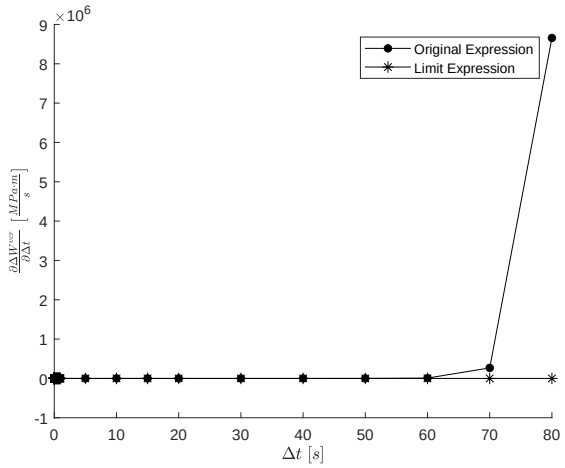

(a) Limit case $\Delta t \to 0$: Evolution of $\frac{\partial \Delta W^{vcr}}{\partial \Delta t}$ over time.

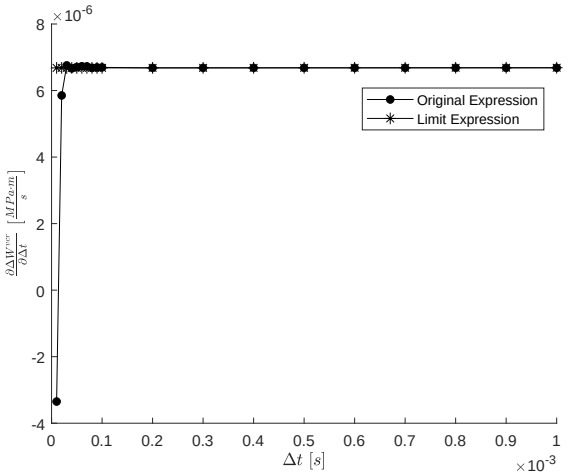

(b) Limit case $\Delta t \to 0$: Evolution of $\frac{\partial \Delta W^{vcr}}{\partial \Delta t}$ in the first moments of time.

Figure C.1: Representation of both original and limit expressions $\left(\frac{\partial \Delta W^{vcr}}{\partial \Delta t}\right)$ for $\Delta t \to 0$ limit case.

expressions of tension and compression cases, the first two Taylor's terms are:

$$\begin{aligned} f\left(H \to 0\right) = \left(\sigma_{T0} + \sigma_{N0}\tan\phi\right) m_T \left[\frac{F_0}{\eta\overline{F}} + \frac{1}{2\eta\overline{F}}\left(\boldsymbol{n} : \Delta\boldsymbol{\sigma}_{\mathrm{J}}\right)\right] + \\ + \left(\Delta\sigma_T + \Delta\sigma_N \tan\phi\right) m_T \left[\frac{F_0}{2\eta\overline{F}} + \frac{1}{3\eta\overline{F}}\left(\boldsymbol{n} : \Delta\boldsymbol{\sigma}_{\mathrm{J}}\right)\right] \end{aligned} \tag{C.41}$$

$$\begin{aligned} f'\left(H \to 0\right) = \left(\sigma_{T0} + \sigma_{N0}\tan\phi\right) m_T \left[-F_0\frac{\Delta t}{\left(\eta\overline{F}\right)^2} - \frac{\Delta t}{3\left(\eta\overline{F}\right)^2}\left(\boldsymbol{n} : \Delta\boldsymbol{\sigma}_{\mathrm{J}}\right)\right] + \\ + \left(\Delta\sigma_T + \Delta\sigma_N \tan\phi\right) m_T \left[-2F_0\frac{\Delta t}{3\left(\eta\overline{F}\right)^2} - \frac{\Delta t}{4\left(\eta\overline{F}\right)^2}\left(\boldsymbol{n} : \Delta\boldsymbol{\sigma}_{\mathrm{J}}\right)\right] \end{aligned} \tag{C.42}$$

Composing the resulting limit expression of $\frac{\partial \Delta W^{vcr}}{\partial \Delta t}$ from these two terms of the Taylor series approximation, it is observed that the limit expression deduced for both cases $\Delta t \to 0$ and $H \to 0$ is exactly the same (Eq. C.40). The parameters used in this case for the graphic verification are the same as those used for the previous case $\Delta t \to 0$ (Sec. C.2.1.1) only substituting the H parameter by $\Delta t = 1.0\,s$.

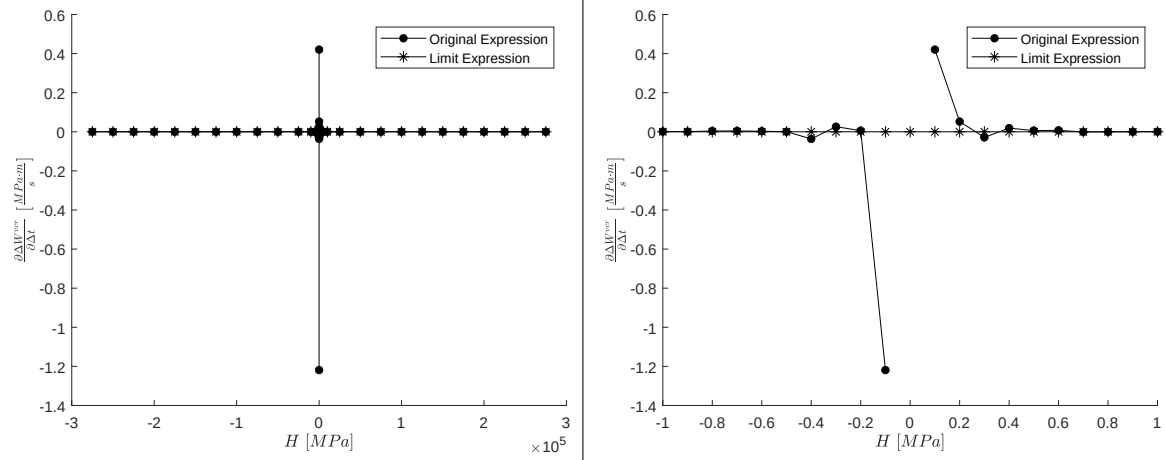

(a) Limit case $H \to 0$: Evolution of $\frac{\partial \Delta W^{vcr}}{\partial \Delta t}$ along H.

(b) Limit case $H \to 0$: Evolution of $\frac{\partial \Delta W^{vcr}}{\partial \Delta t}$ in the near zero H values.

Figure C.2: Representation of both original and limit expressions $\left(\frac{\partial \Delta W^{vcr}}{\partial \Delta t}\right)$ for $H \to 0$ limit case.

C.2.2 Limit cases of $\frac{\partial \Delta W^{vcr}}{\partial \Delta \sigma_J}$ when Δt or H tend to zero

As it was explained at the beginning of this section (Sec. C.2), in this case normal and tangential stress components must be considered to perform the derivative of the visco-plastic fracture dissipation with respect to the stress increment (Eqs. C.36 and C.37 respectively).

C.2.2.1 Case $\frac{\partial \Delta W^{vcr}}{\partial \Delta \sigma_N}$ when $\Delta t \to 0$

Developing the Taylor series approximation for $\frac{\partial \Delta W^{vcr}}{\partial \Delta \sigma_N}$ (Eq. C.36) when $\Delta t \to 0$, note that the first term of the Taylor development is zero: $f = \frac{\partial \Delta W^{vcr}}{\partial \Delta \sigma_N}(\Delta t = 0) = 0$.

Then, the second Taylor's term which requires the first derivative of equation C.36 with respect to Δt, $f'(\Delta t)$, is specified below together with its limit expression when $\Delta t \to 0$:

$$
\begin{aligned}
f'(\Delta t) = {} & (\sigma_{T0} + \sigma_{N0}\tan\phi)\frac{m_T}{H\Delta t^2}\left(-\Delta t e^{\frac{-H}{\eta\overline{F}}\Delta t} n_N - \frac{\eta\overline{F}}{H} e^{\frac{-H}{\eta\overline{F}}\Delta t} n_N + \frac{\eta\overline{F}}{H} n_N\right) + \\
& + \frac{1}{H\Delta t^3}\left[\tan\phi m_T\left(F_0\frac{H}{\eta\overline{F}}\Delta t^3 e^{\frac{-H}{\eta\overline{F}}\Delta t} - F_0\frac{\eta\overline{F}}{H}\Delta t + F_0\frac{\eta\overline{F}}{H}\Delta t e^{\frac{-H}{\eta\overline{F}}\Delta t} + F_0\Delta t^2 e^{\frac{-H}{\eta\overline{F}}\Delta t}\right) + \right. \\
& + \left(2m_T n_N \Delta\sigma_N \tan\phi + \left(m_T n_T \tan\phi + m_T n_N\right)\Delta\sigma_T\right)\left(-\Delta t^2 e^{\frac{-H}{\eta\overline{F}}\Delta t} + \right. \\
& \left.\left. + \frac{2\left(\eta\overline{F}\right)^2}{H^2} - \frac{2\left(\eta\overline{F}\right)^2}{H^2} e^{\frac{-H}{\eta\overline{F}}\Delta t} - 2\frac{\eta\overline{F}}{H}\Delta t e^{\frac{-H}{\eta\overline{F}}\Delta t}\right)\right]
\end{aligned}
\tag{C.43}
$$

$$f'\left(\Delta t \to 0\right) = \left(\sigma_{T0} + \sigma_{N0}\tan\phi\right) m_T \left(\frac{1}{2\eta\overline{F}} n_N\right) + \tan\phi m_T \left(\frac{F_0}{2\eta\overline{F}}\right) + \\ + \left(2 m_T n_N \Delta\sigma_N \tan\phi + \left(m_T n_T \tan\phi + m_T n_N\right)\Delta\sigma_T\right)\left(\frac{1}{3\eta\overline{F}}\right) \tag{C.44}$$

In this case, it is suitable to evaluate the third Taylor's term in order to obtain a better approximation. Therefore, evaluating this term the second derivative of equation C.36 with respect to Δt, $f''\left(\Delta t\right)$, must be considered. This is presented below together with its limit expression when $\Delta t \to 0$:

$$f''\left(\Delta t\right) = \left(\sigma_{T0} + \sigma_{N0}\tan\phi\right)\frac{m_T}{H\Delta t^3}\left(\frac{H}{\eta\overline{F}}\Delta t^2 e^{\frac{-H}{\eta\overline{F}}\Delta t} n_N + 2\Delta t e^{\frac{-H}{\eta\overline{F}}\Delta t} n_N + 2\frac{\eta\overline{F}}{H} e^{\frac{-H}{\eta\overline{F}}\Delta t} n_N - 2\frac{\eta\overline{F}}{H} n_N\right) + \\ + \frac{1}{H\Delta t^4}\left[\tan\phi m_T\left(-F_0\frac{H^2}{\left(\eta\overline{F}\right)^2}\Delta t^4 e^{\frac{-H}{\eta\overline{F}}\Delta t} - F_0\frac{H}{\eta\overline{F}}\Delta t^3 e^{\frac{-H}{\eta\overline{F}}\Delta t} + 2F_0\frac{\eta\overline{F}}{H}\Delta t + \right.\right. \\ \left. -2F_0\frac{\eta\overline{F}}{H}\Delta t e^{\frac{-H}{\eta\overline{F}}\Delta t} - 2F_0\Delta t^2 e^{\frac{-H}{\eta\overline{F}}\Delta t}\right) + \left(2 m_T n_N \Delta\sigma_N \tan\phi + \left(m_T n_T \tan\phi + m_T n_N\right)\Delta\sigma_T\right)\cdot \\ \left.\cdot\left(\frac{H}{\eta\overline{F}}\Delta t^3 e^{\frac{-H}{\eta\overline{F}}\Delta t} + 3\Delta t^2 e^{\frac{-H}{\eta\overline{F}}\Delta t} - 6\frac{\left(\eta\overline{F}\right)^2}{H^2} + 6\frac{\left(\eta\overline{F}\right)^2}{H^2} e^{\frac{-H}{\eta\overline{F}}\Delta t} + 6\frac{\eta\overline{F}}{H}\Delta t e^{\frac{-H}{\eta\overline{F}}\Delta t}\right)\right] \tag{C.45}$$

$$f''\left(\Delta t \to 0\right) = \left(\sigma_{T0} + \sigma_{N0}\tan\phi\right) m_T\left(-\frac{H}{3\left(\eta\overline{F}\right)^2} n_N\right) + \tan\phi m_T\left(-2F_0\frac{H}{3\left(\eta\overline{F}\right)^2}\right) + \\ + \left(2 m_T n_N \Delta\sigma_N \tan\phi + \left(m_T n_T \tan\phi + m_T n_N\right)\Delta\sigma_T\right)\left(-\frac{H}{4\left(\eta\overline{F}\right)^2}\right) \tag{C.46}$$

The resulting limit expression of $\frac{\partial\Delta W^{vcr}}{\partial\Delta\sigma_N}$ is composed by grouping the limit expressions of each term of the Taylor series approximation previously shown (Eqs. C.44 and C.46) as follows:

$$\left.\frac{\partial\Delta W^{vcr}}{\partial\Delta\sigma_N}\right|_{Limit} = \left(\sigma_{T0} + \sigma_{N0}\tan\phi\right) m_T\left(\frac{\Delta t}{2\eta\overline{F}} n_N\right) + \left(F_0\frac{\Delta t}{2\eta\overline{F}}\right)\tan\phi m_T + \\ + \left(\frac{\Delta t}{3\eta\overline{F}}\right)\left(\tan\phi m_T\left(n_N\Delta\sigma_N + n_T\Delta\sigma_T\right) + \left(\Delta\sigma_T + \Delta\sigma_N\tan\phi\right) m_T n_N\right) + \\ + \left(\sigma_{T0} + \sigma_{N0}\tan\phi\right) m_T\left(-\frac{\Delta t^2}{6\left(\eta\overline{F}\right)^2} n_N\right) H + \left(-F_0\frac{\Delta t^2}{3\left(\eta\overline{F}\right)^2}\right)\tan\phi m_T H + \\ + \left(-\frac{\Delta t^2}{8\left(\eta\overline{F}\right)^2}\right) H\left(\tan\phi m_T\left(n_N\Delta\sigma_N + n_T\Delta\sigma_T\right) + \left(\Delta\sigma_T + \Delta\sigma_N\tan\phi\right) m_T n_N\right) \tag{C.47}$$

The graphical comparison between the original equation (Eq. C.36) and the limit one (Eq.

C.47) of $\frac{\partial \Delta W^{vcr}}{\partial \Delta \sigma_N}$ when $\Delta t \to 0$ is shown in the following figure (Fig. C.3). The parameters used are those defined in the previous Section C.2.1.1.

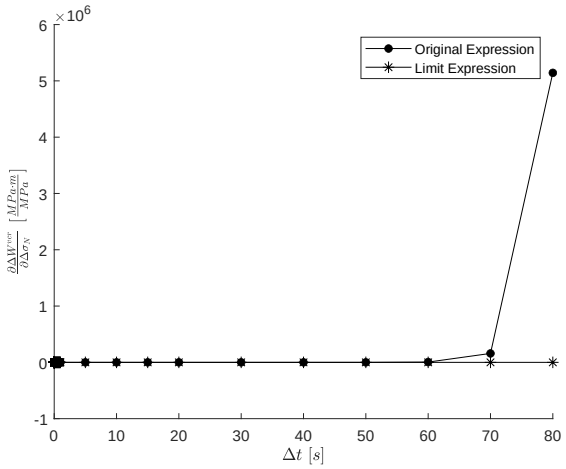

(a) Limit case $\Delta t \to 0$: Evolution of $\frac{\partial \Delta W^{vcr}}{\partial \Delta \sigma_N}$ over time.

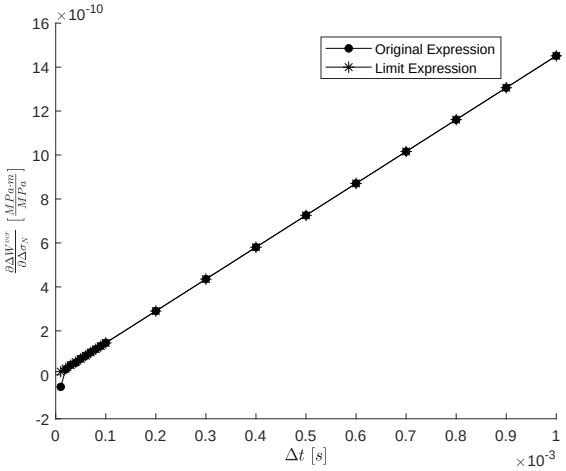

(b) Limit case $\Delta t \to 0$: Evolution of $\frac{\partial \Delta W^{vcr}}{\partial \Delta \sigma_N}$ in the first moments of time.

Figure C.3: Representation of both original and limit expressions $\frac{\partial \Delta W^{vcr}}{\partial \Delta \sigma_N}$ for $\Delta t \to 0$ limit case.

C.2.2.2 Case $\frac{\partial \Delta W^{vcr}}{\partial \Delta \sigma_N}$ when $H \to 0$

The other limit case of the function $\frac{\partial \Delta W^{vcr}}{\partial \Delta \sigma_N}$ (Eq. C.36) is when $H \to 0$, the limit expression of the first term of the Taylor development is presented below:

$$\begin{aligned} f\left(H \to 0\right) = \left(\sigma_{T0} + \sigma_{N0} \tan\phi\right) m_T \left(\frac{\Delta t}{2\eta \overline{F}} n_N\right) + \left(F_0 \frac{\Delta t}{2\eta \overline{F}}\right) \tan\phi m_T + \\ + \left(\frac{\Delta t}{3\eta \overline{F}}\right) \left(\tan\phi m_T \left(n_N \Delta\sigma_N + n_T \Delta\sigma_T\right) + \left(\Delta\sigma_T + \Delta\sigma_N \tan\phi\right) m_T n_N\right) \end{aligned} \tag{C.48}$$

The second Taylor's term requires the first derivative of equation C.36 with respect to H, $f'\left(H\right)$, presented below followed by its limit expression when $H \to 0$:

$$f'(H) = (\sigma_{T0} + \sigma_{N0}\tan\phi)\frac{m_T}{H^3}\left(-e^{\frac{-H}{\eta\overline{F}}\Delta t}Hn_N + Hn_N - 2\frac{\eta\overline{F}}{\Delta t}e^{\frac{-H}{\eta\overline{F}}\Delta t}n_N + 2\frac{\eta\overline{F}}{\Delta t}n_N - 2Hn_N\right) +$$
$$+ \frac{1}{H^4}\left[\left(H^3F_0\frac{\Delta t}{\eta\overline{F}}e^{\frac{-H}{\eta\overline{F}}\Delta t} - 2HF_0\frac{\eta\overline{F}}{\Delta t} + 2HF_0\frac{\eta\overline{F}}{\Delta t}e^{\frac{-H}{\eta\overline{F}}\Delta t} + 2H^2F_0e^{\frac{-H}{\eta\overline{F}}\Delta t}\right)\tan\phi m_T +\right.$$
$$+ \left(-H^2e^{\frac{-H}{\eta\overline{F}}\Delta t} + 3\frac{\left(\eta\overline{F}\right)^2}{\Delta t^2} - 3\frac{\left(\eta\overline{F}\right)^2}{\Delta t^2}e^{\frac{-H}{\eta\overline{F}}\Delta t} - 3H\frac{\eta\overline{F}}{\Delta t}e^{\frac{-H}{\eta\overline{F}}\Delta t} - \frac{1}{2}H^2\right)\cdot$$
$$\left.\cdot\left(\tan\phi m_T\left(n_N\Delta\sigma_N + n_T\Delta\sigma_T\right) + \left(\Delta\sigma_T + \Delta\sigma_N\tan\phi\right)m_Tn_N\right)\right] \tag{C.49}$$

$$f'(H\to 0) = (\sigma_{T0} + \sigma_{N0}\tan\phi)\,m_T\left(-\frac{\Delta t^2}{6\left(\eta\overline{F}\right)^2}n_N\right) + \left(-F_0\frac{\Delta t^2}{3\left(\eta\overline{F}\right)^2}\right)\tan\phi m_T +$$
$$+ \left(-\frac{\Delta t^2}{8\left(\eta\overline{F}\right)^2}\right)\left(\tan\phi m_T\left(n_N\Delta\sigma_N + n_T\Delta\sigma_T\right) + \left(\Delta\sigma_T + \Delta\sigma_N\tan\phi\right)m_Tn_N\right) \tag{C.50}$$

Composing the resulting limit expression from Eqs. C.48 and C.50, this equation is the same as the one obtained in the previous limiting case $\Delta t \to 0$ (Eq. C.47). Graphically, the comparison between the original equation (Eq. C.36) and the limit one (Eq. C.47) of $\frac{\partial\Delta W^{vcr}}{\partial\Delta\sigma_N}$ when $H \to 0$ is shown in the following figure (Fig. C.4). The parameters used are those defined in the previous Section C.2.1.2.

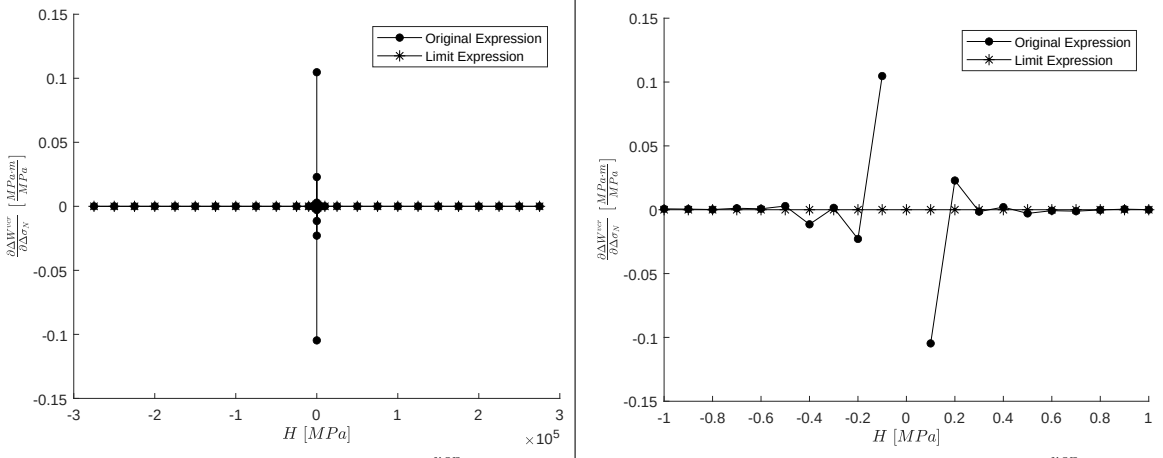

(a) Limit case $H \to 0$: Evolution of $\frac{\partial\Delta W^{vcr}}{\partial\Delta\sigma_N}$ along H.

(b) Limit case $H \to 0$: Evolution of $\frac{\partial\Delta W^{vcr}}{\partial\Delta\sigma_N}$ in the near zero H values.

Figure C.4: Representation of both original and limit expressions $\frac{\partial\Delta W^{vcr}}{\partial\Delta\sigma_N}$ for $H \to 0$ limit case.

C.2.2.3 Case $\frac{\partial \Delta W^{vcr}}{\partial \Delta \sigma_T}$ when $\Delta t \to 0$

The last case to evaluate is the derivative of ΔW^{vcr} with respect the tangential component of the stress increment (Eq. C.37). Following step by step the procedure performed in the previous case (Sec. C.2.2.1), note that here the limit expression of the first Taylor's term leads to zero and for this reason it is suitable to develop the second and third terms as well.

The second Taylor's term requires the first derivative of equation C.37 with respect to Δt, $f'(\Delta t)$, which is detailed below followed by its limit expression when $\Delta t \to 0$:

$$\begin{aligned} f'(\Delta t) = {} & (\sigma_{T0} + \sigma_{N0}\tan\phi)\frac{m_T}{H\Delta t^2}\left(-\Delta t e^{\frac{-H}{\eta\overline{F}}\Delta t} n_T - \frac{\eta\overline{F}}{H}e^{\frac{-H}{\eta\overline{F}}\Delta t} n_T + \frac{\eta\overline{F}}{H}n_T\right) + \\ & + \frac{1}{H\Delta t^3}\left[m_T\left(F_0\frac{H}{\eta\overline{F}}\Delta t^3 e^{\frac{-H}{\eta\overline{F}}\Delta t} - F_0\frac{\eta\overline{F}}{H}\Delta t + F_0\frac{\eta\overline{F}}{H}\Delta t e^{\frac{-H}{\eta\overline{F}}\Delta t} + F_0\Delta t^2 e^{\frac{-H}{\eta\overline{F}}\Delta t}\right) + \right. \\ & + \left((m_T n_N + m_T n_T\tan\phi)\Delta\sigma_N + 2m_T n_T\Delta\sigma_T\right)\left(-\Delta t^2 e^{\frac{-H}{\eta\overline{F}}\Delta t} + \right. \\ & \left.\left. + \frac{2\left(\eta\overline{F}\right)^2}{H^2} - \frac{2\left(\eta\overline{F}\right)^2}{H^2}e^{\frac{-H}{\eta\overline{F}}\Delta t} - 2\frac{\eta\overline{F}}{H}\Delta t e^{\frac{-H}{\eta\overline{F}}\Delta t}\right)\right] \end{aligned} \tag{C.51}$$

$$\begin{aligned} f'(\Delta t \to 0) = {} & (\sigma_{T0} + \sigma_{N0}\tan\phi)\, m_T\left(\frac{1}{2\eta\overline{F}}n_T\right) + m_T\left(\frac{F_0}{2\eta\overline{F}}\right) + \\ & + \left((m_T n_N + m_T n_T\tan\phi)\Delta\sigma_N + 2m_T n_T\Delta\sigma_T\right)\left(\frac{1}{3\eta\overline{F}}\right) \end{aligned} \tag{C.52}$$

In the same way, the third Taylor's term requires the second derivative of equation C.37 with respect to Δt, $f''(\Delta t)$, which is also detailed below followed by its limit expression when $\Delta t \to 0$:

$$\begin{aligned} f''(\Delta t) = {} & (\sigma_{T0} + \sigma_{N0}\tan\phi)\frac{m_T}{H\Delta t^3}\left(\frac{H}{\eta\overline{F}}\Delta t^2 e^{\frac{-H}{\eta\overline{F}}\Delta t} n_T + 2\Delta t e^{\frac{-H}{\eta\overline{F}}\Delta t} n_T + 2\frac{\eta\overline{F}}{H}e^{\frac{-H}{\eta\overline{F}}\Delta t} n_T - 2\frac{\eta\overline{F}}{H}n_T\right) + \\ & + \frac{1}{H\Delta t^4}\left[m_T\left(-F_0\frac{H^2}{\left(\eta\overline{F}\right)^2}\Delta t^4 e^{\frac{-H}{\eta\overline{F}}\Delta t} - F_0\frac{H}{\eta\overline{F}}\Delta t^3 e^{\frac{-H}{\eta\overline{F}}\Delta t} + 2F_0\frac{\eta\overline{F}}{H}\Delta t + \right.\right. \\ & \left. -2F_0\frac{\eta\overline{F}}{H}\Delta t e^{\frac{-H}{\eta\overline{F}}\Delta t} - 2F_0\Delta t^2 e^{\frac{-H}{\eta\overline{F}}\Delta t}\right) + \left((m_T n_N + m_T n_T\tan\phi)\Delta\sigma_N + 2m_T n_T\Delta\sigma_T\right)\cdot \\ & \left.\cdot\left(\frac{H}{\eta\overline{F}}\Delta t^3 e^{\frac{-H}{\eta\overline{F}}\Delta t} + 3\Delta t^2 e^{\frac{-H}{\eta\overline{F}}\Delta t} - 6\frac{\left(\eta\overline{F}\right)^2}{H^2} + 6\frac{\left(\eta\overline{F}\right)^2}{H^2}e^{\frac{-H}{\eta\overline{F}}\Delta t} + 6\frac{\eta\overline{F}}{H}\Delta t e^{\frac{-H}{\eta\overline{F}}\Delta t}\right)\right] \end{aligned} \tag{C.53}$$

$$f''\left(\Delta t \to 0\right) = \left(\sigma_{T0} + \sigma_{N0}\tan\phi\right) m_T \left(-\frac{H}{3\left(\eta\overline{F}\right)^2} n_T\right) + m_T \left(-2F_0 \frac{H}{3\left(\eta\overline{F}\right)^2}\right) + \\ + \left(\left(m_T n_N + m_T n_T \tan\phi\right)\Delta\sigma_N + 2m_T n_T \Delta\sigma_T\right)\left(-\frac{H}{4\left(\eta\overline{F}\right)^2}\right) \tag{C.54}$$

The resulting limit expression of $\frac{\partial \Delta W^{vcr}}{\partial \Delta\sigma_T}$ is composed from Eqs. C.52 and C.54 as follows:

$$\left.\frac{\partial \Delta W^{vcr}}{\partial \Delta\sigma_T}\right|_{Limit} = \left(\sigma_{T0} + \sigma_{N0}\tan\phi\right) m_T \left(\frac{\Delta t}{2\eta\overline{F}} n_T\right) + \left(F_0 \frac{\Delta t}{2\eta\overline{F}}\right) m_T + \\ + \left(\frac{\Delta t}{3\eta\overline{F}}\right)\left(m_T\left(n_N\Delta\sigma_N + n_T\Delta\sigma_T\right) + \left(\Delta\sigma_T + \Delta\sigma_N\tan\phi\right) m_T n_T\right) + \\ + \left(\sigma_{T0} + \sigma_{N0}\tan\phi\right) m_T \left(-\frac{\Delta t^2}{6\left(\eta\overline{F}\right)^2} n_T\right) H + \left(-F_0 \frac{\Delta t^2}{3\left(\eta\overline{F}\right)^2}\right) H m_T + \\ + \left(-\frac{\Delta t^2}{8\left(\eta\overline{F}\right)^2}\right) H\left(m_T\left(n_N\Delta\sigma_N + n_T\Delta\sigma_T\right) + \left(\Delta\sigma_T + \Delta\sigma_N\tan\phi\right) m_T n_T\right) \tag{C.55}$$

In addition, the graphical verification by means of the comparison between the original equation (Eq. C.37) and the limit one (Eq. C.55) is presented below (Fig. C.5) and the parameters used are those defined in the previous Section C.2.1.1 as well.

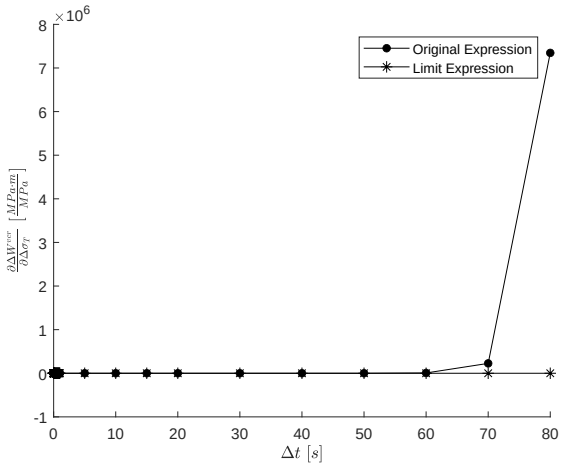

(a) Limit case $\Delta t \to 0$: Evolution of $\frac{\partial \Delta W^{vcr}}{\partial \Delta\sigma_T}$ over time.

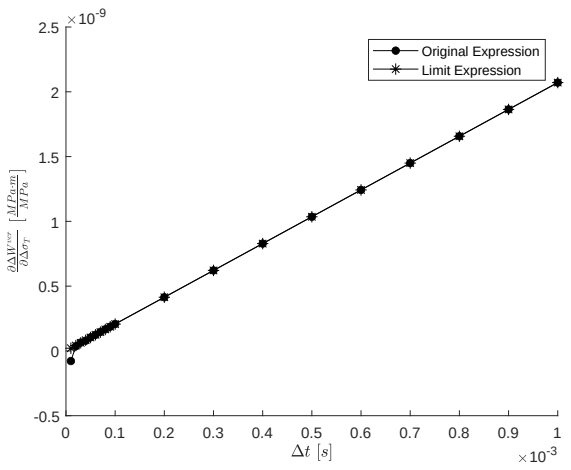

(b) Limit case $\Delta t \to 0$: Evolution of $\frac{\partial \Delta W^{vcr}}{\partial \Delta\sigma_T}$ in the first moments of time.

Figure C.5: Representation of both original and limit expressions $\frac{\partial \Delta W^{vcr}}{\partial \Delta\sigma_T}$ for $\Delta t \to 0$ limit case.

C.2.2.4 Case $\frac{\partial \Delta W^{vcr}}{\partial \Delta \sigma_T}$ when $H \to 0$

The other limit case of $\frac{\partial \Delta W^{vcr}}{\partial \Delta \sigma_T}$ (Eq. C.37) when $H \to 0$, the limit expression of the first term of the Taylor development is presented below:

$$\begin{aligned} f\left(H \to 0\right) = \left(\sigma_{T0} + \sigma_{N0}\tan\phi\right) m_T \left(\frac{\Delta t}{2\eta\overline{F}} n_T\right) + \left(F_0 \frac{\Delta t}{2\eta\overline{F}}\right) m_T + \\ + \left(\frac{\Delta t}{3\eta\overline{F}}\right) \left(m_T \left(n_N \Delta\sigma_N + n_T \Delta\sigma_T\right) + \left(\Delta\sigma_T + \Delta\sigma_N \tan\phi\right) m_T n_T\right) \end{aligned} \tag{C.56}$$

The second Taylor's term requires the first derivative of equation C.37 with respect to H, $f'\left(H\right)$, which is detailed below followed by its limit expression when $H \to 0$:

$$\begin{aligned} f'\left(H\right) = \left(\sigma_{T0} + \sigma_{N0}\tan\phi\right) \frac{m_T}{H^3} \left(-e^{\frac{-H}{\eta\overline{F}}\Delta t} H n_T + H n_T - 2\frac{\eta\overline{F}}{\Delta t} e^{\frac{-H}{\eta\overline{F}}\Delta t} n_T + 2\frac{\eta\overline{F}}{\Delta t} n_T - 2 H n_T\right) + \\ + \frac{1}{H^4} \left[\left(+H^3 F_0 \frac{\Delta t}{\eta\overline{F}} e^{\frac{-H}{\eta\overline{F}}\Delta t} - 2 H F_0 \frac{\eta\overline{F}}{\Delta t} + 2 H F_0 \frac{\eta\overline{F}}{\Delta t} e^{\frac{-H}{\eta\overline{F}}\Delta t} + 2 H^2 F_0 e^{\frac{-H}{\eta\overline{F}}\Delta t}\right) m_T + \right. \\ + \left(-H^2 e^{\frac{-H}{\eta\overline{F}}\Delta t} + 3\frac{\left(\eta\overline{F}\right)^2}{\Delta t^2} - 3\frac{\left(\eta\overline{F}\right)^2}{\Delta t^2} e^{\frac{-H}{\eta\overline{F}}\Delta t} - 3 H \frac{\eta\overline{F}}{\Delta t} e^{\frac{-H}{\eta\overline{F}}\Delta t} - \frac{1}{2} H^2\right) \cdot \\ \left. \cdot \left(m_T \left(n_N \Delta\sigma_N + n_T \Delta\sigma_T\right) + \left(\Delta\sigma_T + \Delta\sigma_N \tan\phi\right) m_T n_T\right)\right] \end{aligned} \tag{C.57}$$

$$\begin{aligned} f'\left(H \to 0\right) = \left(\sigma_{T0} + \sigma_{N0}\tan\phi\right) m_T \left(-\frac{\Delta t^2}{6\left(\eta\overline{F}\right)^2} n_T\right) + \left(-F_0 \frac{\Delta t^2}{3\left(\eta\overline{F}\right)^2}\right) m_T + \\ + \left(-\frac{\Delta t^2}{8\left(\eta\overline{F}\right)^2}\right) \left(m_T \left(n_N \Delta\sigma_N + n_T \Delta\sigma_T\right) + \left(\Delta\sigma_T + \Delta\sigma_N \tan\phi\right) m_T n_T\right) \end{aligned} \tag{C.58}$$

As a result, the limit expression obtained from Eqs. C.56 and C.58 is the same as the one obtained considering $\Delta t \to 0$ (Eq. C.55). Figure C.6 shows the comparison between the original (Eq. C.37) and limit (Eq. C.55) expressions and the parameters used to get these results are those defined in the previous Section C.2.1.2.

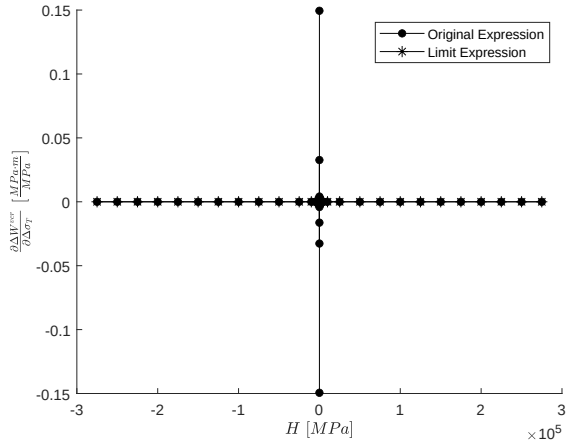

(a) Limit case $H \to 0$: Evolution of $\frac{\partial \Delta W^{vcr}}{\partial \Delta \sigma_T}$ along H.

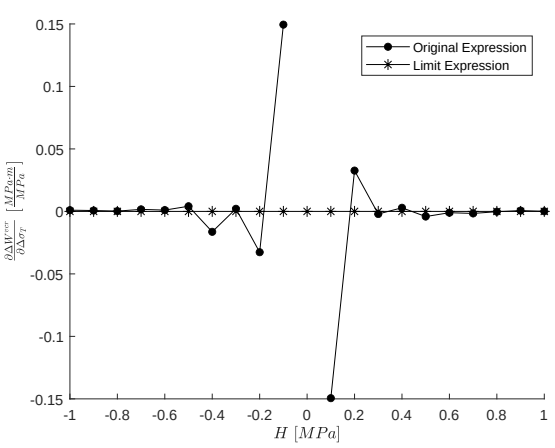

(b) Limit case $H \to 0$: Evolution of $\frac{\partial \Delta W^{vcr}}{\partial \Delta \sigma_T}$ in the near zero H values.

Figure C.6: Representation of both original and limit expressions $\frac{\partial \Delta W^{vcr}}{\partial \Delta \sigma_T}$ for $H \to 0$ limit case.

Appendix D

Visco-plastic Relaxation (VPR) algorithm

Algorithm 1 Visco-plastic relaxation with H/S

Loop Increments
for $iincr = 1, nincr$ **do**
  Part 1
  for $iElem = 1, nElem$ **do**
    for $iGaus = 1, nGaus$ **do**
      CALL VP constitutive law $\begin{cases} \text{IN arguments: } \boldsymbol{\sigma}_{ini}^{P1},\ \boldsymbol{\varepsilon}_{ini}^{P1}, \Delta t,\ \Delta\boldsymbol{\sigma} = 0,\ Vh_{ini}^{P1} \\ \text{OUT arguments: } \boldsymbol{\sigma}_{\text{"}real\text{"}}^{P1},\ \boldsymbol{\varepsilon}_{\text{"}real\text{"}}^{P1}, \boldsymbol{D}^{\text{"}P1},\ Vh_{\text{"}real\text{"}}^{P1} \end{cases}$
      $\Delta\boldsymbol{\varepsilon}^{P1} = \boldsymbol{\varepsilon}_{\text{"}real\text{"}}^{P1} - \boldsymbol{\varepsilon}_{ini}^{P1}$
      $\Delta\boldsymbol{\sigma}^{P1} = \boldsymbol{D}^{\text{"}P1} : \Delta\boldsymbol{\varepsilon}^{P1}$
      $\boldsymbol{\sigma}^{P1} = \boldsymbol{\sigma}_{ini}^{P1} - \Delta\boldsymbol{\sigma}^{P1}$
    end for
    $\boldsymbol{F}_{Int} = \sum_{nElem} \int_{\Omega} \boldsymbol{B}^T \boldsymbol{\sigma}^{P1} d\Omega$
    $\boldsymbol{K} = \sum_{nElem} \int_{\Omega} \boldsymbol{B}^T \boldsymbol{D}^{\text{"}P1} \boldsymbol{B} d\Omega$
  end for
  Get External Forces $\rightarrow \boldsymbol{F}_{Ext}$
  Get Global Residual $\rightarrow \boldsymbol{F} = \boldsymbol{F}_{Int} - \boldsymbol{F}_{Ext}$
  Loop Iterations
  for $iiter = 1, niter$ **do**
    SOLVER $\rightarrow \boldsymbol{K}\mathbf{u} = \boldsymbol{F}$

Part 2
for $iElem = 1, nElem$ **do**
  for $iGaus = 1, nGaus$ **do**
    Stress update considering stress drop calculated in Part 1
    $\boldsymbol{\sigma}^{P2}_{updated} = \boldsymbol{\sigma}^{P2}_{ini} - \Delta\boldsymbol{\sigma}^{P1}$
    Stress update considering the displacements from solver
    $\Delta\boldsymbol{\varepsilon}_{solver} = \boldsymbol{B}\boldsymbol{u}$
    $\Delta\boldsymbol{\sigma}_{solver} = \boldsymbol{D}^{"P1}\Delta\boldsymbol{\varepsilon}_{solver}$
    $\boldsymbol{\varepsilon}^{P2}_{updated} = \boldsymbol{\varepsilon}^{P2}_{ini} + \Delta\boldsymbol{\varepsilon}_{solver}$
    $\boldsymbol{\sigma}^{P2}_{updated} = \boldsymbol{\sigma}^{P2}_{updated} + \Delta\boldsymbol{\sigma}_{solver}$
    $\Delta\boldsymbol{\sigma} = \boldsymbol{\sigma}^{P2}_{updated} - \boldsymbol{\sigma}^{P2}_{ini}$
    CALL VP constitutive law $\begin{cases} \text{IN arguments: } \boldsymbol{\sigma}^{P2}_{ini},\ \boldsymbol{\varepsilon}^{P2}_{ini}, \Delta t,\ \Delta\boldsymbol{\sigma},\ Vh^{P2}_{ini} \\ \text{OUT arguments: } \boldsymbol{\sigma}^{P2}_{"real"},\ \boldsymbol{\varepsilon}^{P2}_{"real"}, \boldsymbol{D}^{"P2},\ Vh^{P2}_{"real"} \end{cases}$
    $\Delta\boldsymbol{\varepsilon}^{P2} = \boldsymbol{\varepsilon}^{P2}_{"real"} - \boldsymbol{\varepsilon}^{P2}_{updated}$
    $\Delta\boldsymbol{\sigma}^{P2} = \boldsymbol{D}^{"P2} : \Delta\boldsymbol{\varepsilon}^{P2}$
    $\boldsymbol{\sigma}^{P2} = \boldsymbol{\sigma}^{P2}_{"real"} - \Delta\boldsymbol{\sigma}^{P2}$
  end for
  $\boldsymbol{F}_{Int} = \sum_{nElem} \int_{\Omega} \boldsymbol{B}^T \boldsymbol{\sigma}^{P2} d\Omega$
end for
Get Global Residual $\rightarrow \boldsymbol{F} = \boldsymbol{F}_{Int} - \boldsymbol{F}_{Ext}$
$\xi = \|\boldsymbol{F}\|$
Automatic time adjustment
if $\xi < Tol_{Inf}$ **then**
  Iteration is acceptable $\rightarrow$ next iiter with $fact_{dt} = 1.35$
else if $\xi > Tol_{Sup}$ **then**
  Iteration not acceptable $\rightarrow$ repeat iiter with $fact_{dt} = 0.5$
else if $\xi < Tol_{Sup}$ and $\xi > Tol_{Inf}$ **then**
  Iteration is acceptable $\rightarrow$ next iiter with $fact_{dt} = 1.0$
end if
$\Delta t = fact_{dt}\Delta t$
Again Part 1:
IF iiter is acceptable $\rightarrow$ preparing the next iiter
IF iiter is not acceptable $\rightarrow$ preparing the iiter repetition
end for
end for

Appendix E

Closed-form expressions deduced to calculate W_{FtR}

The kind of example used to verify the fluid dissipation generated by a fluid flow along rod elements, has made it possible to obtain the closed-form expressions of the pressure gradient in the contact point between the rod element and the continuum, the volume of fluid entering the interface and the fluid dissipation through the rods.

This appendix is dedicated to set out the developments that have made it possible to achieve the aforementioned closed-form expressions.

E.1 The pressure in the contact point rod-continuum

The pressure gradient along each rod element is:

$$\nabla P = \frac{(P - P_0)}{L} = (P - 10) \tag{E.1}$$

where $L = 1\,m$ and $P_0 = 10\,MPa$. Each rod element is connected to the double node interface through its lower node, therefore, the flow that is transferred by this contact is $Q/2$ (each node of the double node interface has $Q/2$ and considering both nodes the total Q defined in the example is guaranteed).

$$\frac{Q}{2} = -K_{\mathrm{RC}}\,\nabla P \tag{E.2}$$

It is assumed that the differential of volume can be expressed as: $dV = Q\,dt$ and it is related to displacements as $du = dV/L$ where $L = 1\,m$ and, as a result, $du = dV$. In this context, the

differential increment of stresses in the continuum is:

$$d\sigma = \frac{E}{L}\, du = \frac{E}{L}\, dV = \frac{E}{L}\, Q\, dt = \frac{E}{L}\, (-2K_{\mathrm{RC}}\, \nabla P)\, dt \tag{E.3}$$

From equation (E.3) and making the equivalence $d\sigma = dP$ (because both variables correspond to a force applied over an area), the differential of pressure is obtained:

$$dP = -\underbrace{2K_{\mathrm{RC}} \frac{E}{L}}_{k} (P - P_0)\, dt = -k\, (P - P_0)\, dt \tag{E.4}$$

Reorganizing the equation (E.4) and integrating:

$$\int \frac{dP}{(P_0 - P)} = \int k\, dt \tag{E.5}$$

$$-\ln (P_0 - P) = k\, t + C \tag{E.6}$$

Considering $P = 0\, MPa$ and $t = 0\, s$, the integration constant is obtained: $C = -\ln P_0$. From this, the equation (E.6) can be rewritten as:

$$\ln \frac{P_0}{(P_0 - P)} = k\, t \tag{E.7}$$

Finally, rearranging equation (E.7) the ultimate closed-form expression for pressure is obtained:

$$P = P_0 \left(1 - e^{-kt}\right) \tag{E.8}$$

E.2 The total volume entering the interface

The total volume entering through both ends of the interface through the respective lower nodes is calculated as:

$$V = \int Q\, dt \tag{E.9}$$

On the other hand, combining the equations (E.2) and (E.8) the following flow expression is obtained:

$$Q = -2K_{\mathrm{RC}} \nabla P = -2K_{\mathrm{RC}}\, (P - P_0) = -2K_{\mathrm{RC}} \left(\left(P_0 \left(1 - e^{-kt}\right)\right) - P_0\right) = 2K_{\mathrm{RC}} P_0 e^{-kt} \tag{E.10}$$

Therefore:

$$V = \int 2K_{\mathrm{RC}}\, P_0\, e^{-kt}\, dt = 2K_{\mathrm{RC}}\, P_0 \int e^{-kt}\, dt = 2K_{\mathrm{RC}}\, P_0 \frac{1}{-k} e^{-kt} + C \tag{E.11}$$

Integration constant C may be obtained considering that the volume is zero at the beginning when $t = 0\,s$. As a result, $C = 2\frac{K_{\mathrm{RC}}}{k} P_0$. Substituting the constant C and the parameter k defined in the previous Section E.1 into the volume equation (E.11), the expression of the total volume entering the interface is obtained:

$$V = 2\frac{K_{\mathrm{RC}}}{k} P_0 \left(1 - e^{-kt}\right) = \frac{L}{E}\, P_0 \left(1 - e^{-kt}\right) \tag{E.12}$$

E.3 Fluid dissipation through the rods

Equation (4.35) is taken as a starting point and substituting the pressure gradient for equation (E.1):

$$W_{Ft\mathrm{R}} = \int \frac{K_{\mathrm{RC}}}{\gamma^f} (P - P_0)^2\, dt = \frac{K_{\mathrm{RC}}}{\gamma^f} \int (P - P_0)^2\, dt = \frac{K_{\mathrm{RC}}}{\gamma^f} \int \left(P^2 + P_0^2 - 2PP_0\right) dt \tag{E.13}$$

Replacing the pressure P by the closed-form expression (E.8):

$$W_{Ft\mathrm{R}} = \frac{K_{\mathrm{RC}}}{\gamma^f} \left[\underbrace{\int \left(P_0 \left(1 - e^{-kt}\right)\right)^2 dt}_{A} + \underbrace{\int \left(P_0^2\right) dt}_{B} \underbrace{-2 \int P_0^2 \left(1 - e^{-kt}\right) dt}_{D} \right] \tag{E.14}$$

The result of each integral is detailed below:

$$A = \int \left(P_0 \left(1 - e^{-kt}\right)\right)^2 dt = P_0^2\, t - \frac{P_0^2}{2k} e^{-2kt} + 2\frac{P_0^2}{k} e^{-kt} \tag{E.15}$$

$$B = \int \left(P_0^2\right) dt = P_0^2\, t \tag{E.16}$$

$$D = -2 \int P_0^2 \left(1 - e^{-kt}\right) dt = -2P_0^2 \left(t + \frac{1}{k} e^{-kt}\right) \tag{E.17}$$

Therefore:

$$W_{Ft\mathrm{R}} = \frac{K_{\mathrm{RC}}}{\gamma^f} \left[\left(P_0^2\, t - \frac{P_0^2}{2k} e^{-2kt} + 2\frac{P_0^2}{k} e^{-kt}\right) + P_0^2\, t - 2P_0^2 \left(t + \frac{1}{k} e^{-kt}\right) \right] + C \tag{E.18}$$

Here again, the integration constant C may be obtained considering that $W_{Ft\mathrm{R}} = 0\,MJ$ when $t = 0\,s$, with this $C = \frac{K_{\mathrm{R}C}}{\gamma^f}\frac{P_0^2}{2k}$.

Finally, substituting the constant C in the equation (E.18):

$$W_{Ft\mathrm{R}} = \frac{K_{\mathrm{R}C}}{\gamma^f}\left[P_0^2\left(t + \frac{2}{k}e^{-kt} - \frac{1}{2k}e^{-2kt}\right) + P_0^2\,t - 2P_0^2\left(t + \frac{1}{k}e^{-kt}\right)\right] + \frac{K_{\mathrm{R}C}}{\gamma^f}\frac{P_0^2}{2k} \tag{E.19}$$